ULTRA-COMPACT AND ULTRA-DIFFUSE STELLAR SYSTEMS IN NEARBY GALAXY CLUSTERS: SIGNS OF ENVIRONMENTAL INFLUENCE?

CAROLIN WITTMANN

Dissertation
submitted to the
Combined Faculties of the Natural Sciences and Mathematics
of the Ruperto-Carola-University of Heidelberg, Germany
for the degree of
Doctor of Natural Sciences

Put forward by
Carolin Wittmann
Born in: Heilbronn, Germany
Oral examination: 09 February 2018

Dedicated to my parents

Der Naturwissenschaftler findet seinen Lohn in dem, was Henri Poincaré die Freude des Begreifens nennt und nicht in den Möglichkeiten der Anwendung, zu denen Entdeckungen führen können.

— Albert Einstein

ABSTRACT

In this thesis we investigate ultra-compact and ultra-diffuse stellar systems in the cores of the nearby Perseus and Fornax galaxy clusters for signs of environmental influences. We search for possible disturbances of their stellar structures by examining their light distributions in deep optical wide field imaging data. In the Fornax cluster we analyse a sample of 355 spectroscopically confirmed compact stellar systems. Our data reveal that many objects show distorted outer structures, although we do not find long tidal streams around any of them. We investigate their spatial and phase-space distributions, and interpret our results in the framework of proposed formation scenarios. In the Perseus cluster we identify a population of 89 diffuse low surface brightness galaxy candidates for which we perform photometry. The majority of the diffuse candidates appear unperturbed based on their stellar structures. We find, however, that galaxies with large sizes seem to be absent in the dense cluster core region. We discuss possible implications for the dark matter content of these systems and compare our sample to faint low surface brightness galaxies in the Coma cluster. Our data reveal a few low-mass galaxies with tidal tails or disturbed morphology, and several diffuse streams and tidal debris. Nevertheless, the number of recent galaxy disruption events seems to be very low in both the Perseus and Fornax galaxy cluster cores, indicating that most of the low-mass galaxy population was probably shaped at earlier epochs.

ZUSAMMENFASSUNG

In dieser Doktorarbeit untersuchen wir ultra-kompakte und ultra-diffuse stellare Systeme in den Zentren des Perseus- und Fornax-Galaxienhaufens auf Anzeichen von Umgebungseinflüssen. Basierend auf tiefen optischen Bilddaten überprüfen wir, ob diese Systeme mögliche strukturelle Störungen ihrer Sternverteilung aufweisen. In Fornax analysieren wir einen Datensatz von 355 kompakten stellaren Systemen, die spektroskopisch bestätigte Haufenmitglieder sind. Unsere Daten zeigen, dass viele Objekte eine deformierte äußere Sternstrukur haben, aber keine langen Gezeitenarme. Wir untersuchen die räumliche und Phasenraum Verteilung und interpretieren unsere Ergebnisse im Rahmen der diskutierten Entstehungs-Szenarien. In Perseus identifizieren wir eine Population von 89 diffusen Galaxien mit sehr geringer Sterndichte, die mögliche Haufenmitglieder sind, und bestimmen deren photometrische Eigenschaften. Die Mehrheit der Galaxien weist keine erkennbaren strukturellen Störungen auf. Allerdings finden wir, dass diffuse Galaxien mit großen Radien im dichten Haufenzentrum zu fehlen scheinen. Wir diskutieren, was dies im Hinblick auf deren Gehalt an dunkler Materie bedeuten könnte, und vergleichen die Galaxien mit diffusen Galaxien im Coma-Galaxienhaufen. Wir finden in unseren Daten sowohl einige massearme Galaxien mit Gezeitenarmen oder strukturellen Störungen als auch mögliche diffuse Galaxienüberreste. Insgesamt erscheint die Anzahl von Galaxien, die möglicherweise kürzlich zerissen wurden, in den Zentren beider Galaxienhaufen jedoch sehr gering. Dies könnte darauf hinweisen, dass die meisten massearmen Galaxien schon vor längerer Zeit ihre heutige Struktur erhalten haben.

CONTENTS

LIST OF FIGURES

LIST OF TABLES

INTRODUCTION

1.1 A COSMOLOGICAL VIEW ON LARGE-SCALE STRUCTURE FORMATION IN OUR UNIVERSE

Galaxies are not uniformly distributed in space but arranged in a filamentary structure. Regions of high galaxy density, where filaments intersect, can harbour rich galaxy clusters and contrast with very empty regions, so-called 'voids'. Fig. 1.1 (bottom) shows the spatial distribution of galaxies in the nearby Universe out to a redshift of $z = 0.2$, forming a huge 'cosmic web'. At the scales of galaxies, galaxy clusters and even clusters of galaxy clusters our Universe appears highly structured and inhomogeneous, with the largest structures extending up to a few 100 Mpc across in size. At larger scales, however, our Universe seems very *homogeneous*, i.e. on average we measure roughly the same galaxy density everywhere. At large scales we even can call our Universe *isotropic*, implying that there is no preferred direction.
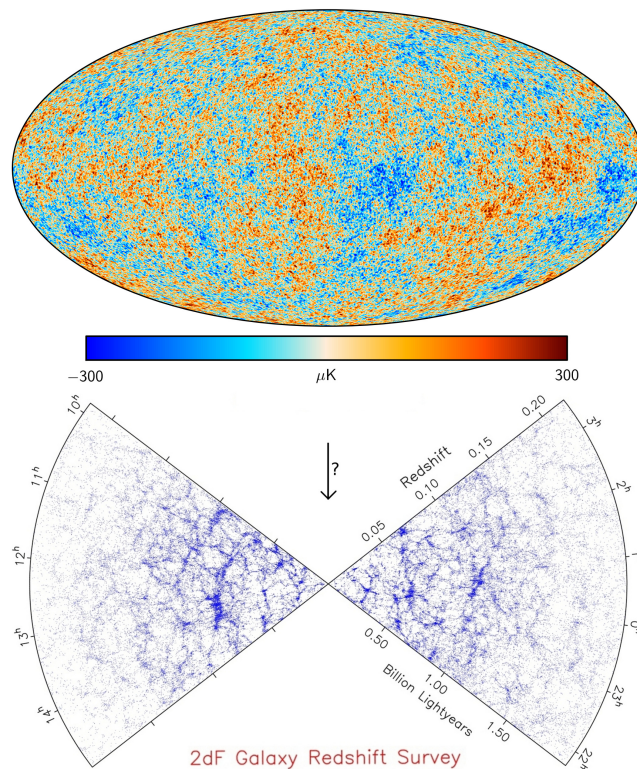
FIGURE 1.1: Top: Temperature map of the cosmic microwave background (CMB), observed with the *Planck* satellite. The map shows tiny temperature fluctuations on the order of 10^{-5} imprinted in the otherwise very homogeneous CMB. (Image credit: ESA and the Planck collaboration.) Bottom: Distribution of galaxies in the nearby Universe as a function of redshift (or lookback time) and right ascension, observed by the 2dF Galaxy Redshift Survey (Colless et al. 2001). In total, more than 200 000 galaxies were observed in a slice of $75 \times 10 \deg^2$ in the northern Galactic hemisphere (left wedge), and in a slice of $80 \times 15 \deg^2$ in the southern Galactic hemisphere (right wedge). A redshift of 0.2 corresponds to a comoving radial distance of about 800 Mpc.

Looking out across ever greater distances in our Universe is equivalent to looking back to ever earlier times, due to the finite speed of light. The earliest time to which we can look back is the time when the cosmic microwave background (CMB) radiation was emitted, at a redshift of about 1100, long before the first stars and galaxies had formed. The CMB radiation is received from every direction of the sky and emits a nearly perfect black body spectrum with a temperature of about $3\,$K. It is highly homogeneous and isotropic, but exhibits tiny temperature fluctuations on the order of 10^{-5} (see Fig. 1.1, top). These temperature fluctuations originate from density fluctuations of the same relative size. Thus, the CMB shows a picture of how matter was distributed in the early Universe.

Fundamental cosmological questions involve how the tiny density fluctuations in the CMB could grow to the large-scale structure we observe today; how the once so homogeneous Universe became inhomogeneous and so highly structured on small scales, giving rise to highly complex structures like galaxies, stars, planets and even life; and, ultimately, what caused the density fluctuations in the CMB itself.

One key point towards a better understanding of our Universe was the realisation that the Universe is expanding. Galaxy spectral lines were found to be shifted towards the red end of the spectrum (e.g. Slipher 1917; Strömberg 1925), implying that they are receding away from us. Lemaître (1927) explained the recessional velocities of the galaxies as a 'cosmical effect of the expansion of the Universe'. Based on spectroscopic data for 24 galaxies with available distance measurements, Hubble (1929) established a linear relationship between distance and radial velocity. Today we use the time-dependent proportionality factor, referred to as the 'Hubble parameter', as a measure for the expansion rate of our Universe. Its value today is $H_0 = 73.24\,\mathrm{km\,s^{-1}\,Mpc^{-1}}$ (Riess et al. 2016) and is called 'Hubble constant'.

The mathematical description of the evolution of our Universe is based on Einstein's field equations of his theory of general relativity (Einstein 1916). Friedmann (1922) and Lemaître (1927) provided a solution to Einstein's equations for a dynamical cosmological model. The cosmological model is based on the two fundamental assumptions of homogeneity and isotropy. Robertson (1929) and Walker (1935) derived all metrics that satisfy these assumptions and fulfil Einstein's equations. The non-stationary, dynamical, solution of the latter yields the cosmological model from Friedmann (1922) and Lemaître (1927) that is still in use today. The cosmological model depends on a number of parameters that have to be determined by observations. The most important cosmological parameters are the present-day expansion rate, given by the Hubble constant H_0, and the density parameters Ω, which describe the geometry as well as the matter and energy content of the Universe. The curvature parameter Ω_k defines the large-scale geometry of the Universe, which can be either open, closed or flat. The radiation density Ω_r refers to the relativistic matter content, whereas the matter density Ω_m accounts for all non-relativistic matter. Ω_Λ denotes the cosmological constant. Einstein originally introduced this term in order to allow a static solution of his equations, but rejected it again when it was widely accepted that the Universe is expanding. Today we include Ω_Λ to account for an accelerated expansion of the Universe (see below).

Reversing the expansion leads to the conclusion that our Universe may have been much denser and hotter at earlier times, and eventually had a beginning – the 'Big Bang'. In fact, there is strong observational support for the possible aftermath of such a Big Bang. Its origin and nature is, however, still subject to speculation. In the very early Universe, where both density and temperature grew to infinite

numbers, the physics are only poorly understood. When the temperature is of the order of one Planck mass $M_P \approx 10^{19}$ GeV or higher, the description of general relativity breaks down and quantum gravitational effects are expected to become important. There are a number of new theories such as string theory that propose various scenarios probing this very early phase of the Universe. In the following we will refer to the Big Bang, irrespective of its nature, as the zero point for counting time.

It is suggested that within a few fractions of a second after the Big Bang our Universe experienced a brief epoch of exponential expansion, called 'Inflation'. According to this scenario the Universe expanded by at least a factor of 10^{26} before entering the more gradual Hubble expansion. The idea of Inflation was originally introduced by Guth (1981), who pointed out that the standard model of cosmology faces two problems, the so-called 'Horizon' and 'Flatness' problem. The Horizon problem (e.g. Rindler 1956; Weinberg 1972; Misner et al. 1973) states that two regions in the sky, which are today separated by more than one degree, could not have been in causal contact since the Big Bang, according to the standard Hubble expansion. This is in contradiction with the assumed homogeneity and isotropy of our Universe, which is observed for example in the temperature distribution of the CMB. Due to the rapid exponential expansion associated with the Inflation scenario, the entire visible Universe could, however, already have been in causal contact prior to the release of the CMB, making it possible to attain a very uniform temperature across the sky. The Flatness problem (e.g. Dicke and Peebles 1979) points out the incredible accuracy to which the initial value of the Hubble parameter must have been fine tuned in order to result in the Universe of flat spatial geometry that we observe today. This problem could be solved with the assumption of exponential expansion during Inflation, too, where any initial curvature of the Universe would flatten out at very early times.

Inflation also provides a possible explanation for the density fluctuations imprinted in the CMB (e.g. Lyth and Riotto 1999). According to Heisenberg's uncertainty principle, matter can be spontaneously created in particle-antiparticle pairs that annihilate almost instantaneously. It is assumed that such quantum fluctuations occur in the inflaton field. During Inflation, the quantum fluctuations would be amplified to macroscopic scales, and may be responsible for the density fluctuations we observe in the CMB.

According to our current understanding, the Universe was filled with a hot plasma of elementary particles after Inflation, including electrons, positrons, photons and neutrinos, as well as protons and neutrons that formed from quarks when the Universe was still hotter. The particles were kept in thermal and chemical equilibrium by scattering processes and pair production–annihilation reactions. As the Universe expanded and cooled, some reactions could no longer take place, since the reaction rate fell below the expansion rate of the Universe. For example, when the temperature dropped below 0.5 MeV the photons were no longer sufficiently energetic to enable the production of electron–positron pairs. Since electrons and positrons continued to annihilate, the number density of this particle species decreased rapidly. Only due to a small excess of electrons over positrons did some electrons survive the annihilation. Without this slight matter–antimatter asymmetry, which must also have been the case at earlier times when proton–antiproton pairs annihilated, there would not be any baryonic matter today! The origin of the matter-antimatter asymmetry still remains a puzzle. Several proposed scenarios are discussed in Dine and Kusenko (2003).

At around one second after the Big Bang, when the temperature dropped below 1 MeV, the Universe had cooled sufficiently to enable the formation of atomic nuclei by the fusion of protons and neutrons, in an epoch called 'Nucleosynthesis'. The principle of primordial element formation was already recognized by Alpher et al. (1948) and Alpher (1948). During this period, the reactions that kept neutrons and protons in chemical equilibrium dropped out of equilibrium and the neutrons decayed into protons and electrons. The onset of Nucleosynthesis prevented the decay of all neutrons by binding them in nuclei. First deuterium formed by the fusion of protons and neutrons. With increasing deuterium density, essentially all deuterium combined to form helium (He^4), which is the most stable light element; traces of He^3 and lithium (Li^7) were also produced. Elements heavier than Li^7 could only later be synthesised in stars. The theory of Big Bang Nucleosynthesis predicts that three minutes after the Big Bang, the baryonic matter in our Universe was made up of 75 per cent hydrogen (H), 25 per cent He^4, and traces of other light elements. The predicted abundances are in good agreement with the primordial light element abundances inferred from observations (see Beringer et al. 2012 for a review).

About 400 000 years after the Big Bang, when the temperature of the Universe has dropped to about 3000 K, it was cool enough for the electrons to combine with atomic nuclei and form neutral atoms. This epoch is referred to as 'Recombination'. From this time on, photons could travel freely through space without further interactions. The formerly opaque Universe thus became transparent to radiation. Alpher and Herman (1949) postulated that this radiation should still be detectable today, although redshifted to lower temperatures. And indeed, this relic background radiation, which now has a mean temperature of 2.72548 K (Fixsen 2009), was detected in the microwave regime by Penzias and Wilson (1965) – the 'CMB'. Although searched for early on, the tiny temperature fluctuations in the CMB were only detected in the 1990s with the *Cosmic Background Explorer* (*COBE*) satellite (Smoot et al. 1992). The next generation satellite missions *Wilkinson Microwave Anisotropy Probe* (*WMAP*; Bennett et al. 2003, 2013) and *Planck* (Planck Collaboration et al. 2014) significantly improved the spatial coverage and accuracy of the CMB measurements. Figure 1.1 (top) shows a map of the CMB as observed with *Planck*.

The temperature fluctuations in the CMB yield detailed information on the geometry and matter content of the early Universe. The strength of the fluctuations on different angular scales can be described by the angular power spectrum of the CMB. By fitting a cosmological model to the latter, it is possible to constrain the cosmological parameters. The CMB power spectrum is not the only approach to measure the cosmological parameters. To date, several independent methods exist, including galaxy clustering analysis (e.g. Percival et al. 2010), measurements of Type Ia supernova distances (e.g. Suzuki et al. 2012; Rest et al. 2014), and weak gravitational lensing (e.g. Heymans et al. 2013). These methods all agree remarkably well in their measured parameters and thus strengthen the consistency of the cosmological model.

The current best-fit parameters obtained from *Planck* are $\Omega_m = 0.308$ and $\Omega_\Lambda = 0.692$ with a derived age of the Universe $t_0 = 13.799$ Gyr (Planck Collaboration et al. 2016). The curvature parameter is found to be very close to zero, consistent with a spatially flat Universe. The radiation energy density can be determined directly from measurements of the CMB temperature and is on the order of $\Omega_r \propto 10^{-5}$ today. Only a minor fraction of the matter content of the Universe is in the form

of visible, baryonic matter. The rest seems to be in a form of unseen, 'dark matter'. The measured cosmological parameters are $\Omega_b = 0.049$ and $\Omega_{dm} = 0.262$, respectively. Of particular note is the large cosmological constant. Indications for a non-zero cosmological constant were first provided from observations of Type Ia supernovae. Riess et al. (1998) and Perlmutter et al. (1999) discovered that supernovae at high redshift are located at greater distances from us than would be expected according to a normal Hubble expansion. Their results imply a Universe with a positive cosmological constant that is currently expanding at an accelerating rate! A so-called 'dark energy' is postulated as the driver for this accelerated expansion, which has a gravitationally repulsive effect. Its nature remains one of the currently unsolved puzzles of modern cosmology.

How could the tiny density fluctuations implied by the CMB anisotropy grow to the pronounced structure we see today in our Universe? – In an expanding Universe, initially slightly denser regions are expected to expand more slowly due to their stronger self-gravity, whereas regions of lower density will expand faster than the average expansion rate. This will inevitably generate an amplification of the density fluctuations over time. If we assume, however, that our Universe consists out of purely baryonic matter, linear perturbation theory predicts density fluctuations of a higher amplitude than observed in the CMB (e.g. Peebles and Yu 1970). Thus, the density perturbations would not have had sufficient time to grow to the scale of the observed present-day structure in our Universe! This problem can be solved with the presence of dark matter. Peebles (1982) suggested 'if the Universe is dominated by massive weakly interacting particles', the density fluctuations could already have started growing before the CMB was released. While the constituents of dark matter are proposed not to interact with photons or baryons, the baryons and photons were tightly coupled before recombination, which prevented the baryons from gravitationally contracting. When the radiation pressure became negligible at the epoch of recombination, the baryons were free to collapse into the potential wells generated by the dark matter perturbations.

There are three kinds of dark matter considered, namely hot, warm, and cold dark matter. They differ in the thermal velocities of their constituents at the time when the matter and radiation densities became equal, and range from relativistic for hot dark matter to non-relativistic for cold dark matter. The constitution of dark matter greatly influences the formation of large-scale structure in our Universe. In models of hot dark matter large structures form first and smaller structures form later by fragmentation (e.g. Bond et al. 1980; Doroshkevich et al. 1981). In contrast, cold dark matter models imply a hierarchical growth of structure, where small structures form first and later merge to form larger structures (e.g. Blumenthal et al. 1984). Models with warm dark matter predict similar structures on large scales as cold dark matter models, but less and more diffuse substructure on small scales (Gao and Theuns 2007). There is good evidence from analyses of structure formation in the Universe that supports models where most of the dark matter is cold (CDM). The current standard model of cosmology, which bests fits to the observational data, is therefore also called the 'ΛCDM model'.

When the density fluctuations continue to grow in the expanding Universe, overdense regions will eventually collapse and virialize to form gravitationally bound structures. This is the principle of the 'spherical collapse model' first derived by Gunn and Gott (1972). From this model, it follows that a virialized object will have an average density 178 times the critical density in the early matter-dominated Universe ($\Omega_m = 1$) at that time. Assuming the standard model of cosmology where

most of the matter is dark, such a virialized object is commonly referred to as 'dark matter halo'. Eventually gas will cool and condense in the centres of these dark haloes to form the first stars and galaxies (White and Rees 1978). The Press-Schechter model (Press and Schechter 1974) provides an analytic description of the number density distribution of virialized haloes as a function of mass at a given time or redshift. It predicts that the number density of haloes decreases with halo mass, with an exponential cut-off at the high mass end that grows with time. A direct consequence of the model is that most of the mass is in small haloes that formed at high redshifts, while high mass haloes in the mass range of today's galaxy clusters are very rare and formed more recently by continuous accretion of smaller haloes and mergers (Lacey and Cole 1993). This is the principle of hierarchical structure formation. The Press-Schechter model is in good agreement with the results from numerical simulations.

Numerical simulations are required to describe structure formation in the late Universe where the density perturbations become highly nonlinear. Large simulations, like the Millenium (Springel et al. 2005) and Millenium-II (Boylan-Kolchin et al. 2009) simulation, follow the evolution of the dark matter distribution in the ΛCDM cosmological model. Results of the simulations showed that from the initially smooth dark matter distribution a large-scale filamentary structure condenses out, with high concentration knots where filaments intersect, and large voids in between. The simulated dark matter distribution appears remarkably similar to the observed large-scale distribution of galaxies, as obtained from redshift surveys, like the 2dF Galaxy Redshift Survey displayed in Fig. 1.1, or from maps of galaxy peculiar velocities (Tully et al. 2014). There are different approaches to link the simulated dark matter distribution to the observed baryonic component. In an empirical method, described by Peacock and Smith (2000), the distribution of galaxies of a given dark matter density field is derived by constraining the number of galaxies that must have formed within virialized dark matter haloes of a certain mass using clustering and abundance analyses of large observational datasets. In another method, followed for example by Moster et al. (2013), galaxies are matched to dark matter haloes by establishing a redshift-dependent relationship between the stellar and the dark matter halo masses. First the simulated dark matter haloes are populated with galaxies according to this relationship. Then the stellar mass function of the model galaxies is computed, allowing the adjustment of the parameters of the stellar-to-halo mass function to match the observed stellar mass functions at various redshifts. An alternative to the above is to directly model the underlying astrophysical processes of galaxy formation. Commonly the output of dark matter simulations is combined with semi-analytical models (e.g. Guo et al. 2011), which describe the physics of gas, stars, super massive black holes and feedback processes. Only recently increasing computational power has allowed large and high-resolution hydrodynamical simulations to be conducted that simultaneously follow the evolution of dark and baryonic matter over cosmic time (Illustris; Vogelsberger et al. 2014). The simulations seem to provide a good match with observations on both large and small scales down to Milky Way mass galaxies, yielding a strong constraint on the underlying cosmological model. Discrepancies, however, remain concerning some of the properties of low-mass galaxies, requiring a better understanding of their formation.

The ΛCDM model is currently accepted as the most successful model describing the gradual built-up of cosmic structure from the density fluctuations imprinted in the CMB to the present-day state of the Universe. However, the nature of two of its

major ingredients, dark matter and dark energy, remain a mystery so far. One possibility to circumvent the requirement of non-baryonic dark matter is to subscribe the observed discrepancy between measured and observed mass in our Universe to a modification of Newtonian dynamics in the regime of very low accelerations that occur on the scales of galaxies or below (MOND; Milgrom 1983b). Indeed, the paradigm of MOND successfully predicts many of the observed properties of galaxies. However, a basic underlying theory for MOND that could provide the framework for cosmic structure formation still has to be established.

1.2 ENVIRONMENT

'Environment' is a commonly used term to specify regions of different matter density, i.e. cosmic over- and underdense regions, which are predefined by the large-scale matter distribution in our Universe. Environment is not static, but constantly evolving. Over- and underdense regions in the cosmic web drive a large-scale flow of matter from regions of lower to regions of higher density (Tully et al. 2014).

The densest environments are rich galaxy clusters, which constitute the largest gravitationally bound structures known. These rare systems, which are thought to have evolved from the highest peaks in the primordial density field, reach masses on the order of 10^{14}–10^{15} M$_\odot$, with corresponding virial radii of about 1–2 Mpc. Galaxy clusters can easily harbour thousands of galaxies of all kinds, with typically tens to hundreds of members with bright luminosity, and with velocity dispersions of about $1000 \, \mathrm{km \, s^{-1}}$. But despite clusters being the places where the highest galaxy number densities in the Universe are reached, the baryons bound in stars in and around galaxies represent only a minor fraction of the overall mass budget of the cluster. In fact, most of the baryons are in the hot diffuse gas that fills the 'intracluster medium' (ICM) in between the cluster galaxies. The diffuse gas has a temperature on the order of 10^7–10^8 K and emits in X-rays. The fraction of the gas mass increases with cluster mass, whereas the fraction of the stellar mass decreases, resulting in a nearly constant baryon fraction in clusters across the considered mass range (Andreon 2010). For a typical cluster with a mass of $10^{14.5}$ M$_\odot$, the stellar mass makes up about 2 per cent of the total cluster mass, whereas the gas mass contributes about 11 per cent. This suggests that about 87 per cent of the total cluster mass is in the form of non-baryonic dark matter.

Galaxy clusters are continuously growing through accretion of individual 'infalling' galaxies, entire galaxy groups or even mergers with other massive clusters. The degree to which the accreted substructure is incorporated within the host cluster potential defines whether we speak of a dynamically relaxed or unrelaxed cluster. Unrelaxed clusters commonly show substructure in their galaxy spatial and velocity distribution, where distinct subclumps of recently accreted galaxies can be identified. Large offsets between the position of the brightest cluster galaxy and the peak of the X-ray emission, which traces the cluster potential, are often taken as an indication that the cluster underwent a recent merger (e.g. Hudson et al. 2010). Relaxed clusters are more regular and typically show a smooth, more concentrated distribution of galaxies, which is well traced by the X-ray emitting gas. There are good indications that the fraction of dynamically relaxed clusters strongly decreases towards higher redshifts (e.g. Mann and Ebeling 2012).

The first large and systematic catalogue of galaxy clusters was established and subsequently extended by Abell (1958) and Abell et al. (1989), containing 4073

clusters in the nearby Universe. Thanks to large spectroscopic galaxy as well as X-ray surveys, important galaxy cluster catalogues were created by Koester et al. (2007) based on the Sloan Digital Sky Survey (SDSS), and Piffaretti et al. (2011) based on X-rays.

Galaxy groups refer to smaller accumulations of galaxies with usually only a few bright members and total masses in the range of 10^{12}–$10^{13} \, M_\odot$. There is, however, a blurred boundary between the definition and properties of groups and clusters. Compared to clusters, the galaxy members of a group typically have a lower velocity dispersion on the order of a few hundreds of $km \, s^{-1}$. X-ray observations indicate that about half of all nearby galaxy groups are emitting in X-rays (Mulchaey 2000), indicating the presence of a hot diffuse 'intragroup medium' similar to the ICM detected in clusters, but with a lower temperature of about 10^6–$10^7 \, K$. Large group catalogues have been established for example based on the 2dF Galaxy Redshift Survey, where Eke et al. (2004) reported that 55 per cent of all detected galaxies are members of galaxy groups with at least two members.

Galaxies that are not gravitationally bound to a galaxy group or a galaxy cluster are commonly referred to as 'field galaxies'. The 'field' denotes an environment that is characterised by the lowest galaxy density and may even be entirely devoid of galaxies.

A galaxy may experience different environments over the course of its lifetime, leaving an imprint on its present-day appearance. We will discuss the observed correlations between galaxy properties with environmental density in Sections 1.3 and 1.4.1, and explain the underlying physical mechanisms that act on galaxies in dense environments in Section 1.4.2.

1.3   GALAXIES

Although galaxies show a wide variety of properties they can be separated into a few major categories according to their morphology. Elliptical galaxies are galaxies with a typically smooth ellipsoidal appearance and no further obvious substructure. Spiral galaxies are characterised by a disk and a bulge component, where the stars and the gas in the disk form a spiral pattern. Some spiral galaxies also harbour a bar in their central region. Lenticular galaxies show a bulge and a disk component like spiral galaxies, but lack spiral arms similar to elliptical galaxies. Galaxies that have neither a bulge nor a disk component and are characterised by a rather patchy morphology without symmetric structures are called irregular galaxies. For historical reasons elliptical and lenticular galaxies are also referred to as 'early-type galaxies', while for spiral and irregular galaxies the term 'late-type galaxies' is used.

The morphological segregation among the population of galaxies motivated the well-known galaxy classification scheme proposed by Hubble (1926). In this scheme elliptical galaxies are arranged in a sequence of increasing ellipticity with types E0-E7, where the integer value denotes the closest value to $10(1 - b/a)$, with semimajor axis a and semiminor axis b. Spiral galaxies are sorted by decreasing bulge-to-disk ratios from types 'Sa' to 'Sc', which also correlates with the tightness with which the spiral arms are wound. Originally, spiral galaxies were further separated into barred and unbarred types, leading to the 'tuning fork' structure of the classification scheme (Hubble 1936). Lenticular galaxies of type 'S0' were initially placed in between the class of elliptical and spiral galaxies.
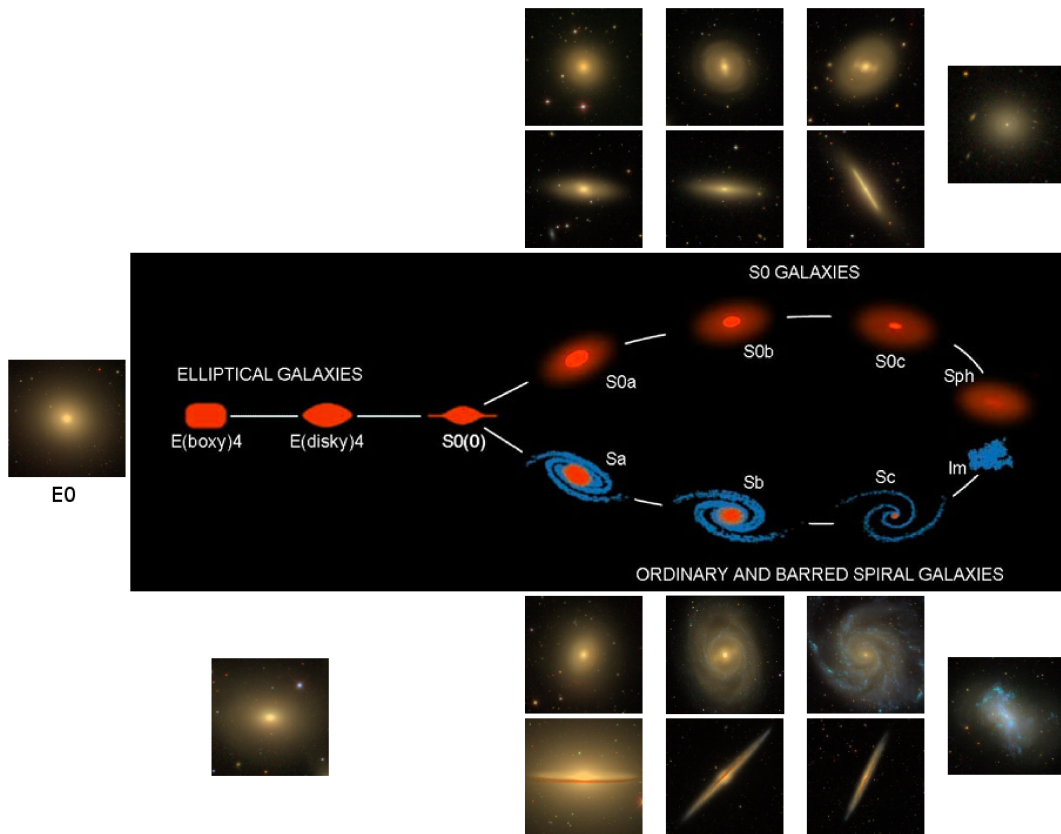
FIGURE 1.2:   Revised morphological galaxy classification scheme proposed by Kormendy and Bender (2012). The main modifications with respect to the original Hubble classification scheme lie in lenticular galaxies being ordered with decreasing bulge fractions in parallel to the spiral galaxies, and bulgeless systems of type Sph and Im being added to the end of both sequences. Both S0a-S0c and Sa-Sc types also exist with central bars. Elliptical galaxies can have isophotes deviating from perfect ellipses, with either 'boxy' or 'disky' shapes. Central panel: Kormendy and Bender (2012). Galaxy images: SDSS Data Release 14.

With growing knowledge of the structural properties of galaxies, modified and extended versions of Hubble's classification scheme were introduced. For example, irregular galaxies, which were not part of the original Hubble sequence, were included as type 'Im' in extension to spiral galaxies. de Vaucouleurs (1959) proposed a classification scheme that distinguishes between finer subclasses among spiral and irregular galaxies, for example with intermediate types 'Sab' or 'Sac'. The observation that lenticular galaxies exist with a wide range of bulge-to-disk ratios similar to that observed for spiral galaxies motivated the classification scheme of van den Bergh (1976) placing lenticular galaxies with types 'S0a' to 'S0c' in parallel to the sequence of spiral galaxies. Fig. 1.2 shows the classification scheme proposed by Kormendy and Bender (2012). It further includes purely spheroidal systems without a bulge component as type 'Sph' as an extension to the sequence of lenticular galaxies. Importantly, many of the intrinsic physical galaxy properties, like star formation activity, stellar population properties or gas content, change along with the morphological sequence.

In general, elliptical and lenticular galaxies do not show ongoing star formation and are characterised by mainly old, passively evolving stellar populations. This is reflected in their predominantly red photometric colour. In contrast, spiral and irregular galaxies typically show ongoing or sustained star formation activity.

Accordingly, young or intermediate-age stellar populations dominate their light distribution and make the colour of the galaxy to appear blue. Typically, the bulge component in spiral galaxies is dominated by older stars, whereas the disk contains stars with a wide variety of ages. For instance, the spiral arms are observed to be sites for the formation of very young stars, but at the same time the spiral structure is also visible in the near infrared, indicating the presence of older stellar populations. Most elliptical and spiral galaxies also show radial colour gradients, with the outer galaxy regions being bluer in colour (e.g. Peletier et al. 1990; Bell and de Jong 2000). This is commonly interpreted in the way that the central regions are older and/or more metal-rich than the outer galaxy regions.

The star formation activity of a galaxy is directly linked to the available reservoir of cold gas. In spiral galaxies, cold gas in the form of neutral hydrogen (H I) and molecular hydrogen (H_2) makes up the major fraction of the total gas mass of the disk. In general, the molecular gas traces the distribution of the stars, whereas the atomic gas can be much more extended. Spiral galaxies also often exhibit regions of ionized hydrogen (H II), which is typically associated with star forming regions. In disk galaxies, the gas mass fraction with respect to the total baryonic mass is observed to increase towards systems of fainter surface brightness. McGaugh and de Blok (1997) found that the gas mass fraction increases from about 10 per cent in brighter surface brightness spiral galaxies to about 80 per cent in low surface brightness spiral galaxies. In elliptical galaxies, cold gas makes up only a minor fraction of the galaxy's gas mass. In fact, the interstellar medium of bright ellipticals is instead dominated by very hot ($\sim 10^7$ K) gas emitting in X-rays, which can contribute as much as $\sim 10^{10}$ $M_\odot$ to their total mass.

The flat morphological structure of spiral galaxies can be explained by their dynamical properties, indicating that they are rotationally supported systems. Early-type galaxies, although characterised by a common morphology, can be separated into two dynamical classes: slow and fast rotators, which are defined according to the ratio of ordered rotation to random motion of their stars. Slow rotators, which are mainly supported by random motions, are almost exclusively very bright elliptical galaxies with magnitudes $M_V \lesssim -21.5$ mag. They are commonly found to be rounder than fast rotating galaxies, with ellipticities smaller than $\epsilon \lesssim 0.4$. The light distribution of slow rotators often cannot be traced by perfectly elliptical isophotes, and is instead described by more rectangular 'boxy' isophotes. Kinematic maps derived from integral field spectroscopy revealed that slow rotators often show a complex dynamical structure, harbouring, for example, kinematically decoupled cores or counter-rotating disks (Emsellem et al. 2011). The majority of normal luminosity early-type galaxies, however, seems to be fast rotators, with kinematical properties similar to that of late-type galaxies with extended disks. Fast rotators often have more disky isophotes and exist with a variety of axis ratios. They can be both galaxies that are morphologically categorized as either elliptical or lenticular galaxies. I.e. a lenticular galaxy seen face-on appears like an elliptical galaxy without a disk. Only kinematics can reveal the presence of a possible disk, independent on the inclination of the galaxy. Cappellari et al. (2011) proposed a galaxy classification scheme based on stellar kinematics, separating galaxies into slow and fast rotators. In this scheme, slow rotators correspond to the morphological types E0-E4. Fast rotators represent the flatter ellipticals E5-E7 and lenticular galaxies S0a-S0c. The latter are again set in parallel to the spiral types Sa-Sc. We will see later that the fast rotator early-type galaxies may be closely connected to the spiral

galaxies with regard to their evolution, while the slow rotators likely followed a different evolutionary path.

According to the virial theorem, the dynamical properties of a galaxy are a direct tracer of its total gravitational mass. Interestingly, at the centre of most nearby early-type galaxies, or bulges of late-type galaxies, the observed stellar velocity dispersion is higher than may be inferred from the mass of the stellar population alone, giving rise to elevated dynamical mass-to-light ratios. This signature is commonly interpreted as a strong indication of the presence of a central super massive black hole (SMBH). The bulge of our Milky Way harbours a SMBH, too, with an inferred mass of $4 \times 10^6 \, M_\odot$ (Gillessen et al. 2009).

Also in the outskirts of spiral galaxies the measured rotation velocities inferred from H I gas are observed to be higher than can be explained by the mass of the stars and the gas alone. This is observed as 'flat' rotation curves, where the rotation velocity remains constant with radius instead of declining as would be expected from Kepler's law for the baryonic mass distribution. This excess rotation speed is commonly interpreted as evidence for extended haloes of dark matter surrounding the galaxies. Various studies derived high dark matter fractions for spiral galaxies on the order of 50-70 per cent within $2.2 \, R_d$, where R_d is the disk scale length (see, e.g., Courteau and Dutton 2015).

Due to the lack of H I gas, the dynamical mass distribution of early-type galaxies is commonly derived from stellar kinematics, using integral field spectroscopy. Following this method, Cappellari et al. (2013) inferred a median dark matter fraction of 13 per cent within one half-light radius for a sample of 260 early-type galaxies. While it seems that early-type galaxies contain a lower dark matter fraction within a given radius compared to late-type galaxies (e.g. Courteau and Dutton 2015), the differences can also be subscribed to, e.g., variations in the initial mass function of early-type galaxies. Overall the general picture seems to be that galaxies typically are baryon-dominated in their centre and dark matter dominated in their outskirts. However, a different interpretation of the observed mass discrepancy is given in the framework of MOND, where a change of Newton's law of gravity in the regime of very low accelerations (a $\lesssim 10^{-10} \, \mathrm{m\,s^{-2}}$; Begeman et al. 1991; McGaugh 2011) predicts the observed galaxy dynamics without the need for dark matter (Milgrom 1983a; de Blok and McGaugh 1998; McGaugh and de Blok 1998).

It was already recognized early on that there exist differences in the galaxy populations between the densest regions of galaxy clusters, where elliptical and lenticular galaxies dominate, and the low-density field, where spiral galaxies are most common (e.g. Hubble and Humason 1931; Oemler 1974). Based on a study of galaxy morphologies in 55 clusters, Dressler (1980) found a relation between local galaxy density and morphological type, where the fraction of elliptical and lenticular galaxies increases with local density while the fraction of spiral and irregular galaxies decreases. This 'morphology-density relation' was subsequently confirmed by many studies and seems to hold for a very large number of galaxies, e.g. the Galaxy Zoo sample with over 10^5 galaxies (Bamford et al. 2009; Skibba et al. 2009). The latter studies further noted that the correlation between galaxy colour and environment might be even stronger compared with the correlation to morphology, with a higher fraction of red galaxies in dense environments. Other galaxy properties were found to show environmental dependencies as well. For example, Cortese and Hughes (2009) found that gas deficient galaxies are preferentially located in high density regions. Cappellari et al. (2011) pointed out that

slow rotator galaxies seem only to exist at the largest environmental densities and are essentially absent in the field.

In clusters at intermediate redshift, Butcher and Oemler (1978) noted that the fraction of blue galaxies is significantly higher compared with nearby clusters, also known as the 'Butcher-Oemler effect'. Furthermore, high resolution imaging studies with the *Hubble Space Telescope* (*HST*) showed that many of the blue cluster members at higher redshift show a disturbed morphology (e.g. Couch et al. 1994). In fact, Delgado-Serrano et al. (2010) found that the fraction of peculiar galaxies with irregular morphology is about five times higher in clusters at $z = 0.4$-0.8 compared with present day clusters, whereas the fraction of regular spiral galaxies seems to be a factor of 2.5 lower. In general, various studies showed that the fraction of spiral galaxies in clusters increases with redshift, whereas the fraction of lenticular galaxies decreases correspondingly (e.g. Dressler et al. 1997; Postman et al. 2005). In contrast, the fraction of elliptical galaxies seems to remain fairly constant, at least out to a redshift of $z \lesssim 1$.

The current picture of galaxy formation and evolution largely emerges from the observed environmental dependencies of galaxy properties. The progenitors of today's spiral galaxies are thought to have formed in regions of initially lower matter density. In the CDM framework of galaxy formation, a rotating disk galaxy may assemble in a dark matter halo through dissipational collapse of a gas cloud with some initial angular momentum (Mo et al. 2010). When the gas in the disk becomes sufficiently dense it will collapse into smaller clumps where the first stars and star clusters are able to form. Eventually a bulge component develops when the clumps migrate to the centre and merge (Bournaud et al. 2007; Dekel et al. 2009). If the galaxy remains in isolation it will continuously grow in mass and size through gas accretion or gas-rich mergers, resembling today's spiral or irregular galaxies. However, if the galaxy instead becomes part of a denser environment, it will lose the ability to efficiently accrete fresh gas since the galaxy no longer resides at the bottom of the gravitational potential. The galaxy may even be stripped of part of its own gas reservoir when it moves through sufficiently dense gas regions of the host halo system (e.g. Boselli and Gavazzi 2006). At the same time, the probability of mass accretion though mergers will decrease, due to the generally higher relative velocities between galaxies in a cluster environment. As a consequence, the galaxy will stop growing in mass and size, and its star formation will be quenched, rendering the galaxy passive. The resulting galaxy will closely resemble today's fast rotator early-type galaxies from its structural and kinematical properties. Thus, there might be a possible evolutionary link between late- and early-type fast rotator galaxies, where the former are transformed into the latter when being accreted into a dense environment (Cappellari 2016).

In contrast, the progenitors of early-type slow rotators are thought to have formed in the initially highest dark matter densities in the early Universe. They are believed to have accreted a lot of gas early on, since they dominate the overall gravitational potential, and formed their stars quickly. Due to the rapid growth in mass, internal quenching mechanisms may have stopped star formation at a very early epoch, resulting in massive elliptical galaxies with passively evolving stellar populations. Unlike fast rotators in dense environments, slow rotators are subsequently expected to grow further in mass and size through dissipationless 'dry' mergers with other gas-poor massive elliptical galaxies (e.g. Khochfar and Burkert 2005; Cox et al. 2006). This additional growth possibly explains why slow rotators are almost exclusively brighter than fast rotators. The observation that slow rota-

tors only exist in the densest environments and often show disturbed kinematics supports this scenario. There is common agreement that there is a dichotomy between the class of today's fast and slow rotating galaxies (e.g. Kormendy and Bender 1996; Cappellari 2016), which may have followed different evolutionary paths driven by their individual merger and accretion history (Khochfar et al. 2011).

1.4   LOW-MASS STELLAR SYSTEMS

Although galaxies with masses and sizes comparable to that of our Milky Way dominate the galaxy population by mass and luminosity, faint and low-mass stellar systems dominate by numbers. Typically, stellar systems are counted amongst the low-mass population when they have total magnitudes fainter than $M_V \simeq -19\,\mathrm{mag}$, or stellar masses below $M_* \simeq 10^{10}\,M_\odot$. Fig. 1.3 shows the luminosity–size distribution for different types of stellar systems. In general, it can be said that luminosity and size are correlated, where larger systems have a brighter luminosity. Interestingly, in the low stellar mass regime the luminosity–size relation broadens and splits up into two distinct branches. One branch is populated by compact stellar systems, which follow the luminosity–size relation of the massive ellipticals, and ranges from compact elliptical galaxies (cEs) at the bright end over the intermediate ultra-compact dwarf galaxies (UCDs) to globular clusters (GCs) at the faint luminosity end. These stellar systems are characterised by rather small sizes for their luminosity resulting in a compact morphology with bright surface brightness. The other branch harbours diffuse stellar systems and includes the diverse population of dwarf galaxies. They generally have by an order of 10-100 larger sizes compared with compact objects of the same luminosity, leading to a fainter surface brightness and a more diffuse morphological appearance. The morphological diversity among the population of low-mass stellar systems is illustrated in the left-hand panels in Fig. 1.3. Shown are stellar systems of similar luminosity, but with different sizes and thus different surface brightnesses.

1.4.1   *The diffuse and compact populations*

Dwarf galaxies were not originally part of the Hubble classification scheme, but were included later as type 'Sph' or 'Im' (e.g. Kormendy and Bender 2012). Im type dwarfs include the dwarf irregular galaxies (dIrrs). They have similar properties as the more massive irregular galaxies, with an irregular morphological appearance, bright H ɪɪ regions, substantial amounts of gas and dust, and ongoing star formation. The galaxies appear overall blue in colour, but Hunter and Elmegreen (2006) pointed out complex colour patterns and a variety of colour gradients for their sample of 136 nearby dIrrs. An extreme type of dIrrs are the blue compact dwarf galaxies (BCDs). They are typically more compact than dIrrs and experience very intense bursts of centrally concentrated star formation. Accordingly, BCDs are very gas-rich systems with a typical gas fraction of about 50 per cent or more with respect to their total baryonic mass (Zhao et al. 2013). While most of the brighter late-type dwarfs seem to be rotationally supported, this is typically not the case for the faintest dIrrs found in the Local Group, which show more complex kinematics (e.g. Mateo 1998). In general, dIrrs seem to have higher dark matter fractions compared to, e.g. spiral galaxies, with being dominated by dark matter even within their visible stellar extent (Côté et al. 2000).
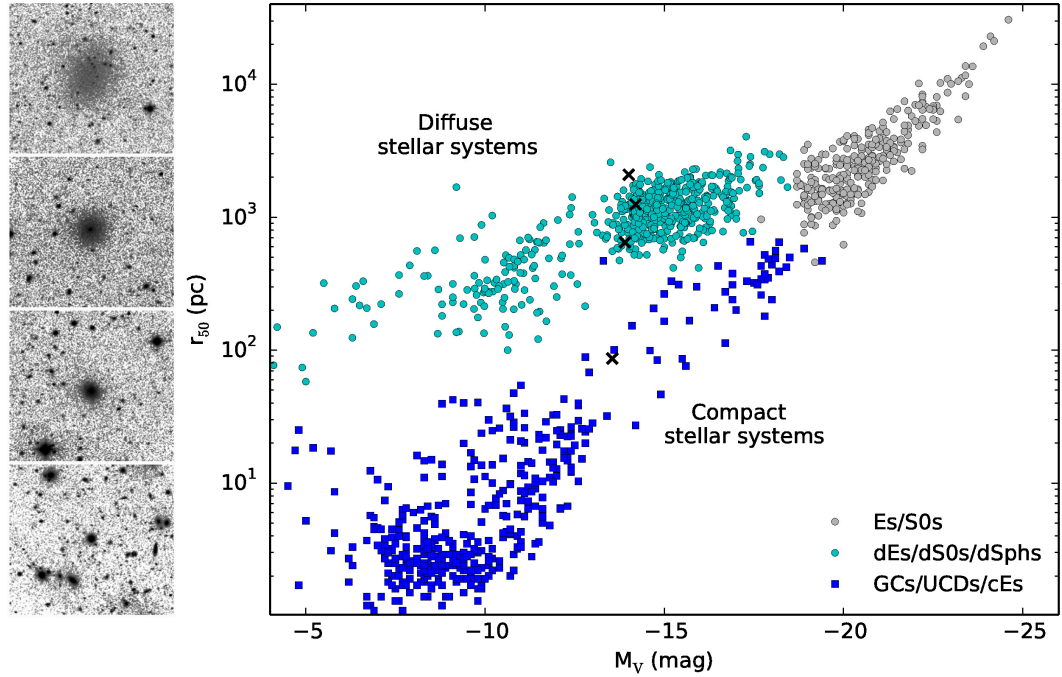
FIGURE 1.3: Luminosity–size relation of different types of stellar systems. The plot shows the total V-band magnitude M_V versus the half-light radius r_{50}. Es/S0s: luminous elliptical and lenticular galaxies (compilation of Norris et al. 2014). dEs/dS0s/dSphs: dwarf elliptical, dwarf lenticular and dwarf spheroidal galaxies (Lieder et al. 2012; McConnachie 2012; compilation of Lisker et al. 2013, based on the Virgo Cluster Catalogue (VCC), Binggeli et al. 1985). GCs/UCDs/cEs: Globular clusters, ultra-compact dwarf galaxies and compact ellipticals (compilation of Norris et al. 2014). The black crosses mark the low-mass stellar systems shown in the four panels on the left-hand side, which are ordered by decreasing half-light radius from top to bottom. The displayed objects are likely and confirmed members of the Fornax galaxy cluster, which is at a distance of about 20 Mpc. The images are cutouts from our final mosaic of the Fornax galaxy cluster (see Chapters 2 and 3). Each panel has the same physical size of $15 \times 15\,\mathrm{kpc}^2$ at the distance of Fornax. The images are shown with the same intensity and contrast scaling.

Dwarf galaxies of the type Sph include the large class of dwarf elliptical and dwarf lenticular galaxies (dEs, dS0s). At first glance they appear as smooth and regular as their more luminous counterparts. Lisker et al. (2006a, 2007) found, however, a surprising complexity in this type of dwarf galaxy: many of the dEs in Virgo harbour stellar disks and exhibit substructures like bars and faint spiral arms. These kinds of feature have also been detected in early-type dwarfs in other nearby galaxy clusters, like Fornax and Coma (e.g. De Rijcke et al. 2003; Marinova et al. 2012). Some early-type dwarf galaxies contain massive star clusters at their centres, with stellar masses in the range of 10^6-$10^8\,\mathrm{M}_\odot$, also called 'nuclei'. Côté et al. (2006) found that between 70-80 per cent of early-type dwarf galaxies with $M_B \leqslant -15$ mag are nucleated, based on a study with *HST* imaging data. In general, non-nucleated dEs were found to be flatter than the nucleated ones (Lisker et al. 2007). The faintest early-type dwarfs with $M_V > -14$ mag are often called 'dwarf spheroidal galaxies' (dSphs), and even fainter ones with $M_V > -8$ mag are referred to as 'ultra faint dwarfs' (UFDs). Similarly, early-type dwarf galaxies with the largest sizes of $r_{50} \geqslant 1.5$ kpc were dubbed 'ultra-diffuse galaxies' (UDGs). However, so far there is no obvious indication that these differently named systems are of physically different nature.

The overall population of dEs seems to be devoid of gas with intermediate to old stellar populations. Compared to more massive early-type galaxies, dEs have, on average, younger ages and are more metal-poor (Michielsen et al. 2008). Rakos and Schombert (2004) found that nucleated dEs appear to be older than non-nucleated ones. The nuclei are mostly observed to have younger ages than their host galaxy and a more metal-rich stellar population (Chilingarian 2009; Paudel et al. 2011). Interestingly, some dEs show blue central colours, possibly indicating an episode of recent star formation in their very centres (Lisker et al. 2006b; Urich et al. 2017). In general dEs seem to show a variety of colour gradients, ranging from constant to radially decreasing metallicity, and constant to mildly increasing stellar age (Chilingarian 2009; Ryś et al. 2015). Urich et al. (2017) showed that dEs with blue cores have the steepest age gradients, but metallicity gradients comparable to those of normal dEs.

In nearby galaxy clusters detailed studies of the kinematic properties of dEs have mainly been limited to the brightest systems so far. Toloba et al. (2009) found that a large fraction of dEs is rotationally supported, while others do not rotate at all. Overall Ryś et al. (2013) and Toloba et al. (2014a) reported a wide variety of kinematical properties, with some dEs harbouring kinematically decoupled cores similarly to those observed in some massive elliptical galaxies. Although dEs do not seem to be dominated by dark matter in their inner regions, with dynamical mass-to-light ratios in the range of about 2-10 (Geha et al. 2002; Toloba et al. 2011; Ryś et al. 2014), Toloba et al. (2014b) derived a dark matter fraction of 46 per cent within one half-light radius, which is higher than observed in massive early-type galaxies. In contrast, the low surface brightness dSphs and UDGs are commonly believed to be highly dark-matter dominated, with dynamical mass-to-light ratios of the order of 100 or higher within one half-light radius (McConnachie 2012; van Dokkum et al. 2016).

An environmentally dependent morphological segregation is also apparent for the class of dwarf galaxies, with the fraction of early-type dwarfs being significantly higher in denser environments, while late-type dwarfs dominate in lower density regions (e.g. Binggeli et al. 1987; Trentham and Tully 2002). Lisker et al. (2007) even reported a morphology-density relation within the class of dEs: those without substructure are preferentially located in high-density regions, dEs with disks reside in intermediate density regions, and dEs with central star formation typically only populate the low-density cluster regions. Correlations to environmental density are also reported with respect to other galaxy properties, which seem to be even more pronounced for dwarfs compared to the more massive galaxy population. For example, Gavazzi et al. (2013a,b) found that low-mass galaxies with redder colours and systems devoid of gas dominate in high density regions. Accordingly, the specific star-formation rate is observed to decrease towards the cluster centre. Furthermore, dEs in the cluster outskirts seem to have several Gyr younger stellar populations compared to those in the cluster core (Paudel et al. 2011; Sybilska et al. 2017). With regard to dynamical properties it is still debated whether there exists a trend with rotationally supported dEs preferentially residing in the cluster outskirts, or not (Toloba et al. 2009; Ryś et al. 2013). Ryś et al. (2014) additionally reported a trend that dEs in the outer cluster regions have on average higher dynamical-to-stellar mass ratios.

The class of compact stellar systems includes the densest stellar systems known in our Universe, reaching densities only found in galaxy nuclei or in the inner

regions of massive galaxies. Commonly three types of compact stellar systems are distinguished, according to their luminosity or stellar mass. Compact objects in the stellar mass range 10^9–$10^{10}\,M_\odot$ and with half-light radii of a few hundred parsec are typically defined as cEs. UCD are known as objects with stellar masses 10^6–$10^8\,M_\odot$ and half-light radii smaller than 100 pc. GCs occupy the low-mass range $M_* \simeq 10^4$–$10^6\,M_\odot$ with half-light radii of only a few parsec. The different types of compact stellar systems are not, however, well separated in the luminosity–size parameter space. Instead UCDs and cEs seem to form a tight luminosity–size relation (e.g. Haşegan et al. 2005) that levels off to constant sizes in the low-mass regime of GCs.

The majority of compact stellar systems are found in association with a galaxy. Galaxies harbouring compact stellar systems are known to exist in all environments, from the field to the centres of rich galaxy clusters. GCs accompany all morphological types of galaxies from dwarf to Milky Way size to the most massive cluster galaxies. They typically form a large GC system that can contain several hundreds of members in the case of a massive galaxy. In general, the properties of the GC system are known to correlate with the properties of the host galaxy (e.g. Brodie and Strader 2006). UCDs and cEs seem to be associated with massive galaxies only. Interestingly, a few cEs were also found in isolation, without a larger host galaxy (Huxor et al. 2013; Paudel et al. 2014; Chilingarian and Zolotukhin 2015). While UCDs are still quite common, cEs seem to be a very rare type of stellar system, with only about 200 detected objects to date (Chilingarian and Zolotukhin 2015).

GCs are among the oldest stellar systems known in our Universe, reaching ages typically older than 10 Gyr. Most galaxies harbour a GC system with a bimodal colour distribution. Spectroscopy has shown that the vast majority of GCs is old and the colour bimodality is due to a metallicity difference, dividing GCs into a blue metal–poor and a red metal–rich population. In nearby spiral galaxies, where GCs have been studied in most detail due to their proximity, the metal-rich population is commonly found to be associated with the bulge component, whereas the metal-poor population resides in the galaxy's halo. In massive elliptical galaxies, the metal-rich GC population is often observed to be more centrally concentrated and to trace the galaxy's overall light, whereas the metal-poor population has a more extended radial distribution. Most often the GC systems commonly extend out to larger galacto-centric distances than the galaxy's field stars. Most UCDs have very old stellar populations, similar to those of GCs. However, a significant fraction of UCDs are known with intermediate ages, in the range of 2–7 Gyr (Janz et al. 2015; Hilker 2017). UCDs show a wide spread of metallicities, but are generally more metal-rich compared to the diffuse galaxy population at the same luminosity. cEs span a range in stellar population ages with the majority having ages as old as 10 Gyr or more, but with many other systems harbouring intermediate age stellar populations. One common characteristic of the cE population seems to be that they are very metal-rich compared to other stellar systems at the same luminosity, reaching metallicities as high as in the centres of more massive galaxies (Janz et al. 2015). In contrast to the population of the diffuse stellar systems, cEs do not seem to show a correlation of their stellar population properties with environment (Chilingarian and Zolotukhin 2015).

GCs typically have dynamical-to-stellar mass ratios close to unity, indicating that they must be largely composed of stars. Interestingly, many UCDs show an elevated mass ratio with a high dynamical mass compared to their stellar mass (e.g.

Forbes et al. 2014). One interpretation is that this may be due to the presence of a central massive black hole. For example, Mieske et al. (2013) argued that elevated mass ratios could be explained by the presence of a black hole which makes up 10–15 per cent of a UCDs' total mass. Indeed, this was confirmed for three nearby UCDs, based on stellar kinematics (Seth et al. 2014; Ahn et al. 2017). Another reason leading to the elevated mass ratios might be a different initial mass function for UCDs compared to GCs (Mieske et al. 2008a), or tidal perturbations of their stellar component, where the high dynamical mass could be caused by the system being currently out of virial equilibrium (Forbes et al. 2014). A high dark matter content is commonly considered to be unlikely as an explanation for the elevated mass ratios (see, e.g., Forbes et al. 2014, and references therein). The population of cEs seems to be characterised by dynamical-to-stellar mass ratios close to unity, as seen for the population of GCs. Nevertheless, central massive black holes have also been detected in a few cEs (Kormendy et al. 1997; van der Marel et al. 1997).

1.4.2 *Environmental influence*

The observed correlations of galaxy properties to environmental density is often taken as indirect evidence of environmental influence on galaxy evolution. Physical processes acting on stellar systems in dense environments like galaxy clusters can be broadly separated into two types: gravitational interactions involving interactions with other galaxies and with the overall cluster potential, and hydrodynamical interactions with the hot ICM of the cluster.

A galaxy orbiting in a cluster experiences the gravitational pull of the cluster potential, giving rise to tidal forces. When the tidal forces exceed the galaxy's own binding forces, its gas, stars and dark matter may be stripped away. Assuming the galaxy has a mass m and is on a circular orbit of radius R within a cluster of mass M, the tidal radius R_t of the galaxy can be defined as $R_t = R(m/3M)^{1/3}$, accounting for the centrifugal force due to the galaxy's circular motion around the cluster centre (King 1962). Thus, the galaxy will experience mass loss as soon as its radius becomes smaller than the tidal radius. Since the galaxy's binding forces weaken with increasing galacto-centric radius, material from the outer galaxy regions will be stripped first. The above dependence of the tidal radius on distance from the cluster centre further implies that tidal stripping is more efficient in the central cluster regions than in the outskirts. In general, tidal stripping is thought to be more severe for low-mass objects compared to the more massive cluster members. However, compact objects have a steeper gravitational potential well where more mass is situated in the centre, while diffuse objects are characterised by a shallower gravitational potential well with a more extended mass distribution. Thus, while both systems would have the same tidal radius when they have a similar mass, the diffuse systems would lose a larger fraction of their total mass. The stripped material trails along the orbit of the galaxy, giving rise to tidal streams or tidal tails. The dispersing tidal tails may then contribute to the build-up of the diffuse intracluster light (e.g. Willman et al. 2004; Mihos et al. 2005).

Galaxy clusters are the environments that reach the highest galaxy number densities and the highest velocity dispersions. Thus, the cluster galaxies may experience close high-speed encounters with other cluster members. The combined effect of multiple high-speed encounters and the overall cluster tidal forces is also described as 'galaxy harassment' (Moore et al. 1996, 1998). During a galaxy en-

counter the galaxies involved will be dynamically heated, leading to an increase of their internal energy, which eventually results in an expansion and mass loss. Simulations of galaxy harassment showed that disk galaxies falling into rich clusters can be almost completely destroyed (Moore et al. 1998). The tidal damage is found to be most severe for low surface brightness disk galaxies, but seems to have little impact on more compact disk galaxies with brighter surface brightness, possibly only inducing a mild disk thickening (Moore et al. 1999). Mastropietro et al. (2005) found that harassed disk galaxies suffer severe structural modifications. Dynamical heating leads to a decrease of the rotation to dispersion velocity ratio and causes the formation of more roundish spheroidal-like galaxies. The numerical simulations of Smith et al. (2015) and Bialas et al. (2015) showed, however, that harassment only strongly affects those galaxies that are on orbits with very close cluster-centric passages, and further depends on the individual disk inclination and internal structure of the infalling galaxy.

As first noted by Gunn and Gott (1972), galaxies moving with high velocities through the hot ICM experience a ram pressure. When the ram pressure overcomes the gravitational pressure of the galaxy, its interstellar medium will be stripped. This process is known as 'ram pressure stripping'. Stripping of gas occurs when the following condition is fulfilled: $\rho_{ICM} v_{gal}^2 \geqslant 2\pi G \Sigma_{star} \Sigma_{gas}$, where ρ_{ICM} is the density of the ICM, v_{gal} the velocity of the galaxy, Σ_{star} the galaxy's stellar surface density and Σ_{gas} its gas surface density. Observations indicate that mainly the atomic gas is stripped, while the molecular gas is more tightly bound to the galaxy and possibly will only be stripped in stronger cases (e.g. Boselli et al. 2014). Due to the gas stripping the star formation of the galaxy will be quenched, transforming it into a 'red and dead' stellar system. Some gas might be retained in the core of a stripped galaxy, where its binding forces are strongest, allowing the galaxy to continue forming stars in its central region. Simulations show that both the stellar and dark matter component remain largely unaffected by ram pressure stripping, although a mild disk thickening and displacement of the stellar and dark matter structure is predicted as a dynamical response to the gas stripping (Smith et al. 2012). Ram pressure stripping is expected to be most effective in the core of a cluster, where both the velocity of the orbiting galaxy and the density of the ICM are maximal. Hovever, Tonnesen et al. (2007) showed that ram pressure still affects galaxies out to the cluster virial radius and even acts upon galaxy groups (Bekki 2009).

There is ample direct observational evidence that ram pressure stripping is influencing the present-day cluster population. For example, many galaxies with trailing H I tails are observed in nearby galaxy clusters (e.g. Gavazzi et al. 1995; Kenney et al. 2004). This is often taken as an indication that ram pressure is the dominant mechanism transforming galaxies in dense environments today (e.g. Boselli and Gavazzi 2014). Direct observations of gravitationally interacting galaxies, however, seem to be relatively rare in nearby rich clusters. It is suggested that gravitational interactions were possibly a more frequent phenomenon in the past, when galaxy clusters were even denser environments (Poggianti et al. 2010), or eventually took place in early group environments that later assembled into clusters. The importance of gravitational interactions over the course of galaxy evolution is currently still being discussed.

1.4.3 *Formation and evolutionary scenarios*

Are dwarf galaxies simply scaled-down versions of their more massive counterparts and do they share a common origin and evolution? For instance, dEs appear very similar to massive elliptical galaxies. Both are characterised by a predominantly smooth morphology with elliptical isophotes, contain mainly old stellar populations and are gas-poor. It has been suggested that there is a continuity from dwarf to normal ellipticals, indicated by various scaling relations (e.g. Graham and Guzmán 2003, 2004; Ferrarese et al. 2006). However, a formation and evolutionary path similar to that of more massive galaxies would imply that the population of dwarfs also experienced a merger-driven evolution, which is considered very unlikely by many authors. Furthermore passive dwarf galaxies do not seem to exist in isolation, whereas cases of passive isolated luminous galaxies are known (Geha et al. 2012). This may point to different internal mechanisms at work at different mass scales, which are able to quench star formation at higher galaxy masses, but not at lower masses. There is good evidence that dwarf galaxies instead require external environmental influences to be quenched.

It is often argued that dEs may instead be linked to the population of late-type galaxies. For instance, Kormendy and Bender (2012) showed that early-type dwarfs follow a structural parameter sequence indistinguishable from that of late-type galaxies. One formation scenario suggests that dEs originate from destroyed more massive late-type galaxies that were transformed and quenched by cluster environment processes (e.g. Moore et al. 1998). Low surface brightness star-forming disk galaxies are commonly envisioned as progenitors, since they are believed to be more susceptible to environmental influence due to their low stellar density. Various simulations confirm that harassment effectively transforms a late-type disk galaxy into a spheroidal object with structural properties similar to those observed for cluster dEs (see Sect. 1.4.2). Some authors believe that dEs were formed at relatively late epochs. This is supported by the velocity distribution of early-type cluster dwarfs, which deviates from a Gaussian distribution observed for massive quiescent galaxies, and is instead more similar to the distribution of infalling low-mass disk galaxies (e.g. Conselice et al. 2001). On the other hand, Lisker et al. (2013) found that the progenitors of today's cluster dEs already suffered strong mass-loss at early times ($z \gtrsim 1$), according to the analysis of a semi-analytical model based on the Millenium-II cosmological simulation. This suggests that the progenitors of today's cluster galaxies were possibly accreted already at higher redshift to the cluster, experiencing continuous tidal influence already for a long time. A significant role could also play that the progenitors were 'pre-processed' in galaxy groups before entering the cluster environment (e.g. De Lucia et al. 2012), where velocity dispersions are lower and tidal encounters happen slower and more often.

An alternative route to dEs might be that they are not destroyed or transformed massive late-type galaxies, but are instead of cosmological origin. Mistani et al. (2016) suggested, based on their cosmological simulations, that dEs are genuine dwarf galaxies that formed similarly to dIrrs but experienced a different evolution, driven by environmental density. While the cosmological dwarfs located in low density environments would continuously grow and form stars until the present-day, the ones accreted onto a group or cluster over the course of their lifetime stop growing as soon as they enter the denser environment. The accreted galaxies likely have their star formation subsequently quenched due to gas removal via ram pressure stripping and experience tidal forces to a degree depending on the time

spent in the dense environment and on their orbital configuration. The simulations of Mistani et al. (2016) show a wide accretion history of dwarfs with some being accreted very early on and others that assembled only a few gigayears ago.

Dwarf galaxies can also form as so-called 'tidal dwarf galaxies' during interactions of massive gas-rich galaxies. Due to their formation out of pre-enriched material these galaxies are characterised by metal-rich stellar populations. In contrast to dwarf galaxies of a cosmological origin, tidal dwarfs are predicted to contain no dark matter (Duc 2012). The majority of identified tidal dwarfs are young and gas-rich objects, spotted in recent merger events (e.g. Weilbacher et al. 2000; Smith et al. 2010). However, Duc et al. (2014) also identified a population of intermediate-age tidal dwarfs with ages of about 4 Gyr in the vicinity of several massive, once interacting, early-type galaxies. It is suggested that evolved tidal dwarf galaxies would become indistinguishable from regular dEs (e.g. Metz and Kroupa 2007; Recchi et al. 2007). How many of the present-day dEs could have formed as tidal dwarf galaxies and also survived until today is still being debated, ranging from a few per cent (Bournaud and Duc 2006) to the majority of the population (Dabringhausen and Kroupa 2013).

The formation of young massive star clusters is directly observed in the present-day Universe. Formation sites are merging gas-rich galaxies, where the merger triggers a starburst associated with the formation of massive star clusters in the interacting galaxies. The most famous example are the Antennae galaxies, a nearby major merger event, where more than 1000 young massive clusters with masses and sizes in the range of GCs and above are observed (e.g. Whitmore et al. 1999). Commonly these young massive star clusters are interpreted as proto-GCs, sharing a similar formation mechanism as their older counterparts (see, however, Brodie and Strader 2006, and references therein for a different view). The old ages of most GCs imply that their formation must already have occured in the early Universe ($z \gtrsim 2$). Observations of high redshift galaxies indicate that they are gas rich, have a clumpy morphology, and are characterised by high gas densities and pressures (e.g. Elmegreen and Elmegreen 2005; Swinbank et al. 2012). Kruijssen (2015) pointed out that in the $z > 2$ Universe the conditions favouring star cluster formation were thus not only limited to galaxy mergers, but took place in situ in 'normal' star-forming galaxies. However, subsequent galaxy merges are required to redistribute the formed star cluster out to larger galacto-centric radii, in order to ensure their survival over a Hubble time. Otherwise the young clusters are likely to become victims of disruption due to close encounters with giant molecular clouds in the gas-rich galaxy disk. Additional young massive clusters may be formed during a starburst triggered by the galaxy merger, as simulated by Renaud et al. (2015) and observed in the Antennae galaxies. The observed colour bimodality of the present-day GC systems in almost all galaxies could be explained by the fact that the metal-poor GCs were donated by accretion and stripping of lower-mass galaxies (e.g. Côté et al. 1998). Thus, the wide spread in metallicity of the GC populations in massive galaxies might be a natural outcome of hierarchical structure formation, where the GC system consists of a composite population of GCs formed in different galaxy hosts.

Following the same luminosity–size relation of massive elliptical galaxies and being characterised by similarly bright surface brightness, it is suggested that cEs represent their lower luminosity counterparts (e.g. Wirth and Gallagher 1984; Kormendy et al. 2009). A common origin would imply that also cEs formed by mergers.

Kormendy et al. (2009) suggested that their high stellar density possibly reflects earlier dissipative (wet) mergers, where gas dissipation and the associated star formation caused the very compact nature of the merger remnant. On the other hand, similarly high stellar densities are also found in galaxy bulges, which occupy the same region in parameter space as cEs (Bender et al. 1992). Since they often reside in very dense environments, it is suspected that cEs might be the remnant bulges of heavily stripped and destroyed disk galaxies (e.g. Faber 1973; Bekki et al. 2001a). In this scenario, their very metal-rich stellar populations compared to galaxies of similar luminosity, and the presence of massive black holes in some cEs could be indirect evidence for cEs originating from once more massive galaxies (e.g. Kormendy et al. 1997; Janz et al. 2015). Direct evidence for cEs in the process of formation was provided by Huxor et al. (2011), showing two cEs embedded in tidal streams possibly pointing to the disruption of their former host galaxy. Although a few cEs are found in isolation, which would not fit into the tidal stripping scenario, Chilingarian and Zolotukhin (2015) proposed that these might have been ejected from their dense host environment due to three- or multiple-body encounters during galaxy interactions.

Being at the boundary between the population of star clusters and galaxies, the origin of the intermediate population of UCDs was called into question at an early stage. – Are they the high-mass end of the GC population and therefore genuine star clusters? Or do they share a similar origin as proposed for the more massive cEs? Due to their similarity to galaxy nuclei, UCDs could be the remnant nuclei of tidally stripped dwarf galaxies. We will address these aspects in more detail in Chapter 2.

1.5 THESIS OUTLINE AND MOTIVATION

Constraining the environmental influence on low-mass stellar systems is essential to understand and correctly interpret their formation and evolution. Did they only experience mild environmental influence, implying that their progenitors possibly closely resemble the present-day populations, having been born as genuine low-mass objects? Or was environmental influence of major importance over the course of their evolution, suggesting that low-mass systems are the descendants of more massive systems that were structurally transformed? Which environmental process was the dominant one in shaping today's low-mass population? Or did the importance of the dominant mechanism change over cosmic time?

This thesis focuses on the importance of environmental influence on the most compact and most diffuse low-mass stellar systems in nearby galaxy clusters. We investigate these populations in the dense core regions of the nearby Fornax and Perseus galaxy clusters. On the basis of deep optical wide-field imaging data we analyse these systems for signs of environmental influence in the form of possible perturbations in their stellar structure. We aim to understand whether the same environmental mechanisms were responsible for the formation and evolution of both the compact and the diffuse populations in galaxy clusters.

This thesis is structured as follows: In Chapter 2 we investigate a population of compact stellar systems in the Fornax cluster core. We use the same dataset in Chapter 3 to search for diffuse low surface brightness galaxies and stellar tidal streams. We present a study of the Perseus cluster low surface brightness galaxy population in Chapter 4 and conduct a systematic study of its diffuse and com-

pact low-mass galaxy content in Chapter 5. The thesis ends with a summary and discussion of our most important results in Chapter 6.

PECULIAR COMPACT STELLAR SYSTEMS IN THE FORNAX CLUSTER

ABSTRACT

We search for hints to the origin and nature of compact stellar systems in the magnitude range of ultra-compact dwarf galaxies in deep wide-field imaging data of the Fornax cluster core. We visually investigate a large sample of 355 spectroscopically confirmed cluster members with V-band equivalent magnitudes brighter than -10 mag for faint extended structures. Our data reveal peculiar compact stellar systems, which appear asymmetric or elongated from their outer light distribution. We characterise the structure of our objects by quantifying their core concentration, as well as their outer asymmetry and ellipticity. For the brighter objects of our sample we also investigate their spatial and phase-space distribution within the cluster. We argue that the distorted outer structure alone that is seen for some of our objects, is not sufficient to decide whether these systems have a star cluster or a galaxy origin. However, we find that objects with low core concentration and high asymmetry (or high ellipticity) are primarily located at larger cluster-centric distances as compared to the entire sample. This supports the hypothesis that at least some of these objects may originate from tidally stripped galaxies.

This study has been published in Wittmann et al. (2016, MNRAS, 459, 4450).

2.1 INTRODUCTION

The discovery of a new type of compact stellar system in the Fornax galaxy cluster, named 'ultra-compact dwarf galaxy' (UCD; Phillipps et al. 2001), was reported by Hilker et al. (1999) and Drinkwater et al. (2000b). With stellar masses in the range $M_* = 10^6 - 10^8\,M_\odot$ and half-light radii $r_{50} = 3$–$100\,pc$, UCDs started to bridge the formerly well separated populations of globular clusters (GCs) and compact elliptical galaxies (cEs). One of the main questions driving the investigation of UCDs is thus whether they rather constitute the high-mass, large-size end of the star cluster distribution, or the low-mass and small-size end of the galaxy population.

Previous studies showed that most UCDs have properties similar to GCs with regard to their ages, metallicities and α-element abundances (e.g. Frank et al. 2011; Francis et al. 2012). Furthermore, on the basis of number counts, Mieske et al. (2012) concluded that UCDs in the Fornax cluster would statistically be fully consistent with being the brightest members of the central cluster galaxy's GC population. There is an ongoing discussion on the formation scenarios of GCs themselves (e.g. Kruijssen 2014, 2015). One model suggests that GCs may have formed under similar conditions as young massive star clusters during major mergers of gas-rich galaxies (Ashman and Zepf 1992). Observations revealed that the newly formed star clusters often reside in larger star cluster complexes, consisting of up to hundreds of individual young massive clusters (e.g. Whitmore and Schweizer 1995). According to numerical simulations, the merging of young massive star clusters in such complexes may lead to the formation of a compact object with parameters in the range of a typical UCD (Fellhauer and Kroupa 2002; Brüns and Kroupa 2011). Renaud et al. (2015) concluded, however, that according to their hydrodynamical

simulation the formation of UCD-like objects during a galaxy merger does not necessarily need to be tied to hierarchical merging of star clusters, but may also arise from merging of gas clumps during their formation. Based on observations of UCDs in the Perseus cluster, Penny et al. (2012) suggested a star cluster origin for two UCDs with very blue colours, residing in star-forming filaments of the central cluster galaxy.

Since their discovery, it has also been discussed that UCDs could be related to the population of galaxies. It was proposed that UCDs might be the remnant nuclei of nucleated dwarf ellipticals that were tidally stripped while orbiting in the gravitational field of a galaxy cluster (Bekki et al. 2001b; Drinkwater et al. 2003). Various simulations of this tidal stripping scenario demonstrated that the stripped galaxy remnants would closely resemble observed UCDs from their structural parameters (Bekki et al. 2003b; Goerdt et al. 2008; Pfeffer and Baumgardt 2013). Observational signatures for a stripped galaxy origin were found by several authors. For example, Norris et al. (2015) detected an extended star formation history for UCD NGC 4546-UCD1 ($M_* = 3.3 \times 10^7 \, M_\odot$, $r_{50} = 25.5 \, pc$). Also, Strader et al. (2013) found strong indications for a galaxy origin of UCD M60-UCD1 ($M_{dyn} = 2.0 \times 10^8 \, M_\odot$, $r_{50} = 24.2 \, pc$), which harbours a central X-ray source and shows strong indications for the presence of a massive black hole that makes up 15 per cent of the UCD's mass (Seth et al. 2014). The presence of a massive black hole could also be the cause of the elevated dynamical-to-stellar mass ratio that was inferred for UCD M87-S999 ($M_{dyn}/M_* = 8.2$, $M_* = 3.9 \times 10^6 \, M_\odot$, $r_{50} = 20.9 \, pc$) (Janz et al. 2015). Another example is UCD NGC 1275-UCD13 ($M_* = 4.4 \times 10^7 \, M_\odot$, $r_{50} = 85 \, pc$), for which Penny et al. (2014) concluded that the UCD's colour, size, metallicity, internal velocity dispersion, dynamical mass, and close proximity to the central cluster galaxy likely point to a stripped galaxy origin. Janz et al. (2016) observed that high-mass UCDs with $M_* \gtrsim 10^7 \, M_\odot$ seem to be generally metal-rich in comparison to early-type galaxies in the same stellar mass range. This may indicate that the objects once were more massive galaxies that were stripped off their stellar material while retaining their central metallicity.

In general it is believed that both formation channels coexist for the population of UCDs (e.g. Hilker 2009; Norris et al. 2014). For a few UCDs, some of which are mentioned above, either a star cluster or a galaxy origin was found to be more likely. In most cases, however, it was not possible so far to robustly distinguish between the proposed formation scenarios from the observed properties. This is also due to limited resolution and image depth, restricting a detailed analysis of the internal properties mainly to the brighter objects. Furthermore, due to the existence of a luminosity-size relation for the brighter UCDs (e.g. Evstigneeva et al. 2008; Caso et al. 2013), with the fainter objects having smaller half-light radii, most of them appear unresolved or only partly resolved in seeing-limited observations.

Already in the early phase of UCD research, Drinkwater et al. (2003) found that the brightest UCD in Fornax (UCD 3) is significantly extended compared to the few other UCDs known at that time. Structural analysis in high resolution *HST* imaging of Virgo and Fornax cluster UCDs showed that some of the brightest UCDs are characterised by a two-component surface brightness profile with a compact core and an extended low surface brightness envelope (De Propris et al. 2005; Evstigneeva et al. 2007, 2008). In ground-based imaging, a large number of UCDs with faint envelopes were detected in the Virgo cluster (Liu et al. 2015). In the Fornax cluster, Richtler et al. (2005) and Voggel et al. (2016) reported that a few extended objects appear peculiar since they show asymmetric structures.

In deep imaging data of the Fornax cluster core, we search the known population of compact stellar systems for objects that appear significantly extended and/or exhibit peculiar structures. We visually investigate a large sample of 355 spectroscopically confirmed compact systems with $V-$band equivalent magnitudes between -14 and -10 mag for the presence of faint structures extending significantly beyond the point spread function (PSF). We quantify structure by introducing parameters that measure the core concentration, as well as the outer asymmetry and ellipticity. Then we relate these parameters to the spatial and phase-space distribution within the Fornax cluster. We limit our analysis to objects brighter than -10 mag, which corresponds to the magnitude range of UCDs or bright GCs (Misgeld and Hilker 2011; Norris et al. 2014). Since there is no unambiguous distinction of objects that have previously been classified as bright GCs and objects that were named UCDs, we will speak of 'compact stellar systems' throughout this work.

We describe the observations and the sample definition in Section 2.2. Details of the analysis are given in Section 2.3. We present our results in Section 2.4 and discuss them in Section 2.5. The conclusions follow in Section 2.6.

2.2 DATA

2.2.1 *Observations*

The data were acquired in 2008 and 2010 with the WFI at the *ESO/MPG 2.2 m telescope* and are fully characterised in Chapter 3. We used a transparent filter that nearly equals the no-filter throughput (> 10 per cent in the range 350–900 nm) and thus provides a high signal-to-noise ratio. Fig. 2.1 shows our deep image of the Fornax cluster core, covering a region of 97 arcmin in east–west and 76 arcmin in north–south direction. This corresponds to 559 and 438 kpc, respectively, at a distance of 20.0 Mpc for Fornax (using 5.76 kpc arcmin^{-1}; Blakeslee et al. 2009), which we adopt throughout this work.

In Chapter 3 we determined an approximate '$V-$equivalent' magnitude calibration, based on spectroscopically confirmed foreground stars from Mieske et al. (2002, 2004). In the following we denote $V-$equivalent magnitudes and surface brightnesses with the subscript 'Ve'. Our data reach a $V-$equivalent depth of 26.58 and 26.76 mag arcsec^{-2} for the median and 75th percentile, respectively, at $S/N = 1$ per pixel (1 pixel $\widehat{=}$ 0.238 arcsec, or 22.848 pc). The seeing PSF full width at half-maximum (FWHM) varies over the image (see also Fig. 2.2), but is typically about 1 arcsec. Details of the observations, data reduction, and data characterization are provided in Chapter 3, Sections 3.2 and 3.3.

2.2.2 *Catalogue compilation*

Before defining our working sample, we first compiled a list of published compact stellar systems with spectroscopically confirmed Fornax cluster membership. We used the SIMBAD data base (Wenger et al. 2000) to identify relevant source catalogues, which yielded the following references: Schuberth et al. (2010), Dirsch et al. (2004), Bergond et al. (2007), Firth et al. (2007), Gregg et al. (2009), Mieske et al. (2004, part of the Fornax Compact Object Survey), Mieske et al. (2002, part of the Fornax Compact Object Survey), Firth et al. (2008), Drinkwater et al. (2000a, part of the Fornax Cluster Spectroscopic Survey), Kissler-Patig et al. (1999), and Kissler-
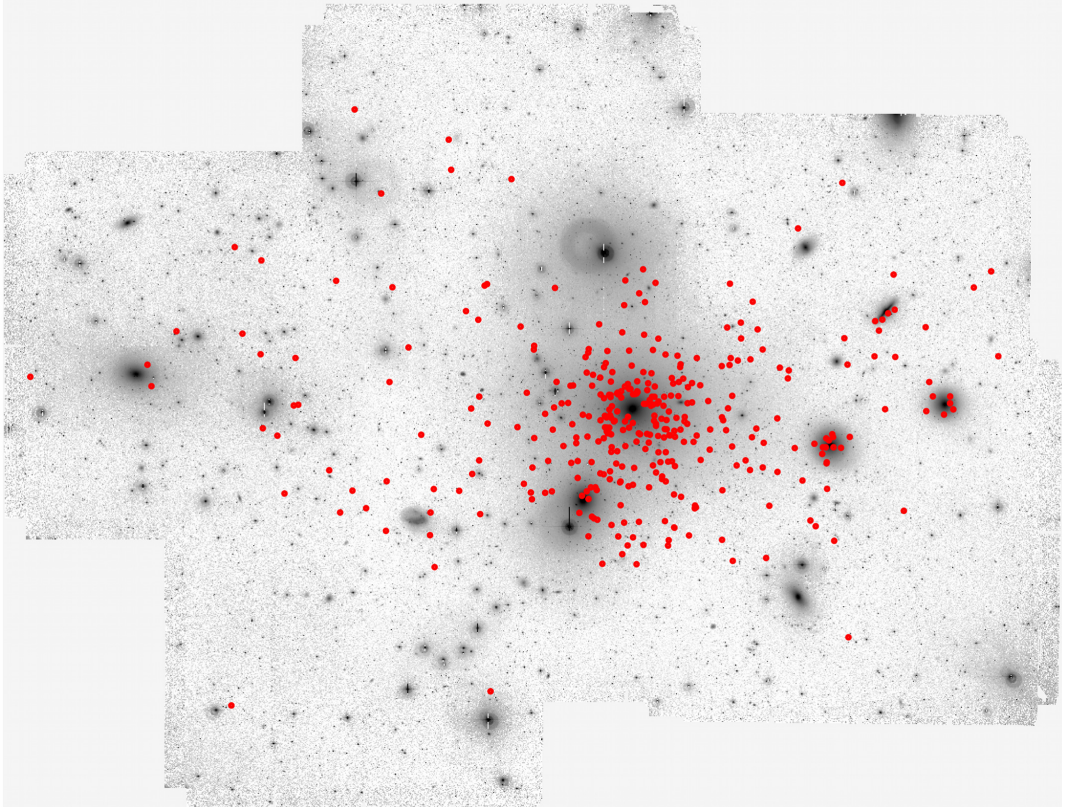
FIGURE 2.1:   Deep wide-field imaging of the Fornax cluster core. Image dimensions: $97 \times 76 \, \text{arcmin}^2$, corresponding to $559 \times 438 \, \text{kpc}^2$ when assuming a distance of $20.0 \, \text{Mpc}$ for Fornax. North is up and east is to the left. Red dots indicate our sample of spectroscopically confirmed compact stellar systems with $m_{V_e} < 21.5 \, \text{mag}$. The central galaxy is NGC 1399.

Patig et al. (1998). Tabulated cluster members from these references, in the given order, were appended to our object list if they were not within 1 arcsec of objects already in the list. Duplications within the same catalogue, which are present in Schuberth et al. (2010) and Dirsch et al. (2004), were excluded. Based on this sequence, 695 objects were taken from Schuberth et al. (2010), 113 from Dirsch et al. (2004), 151 from Bergond et al. (2007), and 123 from the remaining references (with no contributed objects from Drinkwater et al. 2000a and Kissler-Patig et al. 1998), resulting in 1082 confirmed cluster members, of which 1058 were listed as compact systems and 24 as dwarf galaxies.

After excluding eight objects that lie outside of our mosaic, we visually inspected the remaining objects on the mosaic at their literature positions, using SAOIMAGE DS9 (Joye and Mandel 2003). We identified another 75 unambiguous duplications, as well as 20 published object coordinates for which we do not see an optical counterpart in our image within 3 arcsec[1]. For 50 further published object coordinates, the match to the visible sources is ambiguous — mostly due to the presence of multiple sources, but in a few cases also due to the fact that the only nearby visible source lies almost 3 arcsec away from the literature position. All of these published objects were excluded from our list, as well as one further object that potentially

---

[1] These are the objects 78:103, GS04-M03:9, GS04-M03:30, and GS04-M03:127 from Schuberth et al. (2010), objects 75:56, 76:112, 78:13, and 78:110 from Dirsch et al. (2004), and the following objects from Kissler-Patig et al. (1999): ntt 201, ntt 203, ntt 407, ntt 410, ntt 414, ntt 109, ntt 119, ntt 122, ntt 123, ntt 124, ntt 126, and ntt 127. We used the NED Coordinate and Extinction Calculator (http://ned.ipac.caltech.edu/forms/calculator.html) as a check to make sure that our coordinate conversion from the B1950.0 values of Kissler-Patig et al. to J2000.0 was done correctly.

TABLE 2.1:   Catalogue of compact stellar systems compiled from the literature. The first five objects are given to illustrate the format of the table. The complete catalogue is provided in the Appendix, Table A.4. For each object we list our ID, the position based on our astrometry, as well as the SIMBAD identifier. The object IDs are sorted by increasing right ascension. The given velocity corresponds to the velocity with the smallest error from all compiled velocities. The respective literature source is listed in the last column, where 1 = Schuberth et al. (2010), 2 = Dirsch et al. (2004), 3 = Bergond et al. (2007), 4 = Firth et al. (2007), 5 = Gregg et al. (2009), 6 = Mieske et al. (2004), 7 = Mieske et al. (2002), 8 = Firth et al. (2008), 9 = Kissler-Patig et al. (1999), 10 = Drinkwater et al. (2000a), 11 = Kissler-Patig et al. (1998).

ID	R.A. (J2000)	DEC. (J2000)	SIMBAD ID	v (km s^{-1})	LIT.
1	03 35 38.87	-35 21 53.3	[BAL2007] gc144.6	1388 ± 32	3
2	03 35 42.52	-35 13 51.8	[BAL2007] gc290.6	1901 ± 16	3
3	03 35 50.49	-35 15 24.2	[BAL2007] gc302.6	1166 ± 6	3
4	03 35 59.56	-35 26 56.7	[BAL2007] gc21.70	1272 ± 12	3
5	03 36 01.09	-35 25 43.0	[BAL2007] gc69.70	1389 ± 8	3

has wrong published coordinates[2]. This results in a final catalogue of 904 compact stellar systems that are spectroscopically confirmed cluster members, are covered by our mosaic, and are visually unambiguously identified with an optical source. The catalogue is provided in the Appendix, Table A.4. An excerpt is shown in Table 2.1.

Despite the visually unique match, the literature position may of course still be slightly offset from the image position[3], and other neighbouring sources may be present. In order to characterise this situation, we determined for each catalogue position whether a single source or multiple image sources are present within a 1 arcsec and 3 arcsec radius. For 792 catalogue positions (88 per cent) there is only a single image source within 1 arcsec and no further image source within 3 arcsec. For 95 catalogue positions (11 per cent) there is a single image source within 1 arcsec, and at least one further source within 3 arcsec. For 17 catalogue positions (2 per cent) there is no image source within 1 arcsec, but either a single image source within 3 arcsec (15 objects) or multiple sources (2 objects[4]). We remind that a *visually unambiguous* match is present for *all* 904 catalogue objects, including the 17 just mentioned.

2.2.3   *Velocity compilation*

In the literature compilation described in Section 2.2.2 that serves as the basis for our sample, each object only appears once, even if it is listed in several of the references. In order to compile *all* published heliocentric velocity measurements of a given object, we employed the following steps. First, we went through the list of compiled *literature positions* of our sample and extracted the nearest matching

---

2 Object 37 in table 2 of Gregg et al. (2009) is marked there as being the same source as object gc212.2 from Bergond et al. (2007), but that object actually has different coordinates, offset by about 0.5 arcmin. We therefore excluded object 37 from our list.

3 The image position is based on the astrometric calibration of our mosaic (using the 2MASS catalogue), and obtained by fitting the PSF of the objects using the task *allstar* of the IRAF package DAOPHOT.

4 The two objects are not part of our working sample, since they have $m_{V_e} \geqslant 21.5$ mag.

object within 1 arcsec from each of the literature references given in Section 2.2.2. Secondly, we repeated this for the list of *image positions* of our sample. Thirdly, we visually inspected the location of all compiled positions, and only kept the unambiguous ones.

This resulted in 440 objects of our sample having at least two velocity measurements, 80 having at least three, and 37 with four or more. For each object we adopted the velocity with the smallest error from all compiled velocities, which we include in our catalogue (see Table 2.1).

2.2.4 *Working sample*

The compiled catalogue contains objects in both the UCD and GC magnitude range. In the study presented here we define our working sample to include all objects brighter than $m_{Ve} = 21.5$ mag, corresponding to $M_{Ve} < -10.0$ mag at the distance of Fornax, i.e. the range of UCDs and bright GCs in the literature (Misgeld and Hilker 2011; Norris et al. 2014). Due to the depth and seeing-limited resolution of our data, fainter objects (with their smaller intrinsic sizes, see e.g. Caso et al. 2013) could not be analysed robustly. In total our working sample contains 355 compact systems, which are indicated in Fig. 2.1. Their V-equivalent magnitudes ('mag best') and the corresponding uncertainties (based on the weight image) were obtained with SExtractor[5] (Bertin and Arnouts 1996) and are provided in Table 2.3.

A rough estimate of the completeness of known compact stellar systems with $M_V < -10.3$ mag in Fornax is given by Mieske et al. (2012). Between distances of 50–100 kpc from the cluster centre (corresponding to 0.15° and 0.29°, respectively) the authors considered their sample to be complete to 60–70 per cent. At larger cluster-centric distances the completeness is expected to drop below 50 per cent. As discussed in Section 2.5.3 this does not affect the conclusions of our study.

2.3 ANALYSIS

The analysis of our working sample is based on both a visual investigation as well as on a parametrisation of selected sample properties. We introduce parameters as a measure for the central core concentration as well as for the shape of the outer light distribution. The analysis is carried out relative to the PSF, which is determined from point sources in our data. Prior to the analysis we have removed large galaxies and stellar haloes by fitting and subtracting their light profile with the IRAF[6] task *ellipse* (see Chapter 3, Fig. 3.3).

2.3.1 *PSF analysis and background correction*

Due to changing seeing conditions over the course of our observing runs, aside from possible intrinsic variations due to the instrument, the PSF varies across the image. We therefore divided the mosaic into regions of similar FWHM, as indicated in Fig. 2.2, and according to the distribution of our sample, i.e., only if an

---

5 For five objects from our working sample we adopted the magnitude and corresponding uncertainty obtained from PSF fitting, due to imperfect deblending in SExtractor.

6 IRAF is distributed by the National Optical Astronomy Observatory, which is operated by the Association of Universities for Research in Astronomy (AURA) under a cooperative agreement with the National Science Foundation.
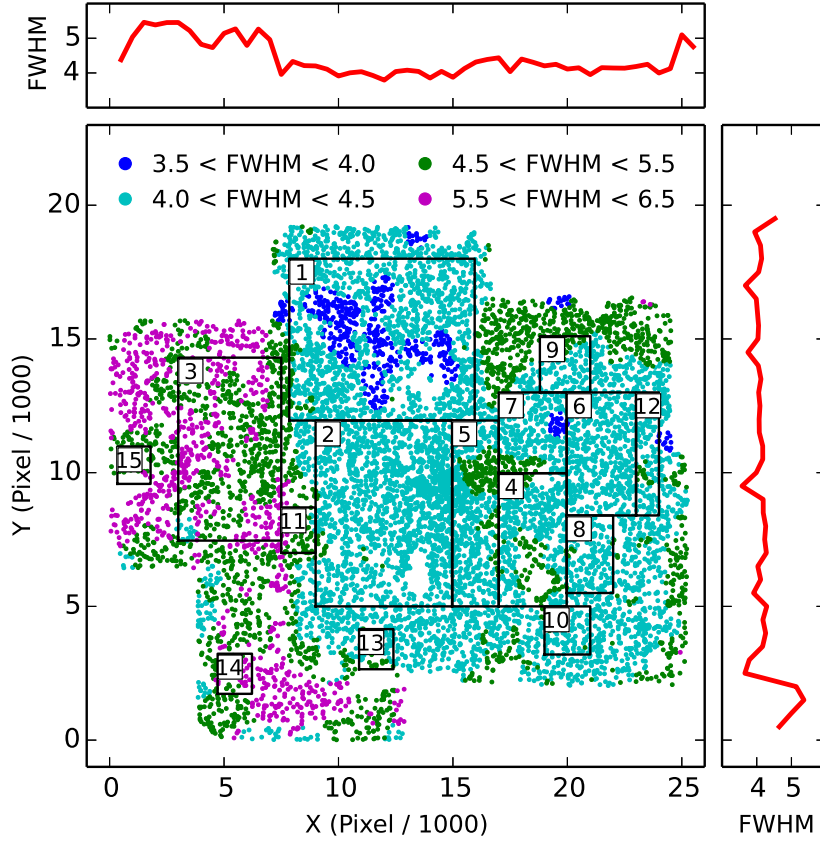
FIGURE 2.2: Central panel: variation of the PSF FWHM across the mosaic. The positions of objects brighter than $m_{Ve} = 22$ mag and with an FWHM below 7.5 pixels are shown, which were detected with SExtractor. The symbols are colour-coded according to the local minimum FWHM, determined within a circle of 500 pixels radius. We measured the FWHM of all SExtractor-detected objects with the IRAF task *psfmeasure*, using a Gaussian profile for the PSF. The numbered boxes indicate regions for which we determined an individual PSF. North is up and east is to the left. Side panels: variation of the minimum FWHM along x-/y-direction. The average of the 10 smallest FWHM values that occur in bins of 500 pixels is plotted (1 pixel $\widehat{=}$ 0.238 arcsec).

area contains published compact stellar systems, we define it as a PSF region. In each region we determined the PSF from suitable point sources (hereafter 'PSF stars') in the magnitude range $17.6 < m_{Ve} < 22.3$ mag, using routines from the IRAF package DAOPHOT. The PSF was generated by an iterative approach. In a wide circle with a radius of 30 pixels (7.14 arcsec) around each PSF star, all neighbouring sources were subtracted using a first-estimate PSF. A new PSF model was then calculated based on the neighbour-subtracted PSF stars. We performed three iterations, which significantly reduced the contamination of flux from close neighbours to the PSF. The final PSF was subsequently fitted to our sample and subtracted, where we chose the fitting radius to be slightly larger than the typical FWHM of the respective region. Details on the PSF analysis and properties of the resulting PSFs are summarised in Table 2.2.

For the following analysis we corrected large-scale background variations using a SExtractor background map determined from the full image. Remaining local background offsets were corrected for each object individually, by subtracting the median intensity within an annulus 5 pixels wide and with an inner radius of 20 pixels (1 pixel $\widehat{=}$ 0.238 arcsec).

TABLE 2.2:   PSF analysis for regions of similar FWHM on the mosaic (see Fig. 2.2). For each region we specify the size of the region in square pixels, the number of compact stellar systems contained in the region, and the number of PSF stars used to build the PSF. The regions are listed with decreasing size. Working sample: compact objects brighter than $m_{Ve} = 21.5\,$mag. Fainter CSS: compact objects fainter than $m_{Ve} = 21.5\,$mag, which belong to the basis catalogue described in Section 2.2.2 and are given here for completeness only. For the resulting PSF we give the FWHM in pixels (1 pixel $\,\widehat{=}\,0.238$ arcsec) and the ellipticity. Both quantities were obtained with the IRAF task *psfmeasure*, using a Gaussian profile. The last column gives the mean core concentration ($\overline{cc}$) and the corresponding standard deviation of all PSF stars within one region (see Section 2.3.2).

REGION	SIZE	WORKING SAMPLE	FAINTER CSS	PSF STARS	PSF FWHM	PSF ELLIP.	$\overline{cc}$
1	8100×6050	16	4	78	4.1	0.09	1.005 ± 0.025
2	5980×6950	132	223	55	4.3	0.05	1.000 ± 0.019
3	4500×6840	13	10	42	5.6	0.10	1.006 ± 0.027
4	2970×4980	37	40	28	4.6	0.04	1.012 ± 0.031
5	2040×6950	107	246	35	4.5	0.05	1.000 ± 0.037
6	3030×4600	21	2	37	4.4	0.05	1.006 ± 0.029
7	2970×3020	15	24	22	4.4	0.02	1.013 ± 0.042
8	2030×2900	1	0	28	4.5	0.07	1.008 ± 0.026
9	2200×2100	2	0	8	4.4	0.05	1.007 ± 0.018
10	2000×1800	1	0	9	4.4	0.12	1.006 ± 0.022
11	1500×1700	4	0	7	4.9	0.12	1.012 ± 0.040
12	1000×2500	3	0	12	4.3	0.13	0.999 ± 0.020
13	1500×1500	1	0	8	4.7	0.10	1.011 ± 0.024
14	1500×1500	1	0	10	5.8	0.12	1.001 ± 0.031
15	1500×1500	1	0	8	6.2	0.11	1.027 ± 0.049

2.3.2   *Core concentration*

The core concentration is defined as the mean central flux ratio of the object to the fitted PSF and can be expressed in terms of the ratio of the PSF-subtracted residual image to the object image:

$$\text{Core concentration} \quad = \quad \frac{1}{n_{pix}} \sum_{r \leqslant 2\,pix} \frac{I_{obj}}{I_{PSF}} \tag{2.1}$$

$$= \quad \frac{1}{n_{pix}} \sum_{r \leqslant 2\,pix} \left[1 - \frac{I_{res}}{I_{obj}} \right]^{-1},$$

where I_{obj} corresponds to the object intensity, I_{PSF} to the intensity of the fitted PSF, I_{res} to the residual intensity and n_{pix} is the number of pixels within the aperture over which is summed. The aperture width is on the order of one FWHM of the typical PSF. The ratio of the residual to the object image was obtained by dividing both images pixel by pixel. We provide the core concentration for our working sample in Table 2.3.

Fig. 2.3 (upper left panel) shows the distribution of the measured core concentration for our working sample and for the PSF stars used in the analysis. According to equation 2.1, a core concentration close to one indicates a PSF-like core, whereas lower values correspond to a less concentrated core. This is reflected in the distribution of the PSF stars, which is strongly peaked around a value of one. The vast majority of compact stellar systems has lower core concentrations than the PSF

stars and follows a broader distribution that is skewed towards lower values. We find that the brighter objects from our working sample reach on average lower core concentrations than the fainter objects. This at least partly reflects the luminosity-size relation that exists for the brighter compact stellar systems, such that fainter systems appear PSF-like since they are unresolved in seeing-limited observations.

Due to the high S/N of the central pixels, the formal errors in core concentration are very small when considering uncertainties from photon statistics only[7]. An estimate for the (more relevant) uncertainty that stems from PSF fitting is given by the standard deviation of the core concentration of all PSF stars within one region (provided in column 8 of Table 2.2). This reflects the local FWHM variations as compared to the PSF model of the respective region.

TABLE 2.3: Parameter catalogue for our working sample of spectroscopically confirmed Fornax cluster members with $m_{Ve} < 21.5$ mag. The first five objects are printed below to illustrate the format of the table. We provide the complete table in the Appendix, Table A.5. ID: our object ID from Table 2.1. m_{Ve}: V-equivalent magnitude and corresponding uncertainty. Note that the magnitude uncertainties are purely based on S/N and do not include the calibration uncertainties mentioned in Section 2.2.1. Flag: 1 = magnitude and uncertainty obtained from SEXTRACTOR; 2 = magnitude and uncertainty obtained from PSF-fitting. cc: core concentration (uncorrected values, not used in the analysis). cc_{corr}: PSF-corrected core concentration (see Section 2.3.4). An estimate for the uncertainty in core concentration, which is given for each region, can be inferred from column 8 of Table 2.2. ra: residual asymmetry and corresponding uncertainty. el: ellipticity and corresponding uncertainty. For 17 objects it was not possible to determine the ellipticity or residual asymmetry due to too little flux remaining in the residual image. S1: subsample as defined in Table 2.5; cc + ra = 1, cc + RA = 2, CC + RA = 3, cc + EL = 4; S1 = 0 indicates that the object is not part of any subsample. S2: alternative subsample as defined in Table A.1. Reg.: PSF-region (see Table 2.2).

ID	m_{Ve} (mag)	FLAG	cc	cc_{corr}	ra	el	S1	S2	REG.
1	20.394 ± 0.003	1	0.946	0.946	0.504 ± 0.094	0.161 ± 0.067	0	0	12
2	20.576 ± 0.004	1	0.929	0.929	0.429 ± 0.114	0.129 ± 0.097	0	0	12
3	21.379 ± 0.008	1	0.908	0.908	0.403 ± 0.125	0.066 ± 0.078	0	0	12
4	20.737 ± 0.003	1	0.942	0.942	0.520 ± 0.101	0.325 ± 0.084	0	0	6
5	20.645 ± 0.004	1	0.905	0.905	0.759 ± 0.044	0.308 ± 0.028	0	0	6

2.3.3 *Residual asymmetry and ellipticity*

For measuring residual asymmetry and ellipticity, we chose to use the PSF-subtracted residual image with all negative pixels set to zero, to avoid effects from the central oversubtraction of the PSF core (see Fig. 2.4, left-hand panels), as well as noise effects. For simplicity, we refer to this image as the *residual image* in this subsection. The residual asymmetry is defined in analogy to the Asymmetry parameter in Conselice et al. (2000):

$$\text{Residual asymmetry} = \frac{\sum_{r \leqslant 12\text{pix}} |I_{\text{res,corr}} - I_{\text{res,corr},180}|}{\sum_{r \leqslant 12\text{pix}} I_{\text{res}}} \quad (2.2)$$

In order to avoid substantial noise effects due to the small number of pixels (as compared to galaxies), we consider only the flux that exceeds $+1\sigma$ of the noise

7 The relative errors are on the order of 0.04 per cent for objects brighter than $m_{Ve} = 20.0$ mag, and 0.13 per cent for fainter objects from our working sample.
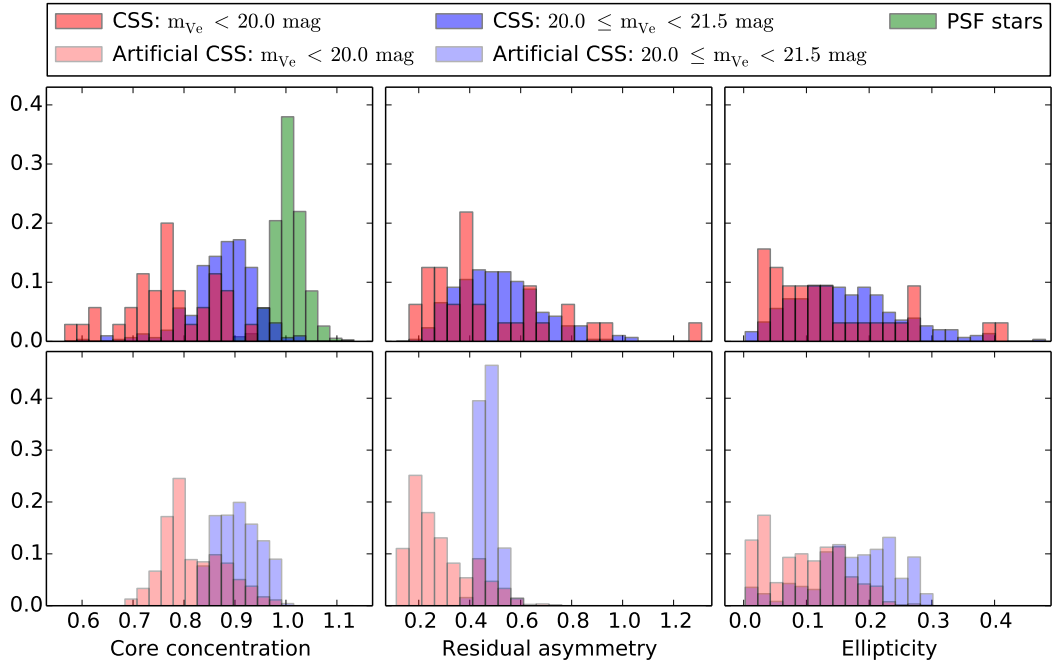
FIGURE 2.3:   Distribution of parameter values for compact stellar systems and PSF stars. Our working sample corresponds to the red and blue histograms in the upper panels. For comparison we show the distributions of the artificial compact objects in the lower panels, which are represented by the red and blue histograms with lighter shading. Darker shading is used where histograms overlap. In both core concentration histograms we plot the PSF-corrected values (see Section 2.3.4). Our sample with $m_{Ve} < 20.0$ mag contains 35 objects, the sample with $20.0 \leqslant m_{Ve} < 21.5$ mag includes 320 objects. For three objects from the brighter and fourteen objects from the fainter sample no useful asymmetry value could be determined due to too little flux remaining in the residual image. The total number of artificial objects corresponds to 1170 for objects with $m_{Ve} < 20.0$ mag, and to 1215 for objects with $20.0 \leqslant m_{Ve} < 21.5$ mag. We note that although both real and artificial compact objects span the same magnitude range, the magnitude distribution of the artificial objects is discrete, since the models were created on the basis of magnitudes and sizes from only 18 real UCDs. Therefore the parameter distributions of the artificial objects should be used for guidance only.

level[8]: $I_{res,corr}$ is the intensity on the residual image minus the noise level of 0.023 counts, and is set to zero if this is negative. $I_{res,corr,180}$ is the corresponding intensity on the image rotated by 180°. The sum of the absolute pixel-by-pixel differences of the original and rotated image is then normalized by the flux of the residual image. We use all pixels within a circular aperture with a radius of 12 pixels (> 2 PSF FWHM) around the object centre. Any residual light from extended structures is essentially unaffected by the PSF at a radius larger than 2 FWHM; thus a fixed radius ensures comparability of such structures across the mosaic. All close neighbouring sources (and their counterparts rotated by 180°) are masked, i.e., their pixels are not taken into account in the asymmetry calculation.

The ellipticity is defined as $1 - b/a$, where b/a denotes the axis ratio. The latter is computed on the residual image from the second-order moments of the intensity distribution (as done in SEXTRACTOR), using the above aperture and neighbour masks.

---

8 The noise level of the deeper regions of the mosaic corresponds to $\mu_{Ve} = 26.76$ mag arcsec^{-2} or 0.023 counts, see Chapter 3.

We estimated the uncertainty in residual asymmetry and ellipticity through error propagation, using the noise level at a given object's position (provided by the weight image) as uncertainty of a pixel's flux. The derived parameter values and corresponding uncertainties are given in Table 2.3. We display the distribution of both residual asymmetry and ellipticity in Fig. 2.3 (upper centre and upper right panels). The relations between core concentration, residual asymmetry and ellipticity are shown in the Appendix, Fig. A.1.

2.3.4 *Comparison to artificial compact objects*

We estimated which parameter values can arise due to the shape of the PSF or the profile type of the objects by comparing the parameters of our sample to the parameter range of artificially created compact objects in the same magnitude and size range. We realized the artificial objects using structural parameters of real Fornax and Virgo cluster UCDs from Evstigneeva et al. (2008), where we selected 18 one-component UCDs, which have $V-$band magnitudes between 20.90 and 18.33 mag and effective radii between 4.0 and 29.5 pc. In addition to the observed structural parameters we created further models with different Sérsic indices ranging from $n = 1$ to 8. We generated each artificial model with a 10 times smaller pixel scale (i.e., 10 times better sampling) than our actual data, and then convolved it with each of our PSFs. This resulted in a set of roughly 2400 artificial objects for which we determined the core concentration, residual asymmetry, and ellipticity in the same way as for the real objects.

For the artificial objects we see a dependence of the core concentration (cc) on the PSF for some of our PSF models. Basically, the more extended (less concentrated) an object's core is intrinsically, the more the cc value gets lowered by the PSF convolution. This effect is enhanced when the PSF is broad, as compared to a reference PSF that is particularly symmetric and peaked. We chose the PSF from *Region 2* (see Table 2.2 and Fig. 2.2) as reference PSF. For those PSFs showing the strongest deviations, the ratio of the cc value obtained with the reference PSF to the cc value obtained with the actual PSF depends roughly linearly on the latter. Therefore, we can determine correction factors, which need to be applied to the real objects to make their core concentration nearly independent of the PSF, and thus comparable to each other. Corrections were only applied for cc values lower than 0.95 and for five different PSFs (*Regions 7, 9, 10, 11* and *13*, see Table 2.2), according to:

$$cc_{corr} = cc\left[1 + k(PSF_i)\ (cc - t)\right], \quad t = \begin{cases} 1.0 & \textit{Regions 10, 13} \\ 0.95 & \textit{Regions 7, 9, 11,} \end{cases} \quad (2.3)$$

where $k(PSF_i)$ is the PSF-dependent correction factor. In total we corrected cc values of 22 objects from our working sample. The difference between the corrected and uncorrected values never exceeds 10 per cent. We include the corrected core concentration in Table 2.3.

We display the distribution of parameter values for the artificial compact objects in the lower panels of Fig. 2.3. These show magnitude-dependent differences in their parameter range: brighter objects can reach lower core concentration, whereas fainter objects have in general somewhat higher residual asymmetry and ellipticity. As a consequence, we apply slightly different parameter cuts to our working sam-

ple for objects with $m_{Ve} < 20.0$ mag and for objects with $20.0 \leqslant m_{Ve} < 21.5$ mag when defining subsamples in the following analysis.

2.4   RESULTS

2.4.1   *Peculiar compact stellar systems*

We visually investigated compact stellar systems with high residual asymmetry and ellipticity as compared to the artificial compact objects. From our sample with $m_{Ve} < 20.0$ mag, we examined those objects with residual asymmetry higher than 0.5 or ellipticity higher than 0.2, corresponding to 34 or 25 per cent of all objects with a measured residual asymmetry parameter in that magnitude range. The overlap with the artificial objects that have residual asymmetries in this parameter range is 6 per cent. The overlap with regard to ellipticity is 5 per cent. From our sample with $20.0 \leqslant m_{Ve} < 21.5$ mag, we looked through all objects with a residual asymmetry higher than 0.55, corresponding to 38 per cent, or ellipticity higher than 0.25, corresponding to 16 per cent of compact stellar systems within that magnitude range. The overlap fractions with the artificial objects are 3 and 15 per cent, respectively.

Our visual investigation revealed peculiar compact stellar systems, which are displayed in Fig 2.4. We compare each peculiar object to an artificial compact object of similar brightness that was convolved with the PSF of the corresponding region (see Fig. 2.4, right-hand panels). The comparison illustrates that the peculiar appearance of the displayed objects is not due to PSF effects.

2.4.2   *Parameters and spatial distribution*

In this section we investigate whether there is a correlation between the parameters defined in Sections 2.3.2 and 2.3.3 and the spatial distribution of the brighter objects in our sample. For each parameter we defined a cut to separate objects with low-value from objects with high-value parameters. We then divided our sample into subsamples by combining different parameter cuts. The definition of the subsamples is specified in Table 2.4. For simplicity, we denote low core concentration with 'cc', high core concentration with 'CC', and analogous for residual asymmetry (ra/RA) and ellipticity (el/EL). The parameter cuts for the defined subsamples are provided in Table 2.5. We adopted the parameter cuts as well as a magnitude limit of $m_{Ve} = 20.6$ mag to yield the statistically most significant differences in the distribution of cluster-centric distance between the different subsamples. We note that the cc+ra subsample contains a higher fraction of bright objects than the other subsamples, yet also has the largest spread in luminosity (also see Fig. A.2). There are five objects with $m_{Ve} < 20.6$ mag that have no measured residual asymmetry and were therefore excluded from the following analysis.

Fig. 2.5 shows the spatial distribution of our sample in the cluster, where we highlight the subsamples cc+ra, cc+RA, CC+RA and cc+EL. For comparison we also include low-mass cluster galaxies in the magnitude range $-19 < M_r < -16$ mag. We probed the differences in the cluster-centric distance distributions (measured from NGC 1399) statistically with a Kolmogorov–Smirnov (KS) test, as summarised in Table 2.6, and provide a comparison of the cumulative distributions of cluster-centric distance for the defined subsamples in Fig. 2.6.
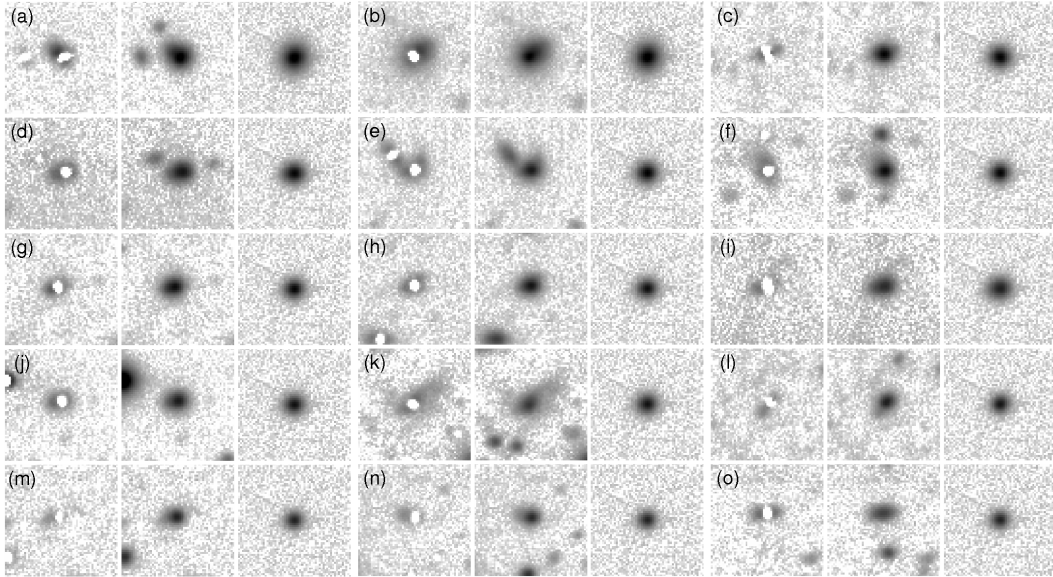
FIGURE 2.4: Peculiar compact stellar systems from our sample (centre sub-panels). The PSF-subtracted residual images are displayed in the left-hand sub-panels. We compare each peculiar object to an artificial compact object of similar brightness that has been convolved with the PSF of the corresponding region (shown in the right-hand sub-panels). The parameters of the artificial objects are based on magnitudes and sizes measured by Evstigneeva et al. (2008) for 18 real one-component UCDs. In addition to the measured Sérsic index, we created further models with a Sérsic index in the range of $n = 1 - 8$. The artificial objects displayed here have an intermediate Sérsic index of $n = 4$. For each peculiar object, we selected the artificial object that is closest in magnitude. The displayed objects are sorted by decreasing magnitude ($V-$band equivalent) from panels (a) to (o). The width of a single sub-panel is 13 arcsec (1.2 kpc). In the following we list the ID of each peculiar object, as given in Tables 2.1 and 2.3: (a) ID=17, (b) 15, (c) 448, (d) 838, (e) 868, (f) 711, (g) 775, (h) 867, (i) 897, (j) 869, (k) 697, (l) 5, (m) 777, (n) 735, (o) 570. The artificial objects shown in each panel are based on r_{50} and m_V of the following objects from Evstigneeva et al. (2008): (a) UCD 1, (b) UCD 1, (c) UCD 41, (d) UCD 41, (e) UCD 41, (f) UCD 48, (g) UCD 48, (h) UCD 55, (i) UCD 55, (j) UCD 55, (k) UCD 33, (l) UCD 54, (m) UCD 21, (n) UCD 21, (o) UCD 21.

We first compared the subsamples cc+ra, cc+RA, CC+RA and cc+EL to the respective other objects in the same magnitude range with $m_{Ve} < 20.6$ mag. We find that both the cc+RA and the cc+EL subsamples are predominantly located at larger cluster-centric distances. This difference is statistically significant according to a KS test, with a probability of 0.0 and 0.5 per cent, respectively, for both subsamples having the same cluster-centric distance distribution as the respective other objects in the same magnitude range. In the cc+ra and CC+RA subsamples most objects have smaller cluster-centric distances. The distribution of the cc+ra subsample is very similar to the overall distribution of respective other objects with $m_{Ve} < 20.6$ mag. The distribution of the CC+RA subsample even appears to be more concentrated[9] than the distribution of objects in the same magnitude range, although this difference has only a low statistical significance. Compared to the low-mass cluster galaxies, we find that the cc+RA and cc+EL subsamples appear similarly distributed, whereas the distribution of the cc+ra and CC+RA subsamples seems to be more centrally concentrated.

---

9 This also shows that the centrally concentrated distribution of the cc+ra subsample is not related to the high fraction of bright objects in it, since the CC+RA subsample consists of fainter objects, but is even more concentrated.

TABLE 2.4:   Definition of subsamples and abbreviations.

SUBSAMPLE	
cc+ra	Low core concentration and low res. asymmetry
cc+RA	Low core concentration and high res. asymmetry
CC+RA	High core concentration and high res. asymmetry
cc+EL	Low core concentration and high ellipticity

TABLE 2.5:   Parameter ranges for the subsamples cc+ra, cc+RA, CC+RA and cc+EL, defined such that they yield the statistically most significant differences in the distribution of cluster-centric distance. We applied slightly different parameter cuts for the bright ($m_{Ve} < 20.0$ mag) and faint ($20.0 \leqslant m_{Ve} < 20.6$ mag) objects of each subsample, respectively (see Section 2.3.4). For each subsample we give the fraction of objects in the respective magnitude range and the overlap fractions with the artificial objects.

SUBSAMPLE	PARAMETER CUTS	OBJECTS (per cent)	ART. OBJECTS (per cent)
cc+ra (bright)	cc < 0.77 and ra < 0.5	46.9	21.2
cc+ra (faint)	cc < 0.83 and ra < 0.55	17.5	0.0
cc+RA (bright)	cc < 0.77 and ra > 0.5	9.4	0.2
cc+RA (faint)	cc < 0.83 and ra > 0.55	19.3	0.0
CC+RA (bright)	cc > 0.77 and ra > 0.5	25.0	5.6
CC+RA (faint)	cc > 0.83 and ra > 0.55	36.8	3.7
cc+EL (bright)	cc < 0.77 and el > 0.2	12.5	0.2
cc+EL (faint)	cc < 0.83 and el > 0.22	14.0	0.0

When comparing the different subsamples to each other, we find the most significant differences between the cluster-centric distance distributions of the cc+RA subsample as compared to the cc+ra and CC+RA subsamples, with a probability of 0.0 per cent, respectively, for having the same cluster-centric distance distribution. This is also seen for the cc+EL subsample, although with a lower statistical significance. We do not find significant differences between the distributions of the cc+ra and CC+RA subsamples. Also the distributions of the cc+RA and cc+EL subsamples are similar. But for the latter this is mainly due to the fact that the subsamples have some overlap in parameter range, since objects with high residual asymmetry can as well have high ellipticity, or vice versa.

In addition to the subsamples defined in Table 2.5 we provide an alternative subsample definition in Appendix A.2, where we set the parameter cut for the core concentration to a higher value in order to increase the number of objects in the subsamples with low core concentration. We do not find that our main results change significantly, although they have mainly lower statistical significances. For the CC+RA subsample, which includes fewer objects according to this parameter cut, we find that the more concentrated distribution, compared to the respective other objects of similar magnitude, becomes statistically more significant than previously, with a probability of 0.8 per cent for the same distribution.
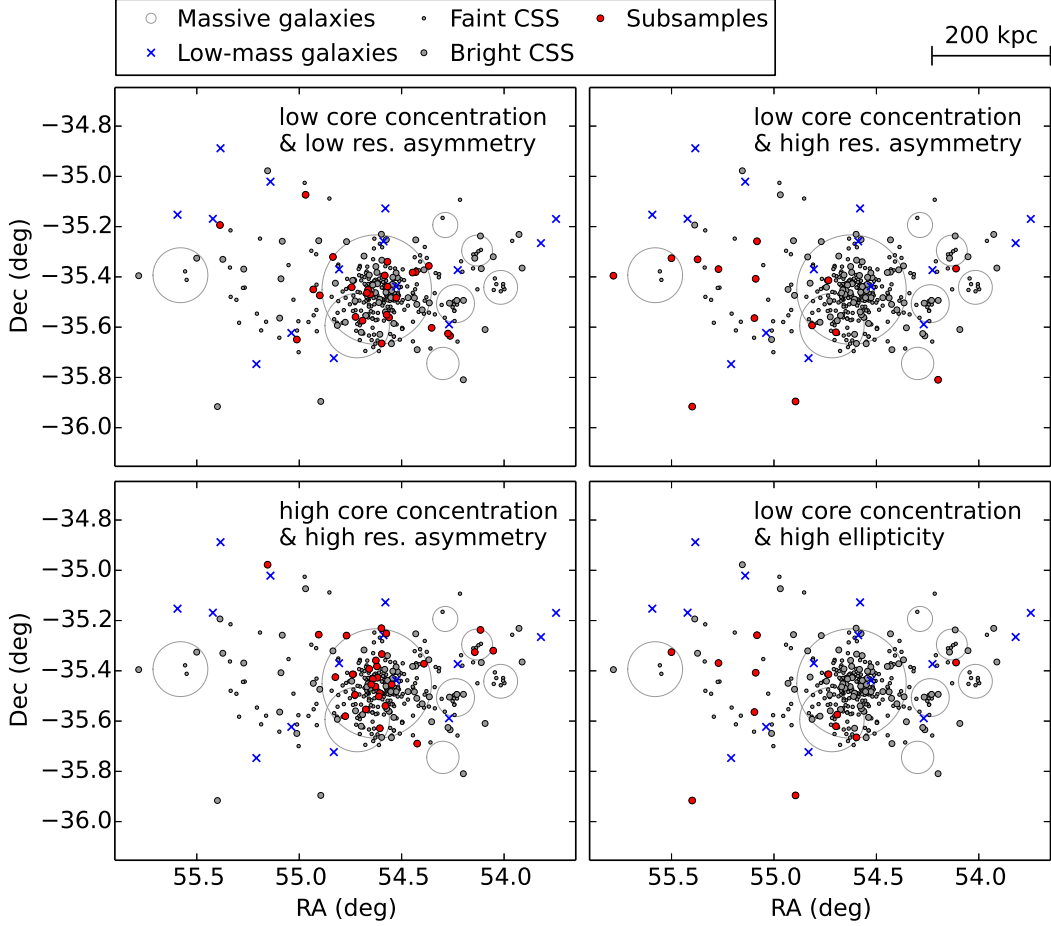
FIGURE 2.5: Spatial distribution of compact stellar systems in the Fornax cluster. For comparison we also show the distribution of the cluster galaxies. Faint CSS: compact objects with $20.6 \leqslant m_{Ve} < 21.5$ mag. Bright CSS: compact objects with $m_{Ve} < 20.6$ mag. Subsamples: cc+ra, cc+RA, CC+RA, cc+EL, as defined in Table 2.5. Low-mass galaxies: galaxies with $-19 < M_r < -16$ mag from the Fornax cluster catalogue (FCC, Ferguson 1989; based on the magnitude conversions of Weinmann et al. 2011). Massive galaxies: galaxies with $M_r \leqslant -19$ mag from the FCC. Each massive galaxy is represented by a circle with three times its isophotal diameter at $\mu_B = 25$ mag arcsec^{-2}, $3\,d_{25}$ (we used the extinction-corrected values for d_{25}, obtained from HyperLEDA; Makarov et al. 2014). The two brightest galaxies are NGC 1399 in the centre and NGC 1404 to the south-east from it.

2.4.3 *Distribution in phase-space*

In order to examine the phase-space distribution of compact stellar systems in the Fornax cluster, we define Δv as an object's relative velocity with respect to the cluster mean velocity ($1460\,\mathrm{km\,s^{-1}}$). The latter is the average velocity of Fornax cluster members within a cluster-centric distance of $1°$, including all compact objects from our catalogue and galaxies from the Fornax cluster catalogue (FCC, Ferguson 1989). We denote the corresponding standard deviation ($324\,\mathrm{km\,s^{-1}}$) as the cluster velocity dispersion σ, R as the cluster-centric distance, and R_{vir} as its virial radius (assumed to be $0.85\,\mathrm{Mpc}$ or $2.5°$, which is the average of the $0.7\,\mathrm{Mpc}$ quoted by Drinkwater et al. 2001 and $1.0\,\mathrm{Mpc}$ quoted by Murakami et al. 2011). The phase-space distribution is shown in Fig. 2.7 as $\Delta v/\sigma$ versus R/R_{vir}. We highlight the subsamples cc+ra, cc+RA, CC+RA and cc+EL, and further discriminate between very faint compact stellar systems in the magnitude range of GCs ($m_{Ve} \geqslant 21.5$ mag,

TABLE 2.6:   KS test probabilities (percentage) for the null hypothesis that two subsamples have the same cluster-centric distance distribution. In the last row the distributions of the individual subsamples are compared to the respective other compact objects with different parameters in the same magnitude range with $m_{Ve} < 20.6\,\text{mag}$.

SUBSAMPLE	cc+ra	cc+RA	CC+RA	cc+EL
cc+ra	100.0	0.0	55.3	0.4
cc+RA		100.0	0.0	98.7
CC+RA			100.0	1.0
cc+EL				100.0
respective other CSS	41.7	0.0	6.7	0.5
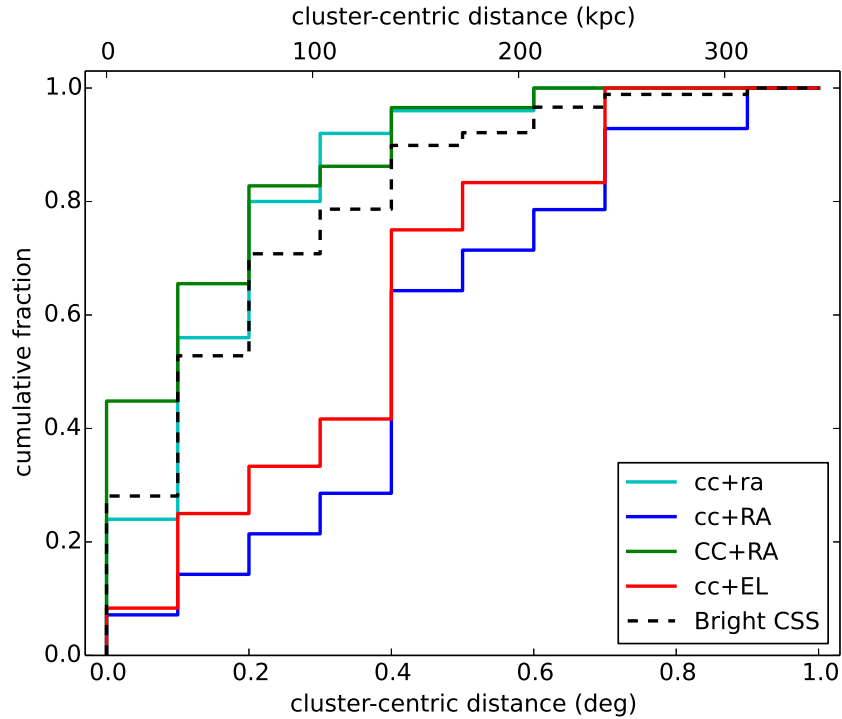
FIGURE 2.6:   Cumulative distribution of projected cluster-centric distance (measured from NGC 1399) for the subsamples cc+ra, cc+RA, CC+RA and cc+EL. The distribution of all objects with $m_{Ve} < 20.6\,\text{mag}$ ('Bright CSS') is shown for comparison.

which are not part of our working sample), faint objects ($20.6 \leqslant m_{Ve} < 21.5\,\text{mag}$), and bright objects ($m_{Ve} < 20.6\,\text{mag}$), and include low-mass galaxies in the magnitude range $-19 < M_r < -16\,\text{mag}$ for comparison. Table 2.7 summarises the velocity dispersion for the various subsamples and cluster populations. We show the phase-space distribution of the alternative subsamples in Appendix A.2 (Fig. A.4 and Table A.3).

Phase-space diagrams allow one to study the accretion history of a cluster population. For example, Noble et al. (2013) used caustic profiles, which are lines of constant $(\Delta v/\sigma) \times (R/R_{\text{vir}})$, to distinguish between infalling and virialized cluster members, where higher values trace systems that were more recently accreted. In Fig. 2.7 we plotted caustic lines of constant $(\Delta v/\sigma) \times (R/R_{\text{vir}})$ at ± 0.1 and ± 0.4, respectively. Cosmological simulations show that early accreted systems would be predominantly located within the inner caustic lines of ± 0.1, systems accreted
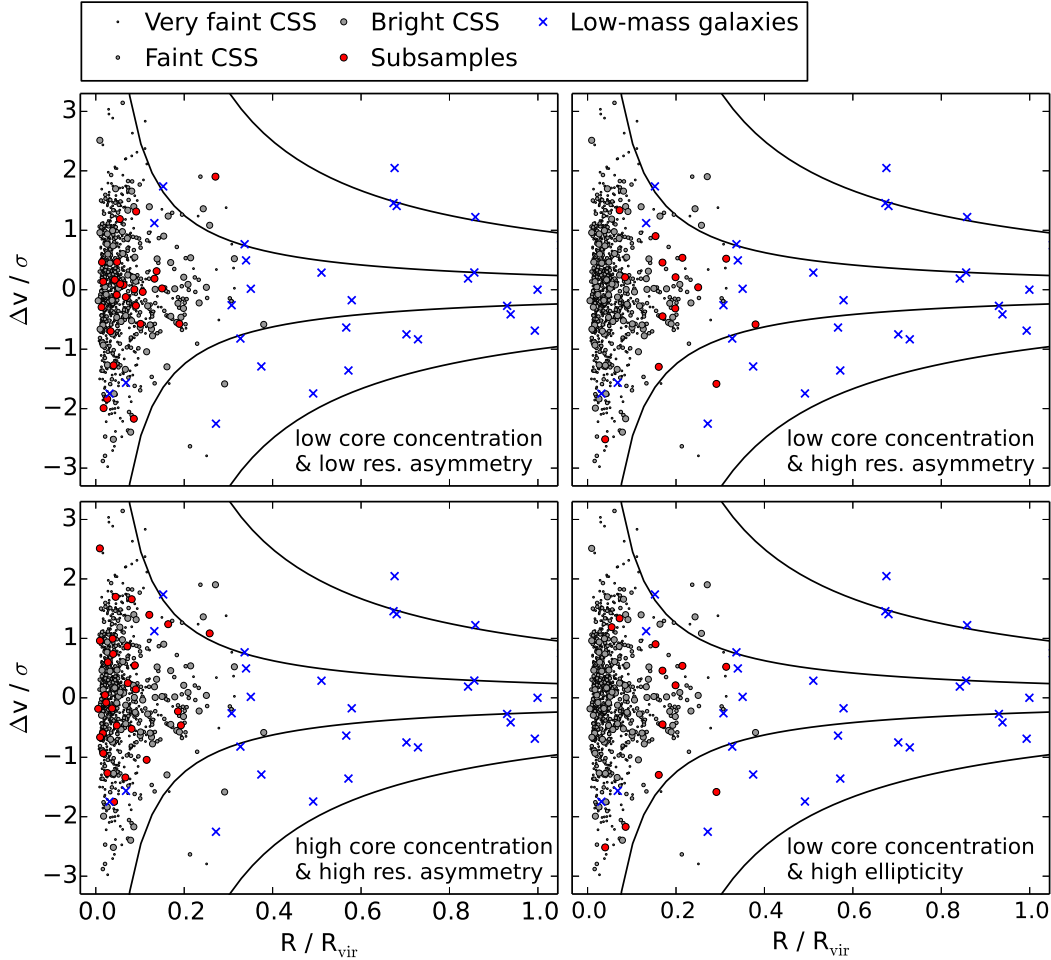
FIGURE 2.7: Phase-space distribution of compact stellar systems and low-mass galaxies in the Fornax cluster. Very faint CSS: compact objects with $m_{Ve} \geqslant 21.5$ mag (not part of our working sample). Faint CSS: compact objects with $20.6 \leqslant m_{Ve} < 21.5$ mag. Bright CSS: compact objects with $m_{Ve} < 20.6$ mag. Subsamples: cc+ra, cc+RA, CC+RA, cc+EL, as defined in Table 2.5. Low-mass galaxies: galaxies with $-19 < M_r < -16$ mag from the FCC (Ferguson 1989; based on the magnitude conversions of Weinmann et al. 2011). Δv is the relative velocity of an object with respect to the cluster mean velocity ($1460\,\mathrm{km\,s^{-1}}$). We denote σ as the cluster velocity dispersion ($324\,\mathrm{km\,s^{-1}}$), R as the cluster-centric distance, and R_{vir} as its virial radius ($2.5°$, see Section 2.4.3). The mean velocity and dispersion were calculated from all compact stellar systems and FCC galaxies within a cluster-centric distance of $1.0°$. The solid lines correspond to caustic lines of constant $(\Delta v/\sigma) \times (R/R_{vir})$ at ± 0.1 and ± 0.4, respectively.

later between the caustics of ± 0.1 and ± 0.4, and recently accreted systems along or outside the caustic lines of ± 0.4 (cf. Haines et al. 2012; Noble et al. 2013).

We find that essentially all compact stellar systems are located within the inner caustics of ± 0.1. Also some low-mass galaxies are found in this region, but many of them occupy the region in between the caustic lines of ± 0.1 and ± 0.4. This is also reflected in the velocity dispersion, where we find the lowest dispersion in particular for the compact stellar systems with $m_{Ve} < 21.5$ mag (the samples comprising the bright and faint CSS) and the highest for the low-mass galaxies.

Among the bright compact stellar systems with $m_{Ve} < 20.6$ mag, we do not find statistically significant differences in the velocity distribution of the four different subsamples. The main difference seems to be in the spatial distribution. However, with respect to the velocity dispersion, we find that the cc+ra subsample has on

TABLE 2.7:   Velocity dispersion for very faint ($m_{Ve} \geqslant 21.5$ mag, not part of our working sample), faint ($20.6 \leqslant m_{Ve} < 21.5$ mag) and bright ($m_{Ve} < 20.6$ mag) compact stellar systems, low-mass galaxies (FCC), and the subsamples cc+ra, cc+RA, CC+RA, cc+EL, as defined in Table 2.5. The velocity dispersion of each subsample is calculated as standard deviation within a cluster-centric distance of $R \leqslant 1.0°$ (σ_{tot}), $R \leqslant 0.4°$ (σ_{in}) or $0.4 < R \leqslant 1.0°$ (σ_{out}), based on the velocities given in Table 2.1. N_{obj} corresponds to the number of objects from the respective subsample in the inner ($N_{obj,in}$) or outer ($N_{obj,out}$) cluster region. The velocity dispersion is given in km s^{-1}. $1.0°$ corresponds to 0.346 and $0.4°$ to 0.138 Mpc at the distance of Fornax.

SUBSAMPLE	σ_{tot}	σ_{in}	$N_{obj,in}$	σ_{out}	$N_{obj,out}$
Very faint CSS	337	336	535	341	14
Faint CSS	297	302	232	252	29
Bright CSS	307	316	73	271	21
Low-mass galaxies	400	505	4	317	7
cc+ra	303	282	23	401	2
cc+RA	326	485	4	330	10
CC+RA	328	338	25	246	4
cc+EL	414	556	5	269	7

average the lowest and the cc+EL subsample the highest velocity dispersion. The two subsamples cc+RA and CC+RA with large residual asymmetry have velocity dispersions in between. In the phase-space diagram we note that especially the cc+EL subsample is predominantly distributed along the inner caustic lines.

2.5   DISCUSSION

2.5.1   *Analysis methods and limitations*

The seeing FWHM varies over the mosaic, since the latter is based on images acquired in multiple nights and observing runs. In the PSF analysis we tried to account for this by determining the PSF in regions of similar FWHM, as indicated in Fig. 2.2. In *Region 3* of our mosaic we observe systematically lower core concentration for our working sample with $m_{Ve} < 21.5$ mag. We investigated whether this effect could be due to a non-matching PSF. We therefore fitted PSFs from other regions on the mosaic to all objects from our working sample that are located in *Region 3*. We find that the core concentration decreases when a PSF of smaller FWHM is used. Thus, if there are variations of the PSF FWHM on scales smaller than the considered region within which the PSF is determined, an artificially low core concentration can occur if an object is located in an area with locally larger FWHM than the PSF FWHM of that region.

   In order to estimate local variations of the FWHM we computed the minimum FWHM around each object from our working sample in *Region 3*. To find the minimum FWHM we first measured the FWHM of all sources in this region with SEXTRACTOR. From all SEXTRACTOR-detected sources brighter than $m_{Ve} = 22$ mag we then determined the minimum FWHM within a circular area of 450 pixels (1.8 arcmin) in radius around each object from our working sample. Finally we compared the local FWHM to the FWHM of the PSF stars from this region. In *Region 3* we neither find a relation of core concentration with local FWHM, nor are

all objects with low core concentration systematically located in areas with large local FWHM.

We extended this test to the full sample of compact stellar systems brighter than $m_{Ve} = 20.6$ mag and investigated how much a locally varying FWHM would affect our results from Section 2.4.2. We first computed the relative local FWHM for each object as difference between the measured local FWHM and the average FWHM of all PSF stars of the respective region. Since we found a slight dependence of the core concentration on the relative local FWHM for objects brighter than $m_{Ve} = 20.6$ mag, we defined a linearly varying parameter cut that follows this relation. We then defined new subsamples, using the parameter cuts for the residual asymmetry and ellipticity as specified in Table 2.5, but with a linearly varying parameter cut for the core concentration. According to this definition, our main result that the subsamples with low core concentration and high residual asymmetry (or high ellipticity) are mainly distributed at larger cluster-centric distances remains unchanged[10].

The angular resolution of our data limits our ability to identify possible blends of close neighbouring sources. Richtler et al. (2005) resolved one of the peculiar compact objects (Fig. 2.4, panel g) into two sources. We therefore attempt to estimate how likely it is that all objects with significant asymmetry or ellipticity are blends. For this purpose we assume that objects that appear asymmetric or elongated could be blends if a close, up to three magnitudes fainter, neighbour source was located within a distance of 4–7 pixels (corresponding to 91 and 160 pc, respectively). When considering all objects from our bright sample ($m_{Ve} < 20.6$ mag) with high residual asymmetry or high ellipticity (according to the definition in Table 2.5), which have cluster-centric distances between 20 and 160 kpc, we find an expected number density of faint sources of 0.09 arcsec^{-2} if all those objects were blends. For comparison, the observed number density of faint sources with magnitudes $20.6 < m_{Ve} < 23.6$ mag located within the same area is 0.003 objects arcsec^{-2}. Thus, only a single one of the 32 bright asymmetric or elongated objects we observe in this area would statistically be expected to be a blend. We note, however, that an overdensity of GCs within 1 kpc of brighter compact stellar systems, including a fraction within 300 pc, was recently reported by Voggel et al. (2016). We may thus expect a few blends among the said objects.

2.5.2 *Peculiar compact stellar systems in the Fornax cluster*

We report the discovery of peculiar compact stellar systems in the Fornax cluster, which appear asymmetric or elongated in our images (illustrated in Fig. 2.4). The presence of a few peculiar objects in Fornax was already noted by Richtler et al. (2005) and Voggel et al. (2016)[11].

Some compact Fornax cluster members have previously been observed with *HST* (Evstigneeva et al. 2008). Two of them are also shown in Fig. 2.4 (panels d and h), but we note that a direct comparison of the inner structure is not possible due to our much broader PSF (see Fig. 2.8). At the same time the *HST* images are too shallow for a comparison of the outer, low surface brightness structure that we

---

10 With probabilities of 0.0 and 0.8 per cent, respectively, for the two subsamples having the same cluster-centric distance distribution as objects in the same magnitude range according to a KS test.

11 Two of our displayed objects were shown in Richtler et al. (2005) (Fig. 2.4, panels g and n). The object in panel (n) was also pointed out by Voggel et al. (2016) to be peculiar.
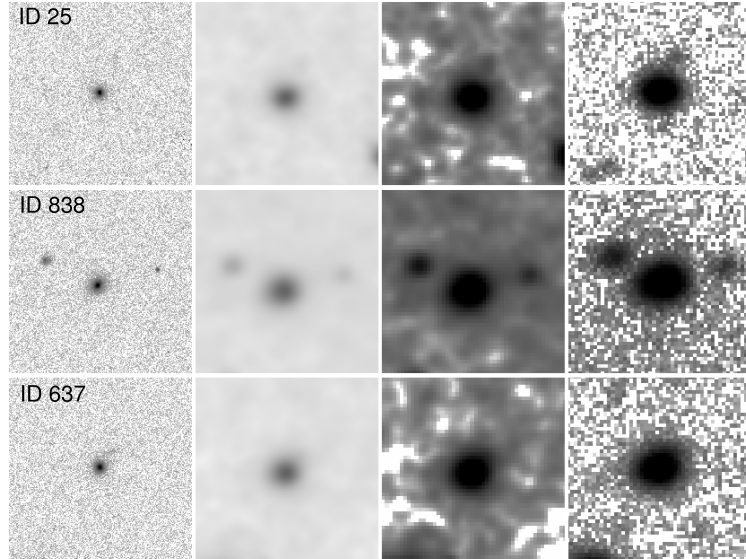
FIGURE 2.8:   Comparison of compact stellar systems observed with *HST* (first column) and *WFI* (last column). We selected the compact objects with the highest ellipticities as measured in the *HST* images (cf. Evstigneeva et al. 2008, table 1: UCDs 16, 50 and 52). The objects with ID 838 and 867 are the objects shown in panels d) and h) of Fig. 2.4. The first column displays the original *HST* data. In the second column the *HST* data were convolved with the *WFI* PSF of the corresponding region. This illustrates that the inner structure of the objects, which is resolved in the original *HST* data, gets blurred out after convolution with the *WFI* PSF. In the third column the convolved *HST* image were scaled to the *WFI* pixel scale. A comparison to the fourth column, showing the original *WFI* data, demonstrates that the latter go deeper in surface brightness than the *HST* data. All images are displayed with the same intensity scale and contrast. The images have sizes of $13 \times 13 \, \mathrm{arcsec}^2$.

are able to measure in our data. The *azimuthally averaged* UCD surface brightness profiles of Evstigneeva et al. (2008) reach $26 \, \mathrm{mag} \, \mathrm{arcsec}^{-2}$ at best (see their fig. 1), whereas we reach an image depth of $26.8 \, \mathrm{mag} \, \mathrm{arcsec}^{-2}$ at S/N = 1 *per pixel* (see Section 2.1).

In the Virgo cluster the structure of a large sample of UCDs has been investigated by Liu et al. (2015), revealing faint envelopes around many of the objects. However, objects with similarly asymmetric appearance as observed in our data were not reported. In the cluster Abell S0740, Blakeslee et al. (2009) detected faint envelopes around candidate UCDs, which show signs of being elongated in *HST* images.

There are two main formation scenarios discussed in the literature, relating UCDs to either the population of galaxies or to the population of star clusters. In the former case, it is suggested that UCDs may be the remnant nuclei of tidally stripped nucleated dwarf galaxies (e.g. Bekki et al. 2003b; Pfeffer and Baumgardt 2013). In a star cluster origin, UCDs may grow to sizes and masses larger than typical GCs, if they form in star cluster complexes by merging of young massive star clusters (e.g. Fellhauer and Kroupa 2005).

According to simulations by Bekki et al. (2003b), observable signatures of a tidal stripping origin would be tidal tails as well as relics from the envelope of the progenitor galaxy that has been stripped. In Chapter 3 we did not find any diffuse streams that would be signs of tidal debris around any of the 904 spectroscopically confirmed objects in our compiled catalogue. As noted in Chapter 3, such streams should be visible in most parts of the mosaic if their surface brightness level is in the range $27.5 \lesssim \mu_{Ve} \lesssim 28.0 \, \mathrm{mag} \, \mathrm{arcsec}^{-2}$. The absence of visible tidal debris

does not necessarily need to be in contradiction to a tidal stripping origin of these objects. Pfeffer et al. (2014) showed, based on cosmological simulations, that most low-mass cluster galaxies were disrupted already many gigayears ago. Thus, if most of the compact stellar systems resulted from early stripping events, we simply might not be able to observe relics of tidal debris any more today, since tidal tails disperse on time-scales of a few Gyr (Pfeffer and Baumgardt 2013). However, Brüns and Kroupa (2012) predicted that an object formed via merging of massive star clusters in a star cluster complex would also be surrounded by a faint stellar envelope, thus exhibiting a similar two-component surface brightness profile as reported in the tidal stripping simulations. Therefore, without the detection of the predicted long tidal streams, we cannot discriminate between a stripping or a merging origin.

In the star cluster merging scenario described by Brüns and Kroupa (2011), the forming object can look quite asymmetric as long as the merger is not yet complete. However, the authors showed that star clusters in a cluster complex typically merge on time-scales of only a few hundred Myr. As a consequence, if the structures we observe for the peculiar systems in Fig. 2.4 are signatures of an ongoing star cluster merger, then these should be comparatively young systems. This seems to be in contradiction with the observation that UCDs have in general old stellar populations (Evstigneeva et al. 2007; Paudel et al. 2010; Francis et al. 2012).

On the other hand, Fellhauer and Kroupa (2005) reported that a merger remnant would be stable over a time-scale of 10 Gyr. Thus, compact objects may have formed from star cluster merging already in very early phases during the formation of the Fornax cluster core, when the merging of gas-rich galaxies possibly offered conditions for strong starbursts in which large star cluster complexes are thought to form. At the same time Fellhauer and Kroupa (2005) demonstrated that such a merger remnant constantly loses some of its mass with every pericentric passage due to the tidal field of the cluster. Therefore the peculiar structures of some compact systems may not stem from an ongoing merger of star clusters, but may be associated with the deformation or disruption of an extended star cluster that formed via star cluster merging when the Fornax cluster core assembled. Disruption signatures can thus not necessarily discriminate between the proposed formation scenarios of compact stellar systems.

To estimate whether tidal stripping would be efficient for disturbing the outer structure of an UCD-like compact object orbiting in the Fornax cluster, we calculate the tidal radius according to King (1962):

$$
R_{\text{tidal}} = R_{\text{peri}} \left(\frac{M_{\text{obj}}}{M_{\text{cl}}(R_{\text{peri}}) \, (3 + e)} \right)^{1/3} , \tag{2.4}
$$

where R_{peri} is the pericentric distance, M_{obj} the total mass of the object, $M_{\text{cl}}(R_{\text{peri}})$ the enclosed cluster mass within R_{peri} and e the eccentricity of the orbit for which we adopt a value of 0.5[12]. For a typical UCD-like object with a mass of $M_{\text{obj}} = 10^7 \, M_\odot$, when assuming it reaches an orbital pericentre of $R_{\text{peri}} = 20 \, \text{kpc}$, the tidal radius would be in the range of $200 - 300 \, \text{pc}$, depending on the adopted mass profile for the Fornax cluster (Drinkwater et al. 2001; Richtler et al. 2008; Schuberth et al. 2010). While this is already on the order of 10 effective radii for a UCD of mass $M_{\text{obj}} = 10^7 \, M_\odot$ (cf. Norris et al. 2014), we would be able to observe such an object

---

12 Bound orbits have an eccentricity of $e < 1.0$. An eccentricity of $e = 0.0$ would correspond to a circular orbit, $e > 0.7$ to a highly eccentric orbit.

out to its tidal radius in our deep imaging data, according to the surface brightness profiles of typical UCDs (see fig. 1 of De Propris et al. 2005). This estimate shows that distortions of the outer structure due to tidal stripping could be expected for objects with close cluster-centric passages. However, since the tidal radius of an object solely depends on its total mass, and not on how the object mass is distributed, it is not possible to infer the nature of the disturbed object, whether it is the remains of a stripped galaxy or an extended star cluster in process of disruption.

For the above estimate of the tidal radius we assumed that the objects would be only influenced by the cluster's tidal field. None the less, some objects may be more strongly affected by very close bright galaxies, especially further out from the cluster centre. Schuberth et al. (2008) investigated whether some compact stellar systems with $M_V < -9.5$ mag were consistent with being associated with any of the ten brightest galaxies in the Fornax cluster core, according to their spatial and velocity distribution. The authors showed that among the compact objects, which are located within a projected distance of $1.5 \, d_{25}$[13] from a bright galaxy, the metal-rich (red) objects have velocities not deviating by more than $100 \, \mathrm{km \, s^{-1}}$ from the velocity of the closest massive galaxy, whereas the metal-poor (blue) objects seem to be characterised by a larger spread in velocities. The remaining objects at distances larger than $1.5 \, d_{25}$ from any bright galaxy seem to be consistent with being kinematically associated with the extended GC system of NGC 1399, out to a cluster-centric distance of 30 arcmin.

In Fig. 2.5, showing the spatial distribution of known Fornax cluster members, we represented each massive galaxy with $M_r \leqslant -19$ mag by three times its isophotal diameter ($3 \, d_{25}$). We find that only few objects from our subsamples lie close in projection to a bright galaxy other than NGC 1399, and of these only a minor fraction also has a similar velocity[14]. Therefore we see no indication that a significant fraction of objects from our subsamples is bound to massive galaxies with $M_r \leqslant -19$ mag other than NGC 1399.

2.5.3 *Spatial and phase-space distribution of compact stellar systems*

In general it is observed that GCs and galaxies have different spatial distributions in galaxy clusters. For example Zhang et al. (2015) observed that in the central core region of Virgo, the dwarf ellipticals (dEs) have a much flatter number density profile than the GCs. In Fornax it was also found that the GC population of NGC 1399 is much more centrally concentrated than the surrounding dEs (Gregg et al. 2009; Hilker 2011). Gregg et al. (2009) reported that the UCDs in Fornax have lower velocity dispersions than both the GCs and the low-mass galaxies in the core region, which we also find in this work. Schuberth et al. (2010) further distinguished between red and blue GCs, and their analysis showed that UCDs have a velocity dispersion lower than that of the blue GCs, but higher than that of the red GCs.

---

[13] d_{25} is the isophotal diameter of a galaxy at $\mu_B = 25 \, \mathrm{mag \, arcsec^{-2}}$.

[14] We find that the following number of objects from our subsamples are located within a distance of $r = 1.5 \, d_{25}$ from a massive galaxy with $M_r \leqslant -19$ mag other than NGC 1399: 4 out of 25 in cc+ra, 3 out of 14 in cc+RA, 7 out of 29 in CC+RA, and 4 out of 12 in cc+EL. When we require additionally a relative velocity smaller than $\Delta v = 200 \, \mathrm{km \, s^{-1}}$, the number of objects is: 1 in cc+ra, 1 in cc+RA, 3 in CC+RA, and 2 in cc+EL.

In Sections 2.4.2 and 2.4.3 we investigated the spatial and phase-space distribution of compact stellar systems in the Fornax cluster, where we focused on the distribution of objects with $m_{Ve} < 20.6$ mag ($M_{Ve} < -11.1$ mag), corresponding to the brighter UCD magnitude range. We compared the differences in the cluster-centric distance distributions of smaller subsamples, where we categorized the objects according their core concentration, residual asymmetry, and ellipticity. In the following we discuss the results on the spatial and phase-space distribution of our subsamples in terms of the origin and nature of compact stellar systems.

We find that the objects in the subsample with low core concentration and high residual asymmetry, as well as in the subsample with low core concentration and high ellipticity, are predominantly distributed at larger cluster-centric distances, compared to objects in the same magnitude range but with different parameters[15]. Their extended galaxy-like spatial distribution might favour a formation scenario in which they are remnants of stripped low-mass galaxies[16]. However, since their location at larger cluster-centric distances implies a currently large tidal radius, their structure could only be explained by tidal stripping if these objects are on rather eccentric orbits with small pericentre distances, such that they possibly approached the cluster centre very closely at earlier times. We observe that especially the subsample with low core concentration and high ellipticity has high velocities relative to the Fornax cluster, which would be expected for radial orbits. This subsample is mainly distributed *along* the inner caustic lines of constant $(\Delta v / \sigma) \times (R / R_{vir}) = \pm 0.1$ and seems to integrate smoothly into the phase-space distribution of low-mass cluster galaxies. This could indicate that these objects, or their progenitors, may have been accreted more recently compared to the overall population of compact stellar systems in the UCD and GC magnitude range, which are predominantly confined *within* those caustics.

In the Virgo cluster, observations of a large sample of UCDs around M87 point in a similar direction: UCDs at cluster-centric distances larger than 40 kpc have a radially biased orbital structure consistent with that of stripped galaxies on radial orbits (Zhang et al. 2015). Although no compact stellar systems with obvious distorted outer structures have been reported in Virgo so far, Liu et al. (2015) observed that compact objects with signs of a faint stellar envelope are found only at distances larger than 0.1° (corresponding to 28.8 kpc at a distance of 16.5 Mpc for Virgo; Blakeslee et al. 2009) from the two brightest cluster galaxies M87 and M49, respectively. Their distribution is, however, still more concentrated than that of the cluster's dwarf galaxy population. The authors interpreted this sequence of decreasing envelope fraction with decreasing cluster-centric distance as an indication that tidal stripping of nucleated dwarf galaxies plays an important role for the population of compact stellar systems in Virgo.

In Fornax, when defining a subsample of objects with no signs of distortions[17], we find the majority of these objects distributed at small cluster-centric distances. This would at least not imply *recent* stripping, if these objects were stripped galaxies at all. Instead, these objects might already be stripped down to their tidal radius.

---

15 We note that the subsamples with larger cluster-centric distances may even be slightly under-represented in our study, as compared to the other subsamples, if the completeness varies with cluster-centric distance (see Section 2.2.4).

16 This does not exclude that some of them formed as massive star clusters in the tidal tails of a major galaxy merger (e.g., Gallagher et al. 2001).

17 By choosing objects with low residual asymmetry and low ellipticity according to Table 2.5, with parameter cuts at ra < 0.5 and el < 0.2 for objects with $m_V < 20.0$ mag, and ra < 0.55 and el < 0.22 for objects with $20.0 \leqslant m_V < 20.6$ mag.

This could be expected if the objects had been accreted at very early times, and had been exposed for longer to the cluster tidal field than, e.g., the objects with low core concentration and high residual asymmetry (or high ellipticity). This would be supported by their lower velocity dispersion, compared to other subsamples. Smith et al. (2015), who studied the effects of harassment on early-type dwarf galaxies in galaxy clusters with numerical simulations, concluded that strongly harassed galaxies would be characterised by low orbital velocities.

However, for this subset of objects with no signs of distortions, we would not exclude a star cluster origin either. Based on the spatial and phase-space distribution alone, it may be difficult to disentangle a star cluster from a galaxy origin — possible progenitor galaxies may have been accreted very early on, or even formed at the same epoch as massive star clusters. For example, Bournaud et al. (2008) predicted that during the formation of giant ellipticals through mergers of gas-rich galaxies, tidal dwarf galaxies ($M_* = 10^8 - 10^9 \, M_\odot$) could form along with massive star clusters ($M_* = 10^5 - 10^7 \, M_\odot$).

Notwithstanding these considerations, the best candidates for a star cluster origin among the considered subsamples seem to be the objects with high core concentration and high residual asymmetry. Their distribution is very centrally concentrated and looks quite different from the distribution one would expect for galaxies. Moreover, this subsample is characterised by a higher core concentration, i.e. having a more star-like central component. Possibly we observe here a population of bright deformed star clusters instead of remnants of stripped galaxies. Since most of the objects are in close proximity to NGC 1399 the tidal radius would be quite small so that current stripping or deformation could indeed be expected. Some objects of this subsample are located in between NGC 1399 and the close elliptical galaxy NGC 1404 to the south-east from it (see Fig. 2.5). Kim et al. (2013) and D'Abrusco et al. (2016) took an overabundance of GCs between NGC 1399 and NGC 1404 (as well as other surrounding galaxies) as an indication for interactions in the recent past, which was also simulated by Bekki et al. (2003a). Thus, some of our objects with high core concentration and high residual asymmetry may have been distorted and also freed from their parent galaxies during possible interactions of massive cluster galaxies in the Fornax cluster core.

2.6 CONCLUSIONS

Our deep imaging data of the Fornax cluster core reveal peculiar compact stellar systems, which appear asymmetric or elongated. From their structure alone we cannot infer their origin, whether these objects are luminous star clusters in the process of disruption or possible remnants of stripped galaxies. However, the spatial distribution of objects with low core concentration and high residual asymmetry (or high ellipticity) at mainly larger cluster-centric distances may be explained with a galaxy origin of at least some of these objects. This is also supported by the high relative velocities we observe in particular for the objects with low core concentration and high ellipticity.

A SEARCH FOR TIDAL STREAMS AND ULTRA-DIFFUSE GALAXIES IN DEEP OPTICAL IMAGING OF THE FORNAX CLUSTER CORE

ABSTRACT

We present a deep optical mosaic of the Fornax galaxy cluster's core, covering 1.6 square degrees. The data were acquired with ESO/MPG 2.2 m/WFI, using a transparent filter that nearly equals the no-filter throughput and thus provides a high signal-to-noise ratio. Based on an approximate conversion to V-band magnitudes, the unbinned and binned mosaics (0.24 and 0.71 arcsec pixel^{-1}) reach a median depth of 26.6 and 27.8 mag arcsec^{-2}, respectively. We identify a previously uncatalogued ultra-diffuse galaxy candidate[1], with a central surface brightness of 27.6 mag arcsec^{-2} and a half-light semimajor axis of 3.9 kpc. The galaxy's significant elongation and truncated light profile imply that it may be in the process of disruption. Since we also identify a long diffuse stream in its vicinity, the object could be merely a galaxy remnant that is now the core of a tidal stream. The existence of these and a few more faint structures is confirmed independently by VST/OmegaCAM data that form part of the Fornax Deep Survey. Another low surface brightness object that had been catalogued as likely background galaxy in an earlier study also qualifies as ultra-diffuse galaxy candidate, based on its appearance in our deep mosaic. Some other diffuse structures we observe may, however, originate from reflections of bright foreground stars. The detection of smooth, extended structures that form part of the intracluster light is hampered by such inhomogeneities on the scale of individual detector chips (9 arcmin or 50 kpc). Our deep mosaic may be useful for future analyses, such as the study of galaxy outskirts or of the galaxy luminosity function.

The results of this study are included in Lisker et al. (submitted to A&A). C. Wittmann was significantly involved in the data reduction and provided the model galaxies for the visual comparison to the identified ultra-diffuse galaxy candidate.

3.1 INTRODUCTION

While galaxies are generally gravitationally bound entities well beyond their visible stellar extent, this can change dramatically when they plunge deep into the gravitational potential well of a massive host galaxy or a galaxy group. Tidal forces are then leading to continuous mass loss, first of the outer dark matter (at least within the standard cosmological model, see e.g. Gnedin 2003b and Villalobos et al. 2012), then of the stellar and gaseous component (McConnachie et al. 2004; Mayer et al. 2006, the latter emphasizing the relevance of ram pressure to efficiently strip the gas). If multiple close pericentric passages occur, or if close encounters with other substructure – e.g. in a galaxy cluster – increase the stripping efficiency (Moore et al. 1998), even total disruption can result (Goerdt et al. 2008), leaving a stream of stellar material that may still be traceable observationally for some time (Mastropietro et al. 2005).

---

1 In the meantime this galaxy candidate has been confirmed by Venhola et al. (2017).

Stellar streams with and without remnant cores of the former galaxies have been found not only around the Milky Way (Belokurov et al. 2007), but also in dedicated observational campaigns with small telescopes that provide a large field-of-view per detector chip (e.g. Martínez-Delgado et al. 2010). Such a deep optical imaging campaign was also done for the core of the Virgo galaxy cluster (Mihos et al. 2005), revealing not only a significant amount of intracluster light at surface brightness levels of $\mu_V \gtrsim 27 \, \mathrm{mag \, arcsec^{-2}}$, but also a number of distinct stellar streams. The detection of such structures is not all surprising, since we know that most cosmic structures are continuously growing through accretion of smaller components (Springel et al. 2005). It is noteworthy, however, that the disruptive processes associated with the infall and accretion of galaxies onto groups and clusters can at the same time serve as formation processes of new objects. The gradual stripping of late-type galaxies in a group-like tidal field, known as *tidal stirring* (Mayer et al. 2001), can form early-type dwarf galaxies[2] in these environments. In the densest regions of galaxy clusters, *galaxy harassment* (Moore et al. 1996) is believed to lead to the partial destruction and structural reconfiguration of late-type galaxies and has become one of the most popular mechanisms to explain the formation and abundance of early-type dwarf galaxies in clusters.

Intriguingly, the same tidal forces that form early-type dwarfs in galaxy harassment simulations are responsible for destroying them in simulations of *tidal threshing* (Bekki et al. 2001b), which was proposed as a mechanism to create the compact stellar systems known as 'ultra-compact dwarf galaxies' (UCDs) as remnant stellar nuclei of disrupted galaxies. While both harassment and threshing are frequently quoted as scenarios commonly occurring in galaxy clusters, a closer look at the required orbital configurations reveals that a complete transformation from a disk to a spheroid (in case of harassment), or complete disruption of the host galaxy (in case of threshing), only occurs on specific orbits with small peri- and apocentres (Mastropietro et al. 2005; Goerdt et al. 2008; Bialas et al. 2015), which are not realized for the majority of cluster galaxies today (Smith et al. 2015). If tidal disruption played a major role in forming new types of objects in clusters, most of it has likely happened many billion years ago (Pfeffer et al. 2014), when the clusters were in earlier stages of their assembly.

Despite the external influence on galaxies in clusters, a number of 'very-large-size, low-surface-brightness dwarfs' exist there (Binggeli et al. 1985), which seem to have escaped disruption. While this type of galaxy, now also known as 'ultra-diffuse galaxy' (van Dokkum et al. 2015a), may be kept stable by a very high mass ratio of dark matter to stars inside the stellar extent (van Dokkum et al. 2015a; Yozin and Bekki 2015) – following the canonical cosmological model – they may also be in the process of expansion due to the external field effect in Modified Newtonian Dynamics (Milgrom 2015) during infall into the cluster potential. Mihos et al. (2015) note that one object has an elongated shape and is embedded in a long diffuse stellar stream, suggesting that it is in the process of being tidally stripped (also see Chapter 4 for a more detailed review on these systems).

The recent attention to ultra-diffuse galaxies provides an additional motivation for our deep optical imaging data of the Fornax cluster core that we present in this study. Its original purpose was to look for diffuse tidal debris that can give hints to recent stripping and disruption events, and thus provide insight into whether and how strongly such processes are still ongoing at present in the Fornax cluster.

---

2 This includes dwarf elliptical galaxies as well as the fainter dwarf spheroidal galaxies, which form a continuous sequence in stellar structure parameter space (Misgeld et al. 2009; Lieder et al. 2012).

While Fornax is less massive than Virgo, their cores have a similar mass density and galaxy number density (McLaughlin 1999; Drinkwater et al. 2001). Therefore, the local strength of disruptive forces should be comparable — while of course the total number of galaxies potentially entering the inner potential well and getting (partially) disrupted is lower in Fornax. Another aspect of targeting the Fornax cluster is that the compact stellar systems known as UCDs were first discovered there (Hilker et al. 1999) and have since become the probably best-studied population of such objects (e.g. Drinkwater et al. 2003; Mieske et al. 2008b; Evstigneeva et al. 2008; Gregg et al. 2009). If a significant part of them formed recently from tidal threshing, simulations predict diffuse debris from the former host galaxy at surface brightness levels still accessible by observations (Bekki et al. 2003b). We therefore present an in-depth analysis of Fornax cluster compact stellar systems in Chapter 2.

While the common reference for Fornax cluster member galaxies is still the Fornax Cluster Catalogue (FCC, Ferguson 1989), based on photographic plates covering the cluster out to about the projected virial radius (Drinkwater et al. 2001), a couple of studies have been published that acquired deeper imaging of certain regions of the cluster in order to detect new faint galaxies (apart from the *HST*/ACS Fornax Cluster Survey that targeted selected galaxies for high resolution studies, Jordán et al. 2007). Based on R-band imaging with very low spatial resolution (2.3 arcsec pixel^{-1}) using the *Curtis Schmidt Telescope* at CTIO, an apparently large number of Fornax cluster dwarf galaxies was identified by Kambas et al. (2000), suggesting a steep faint-end slope of the luminosity function. However, data in the V and I bands acquired at the *Du Pont Telescope* at Las Campanas by Hilker et al. (2003), with better resolution (0.8 arcsec pixel^{-1}) and superior depth, showed that many of these were in fact unresolved background objects, correcting the faint-end slope back to a much flatter value. In the central 2.4 square degrees of the cluster that their data covered, Hilker et al. (2003) identified about 70 previously undetected low surface brightness dwarf galaxy candidates. A follow-up study of Mieske et al. (2007) with *Magellan*/IMACS in V and I, covering 1.1 square degrees in several disjoint deep fields grouped around the cluster centre, with a pixel scale of 0.2 arcsec and median seeing of 0.8 arcsec, identified 12 further faint dwarf galaxy candidates.

The data we present here provide a coherent coverage of the Fornax cluster core in the optical regime (acquired with no wavelength filtering), encompassing 1.6 square degrees with an approximate V-band depth of 26.6 mag arcsec^{-2} at 0.24 arcsec pixel^{-1} and 27.8 mag arcsec^{-2} at 0.71 arcsec pixel^{-1} (refering to a signal-to-noise ratio S/N = 1 per pixel). The coverage is thus larger than the sum of the deep fields of Mieske et al. (2007), with the depth at full resolution being comparable (judging from the published central surface brightness values of the newly detected galaxies of Mieske et al. 2007). While the coverage of Hilker et al. (2003) is larger than ours, the depth at similar pixel scale is shallower. We describe the reduction of our data in Section 3.2, characterise the resulting deep mosaic in Section 3.3, identify possible tidal streams and diffuse objects in Section 3.4, examine a new ultra-diffuse galaxy candidate[1] in Section 3.5, and conclude with a discussion (Section 3.6) and summary (Section 3.7).
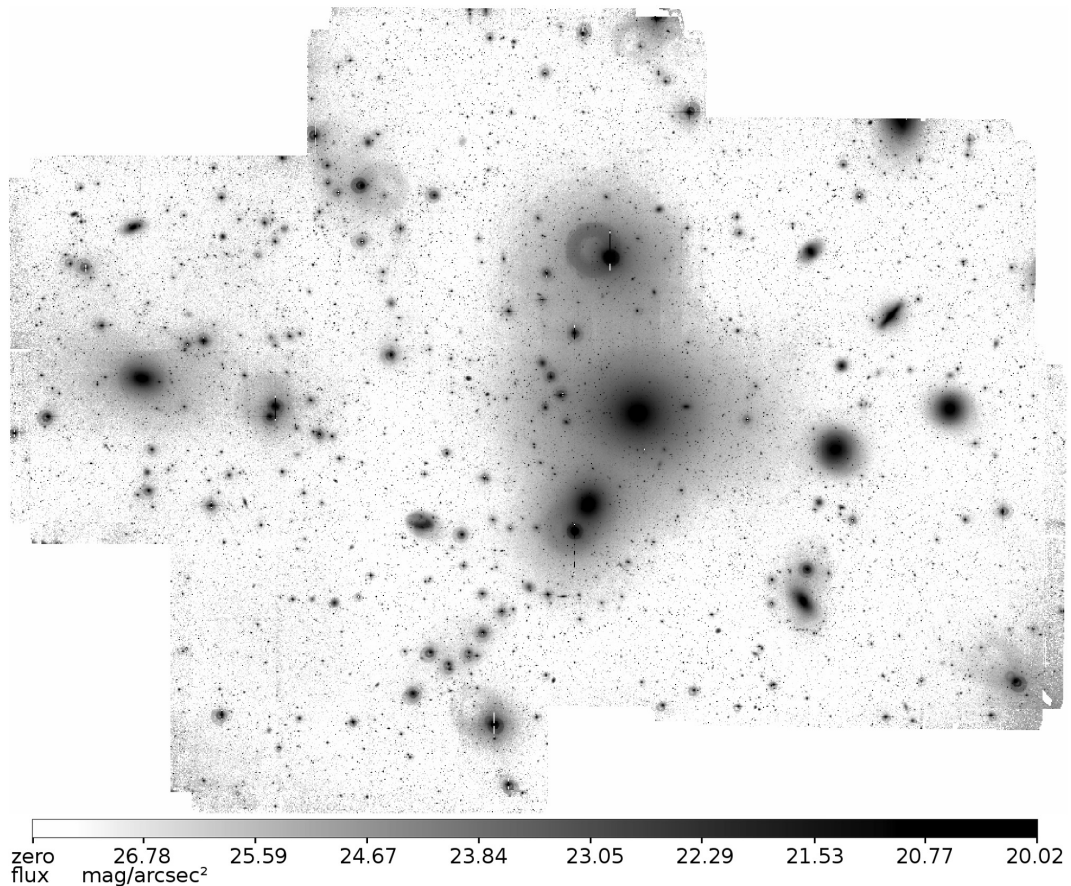
FIGURE 3.1:   Final co-added mosaic of the Fornax cluster core, with its central galaxy NGC 1399. The surface brightness–gray scale mapping is shown in the legend beneath the image. North is up and east is to the left. The mosaic is up to 97 arcmin (24 500 pixels) wide in east-west direction and 76 arcmin (19 200 pixels) in north-south direction. This corresponds to 0.56 Mpc and 0.44 Mpc, respectively, at the Fornax cluster distance of $d = 20.0$ Mpc (Blakeslee et al. 2009).

3.2   DATA ACQUISITION AND REDUCTION

Deep imaging of the Fornax cluster core was acquired through ESO programmes 082.A-9016 and 084.A-9014 (PI A. Pasquali, Guaranteed Time of the Max Planck Institute for Astronomy) in 2008 and 2010 at the *ESO/MPG 2.2 m telescope* with the Wide Field Imager (WFI). The instrument's field of view is $34 \times 33\,\mathrm{arcsec}^2$, corresponding to 196×190 kpc² at the Fornax cluster distance ($d = 20.0$ Mpc, $m - M = 31.51$ mag, 5.76 kpc arcmin⁻¹; Blakeslee et al. 2009). In order to reach very faint surface brightness levels and be able to detect faint, diffuse structures, we observed exclusively with the 'White' filter[3], which is simply a glass that is transparent to the whole optical wavelength range. Its throughput nearly equals the no-filter throughput everywhere except blueward of 450 nm, where it is up to ~ 20 per cent lower. Any of the standard broad-band filters would have required a several times longer total exposure time. The disadvantage of this approach, apart from a suboptimal seeing point spread function (PSF), was the occurrence of strong fringing typically known from red bands, caused by the emission lines of the airglow spectrum.

---

3 See http://www.eso.org/sci/facilities/lasilla/instruments/wfi/inst.html

We used six overlapping pointings covering the Fornax cluster core (Figs 3.1 and 3.2). Our observing strategy was to acquire short (300s) exposures in a rectangular 4-point dither pattern centred on one of the pointings, using offsets of 2.8 arcmin, then move to the next pointing and execute the 4-point dither pattern there. Depending on the priority, the available number of hours, and on whether or not a given pointing was already completed, the observers alternated between either two or three different pointings in a given night (November 2008 and January 2010, western and central pointings), or stayed on a single pointing (March 2010, eastern pointings, away from the central cluster galaxy NGC 1399). Altogether, 149 exposures were acquired. Due to a high background level and a varying background

zero 29.00 27.81 26.89 26.07 25.27 24.51 23.75 22.99
flux   mag/arcsec²

25.00 25.28 25.56 25.84 26.12 26.41 26.69 26.97 27.25
mag/arcsec² at S/N=1 p.pix. on unbinned image
26.21 26.49 26.77 27.05 27.33 27.62 27.90 28.18 28.46
mag/arcsec² at S/N=1 p.pix. on 3x3 binned image
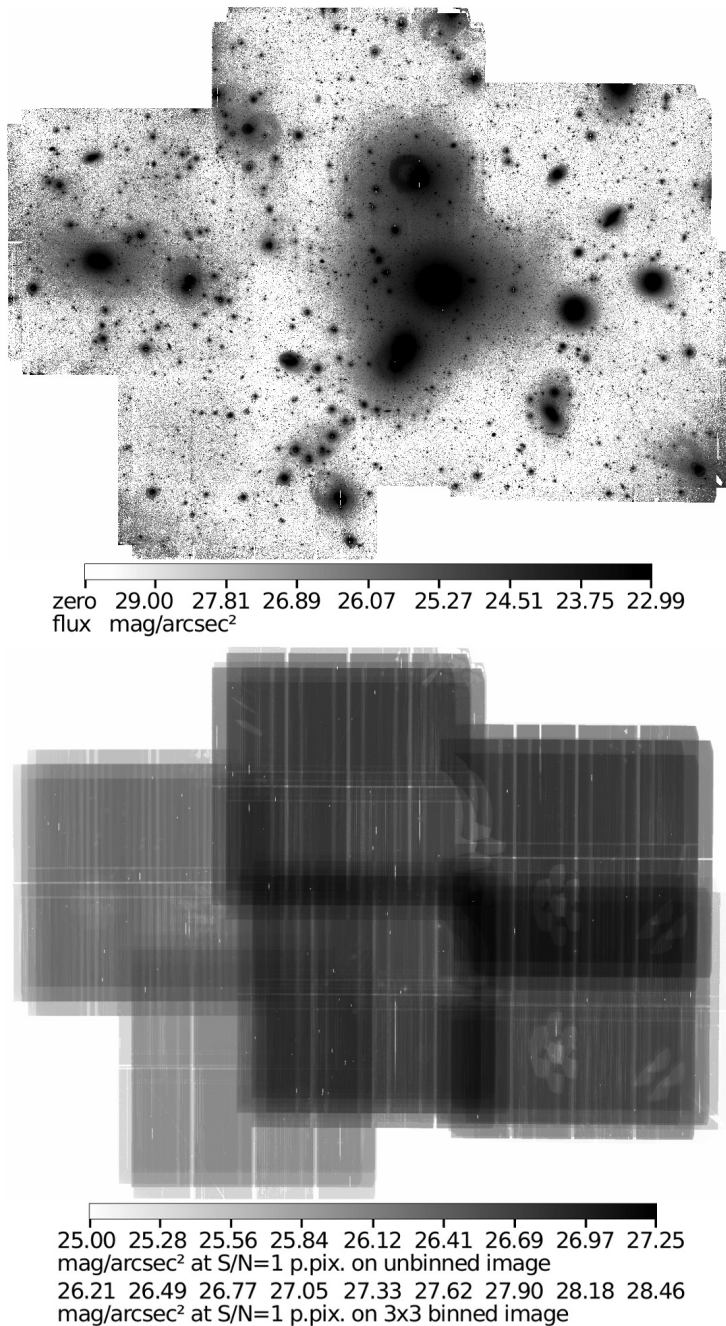
FIGURE 3.2: *Top:* Like Fig. 3.1, but with a different gray scale mapping to make faint structures more visible. *Bottom:* Weight image, indicating the local depth at each point of the mosaic (see the legend beneath the image).

pattern that could not be fully corrected, we later decided to exclude all 12 exposures from 04 March 2015, leaving 137 exposures in our final dataset.

The main reduction steps were carried out with THELI GUI version 1.7.6 (Schirmer 2013), which provides a graphical user interface for conveniently calling various built-in reduction routines of THELI (Erben et al. 2005) as well as other astronomical software packages. THELI was explicitly designed to handle dithered wide-field imaging data, and Erben et al. (2005) emphasized and illustrated that 'a wide dither pattern will lead to an improved sky background from which the S/N will benefit'. This is because the availability of many dithered exposures makes it possible to create a background model directly from the (stacked) science images, which is necessary to remove systematic residual patterns at low intensity levels. These can be caused, for example, by scattered light or by instrumental reflections that effectively redistribute skylight (Erben et al. 2005; Schirmer 2013). While the acquisition of many short, dithered exposures has been the common technique in the near-infrared regime, the challenge of obtaining very deep optical mosaics has made this approach necessary also for CCD imaging (e.g. Mihos et al. 2005; Ferrarese et al. 2012).

In THELI GUI, each exposure was split into individual frames that correspond to the 8 WFI detectors ('chips'), which were then treated separately in most steps of the reduction. Subtraction of the overscan level and of a two-dimensional bias image (resulting from a median stack of bias exposures) was followed by dividing each frame with a corresponding flatfield image, which resulted from a median stack of (normalized) twilight exposures created separately for Nov. 2008, Jan. 2010, the first part and last part of March 2010 data. This step also corrects for differences in the gain level of the different chips, based on the flatfield.

To obtain a first, preliminary, co-added mosaic, the following steps were carried out in THELI GUI, with many parameters set to their default values. All objects on all science frames were masked through automated detection with SEXTRACTOR (Bertin and Arnouts 1996), and the frames were normalized by their mode. Co-adding these frames without alignment then led to a 'science stack', thereby excluding masked pixels. In addition to object masking, at each position the pixel with the highest intensity was rejected from the stack. Science stacks were created separately for the data from 24 November 2008, 25 November 2008, January 2010, and March 2010. The resulting stack was smoothed with a 201 pixel wide kernel to yield the 'background model'. Subtracting this background model from the science stack and smoothing the result with a small median filter of 3×3 pixels yielded the 'fringing model' that represents the fringing pattern. On certain chips, its amplitude reaches up to 4 per cent of the average count level.

Each science frame was then divided by the normalized background model, and the fringing model was rescaled and subtracted. Note that, in this first iteration, we assume implicitly that the background model represents a leftover sensitivity correction ('superflat') that the flatfield did not account for – i.e. a *multiplicative* correction – and only the fringing model represents redistributed light that is *additive* to the flux from astrophysical objects. This has been done for reasons of simplicity and is different from our approach in the final iteration, where the background model is assumed to be predominantly an *additive* component that stems from scattered skylight.

For each chip, a weight map was created based on the flatfield image. In this first iteration, these weight maps were used along with all frames, without taking peculiarities of individual frames into account. This was followed by creating a

source catalogue for each frame, in order to carry out astrometric matching with the 2MASS catalogue (Skrutskie et al. 2006), using *SCAMP* (Bertin 2006) through THELI GUI. This step includes the determination of a relative photometric zeropoint of exposures, thereby accounting for airmass differences or, in general, for transparency variations. A model of the leftover sky background was determined and subtracted using SExtractor through THELI GUI, with a 256 pixel kernel convolution. The frames were then resampled to a pixel scale of 0.71388 arcsec – corresponding to 3×3 binning – using *SWarp* (Bertin et al. 2002) with a Lanczos3 kernel through THELI GUI. Finally, the resampled frames were median-combined to yield the first full mosaic.

While there are obviously a number of configurations and parameter settings that one can try, we found that the following three points were important to improve the data reduction quality and minimize sky background variations in the final deep mosaic. We addressed these items with our own scripts (partly using IRAF, Tody 1993) outside of THELI GUI.

1. Object masks need to be extended to an intensity level that may not be visible in the short individual exposures, but would be detectable in the final mosaic. This is particularly important for objects with large (apparent) size that subtend a significant fraction of a chip, such as the clusters's giant early-type galaxies or the reflection haloes of bright foreground stars.

2. The determination of the sky level that is needed for frame normalization and re-scaling in the background and fringing modeling steps should not be biased by the availability of only a small fraction of unmasked pixels and by their particular location on the chip. This applies especially to the (large!) area affected by the central cluster galaxy's stellar halo. In the presence of a background and fringing pattern, using only a small unmasked area of a given frame to measure its overall intensity level can lead to a bias, depending on where this area falls. The sky level should thus rather be determined for an *exposure* as a whole, not for an individual *frame*.

3. The background pattern shows variations over the course of our observing runs, as does the fringing pattern, mainly in its amplitude. The latter is commonly assumed to scale with the sky brightness to first order, but changes in the airglow spectrum can cause this to vary. The removal of these patterns can be optimized by computing and applying them separately for different subsets of exposures.

While not yet optimally reduced, the first deep mosaic was useful to address the above item 1, namely to create object masks for the most extended objects (including reflection haloes of overexposed foreground stars) that encompass their faint, diffuse outskirts and thus avoid that these pixels are taken to be part of the sky background. The low S/N of individual frames cannot properly account for the faint outer extent of the largest objects. Masks were created from a combination of SExtractor object detection and manual adjustment, using SAOImage DS9 regions (Joye and Mandel 2003).

The large-object masks, together with masks from an improved SExtractor object detection on each defringed frame, were then applied to the debiased and flatfielded frames in another iteration of creating the science stack (from which the background and fringing model follow) and of creating the leftover sky background model. This clearly led to an improved co-added mosaic, preventing neg-

ative ring-like artefacts from too small object masks. The large-object masks were improved based on this new mosaic, and object masks for the individual frames were created anew from the improved defringed frames. We also used these masks on the debiased and flatfielded science frames to re-determine chip-to-chip gain differences from the median level of the masked images.

Item 2 was realized by computing the median level from all unmasked pixels of a given exposure, i.e. a set of eight frames. For each exposure, this value was subsequently used as the sky level of each of its frames when normalizing them for the science stack and re-scaling the fringing pattern.

For optimizing the background and fringing models (item 3), we tried a dynamical variant that would use a window of a certain number of exposures around the current one, as well as an analogous variant whose window slides along increasing sky level instead of date. However, eventually the best solution was to empirically define a small number of exposure subsets that seemed to share common properties with regard to the background pattern and – in different combinations – the fringing pattern. These subsets should ideally not contain too few frames, in order to avoid introducing artefacts from small differences between frames while at the same time trying to get rid of artefacts from suboptimal fringing correction. In a few cases, however, a small part of the fringing model itself had to be masked, resulting in propagated masks on the frames to which it was applied, and therefore leading to a distinct pattern in the weight image (Fig. 3.2, bottom), consisting of small shallower patches whose arrangement reflects the dithering.

For the final reduction, we refrained from carrying out any modeling and subtraction of a potential leftover sky background on individual frames, since tidal debris or intracluster light could be inadvertently subtracted in such a step. Instead, we relied solely on subtracting the background model that resulted from the science stack only, as outlined above.

One further step of improvement was possible before finalizing the reduction. Despite having already chosen a very extended mask for the central cluster galaxy's halo, it could still be noticed that the farthest outskirts were unmasked and thus affected the overall flux level of the corresponding frames. On the other hand, it was clear that these far outskirts of the stellar halo have such a homogeneous distribution on the scale of a single chip that it should still be possible to use the corresponding frames in the determination of the background model (more contributing frames ensure better statistics), and that it would seem somewhat inappropriate to mask out the information that is there. We therefore decided to mask the central galaxy's halo out to an east-west semimajor axis of 18.5 arcmin (107 kpc) and a north-south semiminor axis of 13.1 arcmin (76 kpc). Beyond this elliptical mask, we carried out a subtraction of the galaxy's smooth light, which was achieved through fitting consecutive ellipses with varying ellipticity and orientation (but fixed beyond 8 arcmin) to the light of NGC 1399 on a preliminary co-added mosaic and building a model from the output, using the IRAF routines *ellipse* and *bmodel*. The galaxy model was subtracted from the individual debiased and flatfielded frames by using an already determined astrometric solution. The resulting frames were then used for the final iteration of the reduction. Artefacts present on individual frames were now assigned a weight of zero on their corresponding individual weight maps. The final resulting mosaic and weight image are shown in Figs 3.1 and 3.2.

Even though our data were acquired using the 'White' filter, we provide an approximate $V-$band calibration, based on spectroscopically confirmed foreground

stars from Mieske et al. (2002, 2004). These stars were selected to have a $V-I$ colour between 1.0 and 1.2, since this is typical for the compact stellar systems we study in Chapter 2, and to not lie in regions of low S/N (mostly the mosaic edges). Stars were only used if they are located in the mosaic areas populated by the published compact stellar systems compiled in Chapter 2, which mainly omits regions in the south and also the north of the mosaic. We end up with 18 stars, for which we compare the literature $V-$band magnitudes to the uncalibrated PSF magnitudes.[4] The median magnitude difference is 25.79 mag; 16 stars lie within ±0.1 mag of it. Therefore, we adopt this value as our zeropoint to determine approximate 'V−equivalent' magnitudes and surface brightnesses, which will be denoted with m_{Ve} and μ_{Ve} in the following.

3.3 THE RESULTING DEEP MOSAIC
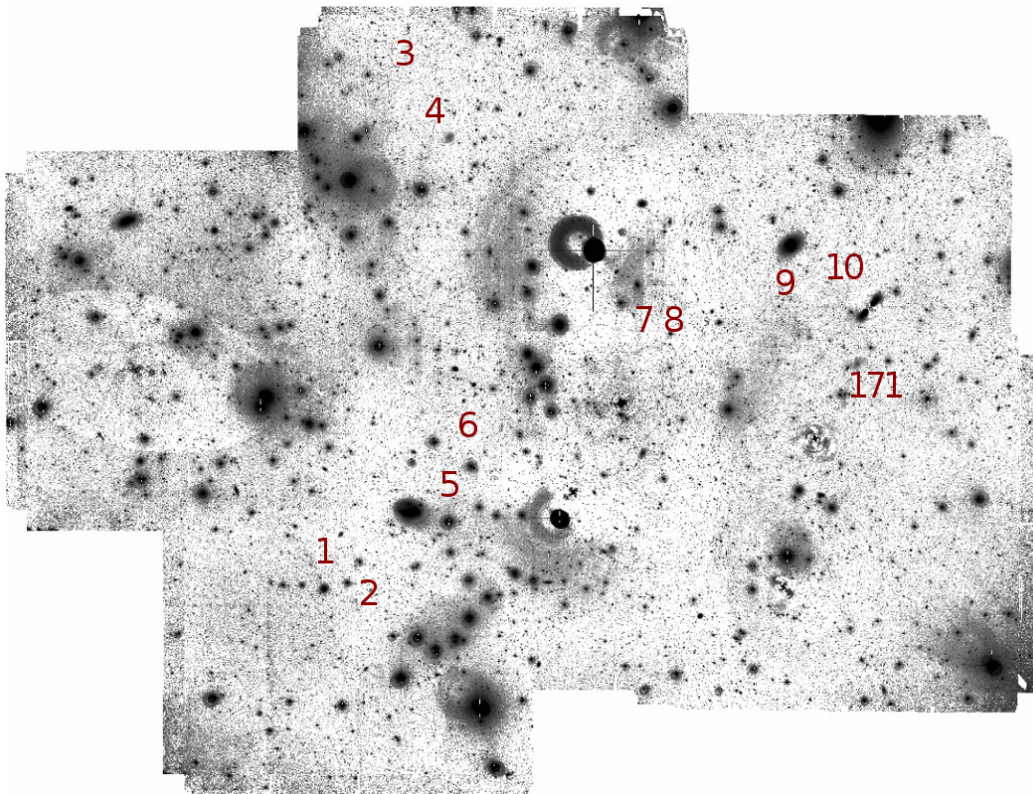
FIGURE 3.3:   Final mosaic with the largest objects (bright galaxies and stellar haloes) modelled and subtracted, using ellipse fitting. The same gray scale mapping applies as in Fig. 3.2 (top panel). All of our candidate tidal streams and diffuse objects listed in Table 3.1 and described in Section 3.4 are labelled in the image; the number 171 refers to galaxy FCC 171 (see Section 3.4).

The final deep mosaic is shown in Figs 3.1 and 3.2. It has the same pixel scale as the WFI instrument provided, namely 0.23796 arcsec pixel^{-1}, and covers 1.64 square degrees.[5] It is up to 97 arcmin wide in east-west direction and 76 arcmin in

---

4 PSF models were determined from point sources in regions with similar full width at half maximum (FWHM), using routines from the IRAF package DAOPHOT. The corresponding PSF model was then fitted to each star, yielding its PSF magnitude. See Chapter 2, Section 2.3.1 for further details.

5 In our figures and when quoting angular extent and depth, we only consider reasonably deep regions that have an image depth of at least $\mu_{Ve} = 25.0$ mag arcsec^{-2} at S/N = 1 per pixel on the

north-south direction. This corresponds to 0.56 Mpc and 0.44 Mpc, respectively, at the Fornax cluster distance of d = 20.0 Mpc (Blakeslee et al. 2009).

The image depth is not homogeneous across the mosaic, due to its composition from multiple nights and observing runs, as well as due to the overlap regions, where more exposures contribute. The weight image shown in Fig. 3.2 (bottom) illustrates the depth, with darker shading representing greater depth, i.e. higher weight (inverse variance). We find the 25th percentile, median, and 75th percentile of $V-$equivalent depth to be 26.15, 26.58, and 26.76 mag arcsec^{-2}, respectively, at S/N = 1 per pixel.[6]

In order to analyse the PSF in all regions of the mosaic, we first subtracted large elliptical galaxies and stellar haloes by fitting and modeling their light profile with IRAF/*ellipse* and *bmodel*. For each object that we removed, we obtained a first residual image from a preliminary fit, and then used this image to detect and mask underlying and neighbouring sources. In a second pass, we then ran *ellipse* with these sources masked, leading to a mosaic with improved object subtraction (shown in Fig. 3.3). On this mosaic, we first used SExtractor to select all objects brighter than $m_{Ve} = 22$ mag and with a FWHM below 7.5 pixels. We then estimated the PSF FWHM with IRAF/*psfmeasure*, using a Gaussian profile for the PSF. We found that the FWHM varies across the mosaic (see Chapter 2, Fig. 2.2), with the variations being mainly related to the different observing runs. The FWHM is narrowest in the central pointings, with $3.5 - 4.5$ pixels (less than 1 arcsec), broadest in the eastern pointings, with $4.5 - 6.5$ pixels, and varies between $4 - 5.5$ pixels in the western pointings.

In addition to the original, full-resolution mosaic, we also produced a binned mosaic with a resampled pixel scale of 0.71388 arcsec pixel^{-1}, equivalent to 3×3 binning. Consequently, a greater image depth is reached. The 25th percentile, median, and 75th percentile now are 27.37, 27.79, and 27.96 mag arcsec^{-2}, respectively, i.e. deeper by 1.2 mag due to the binning.

We note, however, that regions of larger depth in the 3×3-binned mosaic are limited not only by the exposure time-dependent S/N, but by inhomogeneities of the sky background and straylight determination, which leave sky subtraction residuals, as well as by extended reflections from bright stars. Despite the dithered observations, any systematic inhomogeneities can only be reliably determined on scales *below* the width of one chip (9 arcmin or 50 kpc), which is small compared to the total mosaic. Unfortunately, this hampers any reliable assessment of the presence of intracluster light (apart from well-defined streams, see below). This is one of the advantages of telescopes with small apertures (below one meter; see, e.g., Mihos et al. 2005), where the field-of-view *per chip* is typically much larger, and hence a more homogeneous sky and straylight reduction can be achieved with appropriate dithering techniques.

Both mosaics and their corresponding weight images are going to be publicly released through the German Astrophysical Virtual Observatory. The raw data are available through the ESO Science Archive Facility. A mosaic where the brightest galaxies have been subtracted can be provided on request.

---

unbinned mosaic, thereby omitting mainly some narrow edge regions where only a single exposure contributed.

6 To determine these values we have used IRAF/*imstat*, which does not compute a true median, but is instead based on the area under the histogram of pixels, and approximates the point where 50 per cent of the total area are reached.
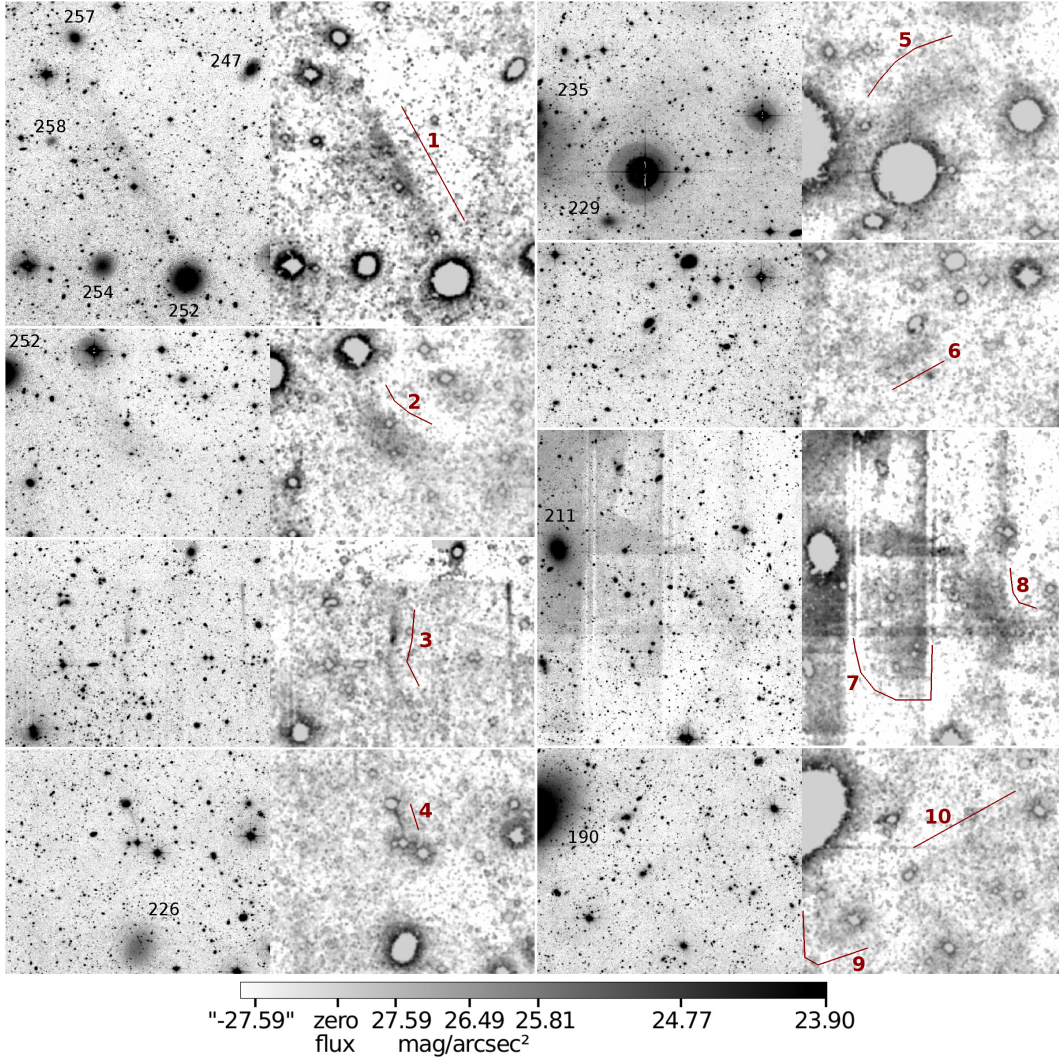
FIGURE 3.4:   Candidate structures of tidal origin and diffuse galaxies, numbered as in Table 3.1 and marked on Fig. 3.3. For each object, outlined and labelled in red, the respective left-hand panel shows the object-subtracted binned mosaic and the right-hand panel shows the smoothed mosaic (see text for details). North is up and east is to the left. Each panel is 12 arcmin or 67 kpc wide. FCC galaxies that are certain or likely cluster members are marked with black numbers. The surface brightness–gray scale mapping of the respective left-hand panels is shown at the bottom. The surface brightness reached by object 1 in its brightest patches is $\mu_{Ve} \approx 27.5$ mag arcsec^{-2}. Due to the uneven local background around objects 7 and 8, and for the overall visual appearance, the gray scale has been chosen to encompass a range of negative fluxes. The label '-27.59' means a negative flux whose absolute value would correspond to 27.59 mag arcsec^{-2}.

3.4 POSSIBLE TIDAL DEBRIS AND DIFFUSE OBJECTS

The main motivation for acquiring this deep image of the Fornax cluster core was to look for tidal debris that can give hints to recent and ongoing disruption events. For this investigation, we took the mosaic where the brightest galaxies and the most extended stellar haloes were subtracted – with some residuals remaining – and used SExtractor to identify and subtract all objects detected with at least 5 connected pixels above 1.5 σ of the noise. We then block-averaged the mosaic, using IRAF/*blkavg* with 3 × 3-pixel blocks, and smoothed the resulting image with a circular Gaussian kernel with σ = 2 binned pixels (using IRAF/*gauss*).

TABLE 3.1: Candidate streams and diffuse objects. A label '(bg)' in the last column indicates that the structure is likely not part of the Fornax cluster, but instead probably associated with background galaxies. Objects 1, 2, 4, 8 and 9 are independently seen in a preliminary reduction of *VST*/OmegaCAM images in g and r (Venhola et al. 2017, see text for details), which is why they are marked as 'confirmed'. Object 8 is galaxy WFLSB 04-06 in Mieske et al. (2007), see Section 3.5 for further remarks on this object.

NO.	α (J2000)	δ (J2000)	REMARK
1	03:40:56.75	−35:42:14.6	Confirmed stream
2	03:40:35.19	−35:46:30.4	Confirmed galaxy
3	03:40:17.50	−34:53:08.8	Likely artefact
4	03:39:50.92	−34:58:06.4	Confirmed stream (bg)
5	03:39:49.90	−35:36:47.1	Likely reflection
6	03:39:45.02	−35:27:36.2	Likely reflection
7	03:38:11.45	−35:17:50.7	Likely artefact
8	03:38:00.98	−35:17:02.2	Known galaxy
9	03:37:04.00	−35:14:09.9	Confirmed object
10	03:36:48.30	−35:12:15.8	Likely artefact

We visually inspected the original unbinned and binned mosaics, as well as the object-subtracted binned and smoothed image just described, for the presence of extended low surface brightness structures. We identified a small number of faint structures that have a stream-like appearance, some of which are very thin and may be in the background. We also identified a few objects that appear more like elongated, very low surface brightness galaxies. All candidate streams and galaxies are listed in Table 3.1 and shown in Fig. 3.4, sorted from east to west. We refrained from including those straight and narrow structures seen in the field of objects 7 and 8 that are exactly vertical or horizontal, as these are likely artefacts originating from chip boundaries.

In addition, our images reveal a diffuse extension of the early-type dwarf galaxy FCC 171, shown in Fig. 3.5. The stellar material that appears to be stripped is distributed in a broad 'S' shape, typical for tidal arms. We note that the galaxy located 'inside' the eastern tidal arm is a confirmed background object (FCC B1102) with a heliocentric velocity of 11971 km s^{-1} (Fornax Cluster Spectroscopic Survey, Drinkwater et al. 2000b).

A general difficulty in the identification of faint structures lies with the presence of residual straylight and reflections from bright stars, or what remained from them when co-adding individual frames to the final mosaic. Residuals from subtracting the brightest galaxies and stellar haloes can also be disturbing, although they occur mainly in the centre and along the edge of the regions subject to subtraction. For most of the structures we identified, comparison with an independent dataset is necessary to conclude with certainty whether a stream or galaxy is real.

The easternmost candidate stream in our mosaic is also the brightest one: object 1, reaching $\mu_{Ve} \approx 27.5$ mag arcsec^{-2} in its brightest patches, which means a S/N $\approx$ 0.75 per pixel locally in the 3×3-binned mosaic. It is located between the early-type dwarf galaxies FCC 252 and 257 (see Fig. 3.4), spanning about 3.6 arcmin (21 kpc) in length. Its elongation is perpendicular to the direction toward NGC 1399. The light it contains – after masking out other objects – corresponds to $m_{Ve} \approx 18.6$ mag or $M_{Ve} \approx -12.9$ mag at the Fornax cluster distance, i.e. comparable to a dwarf spheroidal galaxy.
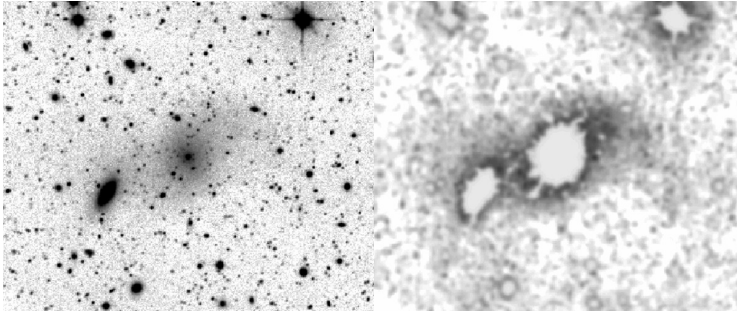
FIGURE 3.5:   Like Fig. 3.4, but showing the early-type dwarf galaxy FCC 171. The elongated, high surface brightness galaxy to the southeast is FCC B1102, a confirmed background object. Each panel is 4.2 arcmin or 24 kpc wide. North is up and east is to the left. The same gray scale mapping applies as shown at the bottom of Fig. 3.4.

The stream happens to fall into our mosaic's region with the lowest depth, namely the southeastern region. Since most other regions of the mosaic are deeper by $0.6 - 0.8$ mag, streams of $\mu_{Ve} \approx 28.2$ mag arcsec^{-2} and similar extent could be identified across a large portion of the mosaic, if they were present (nevertheless still depending on the presence of reflections and other residual features).

From east to west, the candidate objects 3, 4, 5, and 10 may be additional possible streams. Objects 3 and 4 are much narrower than the others; we therefore consider them candidates for streams associated with background galaxies. Object 5 may be merely part of a reflection caused by one of the bright foreground stars nearby. Object 10 needs independent data for a reliable judgement (see further below). We point out that we observe no stream around any of the 904 spectroscopically confirmed compact stellar systems of the cluster that we compiled from the literature in Chapter 2. This statement does not include the search for smaller elongations or for asymmetries in these objects' outskirts, which is the focus of the analysis in Chapter 2.

The remaining candidate objects of Table 3.1 appear more like galaxies than like streams — some more distorted or irregular than others. Probably the clearest galaxy candidate is object 2, located very close to stream 1 (see Fig. 3.4). It has not been catalogued so far[1] – no matching entry is found in the NED[7] and HyperLeda (Makarov et al. 2014) databases – and its appearance suggests similarity with the recently described ultra-diffuse galaxies. We therefore analyse object 2 more quantitatively in Section 3.5. We note that, despite its proximity to stream 1, the mosaic is deeper by about 0.4 mag for the left (eastern) part of object 2, and by about 0.6 mag for its right (western) part, than for stream 1.

Object 8 appears similarly bright and extended as object 2, yet it falls into an area northwest of the central cluster galaxy NGC 1399 and southwest of the brightest foreground star of the mosaic. There, both the galaxy's stellar halo and the reflection halo of the star extend over the scale of multiple chips, making a clean determination of straylight and sky background impossible. Despite our ellipse-fit modelling and subtraction of both haloes, the residual image (Fig. 3.3) is still very inhomogeneous there. Nevertheless, object 8 is, in fact, the only known galaxy among our candidate objects: it has been identified by Mieske et al. (2007) as WFLSB4-6

---

7 The NASA/IPAC Extragalactic Database (NED) is operated by the Jet Propulsion Laboratory, California Institute of Technology, under contract with the National Aeronautics and Space Administration.

(as listed by CDS/VizieR[8], and named WFLSB 04-06 in NED). The authors labelled it as 'probable background based on morphological assessment', for which we can not see an obvious reason in our data. Given its similarity in appearance to object 2, we will take this point up again in Section 3.5.

Object 6 has a galaxy-like appearance, but is fainter than object 2, and is not much brighter than surrounding inhomogeneities (Fig. 3.4). Independent data are necessary for confirmation or rejection (see below). Object 7 is likely an artefact from straylight or reflections, since it is cut off vertically on the right-hand side, just as it would be expected if reflections occur only in a certain subset of the frames that contributed there.

Finally, object 9 can neither be described as stream-like, nor as galaxy-like. It appears asymmetric and may be tidal debris, a stream seen under a specific angle, or a galaxy in an advanced stage of disruption. It is comparably faint and uncertain as object 6, and a foreground star is located in front of its western end (although not a particularly bright one). This object also needs independent data for reliable judgement. No matching entry is found in NED and HyperLeda.

Fortunately, an independent dataset covering our candidate objects was provided by a preliminary reduction of *ESO VST*/OmegaCAM images in g and r (Venhola et al. 2017, programmes 094.B-0512 and 096.B-0501, P.I. R. Peletier), which is part of the ongoing Fornax Deep Survey (FDS) led by M. Capaccioli and R. Peletier. Visual inspection of these data not only confirm stream 1 and galaxy 2, but also the faint object 9. Of the two narrow candidate background streams, only stream 4 is confirmed. At all positions, the preliminary FDS g-band data are of comparable depth as our WFI data and should thus be sufficiently deep to serve as independent check. We therefore mark objects not seen in the FDS dataset as 'likely reflection' or 'likely artefact' in Table 3.1.

3.5 ULTRA-DIFFUSE GALAXIES

In order to determine whether our candidate galaxy, object 2 in Fig. 3.4, falls within the range of ultra-diffuse galaxies of van Dokkum et al. (2015a, Coma cluster) and Mihos et al. (2015, Virgo cluster), we first compare our galaxy visually to the three objects of Mihos et al. (2015). For this purpose, we create artificial images using their published structural parameters – taking into account the slightly larger distance to Fornax as compared to Virgo (Blakeslee et al. 2009) – and insert those into the mosaic, close to our galaxy. Each panel of Fig. 3.6 holds only one of the galaxies from Mihos et al. (2015), but inserted at three different locations (red arrows). This also helps to take into account local variations of background and depth; the latter is increasing from east to west. The lower panels of the figure were object-subtracted and Gaussian-smoothed in the same way as the respective panels of Fig. 3.4.

We can see that the peak surface brightness of our galaxy is somewhat brighter than VLSB-A and slightly fainter than VLSB-B of Mihos et al. (2015). Furthermore, it appears more extended than VLSB-B and less extended than VLSB-C. Already from this qualitative assessment, it is clear that it would indeed fall into the parameter regime of ultra-diffuse galaxies (cf. fig. 3 of Mihos et al. 2015).

---

8 We acknowledge the use of the VizieR catalogue access tool, CDS, Strasbourg, France. The original description of the VizieR service was published in A&AS 143, 23.
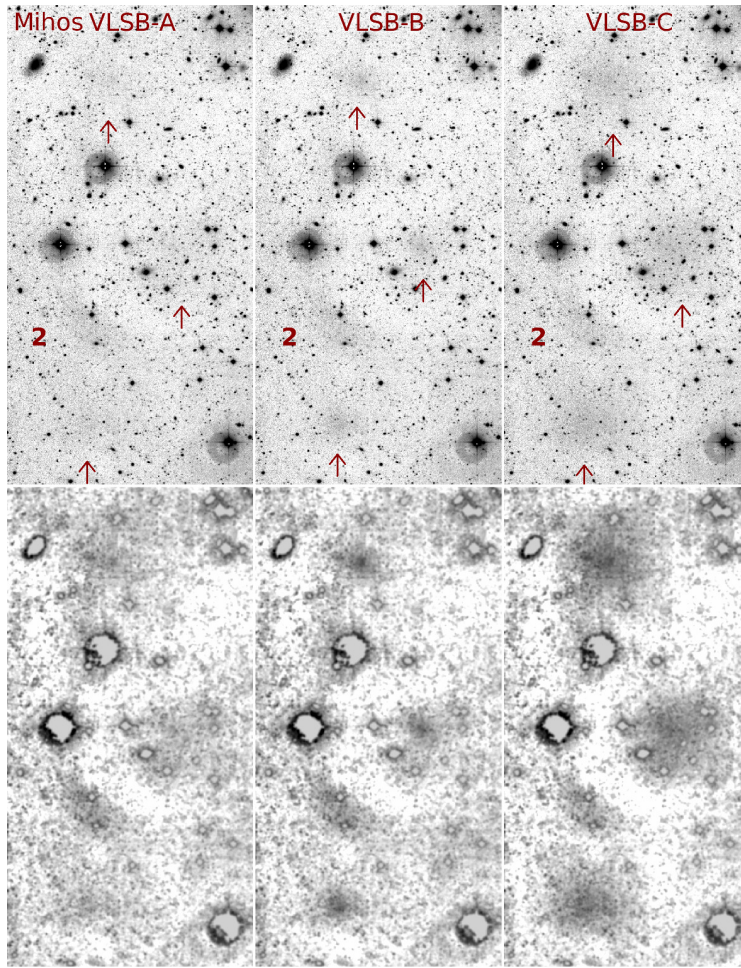
FIGURE 3.6:   Comparison of our object 2 with the three ultra-diffuse Virgo cluster galaxies presented by Mihos et al. (2015). The three top panels show object 2 (marked with a red '2') and the area around it on our binned mosaic, using the same gray scale mapping as in Fig. 3.4. In each panel, one of the galaxies from Mihos et al. (2015) (VLSB-A, VLSB-B, VLSB-C) was artificially inserted at three locations (marked with red arrows), using the published Sérsic index (1.2, 0.8, 0.7), effective radius (9.7, 2.9, 5.5 kpc), and central surface brightness ($\mu_{V,0} = 27.0, 26.7, 26.7$ mag arcsec^{-2}, see their table 1). We use the ellipticities from Mihos et al. (2015) of 0.17 and 0.12 for VLSB-B and VLSB-C, respectively, and assume a value of 0.22 for VLSB-A, for which no value was published. The bottom three panels show the object-subtracted, Gaussian-smoothed images, analogous to Fig. 3.4. Each panel is 6.4 arcmin or 37 kpc wide. Note that the depth of our mosaic increases by about 0.5 mag from the left to the right (east to west) of each panel.

Our galaxy's surface brightness profile is shown in Fig. 3.7, both in surface brightness units (top) and linear counts (bottom). It was derived by first finding suitable centre coordinates and ellipse parameters through several iterations of ellipse fitting with IRAF/*ellipse* – thereby masking contaminating fore-/background objects – and then keeping these parameters fixed for the final profile extraction. Due to the low S/N, this approach turned out more reliable than profile extraction with free ellipse parameters. Interestingly, the galaxy's surface brightness is nearly constant over several kiloparsec, and then drops off rather steeply, similar to a Sérsic profile with an index well below the exponential $n = 1$. Especially in the linear depiction, this appears like a truncation of the profile. Clearly, a single Sérsic fit would *not* be a good representation, in contrast to the three objects of Mihos et al. (2015).
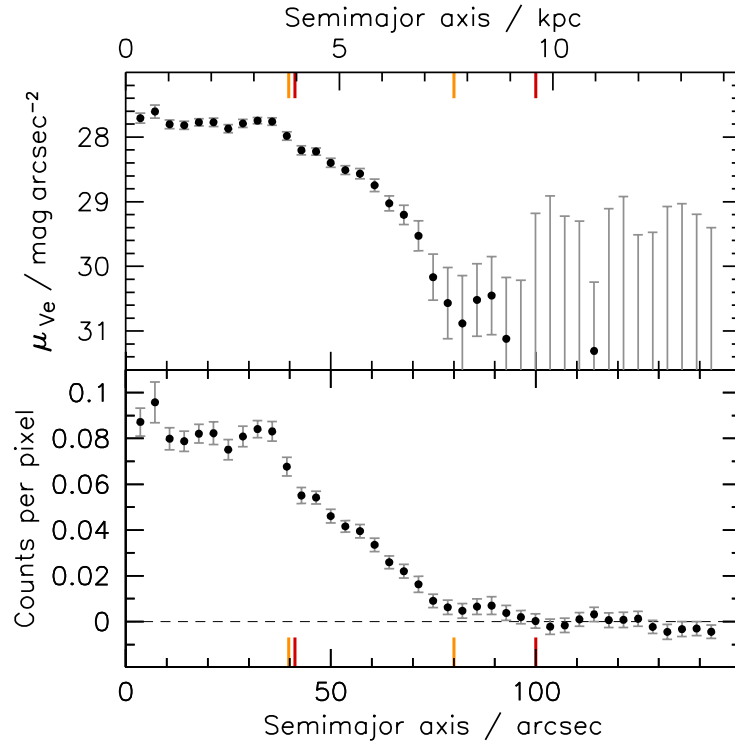
FIGURE 3.7:   Radial surface brightness profile of object 2 (top panel), as well as the radial profile in counts per binned pixel (bottom panel). 1 count corresponds to a $V-$equivalent magnitude of 25.79, see Section 3.2. The profile was determined from consecutive elliptical annuli with a width of 10 binned pixels (7.1 arcsec), in steps of 5 pixels (3.6 arcsec), adopting an ellipticity of 0.5 and a position angle of 43°. Depending on whether the total flux is taken to be the flux enclosed by a semimajor axis of 80 arcsec (orange tickmark) or 100 arcsec (red tickmark), the half-light semimajor axis lies at 40 or 41 arcsec (orange and red tickmark, respectively). This corresponds to approximately 3.9 kpc, or 2.8 kpc when circularized (multiplied with $\sqrt{0.5}$).

If we add up the galaxy's light out to a semimajor axis of 80 arcsec (orange tickmark in Fig. 3.7), it corresponds to a $V-$equivalent magnitude of 18.11 mag, or -13.40 mag at the Fornax cluster distance. If we choose to add up the light out to 100 arcsec (red tickmark), it gets brighter by 0.06 mag. For both cases, the half-light semimajor axis (inner tickmarks) lies around 40 arcsec or 3.9 kpc (2.8 kpc when circularized), corresponding to an effective surface brightness of $27.3 - 27.4$ mag arcsec^{-2}. This places the galaxy at the faint and diffuse end of the parameter range of ultra-diffuse galaxies from van Dokkum et al. (2015a) and Mihos et al. (2015).

As already remarked in the previous section, object 8 has a similar appearance (surface brightness, size) to object 2. While we need to be careful with our conclusions, because object 8 is located in an area with inhomogeneous sky background and artefacts from reflections, this galaxy also appears diffuse and extended in our OmegaCAM comparison data. Mieske et al. (2007) reported a central $V-$band surface brightness of 26.96 mag arcsec^{-2} for this galaxy (WFLSB4-6), consistent with our visual impression (Fig. 3.4). However, the total magnitude given in table 1 of Mieske et al. (2007) is only 21.67 mag, much fainter than our object 2 and thus also object 8. This suggests that only a small piece of WFLSB4-6 was recognized in the data of Mieske et al. (2007), which would explain why it was categorized as a

'probable background' object. From our data, we conclude that WFLSB4-6 actually is another ultra-diffuse galaxy candidate of the Fornax cluster.

3.6 DISCUSSION

The reduced deep mosaic can be utilised in future studies to measure the outer stellar structure of galaxies. This includes radial profiles, as long as significant colour gradients can either be ruled out or are of secondary importance. Furthermore, the image depth allows the detection and cross-confirmation of previously unknown faint objects, which may e.g. be useful for analysing the faint-end slope of the galaxy luminosity function in the centre of the Fornax cluster (see Kambas et al. 2000; Hilker et al. 2003). In Chapter 2 we make use of these capabilities for analysing the structure of compact stellar objects in the cluster. Since our data were acquired with a filter that spans the whole optical wavelength range, they can only be useful for future *colour* analyses when combined with a dataset from a different wavelength regime, i.e. ultraviolet or near-infrared data, and only in an approximate way.

Faint galaxies with very low surface brightness in the parameter region of what was recently dubbed 'ultra-diffuse galaxies' by van Dokkum et al. (2015a, Coma cluster) and Mihos et al. (2015, Virgo cluster) had been already described by Sandage and Binggeli (1984, Virgo cluster) as a new type of galaxy (also see Chapter 4). Given the effective radius of some of these galaxies of several kpc, it has been remarked that these are 'Milky Way sized' (van Dokkum et al. 2015a; Koda et al. 2015). However, this may not necessarily apply to their *bound* matter — one very large dwarf spheroidal galaxy in the Hydra cluster (HCC 087, Misgeld et al. 2008; Misgeld and Hilker 2011) was found to be in the process of ongoing tidal disruption (Koch et al. 2012). Furthermore, the determination of *half-light* radii requires a good approximation for the *total* light, or equivalently, a good understanding of the outer profile shape: all recent studies named above used Sérsic or exponential profile fits to determine structural parameters. The large radii therefore partially rely on the implicit assumption of a non-truncated surface brightness profile beyond the observationally accessible radius, i.e. on an extrapolation of that profile.

In the most recent literature, radial profiles for this type of galaxy have only been presented by Mihos et al. (2015) for their three Virgo galaxies. Interestingly, those profiles do not appear truncated, but indeed seem to be well described by a single Sérsic profile (close to exponential) out to the visible radius. In contrast, our newly discovered ultra-diffuse galaxy candidate, object 2, does exhibit a truncated surface brightness profile — the flat inner part is followed by a steep decline (Fig. 3.7). This, together with the significant elongation (ellipticity of 0.5), suggests ongoing tidal disruption. While galaxy VLSB-A of Mihos et al. (2015) is not only elongated, but also embedded in a diffuse stream that implies ongoing disruption, our galaxy is in the vicinity of a stream (object 1, $\sim$ 20 kpc away, see Figs 3.3 and 3.4), but it cannot be concluded from the present data whether or not they are physically related.

With an estimated stellar mass of our galaxy of $4 \times 10^7 M_\odot$ (assuming M/L $\approx$ 2 for a non-star-forming population, cf. Bruzual and Charlot 2003) and the Fornax cluster gravitational potential of Drinkwater et al. (2001), if the projected cluster-centric distance of 186 kpc were the true pericentric distance of a circular orbit, the tidal radius would be between 1.4 and 2.0 kpc, hence *smaller* than where we

observe the profile truncation (at ~ 4 kpc). This could be accounted for if the true distance were twice as large as the projected one. Similarly, if the galaxy's total mass within the stellar extent would be ten times the stellar mass, the tidal radius would be 2.2 times larger. While we do not know, of course, what the actual orbit is, these numbers show that tidal disruption by the gravitational potential of the cluster would be possible without the need for any particular circumstances or additional processes. Given that the apparent position angle of object 2 is roughly directed toward FCC 252, which is also the galaxy towards which stream 1 'points' from the other side (see Fig. 3.4), they might even be involved in one and the same disruption process.

While object 2 does neither have a confirmed stellar nucleus nor an obvious candidate, we also observe ongoing disruption - or at least substantial stripping - for the nucleated dwarf elliptical galaxy FCC 171. If the stellar body of the galaxy gets stripped entirely, what remains will be seen as a UCD. While this 'threshing' channel to form UCDs (Bekki et al. 2003b) may have contributed only the minority of the UCD population in clusters (Mieske et al. 2012; Pfeffer et al. 2014; provided that we understand the formation of massive GCs correctly), and while most threshing events have likely occurred many billion years ago within our standard cosmological framework (Pfeffer et al. 2014), our observations show that the formation channel is still active today.

Despite these findings, the number of (candidate) tidal streams we observe seems very small, given that we do reach a surface brightness of $\mu_{Ve} \gtrsim 28$ mag arcsec^{-2}. In the Virgo cluster core, Mihos et al. (2005) observed two very long streams (> 100 kpc) for which we see nothing comparable in our data, and they identified about ten smaller streams and elongated tidal features, of which some can be connected to specific galaxies. However, the Fornax cluster is several times less massive than the Virgo cluster.[9] Even though both clusters reach the same central mass density (McLaughlin 1999; Drinkwater et al. 2001; Jordán et al. 2007) this still means that the *total* number of galaxies potentially affected by the cluster's tidal field is significantly lower in Fornax. This by itself may already be sufficient to explain the lower number of streams. Moreover, stars on a tidal stream within a galaxy cluster disperse and fall below the observable surface brightness level within a comparatively short timescale (< 1 Gyr, see Mastropietro et al. 2005), which makes the number of observable streams depend strongly on whether *recent* accretion and disruption events occurred. With Fornax being probably more dynamically evolved than Virgo (Grillmair et al. 1994; Jordán et al. 2007), most of its interaction processes may have taken place a longer time ago.

3.7   SUMMARY

We present a reduced deep optical mosaic of the Fornax cluster core region, obtained with *ESO/MPG 2.2 m*/WFI. The data have revealed several diffuse objects and structures, among them a stream that contains the stellar mass of a typical dwarf spheroidal galaxy, a previously uncatalogued ultra-diffuse galaxy candidate[1] close to that stream, and another ultra-diffuse galaxy candidate that had previously been considered as a potential background object. At least one of these

---

9 The literature on Virgo cluster mass estimates provides a considerable range of values ($1.4 - 4.0 \times 10^{14} M_\odot$), based on McLaughlin (1999), Schindler et al. (1999), and Urban et al. (2011). For the Fornax cluster, Drinkwater et al. (2001) derived a mass for the main cluster of $5 \times 10^{13} M_\odot$ from integrating the velocity amplitude profile and $9 \times 10^{13} M_\odot$ from the projected mass virial estimator.

galaxies is likely in the process of being disrupted, or may be merely the last remnant of a former galaxy. Furthermore, our data revealed that a known nucleated early-type dwarf galaxy is being tidally stripped, which may eventually lead to a new UCD. The total number of streams in the Fornax cluster is clearly lower than in Virgo at the same surface brightness level, which can at least partly be expected from the mass difference and the different evolutionary state of the clusters. Our deep mosaic can be used in future studies to investigate the faint end of the luminosity function in the cluster core or to analyse the outer structure of cluster galaxies.

A POPULATION OF FAINT LOW SURFACE BRIGHTNESS GALAXIES IN THE PERSEUS CLUSTER CORE

ABSTRACT

We present the detection of 89 low surface brightness (LSB), and thus low stellar density galaxy candidates in the Perseus cluster core, of the kind named 'ultra-diffuse galaxies', with mean effective V-band surface brightnesses 24.8–27.1 mag arcsec^{-2}, total V-band magnitudes -11.8 to -15.5 mag, and half-light radii 0.7–4.1 kpc. The candidates have been identified in a deep mosaic covering 0.3 deg^2, based on wide-field imaging data obtained with the William Herschel Telescope. We find that the LSB galaxy population is depleted in the cluster centre and only very few LSB candidates have half-light radii larger than 3 kpc. This appears consistent with an estimate of their tidal radius, which does not reach beyond the stellar extent even if we assume a high dark matter content (M/L=100). In fact, three of our candidates seem to be associated with tidal streams, which points to their current disruption. Given that published data on faint LSB candidates in the Coma cluster – with its comparable central density to Perseus – show the same dearth of large objects in the core region, we conclude that these cannot survive the strong tides in the centres of massive clusters.

4.1 INTRODUCTION

Galaxies of low surface brightness, once considered a rare part of the overall galaxy population (e.g., van den Bergh 1959), now are recognized to exist in all galaxy mass ranges with a wide variety of properties (e.g., Sprayberry et al. 1995; de Blok et al. 1996; Schombert et al. 2011; Boissier et al. 2016). In addition, improved techniques have led to the detection of increasing numbers of low surface brightness, and thus low stellar density, galaxies (Impey et al. 1996; Dalcanton et al. 1997; Kniazev et al. 2004). These are particularly numerous among the less luminous members of galaxy clusters (e.g., van der Burg et al. 2016).

Galaxy clusters have been and are being surveyed for increasingly faint galaxies, leading to the detection of low-mass dwarf galaxies in the surface brightness regime of Local Group dwarf spheroidals (dSphs) with mean effective surface brightnesses $\langle\mu_V\rangle_{50} > 24\,\text{mag arcsec}^{-2}$, and even ultra-faint dwarfs (e.g. Muñoz et al. 2015; Ferrarese et al. 2016). With this increasing coverage of the parameter space of magnitude, half-light radius and surface brightness, we therefore consider it necessary to distinguish between a regular – even though faint – dwarf galaxy, and a low surface brightness (LSB) galaxy *in the sense of having a surface brightness clearly lower than average at its luminosity*. For example, while the Virgo Cluster Catalogue of Binggeli et al. (1985) contains hundreds of newly identified dwarf galaxies, many of them being faint in magnitude and surface brightness, their catalogue also includes a handful of LSB objects that seemed to form 'a new type of very large diameter (10 000 pc), low central surface brightness ($\geqslant$ 25 B mag arcsec^{-2}) galaxy, that comes in both early (i.e., dE) and late (i.e., Im V) types' (Sandage and Binggeli

1984). Further Virgo cluster galaxies of dwarf stellar mass but with unusually large size and faint surface brightness were described by Impey et al. (1988), and some similar objects were discovered in the Fornax cluster by Ferguson and Sandage (1988) and Bothun et al. (1991). Three decades later, galaxies in the same general parameter range were dubbed 'ultra-diffuse galaxies' by van Dokkum et al. (2015a).

In the Coma cluster, a large number of over 700 very faint candidate member galaxies with total magnitudes $M_B > -13$ mag, half-light radii $0.2 < r_{50} < 0.7$ kpc and central surface brightnesses as low as $\mu_{B,0} = 27$ mag arcsec^{-2} were identified by Adami et al. (2006). In the brighter and overlapping magnitude range $-11 \gtrsim M_g \gtrsim -16$ mag van Dokkum et al. (2015a) and Koda et al. (2015) reported numerous LSB candidates with $\mu_{g,0} \geqslant 24$ mag arcsec^{-2} and half-light radii up to 5 kpc in Coma, of which five large objects with $r_{50} \gtrsim 3$ kpc are spectroscopically confirmed cluster members (van Dokkum et al. 2015b; Kadowaki et al. 2017). The Virgo cluster study of Mihos et al. (2015, 2017) revealed four LSB candidates with even lower central surface brightnesses of $\mu_{V,0} \sim 27$ mag arcsec^{-2} and half-light radii as large as 10 kpc. In the Fornax cluster an abundant population of faint LSB galaxies with $\mu_{r,0} \geqslant 23$ mag arcsec^{-2} were catalogued by Muñoz et al. (2015) and Venhola et al. (2017), of which a few have $r_{50} > 3$ kpc (Venhola et al. 2017). Several such objects in different environments were also reported by Dunn (2010).

Although LSB galaxies have now been detected in large numbers, their origin remains a puzzle. Especially the abundant existence of LSB galaxies of dwarf stellar mass in galaxy clusters raised the question how these low stellar density systems could survive in the tidal field of such dense environments. For example, van Dokkum et al. (2015a) did not report any signs of distortions for the faint LSB candidates identified in the Coma cluster. Other cluster LSB galaxies of dwarf luminosity harbour surprisingly large and intact globular cluster (GC) systems (e.g. Beasley and Trujillo 2016; Peng and Lim 2016). One explanation could be that these galaxies are characterised by a very high dark matter content that prevents disruption of their stellar component. A similar interpretation was given by Penny et al. (2009) for a population of remarkably round and undistorted dSphs in the Perseus cluster core. Dynamical analyses of two faint LSB galaxies in the Coma and Virgo cluster indeed revealed very high mass-to-light ratios on the order of $M/L = 50$–100 within one half-light radius (Beasley et al. 2016; van Dokkum et al. 2016). Similar or even higher M/L ratios are also characteristic for Local Group dSphs with $M_V > -10$ mag or $\langle \mu_V \rangle_{50} > 25$ mag arcsec^{-2} (cf. McConnachie 2012). On the other hand, Milgrom (2015) suggested that within the MOND theory high M/L ratios could also be explained if the LSB galaxies would contain yet undetected cluster baryonic dark matter.

However, apparently the above does not apply to all faint cluster LSB galaxies. For example, two LSB galaxy candidates of very low stellar density in the Virgo cluster show possible signs of disruption (Mihos et al. 2015, 2017). One large LSB candidate of dwarf luminosity with a very elongated shape and truncated light profile was also reported in Fornax (see Chapter 3), and several further elongated large LSB candidates were described by Venhola et al. (2017). In the Hydra I galaxy cluster, Koch et al. (2012) identified a faint LSB galaxy with S-shaped morphology, indicative of its ongoing tidal disruption. Also van der Burg et al. (2016), who studied populations of faint LSB candidates with $r_{50} \geqslant 1.5$ kpc in eight clusters with redshifts $z = 0.044$–0.063, reported a depletion of LSB galaxy candidates in the cluster cores, based on number counts. Similarly, the numerical simulations of

Yozin and Bekki (2015) predict the disruption of LSB galaxies that are on orbits with very close cluster-centric passages.

In this study, we aim to investigate the faint LSB galaxy population of the Perseus cluster core. Perseus is a rich galaxy cluster at a redshift of $z = 0.0179$ (Struble and Rood 1999). While its mass is in between the lower mass Virgo and the higher mass Coma cluster, its core reaches a density comparable to that of the Coma cluster. There are indications that Perseus is possibly more relaxed and evolved than Coma (e.g. Forman and Jones 1982). For example Perseus only has a single cD galaxy in its centre, while the core of Coma harbours two large galaxies. On the other hand, Andreon (1994) interpreted the 'non-uniform distribution of morphological types' in Perseus as an indication that this cluster is not yet virialized and instead dynamically young. This may be supported by the observation that on large scales Perseus is not a spherically symmetric cluster like Coma, but shows a projected chain of bright galaxies extending in east–west direction that is offset from the symmetric X-ray distribution.

While a significant number of regular dwarf galaxies has already been identified in a smaller field of the cluster core by Conselice et al. (2002, 2003), we focus on galaxies in the same luminosity range with $M_V > -16$ mag (corresponding to stellar masses of $M_* \lesssim 10^8\,M_\odot$) but of fainter surface brightness and thus lower stellar density. This is made possible by our deep wide-field imaging data obtained with the 4.2 m *William Herschel Telescope* (*WHT*) Prime Focus Imaging Platform (PFIP), reaching a 5σ V-band depth of about 27 mag arcsec^{-2}. In this work, we concentrate on LSB galaxies with $\langle\mu_V\rangle_{50} \geqslant 24.8$ mag arcsec^{-2}, which corresponds to the currently often adopted surface brightness limit of $\mu_{g,0} \geqslant 24$ mag arcsec^{-2} for the so-called 'ultra-diffuse galaxies'. While the definition of the latter refers to objects with $r_{50} > 1.5$ kpc (e.g. van Dokkum et al. 2015a), we will not apply any size criterion in this study and generally speak of 'faint LSB galaxies', or 'LSB galaxies of dwarf stellar mass'. Previous work on the low-mass galaxy population in Perseus includes also the 29 dwarf galaxies studied by Penny et al. (2009) and De Rijcke et al. (2009) in *Hubble Space Telescope* (*HST*) imaging data, of which six fall within our considered surface brightness range.

This Chapter is organized as follows: in Section 4.2, we describe the observations, data reduction and our final mosaic. We outline the detection of the LSB sources in Section 4.3, and specify their photometry in Section 4.4. We present our results in Section 4.5, where we define our sample of LSB candidates, examine their spatial distribution in the cluster, discuss peculiar candidates and characterise their magnitude–size–surface brightness distribution in comparison to LSB candidates in the Coma cluster. We discuss our results in Section 4.6, followed by our conclusions in Section 4.7. Throughout this work, we assume a distance of 72.3 Mpc to the Perseus cluster with a scale of 20.32 kpc arcmin^{-1} (Struble and Rood 1999, using the 'cosmology-corrected' quantities from NED with $H_0 = 73.0$ km s^{-1} Mpc^{-1}, $\Omega_{matter} = 0.27$, $\Omega_{vacuum} = 0.73$).

4.2 THE DATA

We acquired deep *V*-band imaging data of the Perseus cluster core with PFIP at the *WHT* through the Opticon programme 2012B/045 (PI T. Lisker). The PFIP is an optical wide-field imaging camera with a field of view of 16×16 arcmin^2, corresponding to 325×325 kpc^2 at the distance of Perseus. The observations were
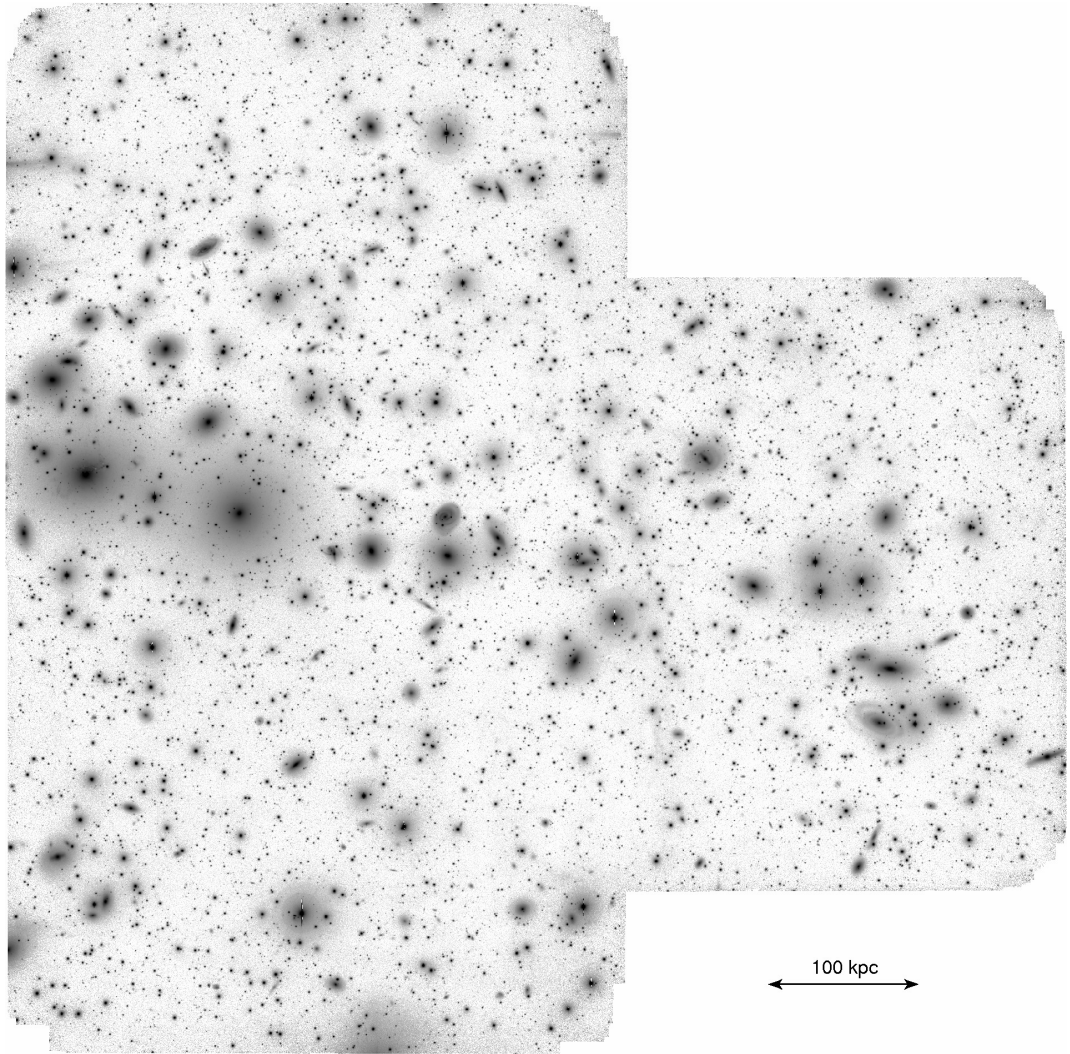
FIGURE 4.1:   Deep V-band mosaic of the Perseus cluster core. The image dimensions are $0.58°(\hat{=}\,0.71\,\text{Mpc at }72.3\,\text{Mpc})$ in east–west and north–south direction. North is up and east is to the left. The two bright galaxies in the east are NGC 1275 and NGC 1272.

carried out 2012 November 12 and 13. We performed dithered observations on three pointings across the cluster core, with individual exposure times of 120 s. In total, 187 science exposures contribute to the final mosaic.

We reduced the data mainly with the image reduction pipeline THELI[1] (Erben et al. 2005; Schirmer 2013), which is especially designed to process wide-field imaging data. For the data reduction each exposure was spatially split into two frames, corresponding to the two detectors of the instrument. All frames were overscan- and bias-corrected, as well as flat fielded using twilight flats. To correct for remaining large-scale intensity gradients that may still be imprinted in the data after flat fielding, a master background, containing only signal from the sky, was created. For the latter the sources in all frames were masked, then the frames were normalized and stacked. Assuming the background inhomogeneities are of additive nature, the master background was subsequently subtracted from all frames. Since applying one common master background was not sufficient to remove the large-scale background variations from all frames, individual background models were created in a next step.

---

1 THELI GUI, version 2.6.2

The individual models are based on object-masked frames, where the masked areas were interpolated based on values from neighbouring unmasked pixels. The resulting images were convolved with a Gaussian kernel with a full width at half-maximum (FWHM) of 512 pixels. The individual background models were subtracted from each frame. We note that the applied filter kernel is large with respect to the extent of our targets, which have typical half-light radii on the order of 20–60 pixels. Then all frames were calibrated astrometrically and distortion corrected, using the Sloan Digital Sky Survey Data Release 9 (SDSS-DR9; Ahn et al. 2012) as a reference catalogue. Finally the frames were resampled and combined to a mosaic, where each frame was weighted according to the square of its inverse sky noise.

In a second iteration of the reduction we improved the individual background models of the frames that were contaminated through the extended haloes of the two brightest cluster galaxies. This optimization was done outside the THELI pipeline, mainly using IRAF.[2] Manually extending the masks would have resulted in a very high fraction of masked pixels on the single frames. To avoid this, we modelled the light distribution of both galaxies in the first iteration mosaic, using IRAF *ellipse* and *bmodel*. We then subtracted the galaxy models from the distortion corrected frames before generating new individual background models with THELI. The new background models were then subtracted from the original science frames, and combined to the second mosaic.

Lastly we corrected our mosaic for spatial zero-point variations, again outside the THELI pipeline. After selecting suitable stars in our mosaic using SExtractor (Bertin and Arnouts 1996), we measured their magnitudes with the IRAF task *photometry* on the individual flat fielded frames, before any background model was subtracted. We calculated the zero-point of each frame as median magnitude offset with respect to the SDSS-DR9 catalogue, using the transformation equations from Jester et al. (2005). The zero-point variations are then given as the deviation of the magnitude offset of individual stars from the zero-point of the respective frame. We rejected stars that deviate by more than 0.2 mag from the zero-point of the respective frame and only considered stars with small magnitude errors in both the SDSS-DR9 catalogue and the measurements with IRAF *photometry*, requiring $\sqrt{\Delta mag_{\mathrm{phot}}^2 + \Delta mag_{\mathrm{SDSS}}^2} < 0.05$ mag. We then established a two-dimensional map yielding the zero-point variations across the detector by fitting a two-dimensional surface to the zero-point variations obtained for all frames. Finally, we divided each frame by this map, and repeated the above described reduction steps leading to the final mosaic. The zero-point of the final mosaic is 26 mag, with a mean variation of 0.02 mag with respect to the SDSS-DR9 catalogue.

Fig. 4.1 shows our final deep mosaic of the Perseus cluster core. It is not centred directly on the brightest cluster galaxy NGC 1275, but on a region including the chain of luminous galaxies that are distributed to the west of it. The mosaic covers an area of $\sim 0.27\,\mathrm{deg}^2$ ($\widehat{=}\,0.41\,\mathrm{Mpc}^2$), and extends to a cluster-centric distance of $0.57°$($\widehat{=}\,0.70\,\mathrm{Mpc}^2$) from NGC 1275. This corresponds to 29 per cent of the Perseus cluster virial radius for $R_{\mathrm{vir}} = 2.44\,\mathrm{Mpc}$ (Mathews et al. 2006), or 39 per cent when adopting $R_{\mathrm{vir}} = 1.79\,\mathrm{Mpc}$ (Simionescu et al. 2011). The mosaic reaches an image depth of 27 mag arcsec^{-2} in the V-band at a signal-to-noise ratio of S/N = 1 per pixel, with a pixel scale of 0.237 arcsec pixel^{-1}. The corresponding 1σ and 5σ

---

2 IRAF is distributed by the National Optical Astronomy Observatory, which is operated by the Association of Universities for Research in Astronomy (AURA) under a cooperative agreement with the National Science Foundation.
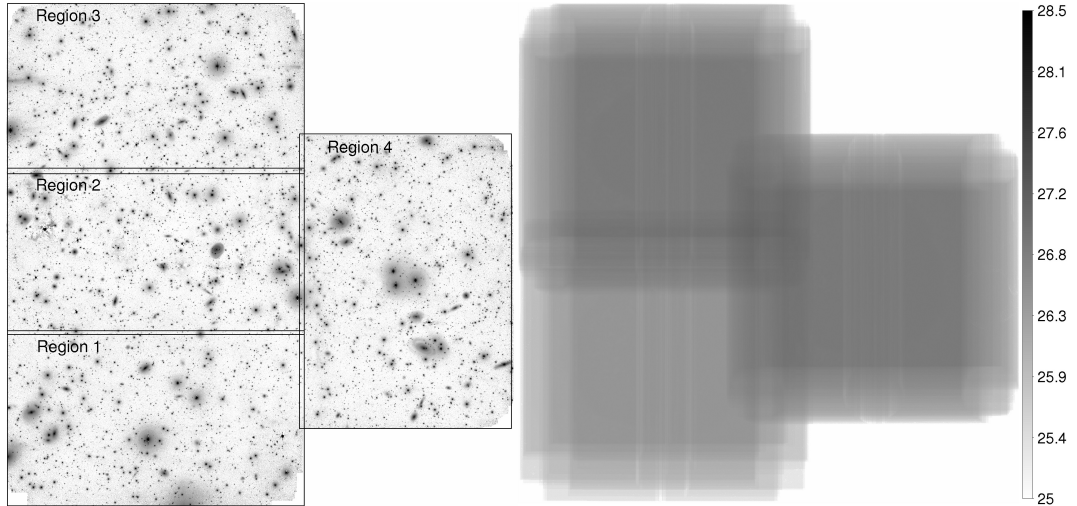
FIGURE 4.2:   Left: Deep V-band mosaic of the Perseus cluster core where most of the bright galaxies and stellar haloes were fitted and subtracted with IRAF *ellipse*. The black boxes indicate how we divided the mosaic into different regions for the detection of LSB sources (see Section 4.3). Right: weight image of the mosaic indicating the image depth in mag arcsec^{-2} at S/N=1 per pixel (see legend on the right-hand side). The image dimensions and orientations are the same as in Fig. 4.1.

depths are 28.6 and 26.8 mag arcsec^{-2}, respectively. The image depth varies across the mosaic, as can be seen in the weight image (Fig. 4.2, right-hand panel). The average seeing FWHM is 0.9 arcsec.

For the subsequent detection and photometry of low surface brightness sources we created one copy of the mosaic where we removed most of the sources with bright extended haloes, including the largest cluster galaxies and the haloes of foreground stars. We fitted the light profiles with IRAF *ellipse*, generated models with IRAF *bmodel* and subtracted them from the mosaic. The partly object-subtracted mosaic is shown in Fig. 4.2 (left-hand panel).

4.3   DETECTION

Motivated by the detection of faint LSB galaxy candidates in the Virgo and Coma galaxy clusters by Mihos et al. (2015) and van Dokkum et al. (2015a), we inserted LSB galaxy models in the same parameter range into our mosaic and then searched systematically for similarly looking objects in Perseus. We decided to search for LSB sources by eye, since automatic detection algorithms often fail in reliably detecting sources with very low S/N. We realized the models with a one component Sérsic profile of Sérsic index $n = 0.7$–1.2 that were convolved with a Gaussian kernel, adopting our average seeing FWHM.

We generated a first set of 27 models in the parameter range $24.6 \leqslant \langle \mu_V \rangle_{50} \leqslant 27.8$ mag arcsec^{-2}, $-14 \geqslant M_V \geqslant -16.6$ mag, and $2.1 \leqslant r_{50} \leqslant 9.7$ kpc, assuming an average foreground extinction of $A_V = 0.5$ mag at the location of Perseus. Among them are nine model types with different magnitudes and half-light radii. For each model type we generated two additional variants with altered position angle and ellipticity, which results in slightly different surface brightnesses. We created a second set of seven nearly round (ellipticity = 0.1) models with $\langle \mu_V \rangle_{50} \leqslant 26.0$ mag arcsec^{-2} that extend the parameter range to smaller half-light radii of 1.5 kpc and fainter magnitudes of -13.5 mag.
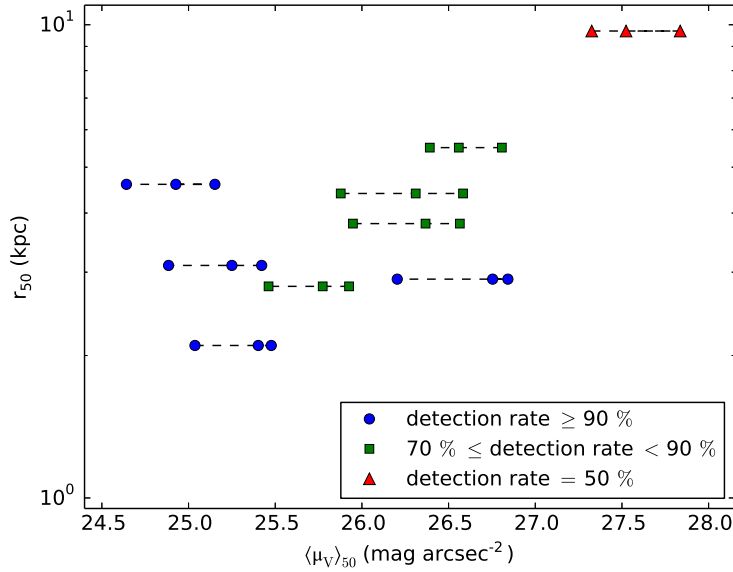
FIGURE 4.3:   Detection rates of visually identified model galaxies as a function of half-light radius and surface brightness. The detection rates are based on 30–40 models of one type, with the same half-light radius and magnitude, but varying ellipticity and thus surface brightness, that were inserted into one copy of the mosaic, respectively. Models of the same type are connected through dashed lines in the plot. The total number of inserted models is 305.

From the first model set, we always inserted 30–40 models of one type, i.e. with the same magnitude and half-light radius but varying ellipticity, into one copy of the mosaic. We generated two additional mosaic copies where we inserted the models from the second model set. We used these copies only at a later stage to focus the detection especially on smaller and fainter LSB sources that turned out to be quite numerous based on the search using the first model set. In total we inserted 305 models from the first model set into nine different mosaic copies, and 56 models from the second set into two further copies.

To facilitate the visual detection of LSB sources, we used the mosaic variant where we previously fitted and subtracted the light distribution of most of the extended sources (see Section 4.2). To remove the remaining bright sources on each copy of the mosaic, we ran SExtractor to detect all sources with more than 10 pixels above a detection threshold of $1.5\,\sigma$, and replaced the pixels above this threshold with zero values, corresponding to the background level of our mosaic. We then convolved the data with a circular Gaussian kernel with $\sigma = 1$ pixel, and demagnified each copy by a factor of 1.5. We further divided each mosaic copy into four smaller regions of different image depth according to the weight image (see Fig.4.2). Finally two of us[3] independently searched visually for diffuse sources in each copy, thereby detecting simultaneously the inserted models and real LSB candidates, without knowing where the former had been inserted. After removing sources that we identified more than once in different copies of the same region, this resulted in a preliminary sample of 214 LSB sources that were identified by at least one of us, and for which we carried out photometry (see Section 4.4).

We used the visually identified models from the first model set to get a rough estimate on our detection rate (see Fig. 4.3). We estimated the detection rate for each model type as fraction of the total number of inserted models that were visually

---

3 C. Wittmann and L. Ambachew Tilahun

identified. We find that the detection rate generally drops with surface brightness. We detected more than 90 per cent of all models with $\langle\mu_V\rangle_{50} < 25.5\,\mathrm{mag\,arcsec^{-2}}$, between 70 and 90 per cent of all models with $25.5 \leqslant \langle\mu_V\rangle_{50} < 27.0\,\mathrm{mag\,arcsec^{-2}}$, and about 50 per cent of all models with $\langle\mu_V\rangle_{50} > 27.0\,\mathrm{mag\,arcsec^{-2}}$.[4]

The models with $\langle\mu_V\rangle_{50} < 27.0\,\mathrm{mag\,arcsec^{-2}}$ are in general clearly visible in our data and the main reason for missing some of them seems to be related to overlap with brighter sources. We estimated the area occupied by remaining bright extended sources in our object-subtracted mosaic to be 12 per cent[5], which compares to an average detection rate of 90 per cent of all models with $\langle\mu_V\rangle_{50} < 27.0\,\mathrm{mag\,arcsec^{-2}}$. Scatter in the trend of decreasing detection fraction with surface brightness can both be caused by our approach of visual source detection, as well as by the different overlap fractions of the inserted models with brighter sources.[6] The detection rate of models with $\langle\mu_V\rangle_{50} < 27.0\,\mathrm{mag\,arcsec^{-2}}$ is similar in all regions of our mosaic, even in the shallowest region (*Region 1*; see Fig.4.2). For models with $\langle\mu_V\rangle_{50} > 27.0\,\mathrm{mag\,arcsec^{-2}}$ we find, however, a lower detection rate in *Region 1* and *Region 2*, compared to the other two regions. While *Region 1* is the shallowest region, the lower detection rate in *Region 2* might be related to the higher galaxy density compared to the other regions.

4.4   PHOTOMETRY

Photometry of LSB sources is challenging and the measurements suffer in general from higher uncertainties compared to sources of brighter surface brightness. One reason for this is that the radial flux profile of the former is characterised by a larger fraction of flux at large radii, where the S/N is typically very low. This also implies that contamination from close neighbour sources and the presence of background gradients is more severe for these objects. We quantify the arising uncertainties in our data using inserted LSB galaxy models (see Section 4.5.3).

We derived magnitudes and sizes from growth curves through iterative ellipse fitting with IRAF *ellipse*, rather than from fits to analytical models. The first step was to obtain a first guess of the centre, ellipticity and position angle of all sources. We used SExtractor to measure the parameters of 131 objects that were detected with a detection threshold of $1\,\sigma$ (128 objects) or $0.8\,\sigma$ (3 objects). For 83 objects that were not detected with SExtractor or that had obviously wrong parameters we estimated their centre and shape visually based on the Gaussian smoothed and demagnified mosaic. Then we ran *ellipse* with fixed parameters, adopting the previously measured or estimated centres, ellipticities and position angles. We chose a linear step-size of 5 pixels for consecutive isophotes. We used the first ellipse fit results to generate two-dimensional brightness models with IRAF *bmodel* that we subtracted from the fitted source.

The residual images served as a basis to create masks of neighbouring sources from SExtractor segmentation images. We ran SExtractor in two passes, one with a minimum number of 28 connected pixels above a detection threshold of $1\,\sigma$, the other with a lower detection threshold of $0.6\,\sigma$ and requiring a minimum

---

4   The given surface brightnesses refer to the average surface brightness of the three model variants with different ellipticity, and thus surface brightness, that exist per model type.

5   This accounts for all sources that were detected with SExtractor with more than 1000 connected pixels above a detection threshold of $1.5\,\sigma$.

6   We note that the fraction of models whose centre overlaps with one of the SExtractor-detected sources above $1.5\,\sigma$ does not exceed 12 per cent per model type.

number of 1000 connected pixels. In both passes, we used SEXTRACTOR with the built-in filtering prior to detection. We combined both segmentation images and extended the masked areas by smoothing with a Gaussian kernel. We ran *ellipse* in a second pass with the masks to exclude that flux from neighbouring sources contributes to the ellipse fits. From the second iteration residual images we created improved masks where the masked regions are somewhat larger. We unmasked the centre of nucleated candidates and ellipse fit residuals when necessary.

The next step was to determine the background level from the third pass ellipse fit results using the improved masks. Getting the background level right is a very subtle task and the major source of the uncertainties in the magnitude and size measurements. Therefore, we determined the background level for each of our detected LSB objects individually. We first measured the radial flux profiles out to large radii (350 pixels) for each object. We then manually adjusted the radius and width of the background annulus, whose median flux we adopted as the background level. The inner radius of the background annulus was set at the first break in the flux profile where the intensity gradient significantly changes and the flux profile levels out. We set the width of the annulus to 50 pixels. Its shape follows the ellipticity and position angle of the measured object.

Although all neighbour sources were carefully masked, still some flux profiles show signs of contamination. Especially at larger radii where faint flux levels are reached, the flux of the LSB source can be comparable to the flux of a neighbour source that still extends beyond the masked area (e.g. some very extended haloes of foreground stars or bright cluster galaxies). Also background inhomogeneities remaining in the data after the reduction can contaminate the flux profiles. Possible contamination can become apparent in a flux profile when, for example, the profile continues to decline after the first break instead of levelling out to zero. In this case we nevertheless set the inner radius of the background annulus to the first break in the profile, and eventually decrease its width to make sure that the flux profile is flat in this region.

Even though we might truncate a galaxy at too high intensity, resulting in a systematically fainter magnitude and a smaller half-light radius, restricting the analysis to the uncontaminated inner profile helps to preserve the true surface brightnesses (see the right-hand panels in Fig. 4.7 and Section 4.5.3). After subtracting the background offset, we then obtained a first estimate of the magnitudes and sizes by running *ellipse* in a fourth pass on the background corrected images and taking into account the masked sources. We determined the total flux from the cumulative flux profile[7] and derived the half-light radius along the semimajor axis, as well as the mean effective surface brightness within one half-light radius.

In the final iteration we measured the centre, ellipticity and position angle of our LSB sources more accurately, using our first guess parameters as input values. We used IRAF *imcentroid* to derive the centre, and calculated the ellipticity and position angle from the image moments within a circular area defined by our first-guess half-light radius. We also further improved the masks by manually enlarging the masks of extended neighbour sources with faint haloes.[8] After that we ran *ellipse*

---

7 We adopted the median of the cumulative fluxes TFLUX_E from the ellipse fit tables, namely of the five isophotes between the inner radius of the background annulus and 20 pixels further, as an estimate of the total flux. Since *ellipse* does not account for masked regions when calculating the total flux within an isophote, we replaced the masked regions with values from the 2-D model created with IRAF *bmodel* from the radial flux profile.

8 Using SAOImage DS9 (Joye and Mandel 2003) *regions* and IRAF *mskregions*.

in a fifth pass with the new parameters and masks to adjust the inner radius of the background annulus. We adopted the new background level and derived the final magnitudes, half-light radii and mean effective surface brightnesses in a last pass of ellipse fitting. We corrected the derived magnitudes for extinction, using the IRSA Galactic Reddening and Extinction Calculator[9], with reddening maps from Schlafly and Finkbeiner (2011). The average foreground extinction of our measured sources is $A_V = 0.5$ mag.

4.5   FAINT LSB GALAXIES IN THE PERSEUS CLUSTER CORE

4.5.1   *Sample*

We define our sample of LSB galaxy candidates to include all objects with $\langle \mu_V \rangle_{50} \geqslant$ 24.8 mag arcsec^{-2}. This corresponds to the currently often adopted surface brightness limit of $\mu_{g,0} \geqslant 24.0$ mag arcsec^{-2} for 'ultra-diffuse galaxies' (e.g. van Dokkum et al. 2015a), when assuming an exponential profile with Sérsic $n = 1$ (cf. Graham and Driver 2005), $g - r = 0.6$ and using the transformation equations from Jester et al. (2005). Of our preliminary sample, 133 objects fall into this parameter range. We carefully examined all of them, both on the original as well as on the smoothed and demagnified mosaic. We also compared them to an independent data set of the Perseus cluster, obtained with *WIYN*/ODI in the g, r and i filters (programme 15B-0808/5, PI: J. S. Gallagher). Since the single-band images are shallower than our data, we used the stacked g, r, i images for the comparison.

Based on a more detailed visual examination of their morphology, we classified 82 of our candidates as likely galaxies. They are characterised by a smooth morphology and are confirmed in the independent data set. We classified seven further candidates as possible galaxies (all of them are shown in Fig. 4.4 in the bottom row). Three of them (candidates 26, 31 and 44) are clearly visible in our data, but their morphology does not appear very regular. Since these objects are also visible in the *WIYN*/ODI data, we rule out that they are image artefacts. However a confusion with cirrus cannot be excluded (see Section 4.5.3). The four other candidates (candidates 27, 49, 57 and 81) are classified as possible galaxies since they are only barely visible in our data, due to their low surface brightness or low S/N, and are not confirmed in the shallower independent data set. We rejected 44 LSB sources from our sample, since we cannot exclude that these are remaining background inhomogeneities from the reduction, or residuals from ellipse fitting of the brighter galaxies. Most of them are of very diffuse nature (80 per cent have $\langle \mu_V \rangle_{50} \geqslant 26.5$ mag arcsec^{-2}) and often do not have a smooth morphology.

Our final sample includes 89 LSB galaxy candidates in the Perseus cluster core. We show our sample in Fig. 4.4 and provide the photometric parameters in Table 4.1. We also compare our sample to overlapping *HST*/ACS images, in order to investigate whether some of our objects would classify as background sources, based on possible substructure in the form of, e.g., spiral arms. Seven of our LSB candidates fall on *HST*/ACS pointings, and none of them shows signs of substructure. We therefore expect that the overall contamination through background galaxies is low in our sample, based on the morphological appearance in the *HST*

---

9 We acknowledge the use of the NASA/IPAC Infrared Science Archive, which is operated by the Jet Propulsion Laboratory, California Institute of Technology, under contract with the National Aeronautics and Space Administration.

as well as in the *WHT* images and due to the location of our sample in the core region rather than in the cluster outskirts. Certain cluster membership can, however, only be established through measurements of radial velocities. The six brightest candidates in the *HST*/ACS images with $24.8 \leqslant \langle \mu_V \rangle_{50} \leqslant 25.4 \, \text{mag arcsec}^{-2}$, as measured in our data, were previously identified in Penny et al. (2009) (candidates 62, 64, 69, 70, 73 and 87). One of them (candidate 62) was first catalogued by Conselice et al. (2002, 2003). The faintest candidate, with $\langle \mu_V \rangle_{50} = 26.5 \, \text{mag arcsec}^{-2}$ (candidate 82), is only barely visible in the *HST*/ACS images and was not published previously.
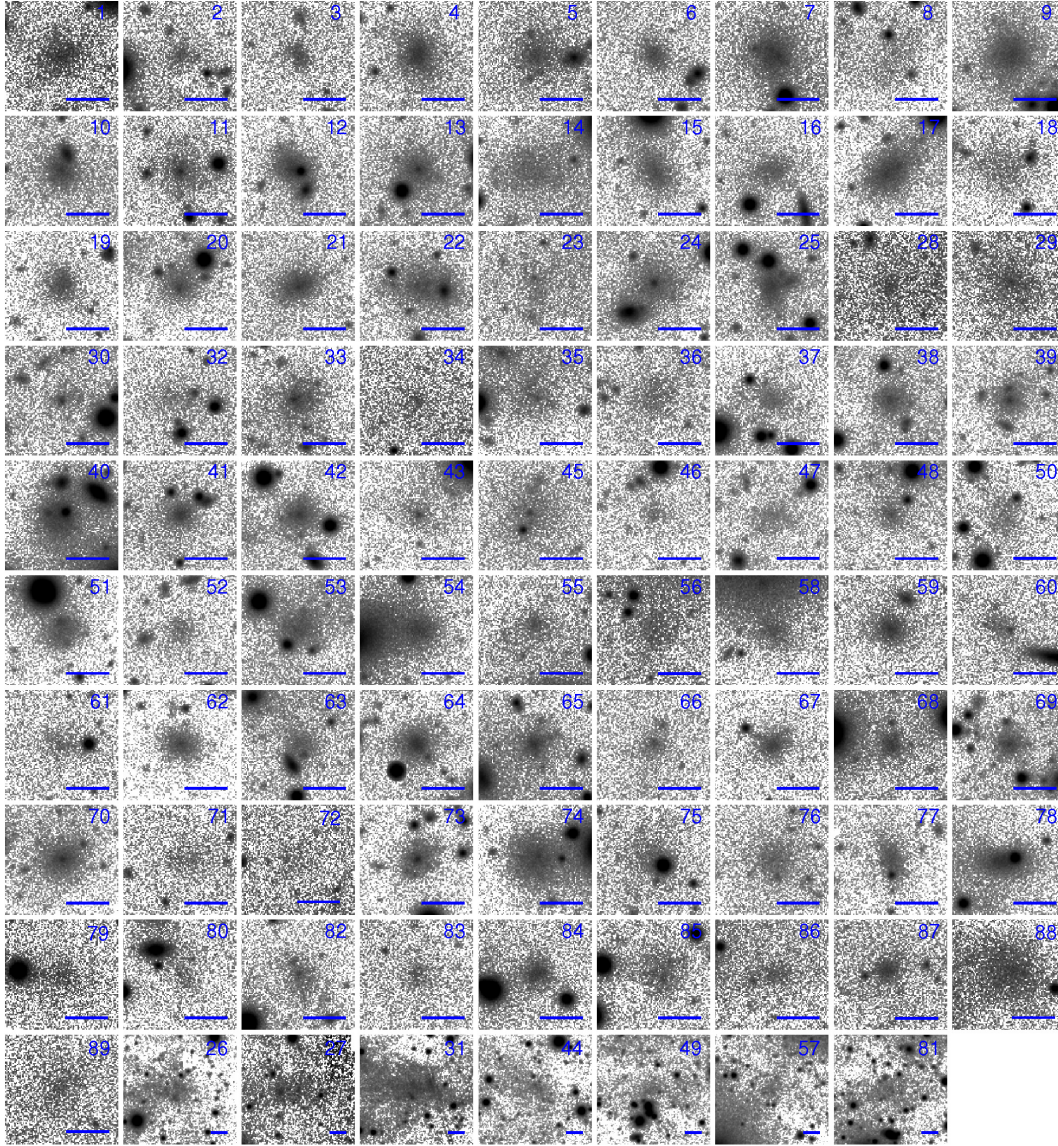
FIGURE 4.4:   Sample of faint LSB galaxy candidates in the Perseus cluster core. The first 82 panels show the LSB candidates in cutout regions of our original data with a size of $21 \times 21 \, \text{arcsec}^2$, respectively. The seven last panels in the bottom row show the LSB candidates classified as possible galaxies (see Section 4.5.1). They are displayed in our smoothed and demagnified data in cutout regions with a size of $53 \times 53 \, \text{arcsec}^2$, respectively. The blue bar in each panel of the figure denotes a length of 3 kpc. The number in each panel corresponds to the ID of the shown object given in Table 4.1. North is up and east is to the left.

TABLE 4.1: Coordinates and structure parameters of faint LSB galaxy candidates in the Perseus cluster core. M_V and $\langle\mu_V\rangle_{50}$ are corrected for Galactic foreground extinction. A_V is derived from the reddening maps of Schlafly and Finkbeiner (2011). ϵ denotes the ellipticity. No reliable individual errors can be provided, but the right-hand panels in Fig. 4.7 illustrate the statistical and systematic uncertainties for the LSB galaxy models in the parameter range of our sample; details are provided in Section 4.5.3. The table is sorted by increasing right ascension.

ID	R.A. (J2000)	DEC. (J2000)	$\langle\mu_V\rangle_{50}$ (mag arcsec^{-2})	M_V (mag)	A_V (mag)	r_{50} (kpc)	ϵ
01	03 17 00.37	+41 19 20.6	24.9	−15.0	0.4	1.9	0.08
02	03 17 03.26	+41 20 29.1	25.9	−12.9	0.4	1.2	0.20
03	03 17 04.42	+41 30 39.2	25.2	−12.7	0.4	0.8	0.17
04	03 17 07.13	+41 22 52.5	25.2	−14.5	0.4	1.7	0.08
05	03 17 11.02	+41 34 03.3	25.3	−14.3	0.4	1.7	0.13
06	03 17 13.29	+41 22 07.6	25.3	−12.9	0.4	0.9	0.10
07	03 17 15.97	+41 20 11.7	25.1	−15.1	0.4	2.1	0.05
08	03 17 19.71	+41 34 32.5	26.3	−13.7	0.4	2.1	0.21
09	03 17 23.50	+41 31 40.1	25.1	−14.2	0.4	1.4	0.01
10	03 17 24.94	+41 26 09.7	25.1	−13.6	0.4	1.1	0.17
11	03 17 35.49	+41 18 12.7	25.2	−13.6	0.4	1.1	0.05
12	03 17 36.78	+41 23 01.6	25.2	−14.0	0.4	1.4	0.09
13	03 17 38.21	+41 31 56.9	25.1	−13.6	0.4	1.1	0.13
14	03 17 39.22	+41 31 03.5	25.9	−13.9	0.4	1.7	0.09
15	03 17 39.42	+41 24 45.0	25.5	−13.7	0.4	1.3	0.13
16	03 17 41.79	+41 24 01.9	25.8	−13.2	0.4	1.2	0.12
17	03 17 44.16	+41 21 18.4	25.0	−14.4	0.4	1.5	0.15
18	03 17 48.34	+41 18 38.9	25.9	−14.1	0.4	2.0	0.13
19	03 17 53.17	+41 19 31.9	25.5	−13.9	0.4	1.4	0.03
20	03 17 54.66	+41 24 58.8	25.2	−13.3	0.4	1.0	0.07
21	03 18 00.81	+41 22 23.0	24.9	−13.6	0.4	1.0	0.11
22	03 18 05.55	+41 27 42.4	25.8	−14.2	0.5	2.1	0.25
23	03 18 09.55	+41 20 33.5	26.4	−12.2	0.5	1.0	0.12
24	03 18 13.08	+41 32 08.3	25.3	−13.8	0.5	1.3	0.11
25	03 18 15.44	+41 28 35.2	24.9	−13.4	0.5	0.9	0.17
26	03 18 19.50	+41 19 24.8	26.5	−13.8	0.5	2.3	0.15
27	03 18 20.79	+41 45 29.3	26.3	−14.0	0.4	2.3	0.14
28	03 18 21.66	+41 45 27.6	25.9	−13.9	0.4	1.8	0.13
29	03 18 23.33	+41 45 00.6	25.6	−14.7	0.4	2.2	0.04
30	03 18 23.40	+41 36 07.7	25.6	−12.3	0.5	0.7	0.08
31	03 18 24.32	+41 17 30.7	26.0	−15.5	0.5	4.1	0.17
32	03 18 24.46	+41 18 28.4	26.5	−13.0	0.5	1.5	0.09
33	03 18 25.86	+41 41 06.9	25.5	−14.0	0.5	1.5	0.06
34	03 18 26.92	+41 14 09.5	25.7	−12.4	0.5	0.8	0.03
35	03 18 28.18	+41 39 48.5	25.8	−13.9	0.5	1.9	0.21
36	03 18 29.19	+41 41 38.9	26.2	−13.1	0.5	1.4	0.04
37	03 18 30.36	+41 22 29.8	25.9	−12.1	0.5	0.8	0.13
38	03 18 32.11	+41 27 51.5	25.4	−13.1	0.5	0.9	0.05
39	03 18 32.13	+41 32 12.3	25.2	−12.8	0.5	0.8	0.19
40	03 18 33.25	+41 40 56.1	25.2	−13.9	0.5	1.3	0.12

TABLE 4.1 – *continued*

ID	R.A. (J2000)	DEC. (J2000)	$\langle \mu_V \rangle_{50}$ (mag arcsec^{-2})	M_V (mag)	A_V (mag)	r_{50} (kpc)	ϵ
41	03 18 33.57	+41 41 58.3	25.2	−13.4	0.5	1.0	0.06
42	03 18 33.60	+41 27 45.5	25.1	−13.5	0.5	1.0	0.04
43	03 18 34.57	+41 24 18.6	26.1	−12.9	0.5	1.3	0.19
44	03 18 34.73	+41 22 40.5	27.1	−13.6	0.5	2.6	0.09
45	03 18 36.14	+41 21 59.4	26.2	−13.9	0.5	2.2	0.22
46	03 18 37.51	+41 24 16.0	26.3	−11.8	0.5	0.8	0.03
47	03 18 38.96	+41 30 06.8	26.6	−12.8	0.5	1.5	0.13
48	03 18 39.53	+41 39 30.4	25.8	−12.6	0.5	1.0	0.20
49	03 18 39.84	+41 38 58.4	27.1	−12.7	0.5	1.9	0.26
50	03 18 39.92	+41 20 09.0	26.3	−13.2	0.5	1.5	0.11
51	03 18 41.38	+41 34 01.3	25.5	−13.7	0.5	1.5	0.27
52	03 18 42.60	+41 38 33.0	26.1	−12.3	0.5	0.9	0.04
53	03 18 44.65	+41 34 07.7	25.4	−13.5	0.5	1.2	0.09
54	03 18 44.95	+41 24 20.4	24.9	−13.9	0.5	1.1	0.11
55	03 18 46.16	+41 24 37.1	26.2	−14.3	0.5	2.4	0.09
56	03 18 48.02	+41 14 02.4	25.9	−14.3	0.5	2.3	0.23
57	03 18 48.43	+41 40 35.1	27.1	−13.3	0.5	2.4	0.11
58	03 18 50.74	+41 23 09.1	25.4	−13.0	0.4	1.0	0.17
59	03 18 54.32	+41 15 29.2	24.9	−14.0	0.5	1.1	0.02
60	03 18 55.38	+41 17 50.0	25.8	−12.5	0.5	1.0	0.18
61	03 18 59.40	+41 25 15.4	26.0	−12.5	0.4	1.0	0.07
62	03 18 59.42	+41 31 18.7	25.4	−13.9	0.4	1.4	0.07
63	03 19 01.50	+41 38 59.0	25.8	−12.9	0.5	1.1	0.17
64	03 19 05.83	+41 32 34.4	24.8	−13.8	0.4	1.1	0.09
65	03 19 07.77	+41 27 12.1	24.8	−12.9	0.4	0.7	0.06
66	03 19 09.32	+41 41 51.7	25.9	−12.5	0.5	0.9	0.06
67	03 19 12.76	+41 43 30.0	25.2	−13.5	0.5	1.1	0.08
68	03 19 15.01	+41 22 31.7	25.1	−13.3	0.4	0.9	0.06
69	03 19 15.70	+41 30 34.6	25.1	−12.9	0.4	0.8	0.05
70	03 19 15.86	+41 31 05.8	25.2	−14.2	0.4	1.4	0.03
71	03 19 16.02	+41 45 45.9	26.1	−13.3	0.5	1.4	0.05
72	03 19 17.53	+41 12 41.3	26.7	−12.8	0.4	1.5	0.02
73	03 19 17.83	+41 33 48.4	24.9	−13.7	0.4	1.0	0.07
74	03 19 21.94	+41 27 22.5	24.9	−14.7	0.4	1.7	0.15
75	03 19 23.06	+41 23 16.8	26.3	−13.7	0.4	2.1	0.20
76	03 19 23.12	+41 38 58.7	26.0	−13.4	0.5	1.5	0.11
77	03 19 32.76	+41 36 12.8	25.7	−13.6	0.4	1.4	0.09
78	03 19 33.80	+41 36 32.5	24.8	−13.6	0.5	1.1	0.34
79	03 19 39.19	+41 12 05.6	25.4	−14.4	0.4	1.8	0.06
80	03 19 39.22	+41 13 43.5	26.3	−12.8	0.4	1.3	0.07
81	03 19 44.03	+41 39 18.4	26.9	−13.8	0.4	2.7	0.14
82	03 19 45.66	+41 28 07.3	26.1	−13.9	0.4	2.0	0.13
83	03 19 47.45	+41 44 09.3	26.0	−12.9	0.4	1.2	0.07
84	03 19 49.70	+41 43 42.6	24.8	−13.5	0.4	0.9	0.05
85	03 19 50.13	+41 24 56.3	25.5	−13.7	0.4	1.3	0.05
86	03 19 50.56	+41 15 33.4	25.6	−12.1	0.4	0.7	0.17

TABLE 4.1 – *continued*

ID	R.A. (J2000)	DEC. (J2000)	$\langle\mu_V\rangle_{50}$ (mag arcsec^{-2})	M_V (mag)	A_V (mag)	r_{50} (kpc)	ϵ
87	03 19 57.41	+41 29 31.2	25.0	−13.3	0.4	0.9	0.05
88	03 19 59.10	+41 18 33.1	24.8	−15.5	0.4	2.2	0.02
89	03 20 00.20	+41 17 05.1	25.7	−13.5	0.4	1.4	0.10

4.5.2 *Properties*

Fig. 4.5 shows the spatial distribution of our sample of 89 faint LSB galaxy candidates in the Perseus cluster core. The sample spans a range of $47 \leqslant d \leqslant 678$ kpc in projected cluster-centric distance, with respect to the cluster's X-ray centre[10] (Piffaretti et al. 2011). This corresponds to $0.02 - 0.28\,R_{vir}$ when assuming a virial radius of $R_{vir} = 2.44$ Mpc (Mathews et al. 2006). About half of our sample is located closer than 330 kpc to the cluster centre.

We find three LSB candidates that appear to be associated with structures resembling tidal streams (see Fig. 4.5, right-hand panels). Candidate 44 seems to be embedded in diffuse filaments, candidates 26 and 31 appear connected via an arc-shaped stream. We find one further galaxy with tidal tails (see Fig. 4.5, bottom left panel), which has a slightly brighter surface brightness of $\langle\mu_V\rangle_{50} = 24.4$ mag arcsec^{-2} and therefore was not included in our sample. We will analyse faint cluster galaxies with brighter surface brightnesses in Chapter 5. It is noticeable that all four objects are confined within one region to the south–west of the cluster centre, within a cluster-centric distance range of about $300 - 400$ kpc. Also the peculiar more luminous galaxy SA 0426-002 (cf. Conselice et al. 2002; Penny et al. 2014) falls on our mosaic, which shows a disturbed morphology with extended low surface brightness lobes (see Fig. 4.5, top left panel).

We show the radial projected number density distribution of our sample in Fig. 4.6. It was derived by dividing the number of galaxies in radial bins of a width of 100 kpc by the area of the respective bin that falls on our mosaic. The bins are centred on the Perseus X-ray centre. We find that the number density is nearly constant for cluster-centric distances $r \geqslant 100$ kpc, but drops in the very centre at $r < 100$ kpc,[11] with a statistical significance of $2.8\,\sigma$ with respect to the average number density at larger radii. For comparison, a preliminary analysis showed that the distribution of bright cluster members is consistent with the expectation of being much more centrally concentrated.

Fig. 4.7 shows the magnitude–size and magnitude–surface brightness distribution of our Perseus cluster LSB galaxy sample. We include the Coma cluster LSB galaxies and candidates from van Dokkum et al. (2015a) and the three very low surface brightness galaxy candidates in Virgo from Mihos et al. (2015). For comparison, we also show Virgo cluster early- and late-type galaxies (compilation of Lisker et al. 2013; based on the Virgo Cluster Catalogue (VCC), Binggeli et al. 1985), Virgo cluster dSphs (Lieder et al. 2012), as well as dSphs from the Local Group (McConnachie 2012).

Our sample spans a parameter range of $24.8 \leqslant \langle\mu_V\rangle_{50} \leqslant 27.1$ mag arcsec^{-2}, $-11.8 \geqslant M_V \geqslant -15.5$ mag and $0.7 \leqslant r_{50} \leqslant 4.1$ kpc. The surface brightness range

---

10 The X-ray centroid almost coincides with the optical location of NGC 1275.

11 Only two galaxies are contained in the central bin with $r < 100$ kpc.
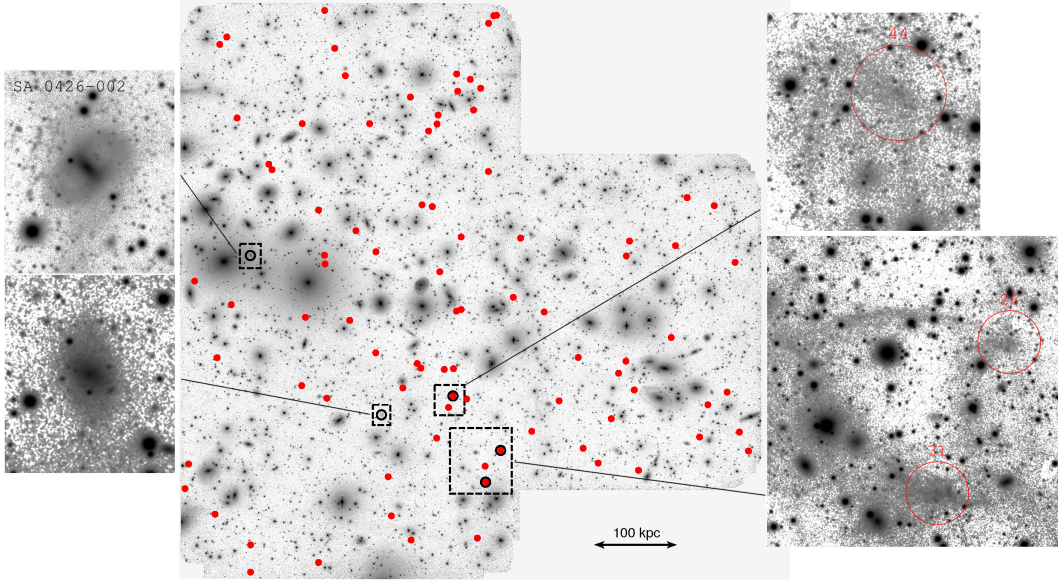
FIGURE 4.5:   Spatial distribution of LSB galaxy candidates in the Perseus cluster core (central panel) and candidates with signs of possible tidal disruption (side panels). Red dots indicate our sample of LSB candidates. The dashed squares on the mosaic indicate the size of the cutout regions shown as side panels. These images were smoothed except the image in the top left side panel, which shows a cutout from the original data. The red dots with black circles mark the positions of candidates 26, 31 and 44 shown in the side panels on the right-hand side. The two galaxies with the tidal structures in the left side panels are not part of our LSB galaxy sample. The image height and width of the mosaic is $0.58\,\mathrm{deg}$ ($\widehat{=}\,0.71\,\mathrm{Mpc}$). North is up and east is to the left.
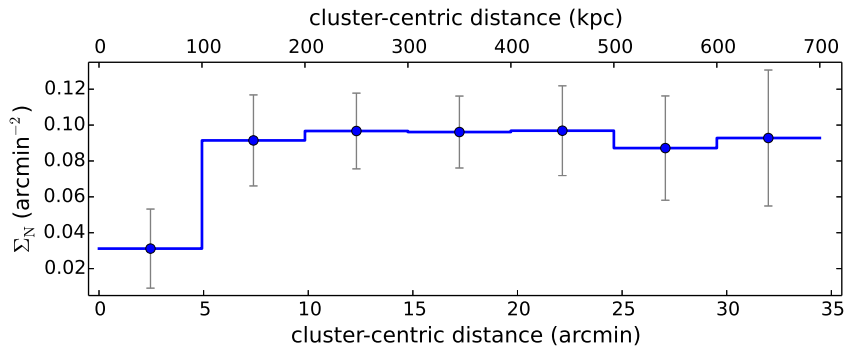
FIGURE 4.6:   Radial projected number density distribution as a function of cluster-centric distance of our sample of LSB galaxy candidates in the Perseus cluster core. The radial bins have a width of $100\,\mathrm{kpc}$. Shown are the statistical error bars.

of our sample is comparable to the LSB galaxy sample from van Dokkum et al. (2015a) and approaches the surface brightness of the two brighter Virgo LSB candidates from Mihos et al. (2015). With regard to magnitudes and sizes our sample includes smaller and fainter LSB candidates than the sample from van Dokkum et al. (2015a), which is likely due to their resolution limit. At faint magnitudes, our samples overlaps with the parameter range of cluster and Local Group dSphs. We note that the apparent relation between magnitude and size of our sample is created artificially. The bright surface brightness limit arises due to our definition of including only sources fainter than $\langle\mu_V\rangle_{50} = 24.8\,\mathrm{mag\,arcsec^{-2}}$ in our sample. The faint limit is due to our detection limit.
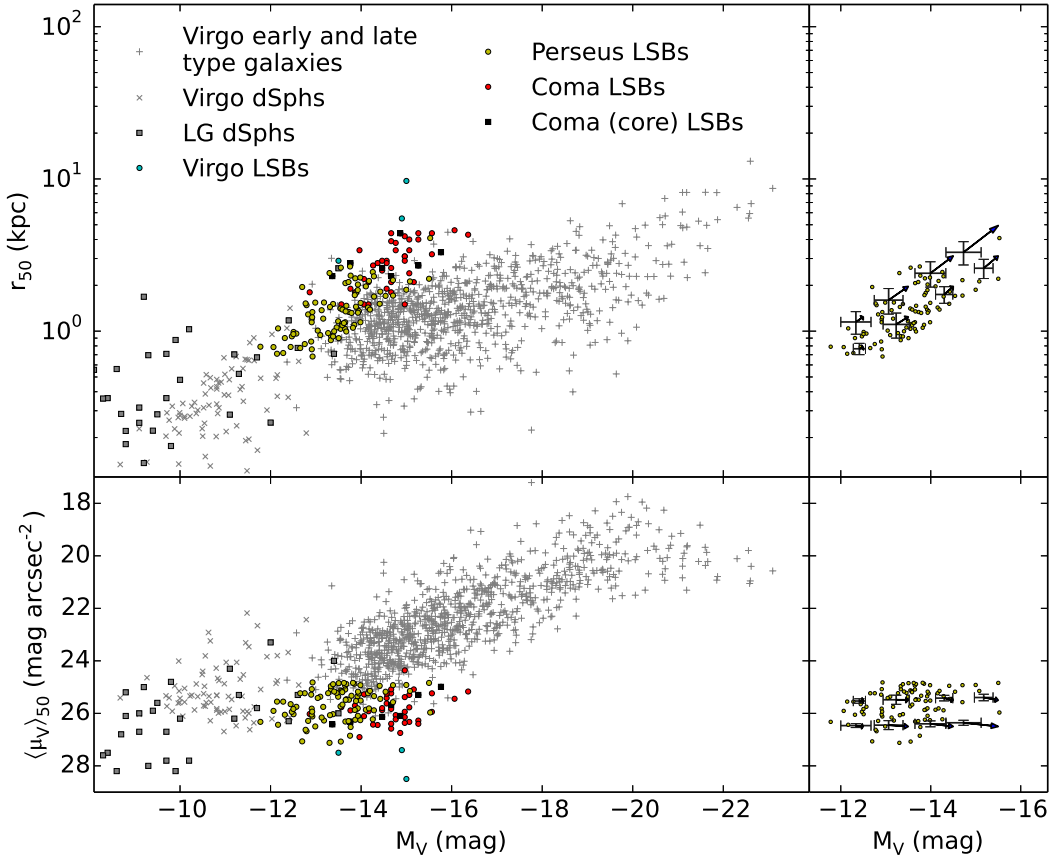
FIGURE 4.7:   Structural parameters of faint LSB galaxy candidates in the Perseus cluster core (left-hand panels). We compare our sample to LSB galaxy candidates in the Virgo cluster (Mihos et al. 2015), and to LSB galaxies and candidates in the Coma cluster (van Dokkum et al. 2015a). We mark those LSB objects in Coma that are located in the cluster core within a circular area with a radius of $R = 0.15\,R_{vir,Coma}$. This corresponds to an area of similar extent as our observed area of the Perseus cluster core (see Section 4.5.2). For comparison, we also show early- and late-type galaxies from the Virgo cluster (compilation of Lisker et al. 2013; based on the VCC), Virgo dSphs (Lieder et al. 2012) and dSphs from the Local Group (McConnachie 2012). We transformed the magnitudes of the LSB candidates from van Dokkum et al. (2015a) and the galaxies from Lisker et al. (2013) with the transformation equations from Jester et al. (2005). For the former, we assumed $g - r = 0.6$, for the latter we used the measured $g - r$ colours. The two panels on the right-hand side show our typical uncertainties that occur for LSB galaxy models ($n = 1$, ellipticity = 0.1) in the parameter range of our sample (see Section 4.5.3). We created eight model types with different parameters. Each model type was inserted 10 times at different positions into one copy of our mosaic. The black arrows indicate our systematic parameter uncertainties. The arrow tips point to the true parameters of the models, the endpoints represent the average measured parameter values of the 10 inserted models of each type. On average the measured M_V values are by 0.4 mag too faint, the measured r_{50} values are underestimated by 0.5 kpc and the measured $\langle \mu_V \rangle_{50}$ values are by 0.1 mag arcsec^{-2} too bright. The error bars represent our statistical uncertainties, and were calculated as standard deviation of the measured values of each model type.

At brighter magnitudes $M_V \leqslant -14$ mag, the LSB candidates of our sample are systematically smaller at a given magnitude than the LSB candidates identified in the Coma cluster, with all but one LSB candidate having $r_{50} < 3$ kpc. However, van Dokkum et al. (2015a) cover a much larger area of the Coma cluster, while we

only surveyed the core region of Perseus.[12] Our total observed area corresponds to $0.41\,\mathrm{Mpc}^2$. This translates to a circular equivalent area with a radius of $R = 0.15\,R_{\mathrm{vir,Perseus}}$, when assuming a virial radius for Perseus of $R_{\mathrm{vir,Perseus}} = 2.44\,\mathrm{Mpc}$ (Mathews et al. 2006).[13]

When selecting all LSB candidates from the van Dokkum et al. (2015a) sample that are located in the core of Coma, within a circular area with cluster-centric distances smaller than $R = 0.15\,R_{\mathrm{vir,Coma}}$, where $R_{\mathrm{vir,Coma}} = 2.8\,\mathrm{Mpc}$ (Łokas and Mamon 2003), seven LSB candidates remain. These are marked with black squares in Fig. 4.7. One can see that also only two of them reach sizes of $r_{50} > 3\,\mathrm{kpc}$. Since the sample of van Dokkum et al. (2015a) has a brighter magnitude and larger size limit than our study, we restrict the comparison to objects with $M_V \leqslant -14\,\mathrm{mag}$ and $r_{50} \geqslant 2\,\mathrm{kpc}$, which should well have been detected by van Dokkum et al. (2015a). Five LSB candidates in the Coma cluster core are in this parameter range, whereas in Perseus we find seven. A similar result is obtained when comparing to the independent sample of Coma cluster LSB galaxy candidates from Yagi et al. (2016). When selecting LSB candidates of the Coma core region in the same surface brightness range as our sample and with $M_V \leqslant -14\,\mathrm{mag}$ and $r_{50} \geqslant 2\,\mathrm{kpc}$, we find 10 LSB candidates in this parameter range, where three LSB candidates have $r_{50} \geqslant 3\,\mathrm{kpc}$. While it seems that the Virgo cluster galaxies shown in Fig. 4.7 are also rare in this parameter range, we note that the catalogue we used is not complete at magnitudes fainter than $M_r = -15.2\,\mathrm{mag}$.

Thus, in summary, we find that first, the core regions of the Perseus and the Coma cluster harbour a similar number of faint LSB galaxy candidates in the same parameter range of $M_V \leqslant -14\,\mathrm{mag}$ and $r_{50} \geqslant 2\,\mathrm{kpc}$, and secondly, that large LSB candidates with $r_{50} \geqslant 3\,\mathrm{kpc}$ seem to be very rare in both cluster cores.

4.5.3 *Uncertainties*

In Fig. 4.7, we try to include realistic photometric uncertainties for our sample. Our major source of uncertainty in the measured total fluxes, which translate to uncertainties in half-light radii and surface brightnesses, lies in the adopted background level (see Section 4.4). To test how large the resulting uncertainties are, we probed this using inserted LSB galaxy models that were generated similarly to those described in Section 4.3. We created eight model types that span the parameter range of our sample. Four model types have $\langle\mu_V\rangle_{50} = 25.5\,\mathrm{mag\,arcsec}^{-2}$, the other four have $\langle\mu_V\rangle_{50} = 26.5\,\mathrm{mag\,arcsec}^{-2}$, with varying magnitudes $M_V = -12.5$ to $-15.5\,\mathrm{mag}$ and sizes $0.8 \leqslant r_{50} \leqslant 4.9\,\mathrm{kpc}$. The models have one component Sérsic profiles with $n = 1$, are nearly round (ellipticity = 0.1) and were convolved to our average seeing FWHM. We inserted 10 models of each type into one copy of our mosaic, respectively. We then measured M_V, r_{50} and $\langle\mu_V\rangle_{50}$ similarly to our sample of real LSB candidates. We calculated the average offset between true and measured parameters for each model type, as well as the scatter of the measured parameters.

We indicate the average parameter offsets with arrows in the right-hand panels of Fig. 4.7. The arrow tips point to the true values, with M_V being systematically estimated as too faint by on average $0.4\,\mathrm{mag}$, and r_{50} being underestimated by on average $0.5\,\mathrm{kpc}$. We largely preserved the true surface brightness, which results from

---

12 According to tests with the inserted model galaxies (see Section 4.3) sources in the surface brightness range of the LSB galaxy sample from van Dokkum et al. (2015a) can easily be detected in our data.

13 We note that our field is not centred directly on the cluster centre, but extends to the west of it.

our approach of considering the uncontaminated part of the flux profile only (see Section 4.4). The offsets in $\langle\mu_V\rangle_{50}$ are small, and do not exceed $0.1\,\mathrm{mag\,arcsec}^{-2}$. In general the parameter offsets are more severe for model types with the largest size and faintest surface brightness, and negligible for model types with the smallest size and brightest surface brightness. The error bars in Fig. 4.7 give the standard deviation of the measured M_V, r_{50} and $\langle\mu_V\rangle_{50}$ values for each model type, with average standard deviations of $\Delta M_V = \pm 0.3\,\mathrm{mag}$, $\Delta r_{50} = \pm 0.3\,\mathrm{kpc}$ and $\langle\mu_V\rangle_{50} = \pm 0.1\,\mathrm{mag\,arcsec}^{-2}$.

We also tested the implications of our estimated uncertainties on our results from Section 4.5.2, and applied the average systematic offsets in M_V, r_{50} and $\langle\mu_V\rangle_{50}$ between the models and the measured parameters of our LSB galaxy sample. In this case the number of LSB candidates in the considered parameter range of $M_V \leqslant -14\,\mathrm{mag}$ and $r_{50} \geqslant 2\,\mathrm{kpc}$ would increase to 25 candidates in the Perseus cluster core, but still only two LSB candidates would have sizes larger than $r_{50} \geqslant 3\,\mathrm{kpc}$. Thus, while the number of LSB candidates would now be significantly higher in Perseus compared to the number of LSB candidates in the same parameter range in the Coma cluster core, the conclusion of only finding very few large LSB galaxy candidates in the cluster core would remain unchanged.

Since the core regions of massive clusters are characterised by a particularly high density of galaxies, one possible concern is that this may have influenced our ability of detecting large LSB galaxy candidates with $r_{50} \geqslant 3\,\mathrm{kpc}$. Our tests with the inserted LSB galaxy models indicate, however, that we are in principle able to detect objects with $r_{50} > 3\,\mathrm{kpc}$ in the surface brightness range $\langle\mu_V\rangle_{50} < 27\,\mathrm{mag\,arcsec}^{-2}$ in our data, if these were present (see Section 4.3). Nevertheless we might have missed objects in close vicinity to bright cluster galaxies or foreground stars, although we modelled and subtracted the light profile of the latter in most cases. The apparent absence of LSB candidates in regions around bright sources in Fig. 4.5 might therefore not be a real effect.

Due to the location of the Perseus cluster at low Galactic latitude ($l = 13°$) we cannot exclude the presence of diffuse emission from Galactic cirrus in our data. Cirrus is often visible in deep wide-field imaging data, and the resulting structures can be very similar in appearance to stellar tidal streams (cf. Miville-Deschênes et al. 2016). We therefore compared our candidates with possible streams to the *WISE*[14] 12μm data that trace Galactic cirrus, in order to search for possible counterparts in the 12μm emission. Fig. 4.8 shows our data in comparison to both the original *WISE* data with 6 arcsec resolution, as well as to the reprocessed data from Meisner and Finkbeiner (2014) with 15 arcsec resolution that were cleaned from point sources. We clearly see diffuse emission in the 12μm data at the position of Perseus. However, we are not able to identify obvious structures in the *WISE* maps that would match to the candidates with possible streams we observe in our data, due to the insufficient resolution of the latter. Therefore, we neither can confirm nor exclude that the nature of these structures may be cirrus emission rather than LSB galaxy candidates with tidal streams.

---

14 *Wide-field Infrared Survey Explorer* (Wright et al. 2010)
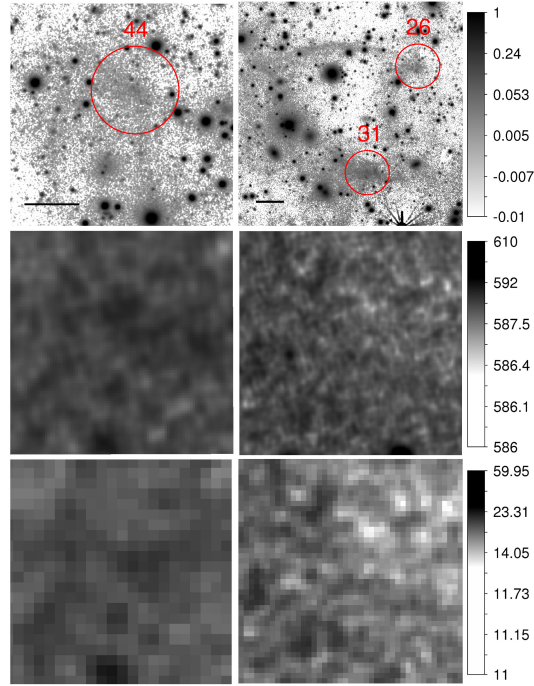
FIGURE 4.8:   Objects from our sample that could be either LSB galaxies with possible tidal streams or cirrus emission. The top panels show the objects in our smoothed data, marked with red circles. The four lower panels show the corresponding regions in the *WISE* 12μm intensity maps that trace Galactic cirrus. The original *WISE* intensity maps with 6 arcsec resolution are displayed in the middle panels, the reprocessed *WISE* intensity maps with 15 arcsec resolution that were cleaned from point sources are shown in the bottom panels. The height and width of the cutout regions is 2 arcmin ($\widehat{=}$ 41 kpc) in the left-hand panels and 4 arcmin ($\widehat{=}$ 81 kpc) in the right-hand panels, respectively. The black bar in the images in the top panels denotes a length of 10 kpc. We see no obvious correspondence between the structures observed in our data and the 12μm emission. We therefore cannot draw any firm conclusions on the nature of these structures.

4.6 DISCUSSION

We detected a large number of 89 faint LSB galaxy candidates with $\langle\mu_V\rangle_{50} \geqslant$ 24.8 mag arcsec^{-2} in the Perseus cluster core. It is interesting to note that all but one candidate have $r_{50} < 3$ kpc. We thus speculate that LSB galaxies with larger sizes cannot survive the strong tidal forces in the core region and possibly have lost already a considerable amount of their dark matter content. This observation is consistent with the study of van der Burg et al. (2016) who found a decreasing number density of faint LSB galaxy candidates in the cores of galaxy clusters. Also, the numerical simulations of Yozin and Bekki (2015) predicted the disruption of LSB galaxies orbiting close to the cluster centre.

The effect of tides on LSB galaxies in galaxy clusters is possibly also reflected in the radial number density distribution we observe for our sample. The nearly constant projected number density for cluster-centric distances $r \geqslant 100$ kpc implies that the three-dimensional distribution should actually increase with distance from the cluster centre. This may be a further argument that LSB galaxies are depleted in the cluster core region due to tidal disruption. Very close to the cluster centre, for cluster-centric distances $r < 100$ kpc, the number density drops, with only two LSB candidates from our sample being located in this region. Here tidal effects from the central cluster galaxy NGC 1275 may become apparent (cf. Mathews et al.

2006, fig. 1). For example, the slightly more compact peculiar galaxy SA 0426-002 ($M_B = -16.3$ mag, $r_{50} = 2.1$ kpc), being located only ~ 30 kpc from the cluster centre, shows signs of being tidally disturbed (see Fig. 4.5, top left panel). Also, in the Fornax cluster core a drop in the number density profile of faint LSB candidates is seen within 180 kpc of the cluster centre (Venhola et al. 2017).

We can use the observed limit in r_{50} as a rough constraint on the dark matter content of the LSB candidates in the cluster centre (cf. Penny et al. 2009). The tidal radius R_{tidal} is given by

$$R_{tidal} = R_{peri} \left(\frac{M_{obj}}{M_{cl}(R_{peri})\,(3+e)} \right)^{1/3} , \tag{4.1}$$

with the pericentric distance R_{peri}, the total object mass M_{obj}, the cluster mass $M_{cl}(R_{peri})$ within R_{peri} and the eccentricity of the orbit e (King 1962). We find about 50 per cent of our sample (44 objects) at projected cluster-centric distances below 330 kpc. Assuming that this is representative of the orbital pericentre for at least a fraction of the population,[15] we estimate R_{tidal} for a typical LSB candidate of our sample with $M_V = -14$ mag and $R_{peri} = 330$ kpc, assuming an eccentric orbit with $e = 0.5$. We adopt the cluster mass profile from Mathews et al. (2006), where $M_{cl}(330\,\mathrm{kpc}) = 1.3 \times 10^{14}\,M_\odot$.

Assuming a galaxy without dark matter, and adopting a mass-to-light ratio of $M/L_V = 2$ for an old stellar population with subsolar metallicity (Bruzual and Charlot 2003), the mass of an object with $M_V = -14$ mag would be $M_{obj} = 7 \times 10^7\,M_\odot$ accordingly, resulting in a tidal radius of 1.8 kpc. This compares to a range of observed $r_{50} \simeq 1.0 - 2.5$ kpc for LSB candidates from our sample with $M_V \simeq -14$ mag. We note that we can generally probe our objects out to more than one half-light radius in our data, thus the tidal radius would be within the observed stellar extent. However, since most objects from our sample do not show obvious signs of current disruption, we suspect that they may contain additional mass in order to prevent tidal disruption.

If we assume a higher mass-to-light ratio of $M/L_V = 10$, the tidal radius of the same object would increase to 2.9 kpc. For $M/L_V = 100$ the tidal radius would be $R_{tidal} = 6.2$ kpc, and for $M/L_V = 1000$ we derive $R_{tidal} = 13.3$ kpc. For M/L_V close to 1000 the tidal radius is significantly larger than the observed range of half-light radii. If such a high mass-to-light ratio would be reached within the tidal radius, we might expect to find a higher number of galaxies with $r_{50} \gtrsim 3$ kpc in the cluster core. However, *for $M/L_V \lesssim 100$, the tidal radius would be on the order of* 1–$2\,r_{50}$, which is also consistent with the mass-to-light ratios derived from dynamical measurements of similar galaxies. For example, van Dokkum et al. (2016) found a mass-to-light ratio of ~ 50 within one half-light radius for one LSB galaxy in the Coma cluster ($M_V = -16.1$ mag, $r_{50} = 4.3$ kpc),[16] and Beasley et al. (2016) derived a mass-to-light ratio of ~ 100 within one half-light radius for one LSB galaxy in Virgo ($M_g = -13.3$ mag, $r_{50} = 2.8$ kpc).[17] We note that based on similar analytical arguments as described above van Dokkum et al. (2015a) also estimated a dark matter fraction of $\gtrsim 100$ per cent within an assumed tidal radius of 6 kpc for a sample of faint LSB candidates within the core region of the Coma cluster.

---

15 While on the one hand, most objects are likely to be situated somewhat further away from the centre than the projected value suggests, on the other hand, it is also likely that their orbital pericentre is located further inwards from their current location.

16 Based on stellar dynamics of the galaxy.

17 Based on GC system dynamics of the galaxy.

While the above approach gives an estimate of the radius beyond which material is likely going to be stripped, another approach to estimate the effect of tides on galaxies in clusters is to compare the density of the tidal field to the density of the orbiting galaxy (cf. Gnedin 2003a). The density of the tidal field ρ_{tidal} is given by Poisson's equation, $\rho_{tidal} = F_{tidal}/(4\pi G)$, where F_{tidal} is the trace of the tidal tensor. We consider the extended mass distribution of the cluster[18] and approximate the strength of the tidal force at a given cluster-centric distance r_0 as $F_{tidal} = |dg(r)/dr|_{r_0}$, where $g(r)$ is the gravitational acceleration exerted by the mass of the cluster. For $g(r)$ we adopt the gravitational acceleration due to the Perseus cluster potential given by Mathews et al. (2006), where we only consider the contribution of the NFW-profile, which is the dominant component at cluster-centric distances $r \gtrsim 10\,kpc$. We approximate the average density of the orbiting galaxy, assuming spherical symmetry, as $\rho_{gal} = M_{gal}(R)/(4\pi R^3/3)$, where $M_{gal}(R)$ is the total mass of the galaxy within a radius R. Requiring that the density of the galaxy is larger than the tidal density to prevent its disruption, the limiting radius R_{lim} is given as

$$R_{lim} \geqslant \sqrt[3]{\frac{3GM_{gal}(R)}{|dg(r)/dr|_{r_0}}} \tag{4.2}$$

Considering again a typical galaxy from our sample, with $M_V = -14\,mag$ at a cluster-centric distance $r_0 = 330\,kpc$, we find $R_{lim} = 0.8\,kpc$ for $M/L_V = 2$, $R_{lim} = 1.3\,kpc$ for $M/L_V = 10$, $R_{lim} = 2.8\,kpc$ for $M/L_V = 100$ and $R_{lim} = 6.1\,kpc$ for $M/L_V = 1000$. Thus, in comparison to the tidal radius derived with the first approach, the limiting radius obtained with the second approach is a factor of two smaller. If we assume that $M/L_V = 100$ would be characteristic for a considerable fraction of our sample, then the limiting radius would be on the order of only $1\,r_{50}$.

Does this imply that a few of the largest LSB candidates in the Perseus cluster core should be in process of tidal disruption right now? – We do identify three LSB candidates in Perseus that show possible signs of disruption (see panels on the right-hand side in Fig. 4.5). Candidate 44 appears to be embedded in stream like filaments. It is, however, unclear whether we see here still a bound galaxy or rather a remnant core of a stream. Candidates 26 and 31 seem to be connected via an arc-like tidal stream. This could point to a low-velocity interaction between those two candidates, since such interactions produce the most severe mass-loss. The convex shape of the stream with respect to the cluster centre might suggest that these two objects are not in orbit around the cluster centre, but instead still bound to a possibly recently accreted subgroup of galaxies. The association with a subgroup could be supported by the observation that these three candidates, together with the candidate of brighter surface brightness with tidal tails (see Fig. 4.5, lower left panel), are located closely together in a region south–west of the cluster centre, within a cluster-centric distance range of 300–400 kpc. It is also interesting to note that Merritt et al. (2016) found a generally more complex and distorted morphology for LSB candidates in galaxy groups than in galaxy clusters, indicating that the group environment may play an important role in shaping galaxies of low stellar density.

The comparison to the LSB galaxy samples in Coma (van Dokkum et al. 2015a; Yagi et al. 2016) showed that both cluster cores hold a similar number of faint LSB candidates with $r_{50} \geqslant 2\,kpc$ and $M_V \leqslant -14\,mag$. Based on the 1.5 times lower

---

18 Unlike in the first approach, where a point-mass approximation was used.

cluster mass of Perseus[19], we would expect a somewhat lower number of all galaxy types in Perseus. However, with regard to the density in the cluster core, both clusters reach a comparable galaxy surface number density within 0.5 Mpc (Weinmann et al. 2011), thus causing comparable disruptive forces in both cluster cores. Therefore, according to the cluster mass and density, we would expect a similar or even lower number of LSB galaxies of such large size in Perseus, which is in agreement with our observations.

One important question to investigate would be whether there exists a possible evolutionary link between LSB galaxies that are red and quiescent and those that are blue and star-forming. The cosmological simulations of Di Cintio et al. (2017) suggest that faint LSB galaxies with large sizes may form as initially gas-rich star-forming systems in low-density environments. In this context, the quenching of star formation should be related to external processes, like, e.g., ram pressure stripping. Román and Trujillo (2017) examined a sample of faint LSB candidates in group environments. Since they found the red LSB candidates closer to the respective group's centre than the blue systems this could imply that the group environment was efficient in removing the gas that fuels star formation. This is also seen among the dwarf galaxies of the Local Group, which show a pronounced morphology – gas content – distance relation (see Grebel et al. 2003). However, a few quiescent and gas-poor LSB galaxies of dwarf luminosity are also observed in isolation (e.g. Papastergis et al. 2017), which would not fit into this scenario. An essential aspect would be to understand whether the physical processes governing the formation and evolution of LSB galaxies are controlled by stellar density or by stellar mass. The latter could possibly explain the observed wide variety of LSB galaxy properties from low-mass dSphs to massive LSB disc galaxies.

4.7 SUMMARY AND CONCLUSIONS

We obtained deep V-band imaging data under good seeing conditions of the central regions of Perseus with PFIP at the *WHT* that we used to search for faint LSB galaxies in the surface brightness range of the so-called 'ultra-diffuse galaxies'. We detected an abundant population of 89 faint LSB galaxy candidates for which we performed photometry and derived basic structural parameters. Our sample is characterised by mean effective surface brightnesses $24.8 \leqslant \langle \mu_V \rangle_{50} \leqslant 27.1$ mag arcsec^{-2}, total magnitudes $-11.8 \geqslant M_V \geqslant -15.5$ mag and half-light radii $0.7 \leqslant r_{50} \leqslant 4.1$ kpc. A comparison to overlapping *HST*/ACS imaging data indicates that the sample is relatively uncontaminated by background objects.

We find good evidence for tidal disruption leading to a deficiency of LSB galaxy candidates in the central regions of the cluster. This is indicated by a constant observed number density beyond cluster-centric distances of 100 kpc and the lack of very large LSB candidates with $r_{50} \geqslant 3$ kpc except for one object. However, only a few candidates show structural evidence of ongoing tidal disruption. If LSB systems are to remain gravitationally bound in the cluster core, the density limits set by the Perseus cluster tidal field require that they have high M/L values of about 100, assuming a standard model for gravity.

---

19 Assuming $M_{\mathrm{vir,Coma}} = 1.3 \times 10^{15}\,M_\odot$ (Łokas and Mamon 2003) and $M_{\mathrm{vir,Perseus}} = 8.5 \times 10^{14}\,M_\odot$ (Mathews et al. 2006).

In comparison to the Coma cluster – with its comparable central density to Perseus – we find that our sample statistically resembles the LSB galaxy population in the central regions of Coma. Given the same dearth of large objects with $r_{50} \geqslant 3\,\mathrm{kpc}$ in both cluster cores we conclude that these cannot survive the strong tides in the centres of massive clusters.

5

THE FAINT LOW-MASS GALAXY CONTENT OF THE PERSEUS CLUSTER CORE

ABSTRACT

We aim to shed light on the assembly history of the Perseus galaxy cluster core through a study of the distribution and properties of its low-mass galaxy population. We therefore established a catalogue of faint galaxies in the direction of the Perseus cluster and defined a sample of low-mass candidates using a criterion based on the well-defined relation between Sérsic index and luminosity. Our sample of over 2000 low-mass galaxy candidates spans a parameter range of absolute V-band magnitudes -9.55 to -19.23 mag, half-light radii 47-5164 pc and effective surface brightnesses 17.35-26.48 mag arcsec^{-2}. In the magnitude–size diagram the Perseus low-mass galaxy candidates largely overlap with the parameters of low-mass galaxies in the Virgo cluster. Our sample includes a few sources in the parameter range of compact elliptical galaxies, and sources that fall into the sparsely populated magnitude–size parameter space between the sequences formed by compact stellar systems and dwarf elliptical galaxies. The projected spatial distribution of our sample does not appear to be centrally concentrated. Instead, we detected an overdensity of low-mass galaxy candidates to the west of the cluster centre. If indeed the majority of our candidates were cluster members, this could indicate a recent accretion event of substructure from the surroundings of the cluster.

5.1 INTRODUCTION

Galaxy clusters continuously accumulate matter from surrounding large-scale filaments in the form of individual galaxies or entire galaxy groups. Since galaxy clusters are dynamically young systems, with dynamical time scales on the order of 1 Gyr, many clusters show substructure in the distribution of their member galaxies indicating that they are not yet fully virialized (e.g. Geller and Beers 1982; Dressler and Shectman 1988; Drinkwater et al. 2001). Dwarf galaxies are the most abundant galaxy type in galaxy clusters. Since they are insensitive to dynamical friction, signatures of their infall and accretion history will still be imprinted in their spatial and velocity distribution after several gigayears (Vijayaraghavan et al. 2015). This makes them to ideal tracers of a cluster's dynamical history.

At the same time dwarf galaxies are valuable indicators to study the influence and strength of environmental processes acting in dense galaxy clusters. Due to their shallow gravitational potential, dwarf galaxies are expected to be very sensitive to external processes like the ram pressure exerted by the intracluster medium (Gunn and Gott 1972), or tidal interactions with the cluster potential or other cluster member galaxies ('galaxy harrassment', Moore et al. 1996, 1998). For example, cluster dwarf galaxies are observed to have very different properties compared to their counterparts in the field, with regard to their gas content, star formation activity, stellar structure and kinematic properties, which is often ascribed to environmental effects. Ultimately, constraining the environmental influence on the population of dwarf galaxies is very important in order to verify or falsify the currently proposed formation and evolutionary paths (also see Chapter 1, Section 1.4.3).

Dwarf galaxies have been and are being studied in great detail in the nearby Virgo and Fornax galaxy clusters, which are at a distance of about 16 and 20 Mpc, respectively. Pioneering work includes the early studies by Binggeli et al. (1985) in Virgo, and Ferguson (1989) in Fornax. Recent deep wide field imaging surveys of both clusters (Next Generation Virgo Cluster Survey (NGVS), Ferrarese et al. 2012; Fornax Deep Survey (FDS), Iodice et al. 2016) now allow to study the dwarf galaxy population to magnitudes and surface brightnesses in the regime of Local Group dwarf spheroidals (dSphs).

The Perseus galaxy cluster is another nearby rich galaxy cluster at a distance of ~ 70 Mpc. It is more massive than the Fornax and the Virgo cluster and, like Virgo, shows signs of not yet being dynamically relaxed. Thus, Perseus constitutes another unique environment to study galaxy evolution, with a possibly different environmental influence on its faint member galaxies. Nevertheless, Perseus has not yet been studied in a similar detail as Virgo or Fornax, due to its location at low galactic latitude, which involves significant Galactic foreground extinction. Perseus is partly covered by the Sloan Digital Sky Survey (SDSS, Ahn et al. 2012), but the data have a rather shallow depth and low resolution, not allowing to probe far into the dwarf galaxy luminosity and size regime. Deeper and higher resolution imaging studies of smaller parts of the cluster core region were conducted by Conselice et al. (2002, 2003), Penny et al. (2009) and De Rijcke et al. (2009) (also see Chapter 4, Section 4.1).

In this study we aim to establish a catalogue of low-mass galaxies in the Perseus cluster core region. We use our deep V-band imaging data of the cluster core obtained with the 4.2 m *William Herschel Telescope* (*WHT*) Prime Focus Imaging Platform (PFIP) described in Chapter 4. This catalogue will serve as a basis for subsequent studies on:

1. The Perseus cluster assembly history through the spatial distribution of dwarf galaxies and their possible association to subgroups that are still bound.

2. The environmental influence on the dwarf galaxy population in the dense cluster core region, which will be identified as possible perturbations of their stellar structure induced by gravitational interactions.

3. A thorough comparison of the Perseus cluster low-mass population to the populations reported in Virgo and Fornax.

This Chapter is structured as follows: In Section 5.2 we outline how we established the catalogue of faint galaxies in the direction of the Perseus cluster. In Section 5.3 we describe the photometric measurements of our working sample. We motivate our sample definition of Perseus cluster low-mass galaxy candidates in Section 5.4, and present their magnitude–size–surface brightness as well as their spatial distribution in Sections 5.5 and 5.6, respectively. We discuss our results in Section 5.7 and provide a summary of our main findings in Section 5.8. Throughout this Chapter we assume a distance of 72.3 Mpc to the Perseus cluster with a scale of 20.32 kpc arcmin^{-1} (Struble and Rood 1999, using the 'cosmology-corrected' quantities from NED with $H_0 = 73.0$ km s^{-1} Mpc^{-1}, $\Omega_{matter} = 0.27$, $\Omega_{vacuum} = 0.73$).
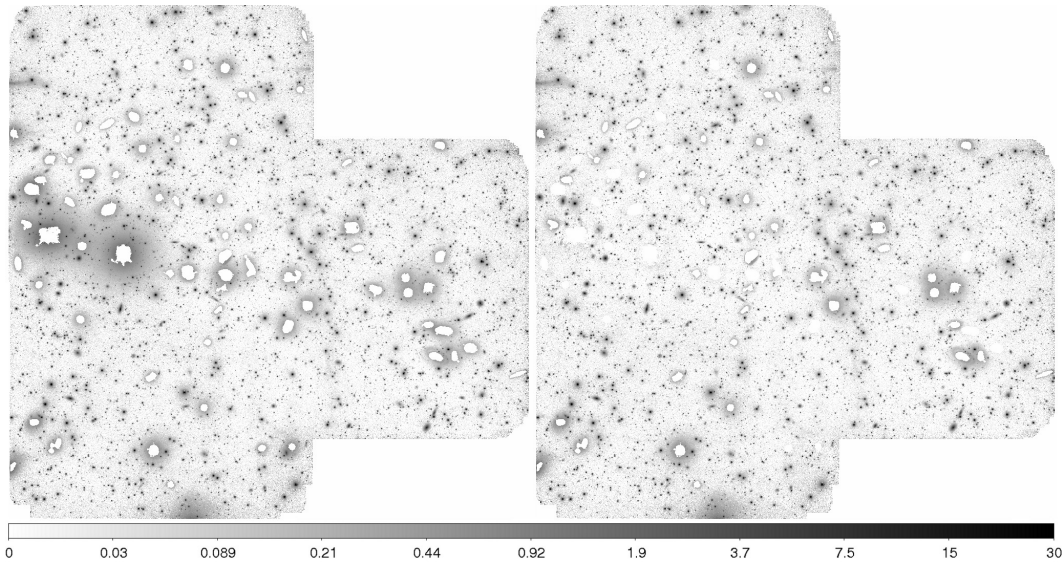
FIGURE 5.1:   Original and partly object-subtracted mosaic with overlayed mask. Left: Deep V-band mosaic of the Perseus cluster core. Right: Mosaic we used for the analysis where most extended high surface brightness sources were subtracted. On both mosaics we overlayed the mask indicating the inner regions of extended high surface brightness sources excluded from the analysis.

5.2   THE CATALOGUE

We established a catalogue of faint galaxies in the direction of Perseus based on source detection with SExtractor[1] (Bertin and Arnouts 1996). Performing an automated detection is essential in order to obtain a quantitative estimate of the completeness of the catalogue, which allows statistical analyses of, e.g., the spatial distribution or the luminosity function.

5.2.1   *Data*

We performed the source detection on our deep V-band mosaic of the Perseus cluster core, which we presented and characterised in Chapter 4. In particular, we used the mosaic were we previously fitted and subtracted most of the bright galaxies and stellar haloes (see Fig. 4.2, left-hand panel). We excluded the inner regions of all subtracted sources, since they often show pronounced residuals, as well as the bright centres of remaining sources that were not subtracted. We therefore masked all regions that were detected with SExtractor in the original Perseus mosaic when requiring a detection threshold above $5\,\sigma$ and more than $10\,000$ connected pixels. The masked regions on the original and partly object-subtracted mosaic are indicated in Fig. 5.1.

5.2.2   *Model galaxies*

We used a set of model galaxies inserted into our data to tailor the SExtractor parameter configuration especially to the detection of faint and extended low surface brightness sources. We generated a set of 69 model galaxies spanning the parameter range of low-mass galaxies from compact elliptical to faint low surface

---

1 SExtractor version 2.8.6

brightness galaxies, with absolute V-band magnitudes $M_V = -10$ to -19 mag, half-light radii $r_{50} = 0.2$-7.8 kpc, and effective surface brightnesses $\langle\mu_V\rangle_{50} = 16$-$27$ mag arcsec^{-2} at the distance of Perseus, and assuming an average extinction of $A_V = 0.5$ mag. In the following we give for all magnitudes and surface brightnesses the extinction-corrected values, and denote not-corrected magnitudes with the subscript 'V0'. We realized all model galaxies with a one-component Sérsic $n = 1$ profile and an ellipticity of $\epsilon = 0.1$, and convolved them with a Gaussian kernel adopting our average seeing point spread function (PSF) full width at half-maximum (FWHM) of 0.9 arcsec. For each model we generated one copy of our mosaic where we inserted about 80 duplicates, requiring that these do not overlap. The total number of models inserted into 69 different mosaic copies amounts to 5615.

5.2.3   SExtractor *parameter configuration*

The kind of sources that are detected by SExtractor can be controlled with the parameters DT and DMIN, specifying the minimum number of connected pixels (DMIN) above a certain detection threshold (DT) that are required to result in a detection. Our tests with the inserted model galaxies showed that with a parameter configuration of DT $= 1.3\,\sigma$ and DMIN $= 25$ pixels we are able to detect more than 90 per cent of all models with $\langle\mu_V\rangle_{50} \leqslant 24$ mag arcsec^{-2} (see Fig. 5.2). A lower detection threshold of DT $= 0.8\,\sigma$ with the same DMIN parameter improves the detection of fainter sources with $\langle\mu_V\rangle_{50} > 24$ mag arcsec^{-2}, albeit the number of false detections increases. For example, the haloes of diffuse sources, which were detected as single objects with the DT $= 1.3\,\sigma$ configuration, were frequently split up into multiple detections when using a detection threshold of DT $= 0.8\,\sigma$. Therefore we run SExtractor in two passes, first with a detection threshold of DT1 $= 1.3\,\sigma$, secondly using a threshold of DT2 $= 0.8\,\sigma$. We then merged the source catalogues of both runs, where we considered all sources from the first SExtractor run, and included additional sources from the second run that did not match to any source detected with DT1 within 1.5 arcsec. A comparison of the detection fractions of inserted models galaxies for both SExtractor runs is shown in Fig. 5.2. In both cases we run SExtractor with internal filtering prior to source detection, adopting a Gaussian filter with FWHM $= 4$ pixel, which is on the order of our average seeing PSF FWHM. We furthermore provided a weight image, generated from our data and described in Chapter 4, as an estimate for the variance across our mosaic.

The detection of faint sources close to or superimposed with brighter sources is very sensitive to the SExtractor deblending parameters as well as to the subtracted background map, which is internally generated by SExtractor. We found that a very low deblending contrast (DEBLEND_MINCONT $= 0.00001$) together with a high number of deblending thresholds (DEBLEND_NTHRESH $= 64$) significantly improves the SExtractor detection of superimposed faint sources. I.e. with this parameter setting a bright source is split up into a sufficient number of sub-detections, allowing to recognize superimposed faint sources as separate detections.

The properties of the subtracted SExtractor background map are regulated by the parameters BACK_SIZE, specifying the size of the region within which the mean background is estimated, and BACK_FILTERSIZE, denoting the width of the filter that is used to smooth the background map. When the size of the background box becomes comparable to the size of a certain object in the data, part of the object flux
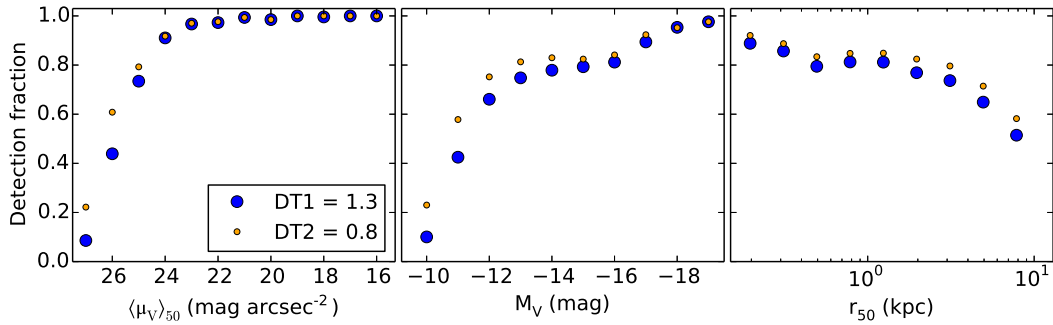
FIGURE 5.2:   Comparison of the detection fractions of the inserted model galaxies for the two considered SExtractor configurations with detection thresholds of DT1 = 1.3 σ and DT2 = 0.8 σ, respectively, as a function of intrinsic model parameters. All other SExtractor configuration parameters were adopted as given in Table 5.1. Models are considered as detected if their position matches to a SExtractor detection within 1.5 arcsec. We included only those models that do not overlap with the masked regions shown in Fig. 5.1.

TABLE 5.1:   Summary of the adopted SExtractor parameters for source detection. DT1 denotes the detection threshold used for the first, DT2 the threshold used for the second SExtractor run (see Section 5.2.3).

PARAMETER	VALUE
DT1	1.3
DT2	0.8
DMIN	25
FILTER	Gauss, FWHM = 4 pixel
DEBLEND_MINCONT	0.00001
DEBLEND_NTHRESH	64
BACK_SIZE	64
BACK_FILTERSIZE	3

will be incorporated in the background map and subtracted. We used a BACK_SIZE parameter of 64 pixel, corresponding to about 15 arcsec or 5 kpc at the distance of Perseus, with a BACK_FILTERSIZE of 3. This ensures to subtract most of the light from extended haloes of bright sources, enabling the detection of underlying faint sources, but at the same time leaves our sources of interest largely unaffected. We show the mosaic with the subtracted SExtractor generated background map in Fig. 5.3.

A summary of our adopted SExtractor parameters is given in Table 5.1. In total we detected 29 111 sources, from which 7899 sources were only detected with the DT1 = 0.8 σ SExtractor run. We excluded sources whose centres fall onto a masked region or are located at the edge of our mosaic with centres falling outside of the observed mosaic region.

5.2.4 *Separating galaxy- from star-like sources*

In order to distinguish between galaxy- and star-like sources, we used the SExtractor stellarity index CLASS_STAR. The index can take values between zero and one, where a value close to zero indicates an extended, galaxy-like source, and a value close to one a compact, star-like source. We found that the majority (97 per cent) of our inserted model galaxies with intrinsic $\langle \mu_V \rangle_{50} \geqslant 20 \, \mathrm{mag \, arcsec}^{-2}$ seems to
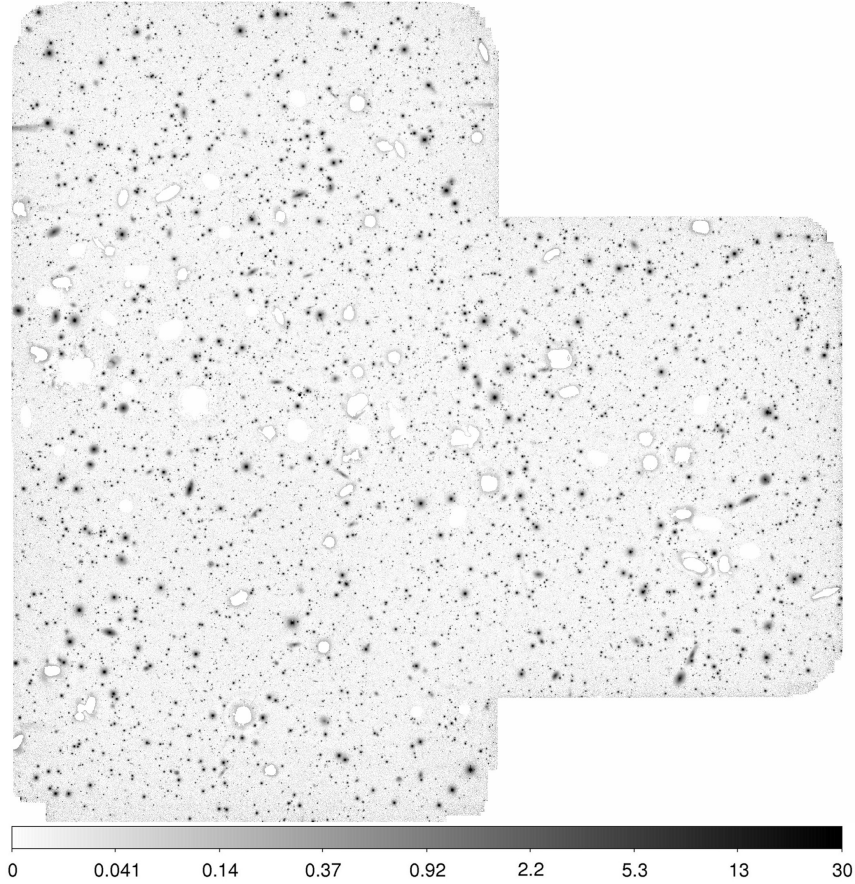
FIGURE 5.3:   Perseus mosaic with subtracted SExtractor background map. The SExtractor background map was generated on, and subtracted from the mosaic where most extended high surface brightness sources were previously subtracted. Overlayed is the mask indicating the regions we excluded from the analysis (also see Fig. 5.1).

be well described by CLASS_STAR $\leqslant$ 0.3. For the more compact model galaxies with intrinsic $\langle\mu_V\rangle_{50} < 20\,\mathrm{mag\,arcsec}^{-2}$ and $r_{50} > 300\,\mathrm{pc}$, 83 per cent have CLASS_STAR $\leqslant$ 0.8. For the smallest compact models, however, with $\langle\mu_V\rangle_{50} < 20\,\mathrm{mag\,arcsec}^{-2}$ and $r_{50} < 300\,\mathrm{pc}$ 74 per cent have CLASS_STAR > 0.8 and are indistinguishable from unresolved point sources.

In Fig. 5.4 we show the distribution of the CLASS_STAR parameter as a function of the maximal surface brightness $\mu_{V,max}$, measured by SExtractor, for the detected model galaxies as well as for real detected sources. The figure illustrates that $\mu_{V,max}$ can be used as a rough proxy to separate between bright and faint surface brightness sources at $\mu_{V,max} = 20\,\mathrm{mag\,arcsec}^{-2}$, for which we applied different CLASS_STAR parameter cuts. Based on the CLASS_STAR–$\mu_{V,max}$ distribution of our model galaxies, we considered all real detected sources with SExtractor output parameters in the regime $\mu_{V,max} \geqslant 20\,\mathrm{mag\,arcsec}^{-2}$ and CLASS_STAR $\leqslant 0.3$, as well as sources with $\mu_{V,max} < 20\,\mathrm{mag\,arcsec}^{-2}$ and CLASS_STAR $\leqslant 0.8$. This resulted in a total number of 13 132 sources we included in our catalogue, where 3980 sources were only detected by the SExtractor DT2 run.

5.2.5 *Working sample*

We cleaned our catalogue from sources with SExtractor flags > 3, only allowing unflagged sources, sources with close neighbours and / or sources that were
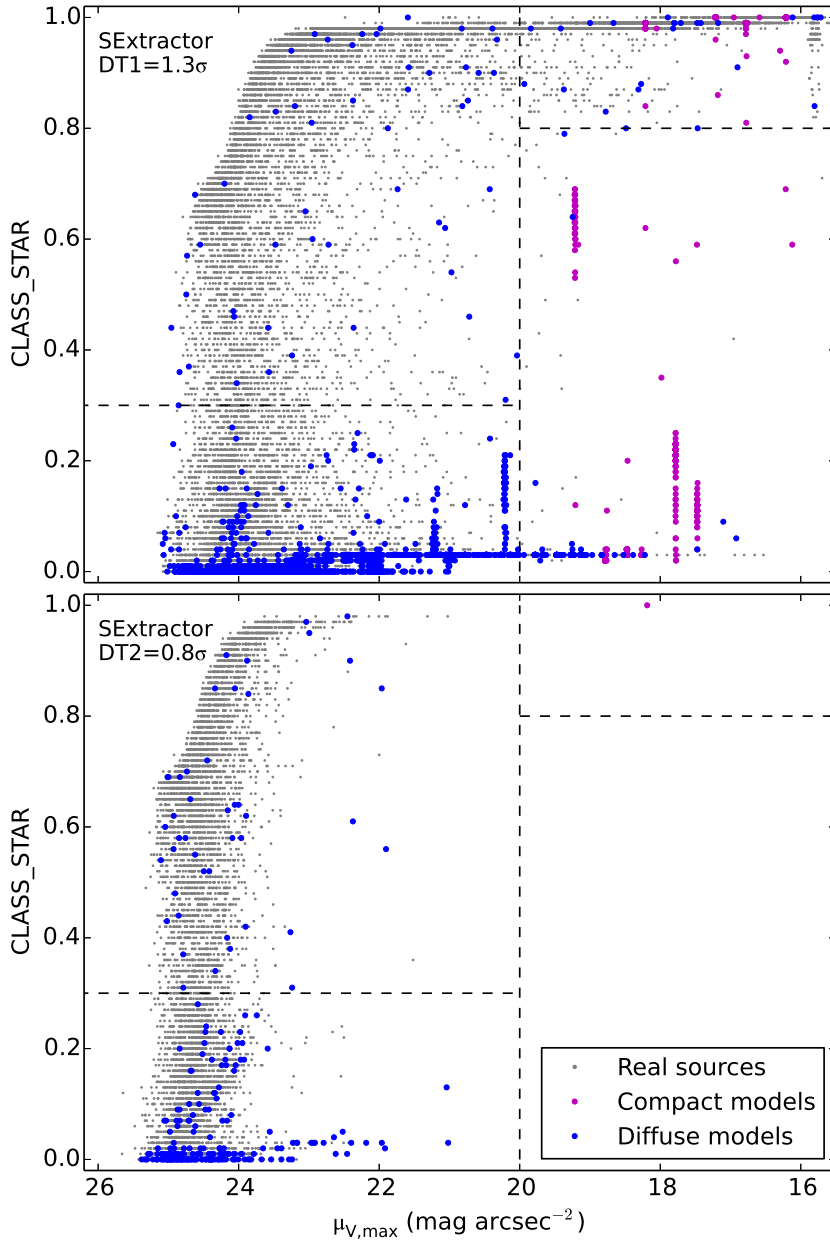
FIGURE 5.4: Separation between galaxy- and star-like sources. The figure shows the SExtractor parameter CLASS_STAR plotted versus the SExtractor parameter $\mu_{V,max}$ for detected model galaxies (coloured dots) and real detected sources (grey dots). Low CLASS_STAR values indicate extended, 'galaxy-like' sources, high values denote compact 'star-like' sources. The top panel shows the resulting detection from the SExtractor run with DT1= 1.3 σ, the bottom panel shows additional detections from the SExtractor DT2 = 0.8 σ run. The dashed lines indicate the CLASS_STAR parameter cuts below which we considered the detected sources for our catalogue. The cuts correspond to CLASS_STAR $\leqslant 0.3$ for sources with $\mu_{V,max} \geqslant 20 \, \mathrm{mag \, arcsec}^{-2}$, and CLASS_STAR $\leqslant 0.8$ for sources with $\mu_{V,max} < 20 \, \mathrm{mag \, arcsec}^{-2}$.

originally blended with another object. This excluded 15 sources from the catalogue. We note that none of the detected models has a SExtractor flag > 3. For the following analysis we concentrated on the brighter sources in the catalogue, since for fainter sources the photometry uncertainties and background contamination significantly increases. We therefore considered all sources with a SExtractor Petrosian magnitude $M_{V,petro} \leqslant -12\,mag$ (see Section 5.3), corresponding to the extinction-corrected absolute magnitude a source would have at the distance of the Perseus cluster. This resulted in a total number of 4085 sources, for which we derived photometry and structure parameters.

5.2.6 *Completeness*

Fig. 5.5 displays a completeness estimate of our catalogue based on the inserted model galaxies. Shown are the detection fractions, which are the ratios of the number of detected models to the total number of inserted models, as a function of the model input parameters. In the top panel, we show the detection fractions achieved with the combined SExtractor runs with DT1 $= 1.3\,\sigma$ and DT2 $= 0.8\,\sigma$. It can be seen that the completeness drops below 50 per cent for models with $\langle \mu_V \rangle_{50} = 27\,mag\,arcsec^{-2}$ and $M_V = -10\,mag$. The middle panel illustrates the detection fractions after having sorted out star-like sources by applying the CLASS_STAR parameter cut defined in Section 5.2.4. As a consequence, the detection fractions of compact models with $\langle \mu_V \rangle_{50} \leqslant 17\,mag\,arcsec^{-2}$ fall below 50 per cent. The bottom panel shows the detection fractions when considering only sources with SExtractor $M_{V,petro} \leqslant -12\,mag$. This results in a detection fraction lower than 50 per cent for models with intrinsic $M_V \geqslant -12\,mag$, since SExtractor tends to underestimate the magnitudes of the detected models.

5.3 PHOTOMETRY

Our aim was to derive structural parameters with GALFIT (Peng et al. 2002, 2010) for our working sample of 4085 sources brighter than $M_{V,petro} \leqslant -12\,mag$ as measured by SExtractor. We first derived Petrosian magnitudes (Petrosian 1976) and half-light radii, using a careful masking of contaminating neighbouring sources, which we later provided as first guess parameters for fitting with GALFIT. Thereby we looked through all sources to reject possible artefacts or too heavily contaminated sources.

5.3.1 *Petrosian magnitudes and half-light radii*

We first generated masks for each source from our working sample. Therefore we run SExtractor with a large BACK_SIZE of 256 pixels on our mosaic in order to mask and not to subtract the faint extended haloes of bright sources, but otherwise adopted the same settings as for our SExtractor run with DT1 (see Table 5.1). We then generated individual masks by unmasking the respective source.

For the photometric measurements we defined the Petrosian radius R_{petro} such that the Petrosian index $\eta(R_{petro}) = 1/0.3$, where η gives the ratio of the average intensity within R_{petro} to the isophotal intensity at R_{petro} (cf. Graham et al. 2005). We measured the total flux within a circular aperture of $1.5\,R_{petro}$ and derived the corresponding half-light radius from it. As a rough estimate for the local
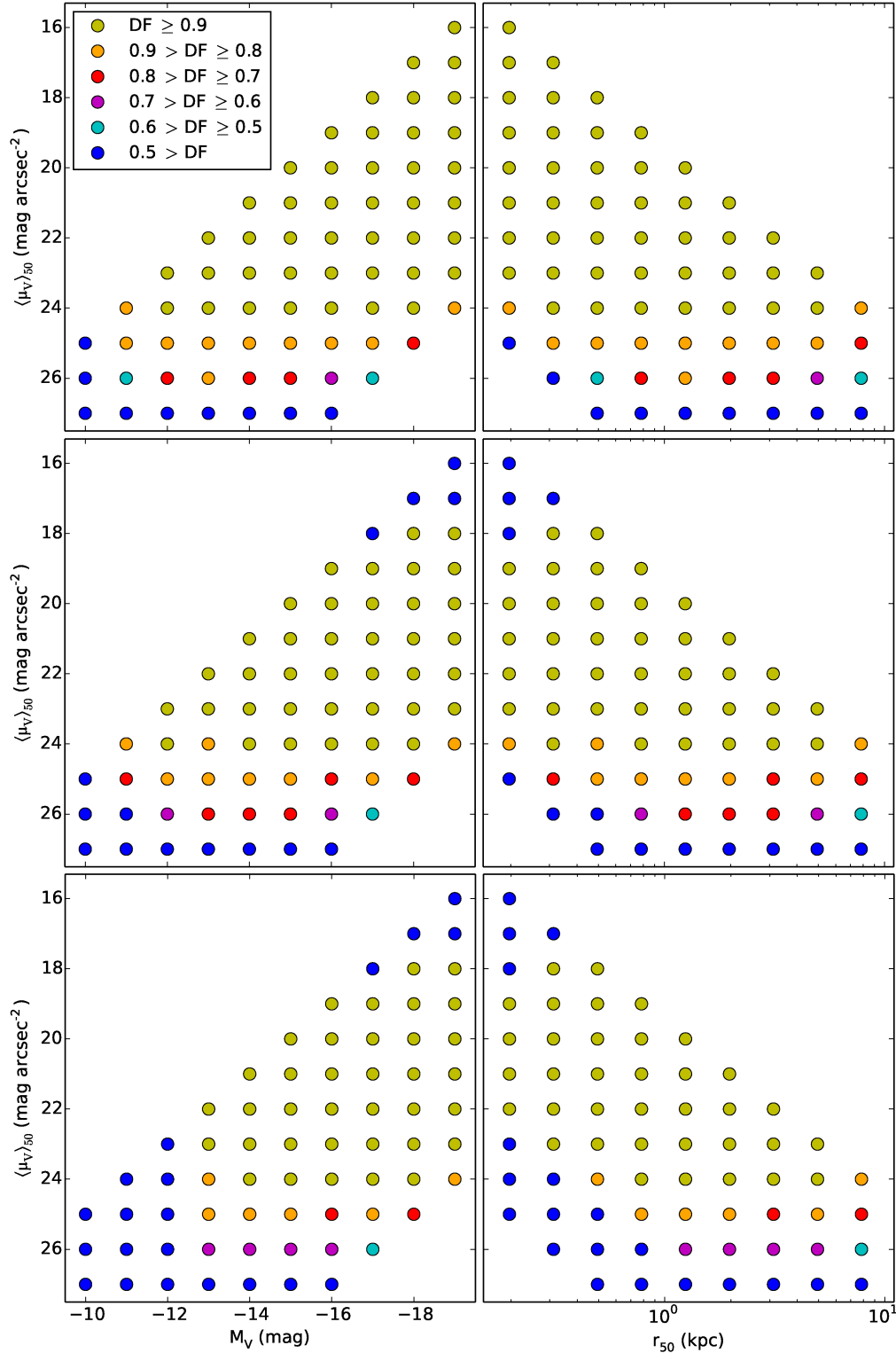
FIGURE 5.5: Completeness estimate based on detected model galaxies. The plots show the detection fractions (DF) of detected to inserted model galaxies as a function of model input parameters. In total 5615 models were inserted into 69 copies of the mosaic. We only considered inserted models that do not overlap with the mask shown in Figs 5.1 and 5.3. The top panels illustrate the completeness we achieve with our combined SEXTRACTOR runs with DT1 = 1.3 σ and DT1 = 0.8 σ. The middle panels show the resulting completeness after having sorted out star-like sources based on a SEXTRACTOR CLASS_STAR parameter cut. The bottom panels indicate the completeness when only considering the brighter detected sources with $M_{V,\text{petro}} \leqslant -12$ mag as measured by SEXTRACTOR.

background underlying a source we used the SExtractor generated background map with a large `BACK_SIZE = 256` pixels. We subsequently carefully visually investigated the measured apertures for each source individually in order to identify cases where the aperture is obviously too large with regard to the visible extent of the source. Most often problems arose due to incomplete masking. Occasionally the automatic unmasking of the source failed, such that large parts of the source were still masked. In other cases the apertures were often contaminated from flux of neighbouring source that required an extension of the mask.

We found about one quarter of our sample to be strongly contaminated due to the presence of bright extended neighbour sources, where even an adjustment of the mask would not bring any improvement of the photometric measurements. Due to the large number of affected sources it was not feasible to fit and subtract the neighbouring objects individually for each source. Instead we used a SExtractor-generated background map with a small `BACK_SIZE` parameter of 32 pixels, corresponding to 7.6 arcsec or 2.6 kpc, meaning that the outer haloes of extended sources were incorporated into the background map and were therefore subtracted (also see Section 5.2.3). The large majority of the contaminated sources appeared quite small in size, compared to the size of the background box, such that we do not expect a major influence on their photometric measurements. We nevertheless flagged each source where we subtracted the SExtractor background with `BACK_SIZE = 32` pixels. Among the contaminated sources we identified 52 visually more extended sources. For these we fitted and subtracted their respective neighbour galaxies or stars with IRAF[2] *ellipse* instead of using the SExtractor background map.

In the following cases we entirely excluded a source from any further analysis:

1. The source is heavily blended into another source where neither a larger mask nor a more radical SExtracor background subtraction would result in reliable photometric measurements. We note that the majority of sources in this category appeared small in size and compact, being possible interlopers suffering from wrong SExtractor photometry and / or `CLASS_STAR` measurements. In the case of extended galaxy-like sources we tried our best to fit and subtract the contaminating neighbouring source.

2. The source is barely visible in our data although having attributed a SExtractor magnitude of $M_{V,petro} \leqslant -12$ mag.

3. The source forms part of another source, i.e. stripped material or spiral arms.

4. The source is likely an artefact, resulting from reflections or stray light in the data.

We also sorted out multiple detections of single sources, that were split up into too many peaks by SExtractor.

In total we successfully derived Petrosian magnitudes and half-light radii for 3166 sources, where 952 of them rely on a subtracted SExtractor background with a back `BACK_SIZE = 32` pixels. For 21 sources we were not able to obtain reliable Petrosian photometry. Despite improved masking and / or background subtraction the Petrosian aperture still appeared much too large for the respective

---

2 IRAF is distributed by the National Optical Astronomy Observatory, which is operated by the Association of Universities for Research in Astronomy (AURA) under a cooperative agreement with the National Science Foundation.

source. We nevertheless processed these sources with GALFIT. We excluded 898 sources from the further analysis.

For the successfully analysed sources we estimated the Sérsic index from the measured concentration r_{90}/r_{50} based on the Petrosian photometry. We then matched the observed concentration to the concentration values calculated for analytic Sérsic profiles with $n = 0.5\text{-}4.0$ for our adopted Petrosian settings. For observed concentrations lower than calculated concentrations of the analytic $n = 0.5$ profile, we adopted a Sérsic index of $n = 0.5$. Similarly, for observed concentrations higher than the calculated concentration of a $n = 4$ profile, we adopted a value of $n = 4$.

5.3.2 GALFIT *structure parameters*

In order to run GALFIT with PSF deconvolution we first generated a PSF from our data using routines from the IRAF package DAOPHOT. We run SExtractor tuned to detect small and compact sources[3] and selected PSF star candidates by requiring that a source has CLASS_STAR > 0.9 and is not flagged. We furthermore rejected sources that are superimposed on bright extended sources by excluding all PSF star candidates that overlap with a mask generated with SExtractor[4]. This mask is much larger than the one shown in Figs 5.1 and 5.3 in order to yield the cleanest possible sample of PSF star candidates. We also excluded PSF star candidates that fall on very low signal-to-noise (S/N) regions in our mosaic, where the pixels have a weight lower than 200, corresponding to $\sigma \sim 0.07\,\text{ADU}$. We subsequently run the IRAF task *phot* to perform aperture photometry[5] and selected all stars brighter than $m_{V0} = 19\,\text{mag}$ that were not saturated. This resulted in a selection of 845 PSF stars in our mosaic, which we display in Fig. 5.6. The figure indicates a few outliers among the selected stars, with large FWHM values. A visual examination revealed that most of them are partly unresolved double sources. We therefore rejected sources with FWHM > 4.5 pixels. In addition, the figure shows a slight upward trend in FWHM towards brighter magnitudes. As a consequence we only considered stars with $m_{V0} > 16.5\,\text{mag}$. The final sample of PSF stars comprises 797 stars with an average FWHM = 3.86 pixels, as measured by SExtractor. We used this PSF star sample to construct a model PSF with the IRAF task *psf*, which consists out of an analytic component obtained by a fit to all the stars in the sample plus a lookup table quantifying the deviations of the analytic function from the empirical PSF.

We derived structure parameters with GALFIT for the 3187 sources that were not rejected after visual inspection, as discussed in Section 5.3.1. We run GALFIT for each source with PSF deconvolution, the previously generated object masks and a sigma image generated from the corresponding weight image of our mosaic, where $\sigma = 1/\sqrt{\text{weight}}$. We fitted each source with a one-component Sérsic profile and used the derived Petrosian magnitude, half-light radius, and estimated Sérsic index, as well as the SExtractor source position, axis-ratio and position angle as first guess parameters for GALFIT. We simultaneously fitted the sky component with GALFIT, which can account both for a background offset as well as for a

---

3 With the configuration DT = 2.5 σ, DMIN = 5 pixels, DEBLEND_NTHRESH = 32, DEBLEND_MINCONT = 0.01, BACK_SIZE = 64 and BACKFILTER_SIZE = 3.

4 Using the configuration DT = 5 σ, DMIN = 10000 pixels, DEBLEND_NTHRESH = 32, DEBLEND_MINCONT = 0.01, BACK_SIZE = 256 and BACKFILTER_SIZE = 3.

5 Using an aperture with a radius of $r = 5$ pixels ($\widehat{=} 1.2\,\text{arcsec}$) and a background annulus with a width of 5 pixels at $r = 15$ pixels.
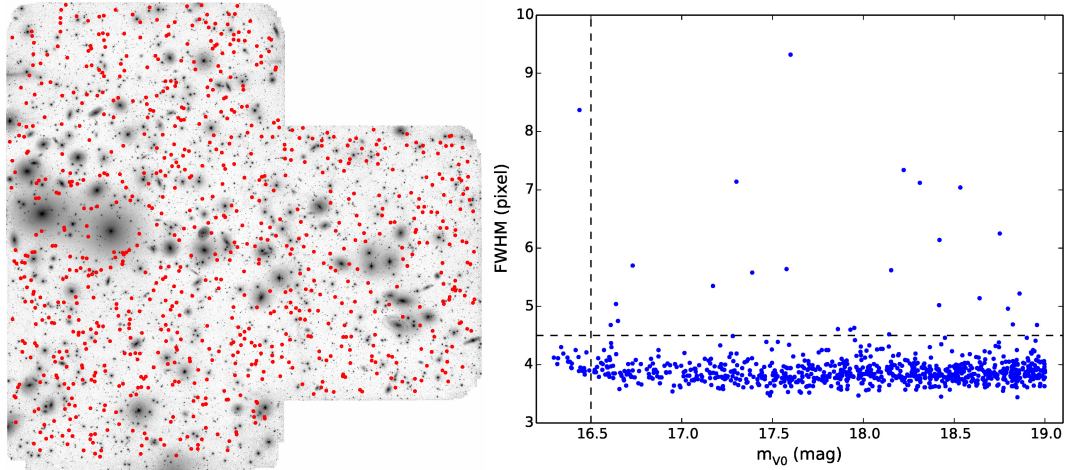
FIGURE 5.6:   PSF star candidates in the Perseus mosaic. The left panel shows the PSF star distribution in the mosaic. In the right panel the FWHM measured by SExtractor is plotted versus the apparent magnitude measured by IRAF *phot*. For the average stacked PSF used by GALFIT we considered all stars with FWHM < 4.5 pixels and $m_{V0} > 16.5$ mag, as indicated by the dashed lines.

gradient. For sources where we previously subtracted the SExtractor-generated background map with a `BACK_SIZE` of 32 pixels in order to eliminate contamination through extended haloes of bright neighbouring sources, we also adopted this background for GALFIT without further fitting of the sky component. For 20 sources we adopted the previously subtracted SExtractor `BACK_SIZE = 256` pixels background map for GALFIT, since simultaneously fitting the source and the background did not succeed. We specified the applied background subtraction method in Table 5.2.

In the first iteration with GALFIT we performed the Sérsic fit with seven free parameters[6], but constrained the Sérsic index to $n \leqslant 4$. We note that due to the limited resolution of our data we are not capable of reliably discriminating between a source with a Sérsic index around $n = 4$ and a larger value, due to the small change in the profile shape for large Sérsic n (see, e.g., Graham and Driver 2005, fig.1). Furthermore, numerical degeneracies between a high Sérsic index and the sky level were reported when simultaneously fitting the Sérsic and the sky component with GALFIT. We subsequently examined the fitted models, which we visually compared to the respective source, as well as the residual images. The vast majority of sources (over 2000) was successfully fitted by GALFIT. We indicate in Table 5.2 when we observed remaining residuals after the subtraction of the model, although the fitted model seemed to provide a good description of the source. In some cases we found that the model did not appropriately follow the shape and the visual extent of the fitted source, i.e. clear mismatches between the observed and fitted position angle and ellipticity occurred, or the fitted model was obviously too large. Other sources did not converge at all, mainly since the fitted axis-ratio or half-light radius fell below a critical value of 0.1 or 0.5 pixels, respectively.

In a second iteration with GALFIT we re-fitted all sources that did not succeed during the first iteration, as well as the sources with a constrained Sérsic index of $n = 4$. We aimed to stabilize the fit by holding the Sérsic index fixed, adopting the Sérsic index estimated from the concentration r_{90}/r_{50}. We again visually examined

---

6 This included the x-, y-position, magnitude, half-light radius, Sérsic index, axis-ratio and position angle.

the fitted models and the residual images. 867 sources were successfully fitted during this iteration. For 77 sources we adopted the former $n = 4$ solution, which yielded less pronounced residuals. For 227 sources that were either fitted with inappropriate models or did not converge, we run GALFIT in a third iteration, where we additionally held the x-, y-position fixed. This method succeeded for another 12 models. The remaining models did not converge since the half-light radius and / or the axis ratio was getting too small during the fit. We re-fitted the affected sources where we additionally held the axis-ratio fixed at 0.1, and / or the half-light radius at 0.5 pixels, which are the lowest possibly parameters accepted by GALFIT in order to fit a source. In cases where the source position derived by GALFIT during the third iteration deviated by more than 10 pixels from the position measured by SEXTRACTOR, we additionally held the x-, y-position fixed during the fit.

Of the 3187 sources processed with GALFIT, we were able to successfully derive structure parameters for 3044 of them. Among them are 120 sources with likely contaminated photometry due to the presence of very close neighbouring sources, and 30 likely double sources. 85 sources fitted with GALFIT had errors in m_V and / or $\langle \mu_V \rangle_{50}$ larger than 1 mag, which we excluded from the subsequent analysis.[7] We nevertheless provided their position in the photometry catalogue. For 45 sources it was not possibly to obtain a good fit with GALFIT but the derived Petrosian parameters seemed to provide a good estimate of the structural parameters. In most of these cases the affected sources were very faint, or showed very strong remaining residuals due to a very complex structure where a single Sérsic fit might not be a good approximation. For 13 sources we were neither able to obtain structure parameters with GALFIT nor with the Petrosian approach and we only included their position in the catalogue.

An excerpt of our photometry catalogue is shown in Table 5.2, including all 3187 sources for which we aimed to derive structural parameters. We also calculated the effective surface brightness $\langle \mu_V \rangle_{50}$ within the half-light radius from the measured parameters, and provided the Galactic foreground extinction A_V at the position of each sources using the IRSA Galactic Reddening and Extinction Calculator[8], with reddening maps from Schlafly and Finkbeiner (2011). We provided a 'processing flag', specifying whether a source was successfully fitted with GALFIT and whether parameters were holding fixed during the fit. A 'background flag' indicates whether we fitted and subtracted the underlying background with GALFIT, or used the background map generated by SEXTRACTOR. The 'quality flag' points out whether systematic residuals are visible after subtracting the model from the source, the photometry might be contaminated due to very close neighbours, or the source is a likely double source. The listed uncertainties are the statistical uncertainties given by GALFIT. The uncertainties in $\langle \mu_V \rangle_{50}$ were calculated from error propagation, accounting for uncertainties in m_V and r_{50}. Parameters that were held fixed during a fit have no error estimates, as well as sources where we adopted the Petrosian photometry. We only provided those measurements that have errors in m_V and / or $\langle \mu_V \rangle_{50}$ smaller than 1 mag.

---

7 These were almost exclusively very faint sources, with 70 of them having $M_V > -12$ mag.

8 We acknowledge the use of the NASA/ IPAC Infrared Science Archive, which is operated by the Jet Propulsion Laboratory, California Institute of Technology, under contract with the National Aeronautics and Space Administration.

TABLE 5.2: Photometry catalogue of 3187 faint sources in the direction of the Perseus cluster. The given m_{V0} and $\langle\mu_{V0}\rangle_{50}$ are not corrected for Galactic foreground extinction. Sources without photometric measurements correspond either to sources were the GALFIT solution yielded very large errors in m_{V0} and $\langle\mu_{V0}\rangle_{50}$ exceeding 1 mag, or to sources where it was not possible to obtain reliable GALFIT or Petrosian photometry. F1 corresponds to the 'processing flag'. F1 = 1: Source fitted with GALFIT with a Sérsic component with free parameters. F1 = 2: Source fitted with GALFIT with a Sérsic component with free parameters, but where the Sérsic index reached the constraint limit of $n = 4$. F1 = 3: Source fitted with GALFIT with a Sérsic component with fixed Sérsic n estimated from the concentration r_{90}/r_{50} but otherwise free parameters. F1 = 4: Source fitted with GALFIT with a Sérsic component with fixed Sérsic n and fixed x-, y-position. F1 = 5: Source fitted with GALFIT with a Sérsic component with fixed Sérsic n and fixed axis ratio of $b/a = 0.1$. F1 = 6: Source fitted with GALFIT with a Sérsic component with fixed Sérsic n and fixed $r_{50} = 0.5$ pixels (0.119 arcsec). F1 = 7: Source fitted with GALFIT with a Sérsic component with fixed Sérsic n, fixed $b/a = 0.1$ and fixed $r_{50} = 0.5$ pixels (0.119 arcsec). F1 = 8: Source fitted with GALFIT with a Sérsic component with fixed Sérsic n, fixed x- y-position and fixed $b/a = 0.1$. F1 = 9: Source fitted with GALFIT with a Sérsic component with fixed Sérsic n, fixed x- y-position, fixed $r_{50} = 0.5$ pixels (0.119) arcsec and fixed $b/a = 0.1$. F1 = 10: Only Petrosian photometry available. F2 corresponds to the 'quality flag'. F2 = 0: Good GALFIT photometry and no remaining residuals / Good Petrosian photometry. F2 = 1: Good GALFIT photometry but remaining residuals. F2 = 2: Photometry possibly contaminated. F2 = 3: Likely double source. F3 corresponds to the 'background flag'. F3 = 0: Background fitted by GALFIT. F3 = 1: Subtracted SExtractor background with BACK_SIZE = 256 pixels. F3 = 2: Subtracted SExtractor background with BACK_SIZE = 32 pixels.

ID	R.A. (J2000)	DEC. (J2000)	m_{V0} (mag)	r_{50} (arcsec)	$\langle\mu_{V0}\rangle_{50}$ (mag arcsec^{-2})	n (mag)	b/a -	θ -	A_V (deg)	F1 -	F2 -	F3 -
01	03 18 44.83	+41 11 49.7	21.22 ± 0.02	0.974 ± 0.031	21.91 ± 0.07	1.1 ± 0.2	0.31 ± 0.03	-73.5 ± 01.6	0.55	1	0	0
02	03 18 26.78	+41 11 49.2	19.81 ± 0.01	0.679 ± 0.010	20.37 ± 0.03	1.0 ± 0.1	0.58 ± 0.01	55.3 ± 01.3	0.56	1	1	1
03	03 19 51.14	+41 11 44.6	–	–	–	–	–	–	–	–	–	–
04	03 19 15.11	+41 46 05.3	20.98 ± 0.02	2.634 ± 0.076	24.14 ± 0.07	0.6 ± 0.0	0.42 ± 0.01	-52.1 ± 01.2	0.45	1	0	0
05	03 19 24.17	+41 46 08.4	20.82 ± 0.01	0.465 ± 0.013	20.71 ± 0.06	0.3 ± 0.1	0.67 ± 0.02	31.3 ± 02.9	0.45	1	0	0
06	03 18 55.50	+41 46 07.9	20.48 ± 0.01	0.838 ± 0.017	21.86 ± 0.05	1.1 ± 0.1	0.81 ± 0.02	-34.4 ± 04.0	0.46	1	0	0
07	03 19 28.24	+41 46 04.9	21.65 ± 0.06	2.234 ± 0.217	24.41 ± 0.22	1.4 ± 0.2	0.40 ± 0.03	41.1 ± 03.0	0.45	1	0	0
08	03 19 34.37	+41 46 04.4	22.59 ± 0.04	0.830 ± 0.089	23.96 ± 0.24	1.2	0.82 ± 0.09	-14.1 ± 21.2	0.45	3	0	0
09	03 18 29.11	+41 46 01.8	21.09 ± 0.01	1.138 ± 0.021	22.51 ± 0.04	0.7 ± 0.1	0.45 ± 0.01	-36.7 ± 01.1	0.44	1	0	0
10	03 18 48.76	+41 46 00.2	22.16 ± 0.03	0.866 ± 0.053	23.12 ± 0.13	1.3	0.51 ± 0.05	-50.7 ± 03.9	0.46	3	0	0
11	03 18 59.51	+41 45 57.4	20.21 ± 0.01	1.461 ± 0.025	22.66 ± 0.04	1.3 ± 0.0	0.71 ± 0.01	-07.4 ± 01.5	0.46	1	1	1
12	03 19 43.43	+41 45 56.3	22.38 ± 0.03	1.150 ± 0.047	24.04 ± 0.09	0.1 ± 0.1	0.56 ± 0.03	-04.5 ± 03.3	0.45	1	0	0

We show the magnitude–size distribution of all our sources with photometric measurements in Fig. 5.7, excluding the sources classified as likely double sources.
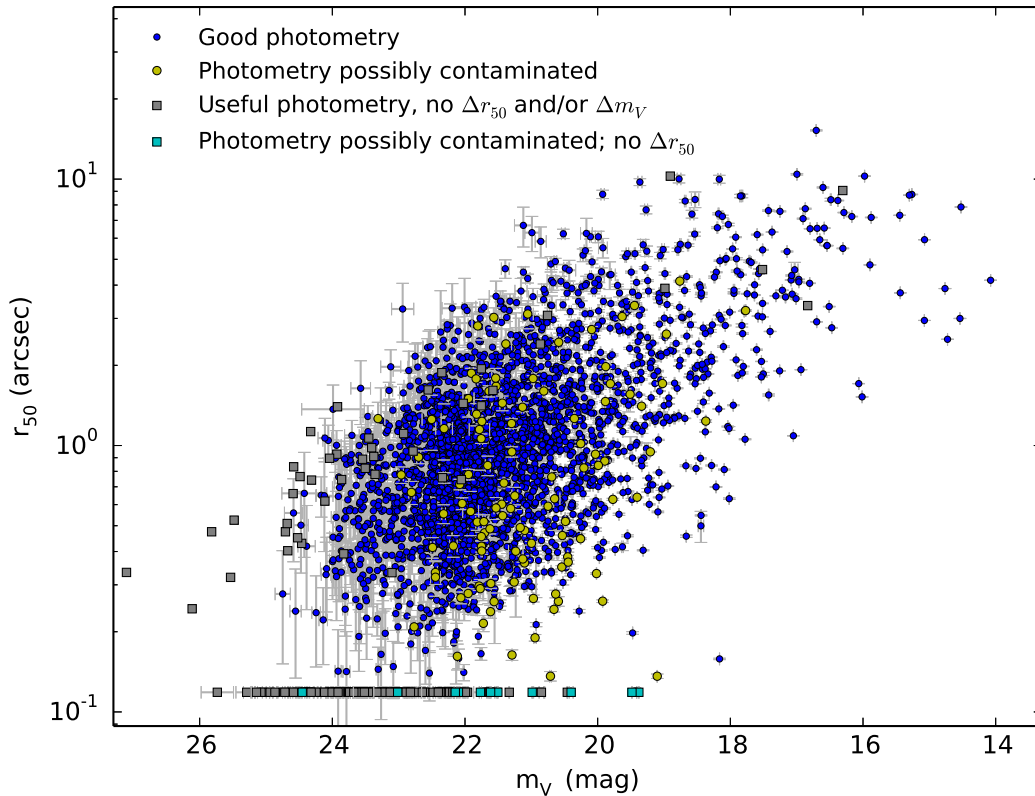
FIGURE 5.7:   Magnitude–size distribution of sources in our catalogue with photometric measurements. We excluded the sources that were classified as likely double sources. Sources without error-measurements in m_V and r_{50} are shown as square symbols, as well as sources that were fitted with fixed $r_{50} = 0.5$ pixels (0.12 arcsec). Sources with possibly contaminated photometry are shown in yellow. The plotted apparent magnitudes m_V are corrected for Galactic foreground extinction.

5.3.3 *Comparison of the GALFIT to the Petrosian magnitudes*

Fig. 5.8 shows a comparison of the magnitudes obtained with GALFIT and those derived from Petrosian photometry. We show the same sources as displayed in Fig. 5.7, but also include the likely double sources. It can be seen that the GALFIT and Petrosian magnitudes agree very well, without any obvious systematic offset. The three sources with larger magnitude offsets labelled with 'good photometry' are among the sources for which we were not able to obtain reliable Petrosian photometry (see Section 5.3.1). The average magnitude difference is -0.08 mag, with the GALFIT magnitudes being on average slightly brighter, and a standard deviation of 0.16 mag, when considering only sources with magnitude differences smaller than ± 1 mag.

We note that slight deviations between the Petrosian and GALFIT measurements are expected, since we measured the Petrosian magnitudes within circular apertures for all sources. This can result in too faint magnitudes for particularly elongated objects. Furthermore, the fraction of flux not captured by the $1.5\,R_{\texttt{petro}}$ aperture increases for flux profiles with higher Sérsic index. For our applied Petrosian settings this can amount to a flux deficit of the order of 0.5 mag for sources
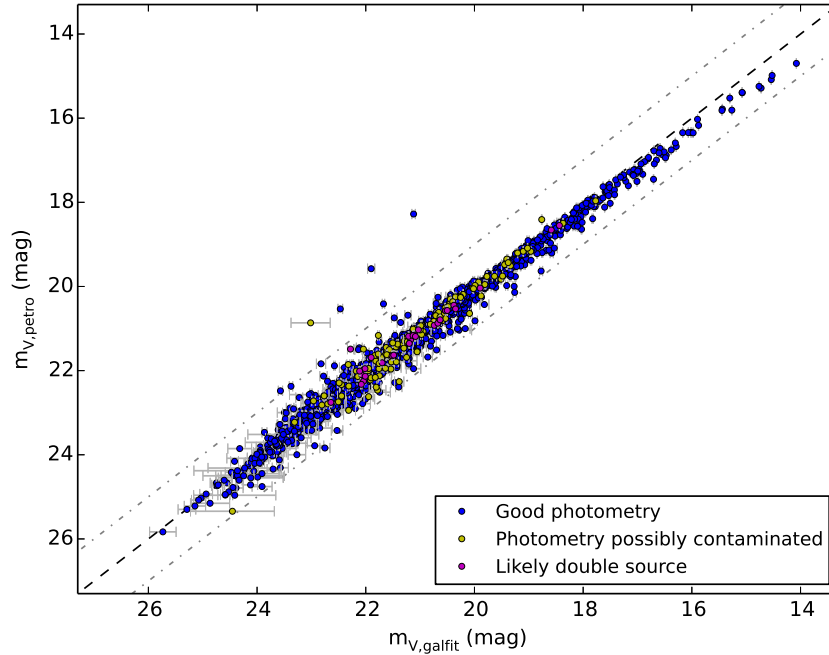
FIGURE 5.8:   Comparison of the magnitudes derived with GALFIT ($m_{V,galfit}$) and the Petrosian magnitudes ($m_{V,petro}$). We show the same sources as displayed in Fig. 5.7, but also include the likely double sources. The black dashed line shows $m_{V,petro} = m_{V,galfit}$, with the dash-dotted grey lines indicating the ± 1 mag interval.

with $n = 4$. We note that we did not find systematic offsets due to the applied background subtraction method, of either using the SEXTRACTOR background with BACK_SIZE $= 256$ pixel, or the background fitted with GALFIT.

5.4   SAMPLE DEFINITION OF LIKELY CLUSTER MEMBERS

The most reliable approach in order to define cluster membership of a galaxy is based on a spectroscopic redshift measurement. Due to the distance of Perseus at $\sim 70\,$Mpc and the faint surface brightnesses of the low-mass cluster population, spectroscopic measurements have so far been restricted almost exclusively to the brighter cluster galaxies. There are nevertheless various techniques proposed in the literature in order to select probable cluster members without redshift information (see, e.g., Conselice et al. 2002). These include, for example, colour-based membership criteria, a selection based on the morphological appearance, or a selection based on the concentration of a galaxy. In this work we established a membership criterion using the Sérsic index, which provides information on the galaxy concentration. It is known that there exists a well-defined relationship between the galaxy luminosity and the Sérsic index, where brighter galaxies have a higher Sérsic index (e.g. Jerjen and Binggeli 1997; Graham and Guzmán 2003; Gavazzi et al. 2005). Various studies (e.g. Misgeld et al. 2009; De Rijcke et al. 2009; Lieder et al. 2012) showed that this relation breaks down at faint magnitudes, where galaxies are commonly described by a close-to-exponential profile with $n \sim 1$.

Fig. 5.9 shows M_V versus n for our sample. We restricted the following analysis solely to catalogue objects with measured errors in m_V and r_{50} (this selection corresponds to sources with blue and yellow symbols in Figs 5.7 and 5.8). We overplotted the M_V–n relation found by Graham and Guzmán (2003) in the magnitude
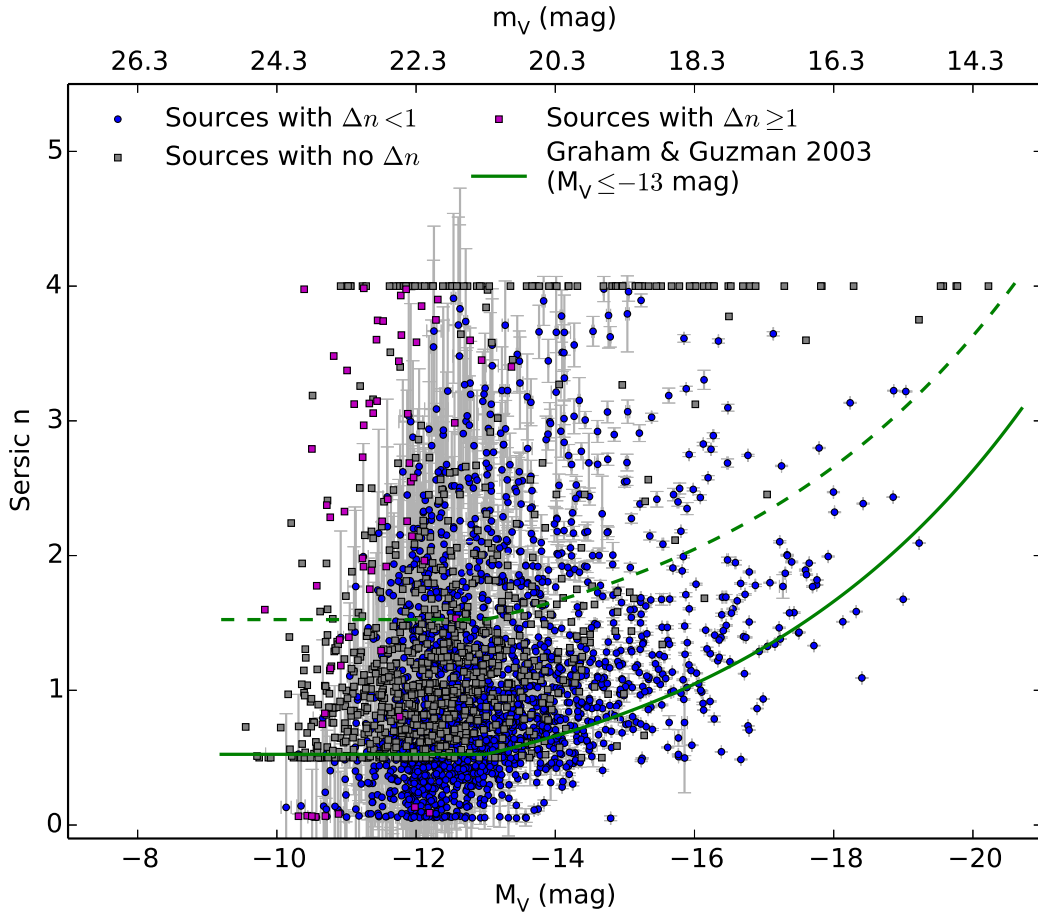
FIGURE 5.9:   Cluster membership criterion based on the M_V–n relation. We only show sources from our catalogue with available errors in m_V and r_{50}. Sources with errors in Sérsic n exceeding 1 and without error measurements in n are plotted as pink and grey square symbols, respectively. The solid green curve shows the M_V - n relation from Graham and Guzmán (2003) for $M_V \leqslant -13$ mag. For fainter magnitudes we adopted the value of n at $M_V = -13$ mag. We considered all sources with Sérsic n values smaller than $n_{lim} + 1$ (dashed green curve) in our sample of Perseus cluster low-mass galaxy candidates (see Section 5.4), where n_{lim} denotes the M_V–n relation. We note that the limit at $n = 0.5$ and $n = 4$ for sources fitted with a fixed Sérsic index (corresponding to the sources marked with grey squares) arises due to our adopted constraint for the Sérsic index estimated from the concentration r_{90}/r_{50} (also see Section 5.3.1).

regime of $M_V \leqslant -13$ mag, and adopted the value of n at $M_V = -13$ mag at fainter magnitudes. It can be seen that many sources in the faint magnitude regime are characterised by high Sérsic n values. These might be galaxies with bright absolute magnitudes that are located in the background of the Perseus cluster. We thus defined a membership criterion where we considered all sources with Sérsic n values smaller than $n_{lim} + 1$, where n_{lim} denotes the M_V–n relation shown in Fig. 5.9.

Weinmann et al. (2011) performed a statistical correction of contaminating background galaxies for their sample of brighter low-mass galaxies in the direction of Perseus. Based on a measurement of the radial galaxy number density profile out to a cluster-centric distance of ~ 3 Mpc, they found a statistical background number density of 45 Mpc^{-2} for galaxies in the magnitude range $-19.0 \leqslant M_r \leqslant -16.7$ mag. We compared this estimate to the difference in the number density profile of our
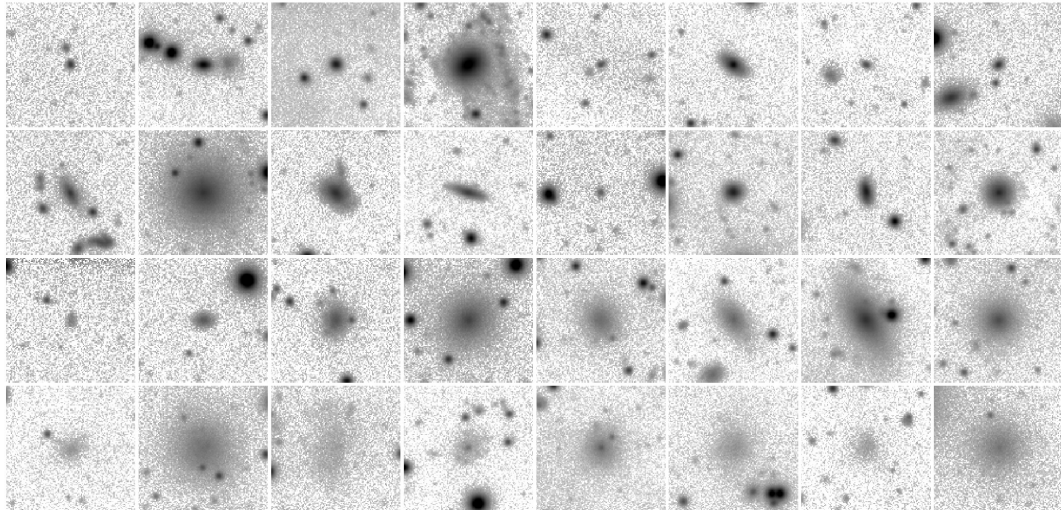
FIGURE 5.10:   Perseus cluster LMG candidates. Illustrated are sources from our catalogue that have a Sérsic index below the limit given in Section 5.4. The sources displayed in the first row have $\langle\mu_V\rangle_{50} \leqslant 20\,\mathrm{mag\,arcsec}^{-2}$, the sources shown in the second row have $20 < \langle\mu_V\rangle_{50} \leqslant 22\,\mathrm{mag\,arcsec}^{-2}$, the sources in the third row have $22 < \langle\mu_V\rangle_{50} \leqslant 24\,\mathrm{mag\,arcsec}^{-2}$ and the sources in the bottom row have $\langle\mu_V\rangle_{50} \geqslant 24\,\mathrm{mag\,arcsec}^{-2}$. Shown are the sources with IDs 57, 119, 1238, 1243, 2542, 2608, 2895, 2923, 64, 71, 117, 219, 752, 787, 821, 1214, 12, 36, 53, 62, 546, 590, 595, 969, 166, 202, 279, 959, 1048, 1285, 2636, 2756. The single panels have a height and width of 29 arcsec and are displayed with the same contrast.

sample in the same magnitude range, before and after applying the Sérsic n cut. We found an average difference in the radial number density of $58\,\mathrm{Mpc}^{-2}$ and $39\,\mathrm{Mpc}^{-2}$ for cluster-centric distances at $0 - 300\,\mathrm{kpc}$ and $300 - 600\,\mathrm{kpc}$, respectively. Thus, our applied Sérsic n cut seems to provide a reasonable estimate on the number of likely background galaxies, at least for the brighter sources in our sample. In the following we will refer to sources from our catalogue fulfilling the Sérsic criterion to Perseus cluster low-mass galaxy (LMG) candidates. In Fig. 5.10 we display some of the sources.

5.5   MAGNITUDE–SIZE–SURFACE BRIGHTNESS DISTRIBUTION

In Fig. 5.11 we show the magnitude–size–surface brightness distribution of the Perseus LMG candidate sample. For comparison we also include high- and low-mass galaxies from the Virgo cluster (compilation of Lisker et al. 2013; based on the Virgo Cluster Catalogue (VCC), Binggeli et al. 1985), faint Virgo dSphs (Lieder et al. 2012), dSphs from the Local Group (McConnachie 2012), as well as compact stellar systems from various nearby galaxy groups and clusters (compilation of Norris et al. 2014). We also show the Perseus cluster faint low surface brightness galaxy candidates that we visually identified in Chapter 4 and that were not detected in this study.[9]

Our sample of Perseus galaxy candidates spans a parameter range of $-9.55 \geqslant M_V \geqslant -19.23\,\mathrm{mag}$, $47 \leqslant r_{50} \leqslant 5164\,\mathrm{pc}$ and $17.35 \leqslant \langle\mu_V\rangle_{50} \leqslant 26.48\,\mathrm{mag\,arcsec}^{-2}$. At $M_V \leqslant -13\,\mathrm{mag}$ our completeness is above 90 per cent for sources with $\langle\mu_V\rangle_{50} \leqslant$

---

9 20 of the 89 low surface brightness galaxy candidates identified in Chapter 4 were not identified by the automated detection performed in this work. We note that 15 of the non-detected sources have very faint surface brightnesses with $\langle\mu_V\rangle_{50} \geqslant 26\,\mathrm{mag\,arcsec}^{-2}$.
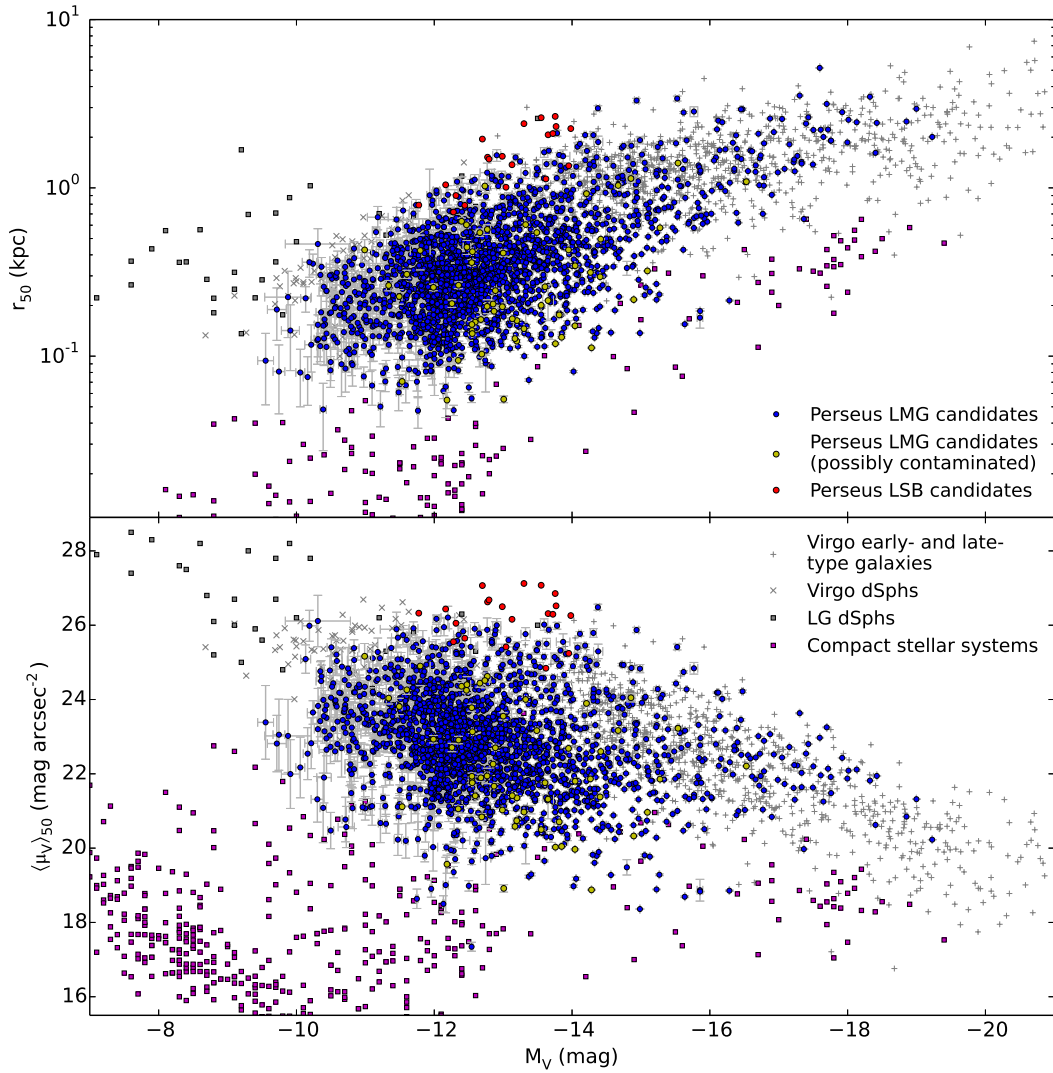
FIGURE 5.11: Magnitude–size–surface brightness distribution of Perseus cluster LMG candidates detected in this study. We compare our sample to Virgo early- and late-type galaxies (compilation of Lisker et al. 2013; based on the VCC), faint Virgo dSphs (Lieder et al. 2012), as well as dSphs from the Local Group (McConnachie 2012). We also include compact stellar systems (compilation of Norris et al. 2014) and visually identified Perseus cluster low surface brightness galaxy candidates from Chapter 4.

24 mag arcsec^{-2}, and above 60 per cent for sources with $\langle \mu_V \rangle_{50} \leqslant 26$ mag arcsec^{-2} (also see Fig. 5.5). Our sample largely overlaps with the parameter range of LMGs in the Virgo cluster, although fainter systems were reported by Lieder et al. (2012). At the low surface brightness end the Local Group dSphs reach to fainter surface brightnesses than our sample. At the bright surface brightness end our sample merges with the sequence formed by the class of compact stellar systems. Due to our selection criterion based on the SExtractor CLASS_STAR parameter our completeness limit drops below 50 per cent for sources with $\langle \mu_V \rangle_{50} \leqslant 17$ mag arcsec^{-2}.

5.6 SPATIAL DISTRIBUTION

We show the spatial distribution of our sample of LMG candidates in the Perseus cluster core in Fig. 5.12 (left-hand panel) as well as the corresponding 2D-density distribution (right-hand panel). The LMG candidates do not appear to be centrally
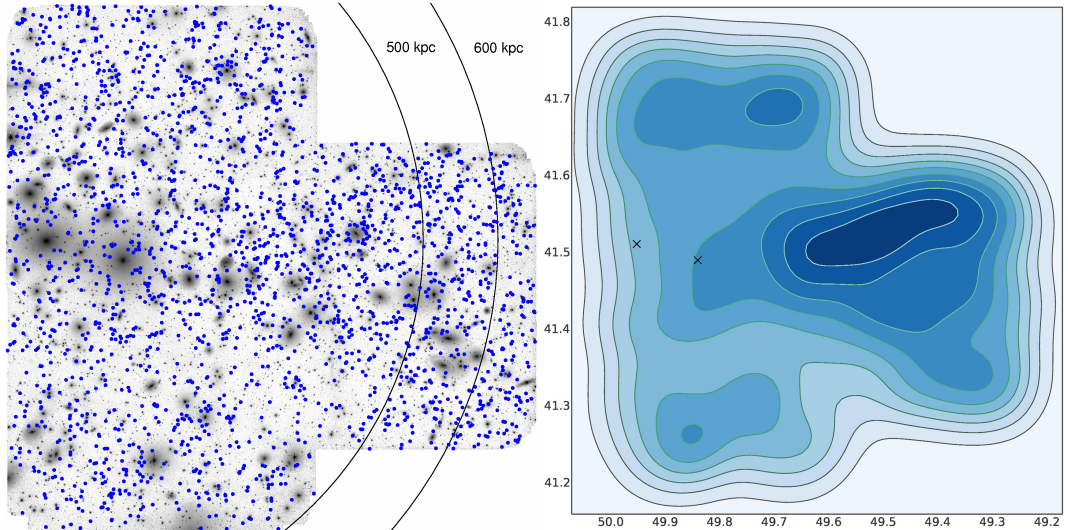
FIGURE 5.12:   Spatial distribution of LMG candidates in the Perseus cluster core. Left-hand panel: The LMG sample (blue dots) overlayed onto our deep V-band mosaic of the Perseus cluster. The solid circles indicate a cluster-centric distance of 500 and 600 kpc, respectively. We measured the cluster-centric distance with respect to the X-ray centre of the cluster (Piffaretti et al. 2011), which almost coincides with the optical position of NGC 1275. Right-hand panel: 2D-density distribution of the LMG sample displayed in the left-hand panel. We indicated the positions of the two brightest cluster galaxies NGC 1275 (R.A. = 49.95°, Dec. = 41.51°) and NGC 1272 (R.A. = 49.84°, Dec. = 41.49°) with black crosses.

concentrated around the cluster centre, which coincides with the brightest cluster galaxy NGC 1275. Instead, we observe an overdensity of LMG candidates towards the west of the centre, which is offset from the prominent chain of luminous galaxies in Perseus. Interestingly, a region south to the cluster centre seems to be only sparsely populated. We note that the southern field is shallowest in image depth (also see the weight image in Chapter 4, Fig. 4.2, right-hand panel). However, if the lower number of sources in this region would be due to the lower S/N of the data, then we should observe a low number of sources across the entire field, which does not seem to be the case.

Fig. 5.13 illustrates the radial projected number density profile of the Perseus LMG candidates. We separated our sample into six magnitude bins for $M_V \leqslant -11$ mag (Fig. 5.13, left-hand panels). In each magnitude bin we further distinguished between faint and bright surface brightness LMG candidates, which we defined according to the mean effective surface brightness of all sources in the respective magnitude bin (Fig. 5.13, right-hand panels).

At bright magnitudes $M_V \leqslant -16$ mag the overall number density profile of the LMG candidates is fairly flat, except for a peak in the number density profile at 500-600 kpc. Looking at the profile split up into bright and faint surface brightness LMG candidates, it becomes apparent that the peak is only visible in the distribution of the bright surface brightness candidates, with a significance of 2.4 σ with respect to the previous bin at 400-500 kpc,. The profile of the faint surface brightness candidates, however, remains flat.

At magnitudes $-16 < M_V \leqslant -15$ mag the overall number density profile is characterised by a continuous rise from 200-600 kpc. The split profile shows that this rise is only present in the number density profile of the brighter surface brightness candidates, which are by a factor of 9.5 more abundant at cluster-centric distances of 500-600 kpc than at 200-300 kpc. The faint surface brightness LMG candidates
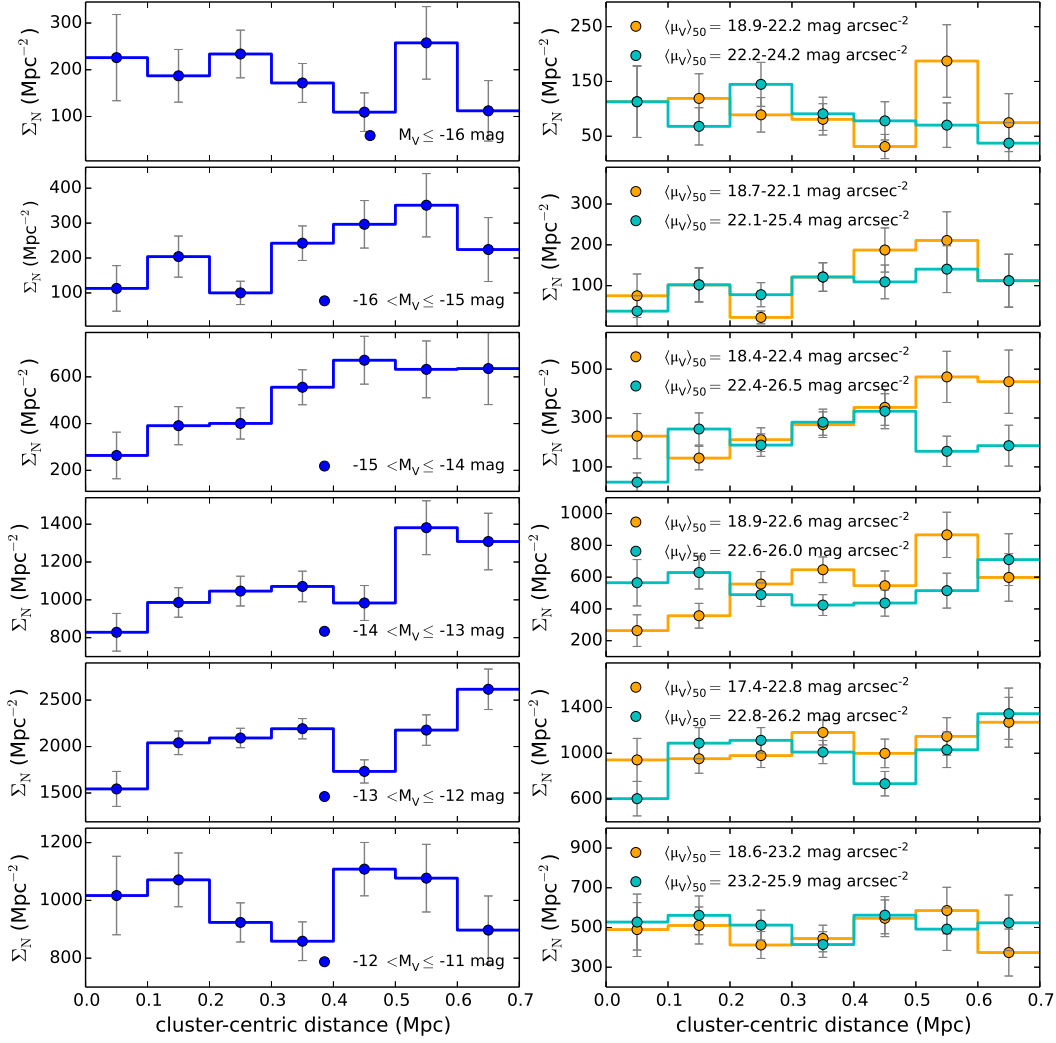
FIGURE 5.13:   Projected radial number density profile of Perseus cluster LMG candidates. We calculated the radial number density for our sample in six different magnitude bins that are indicated in the left-hand panels. In the right-hand panels we separated the sources of each magnitude bin into bright and faint surface brightness sources, according to the mean surface brightness in the respective magnitude bin. The given $\langle\mu_V\rangle_{50}$ limits reflect the brightest, mean, and faintest surface brightness of LMG candidates in the respective magnitude bin. We calculated the radial number density in bins of $100\,\mathrm{kpc}$ width. The given error bars reflect the statistical uncertainties.

instead show a flat number density profile, with a drop at cluster-centric distances smaller than 100 kpc at a significance of 1.7 σ with respect to the number density at 100-200 kpc.

In the magnitude range $-15 < M_V \leqslant -14$ mag the number density profile of the brighter surface brightness LMG candidates displays again a continuous rise from cluster-centric distances 100-600 kpc, with a 2.2 times higher abundance at 500-600 kpc than at 100-200 kpc. The profile of the faint candidates does not follow this rising trend and shows a drop in the number density profile for cluster centric distances smaller than 100 kpc at a significance of 5.8 σ compared to the number density at 100-200 kpc.

The number density profile for LMG candidates with $-14 < M_V \leqslant -13$ mag shows similar trends compared to the profile at $-15 < M_V \leqslant -14$ mag, with a continuous rise in the number density from 0-600 kpc by a factor of 3.3 for the brighter surface brightness population, and a fairly constant profile for the fainter surface brightness LMG candidates. There are, however, no indications for a drop in the number density profile for the fainter surface brightness candidates in this magnitude range.

At magnitudes $-13 < M_V \leqslant -12$ mag the fainter surface brightness LMG candidates show again a drop in the number density profile within a distance of 100 kpc from the cluster centre, at a significance of 3.3 σ with respect to the number density at 100-200 kpc. Otherwise the number density profiles of both the brighter and the fainter surface brightness LMG candidates appear fairly flat, which is also true at fainter magnitudes $-12 < M_V \leqslant -11$ mag.

5.7 DISCUSSION

In the magnitude–size diagram (Fig. 5.11) our sample of LMG candidates in the Perseus cluster core follows the same trend of increasing r_{50} towards brighter absolute magnitudes M_V as seen for LMGs in the Virgo cluster. We note that at the faint magnitude end of the distribution the apparent drop in the number of Perseus LMG candidates at $M_V > -12$ mag is caused by the selection of our working sample, which we limited to sources with $M_{V,petro} \leqslant -12$ mag as measured by SEXTRACTOR (see Section 5.2.5). At brighter magnitudes our sample includes fewer LMGs compared to Virgo, since we solely studied the core region of Perseus, whereas the shown galaxies from Virgo were detected in a much wider region of the cluster.

Our sample also harbours sources in the parameter range of compact elliptical galaxies (cEs). Compared to the literature compilation of cEs (Norris et al. 2014) shown in Fig. 5.11, the Perseus cE candidates do not reach the extremely bright surface brightnesses of some of the literature cEs. We note that our detection was not tuned to the detection of very compact sources, and our selection criteria based on the SExtractor parameter CLASS_STAR resulted in a completeness limit below 50 per cent for sources with $\langle\mu_V\rangle_{50} \leqslant 17$ mag arcsec^{-2} (see Fig. 5.5). Thus, denser compact stellar systems might also exist in Perseus.

The apparent limit at the faint surface brightness end of the magnitude–size distribution is likely not caused by a physical effect, but rather reflects our detection limit at around 26 mag arcsec^{-2} for the automated detection performed in this study. In fact, recent deep wide-field imaging studies like the NGVS (Ferrarese et al. 2012) or the FDS (Iodice et al. 2016) are continuously pushing the faint surface

brightness end of the magnitude–size relation to fainter limits, unveiling an ever increasing number of low surface brightness LMGs well in the $\langle\mu_V\rangle_{50}$ regime of Local Group dSphs. Nevertheless, a physical process causing a limit in surface brightness, and thus stellar density might be expected, below which it is no longer possible to form a gravitationally bound stellar system or no stellar component at all, resulting in a potential 'pure' dark matter halo. Detecting such a limit observationally would be, however, very hard to achieve, but numerical simulations may be able to shed light on this (see, e.g. Sawala et al. 2016).

The bright surface brightness end of the magnitude–size distribution seems to be well traced by luminous ellipticals and compact stellar systems like cEs, ultra-compact dwarf galaxies (UCDs) and globular clusters (GCs). Various authors (Norris et al. 2014; Misgeld and Hilker 2011; Burstein et al. 1997) claimed that there exists a maximum stellar density above which no stellar system can exist, giving rise to the so-called 'zone of avoidance'. Misgeld and Hilker (2011) showed that also high-redshift early-type galaxies at $z \sim 1-2$ are not violating this limit. So far there seems to be no consensus on the physical process that caused the zone of avoidance.

Interestingly, some objects of our sample fall into the region between the formerly distinct sequences of diffuse and compact stellar systems (also see Chapter 1, Fig. 1.3). Both sequences were already observed to merge at faint luminosities with $M_V \gtrsim -10$ mag, where stellar systems named 'extended clusters' (e.g. Huxor et al. 2005; Forbes et al. 2013) and 'faint fuzzies' (Larsen and Brodie 2000, 2002) started to fill the gap between GCs and dSphs in the magnitude–size parameter space. It would thus be interesting to probe whether both families of diffuse and compact stellar systems will ultimately merge to one sequence of low-mass stellar systems, with a continuous range in parameters from bright to faint surface brightnesses.

Our sample of LMG candidates in the Perseus cluster core does not show a centrally concentrated spatial distribution. This becomes apparent in Fig. 5.12 as well as in the projected radial number density profiles shown in Fig. 5.13. In fact, the systems with fainter surface brightnesses even show a drop in the number density profile within cluster-centric distances of 100 kpc in the magnitude range $M_V = -16$ to -14 mag and $M_V = -12$ to -13 mag. A drop in the number density profile within 100 kpc was also seen for the faint low surface brightness galaxy candidates with $\langle\mu_V\rangle_{50} = 24.8\text{-}27.1$ mag arcsec^{-2} in Perseus, which we identified in Chapter 4. This observation possibly reflects that diffuse low-mass stellar systems might not be able to survive in the very cluster centre due to the strong tidal field generated by the central cluster galaxy NGC 1275 and the overall cluster potential.

The spatial distribution of our sample revealed an overdensity of LMG candidates to the west of the cluster centre (see Fig. 5.12, right-hand panel). This observation is also manifested in the radial number density profiles as a continuous rise in the number density towards larger cluster-centric distances. Interestingly, this rise is only seen in the number density profiles of the brighter more compact sources, with $\langle\mu_V\rangle_{50} \lesssim 22.5$ mag arcsec^{-2} and $M_V \leqslant -13$ mag. Due to their compact morphology, the overdensity may correspond to an accumulation of intrinsically brighter galaxies in the background. If the majority of our candidates were, however, true cluster members, this region would hold a higher density of LMGs than the area immediately around the central galaxies. In this case, the overdensity could be associated with a currently infalling galaxy group or the accretion of individual galaxies that are fed into the cluster along large-scale filaments. In Fig. 5.14
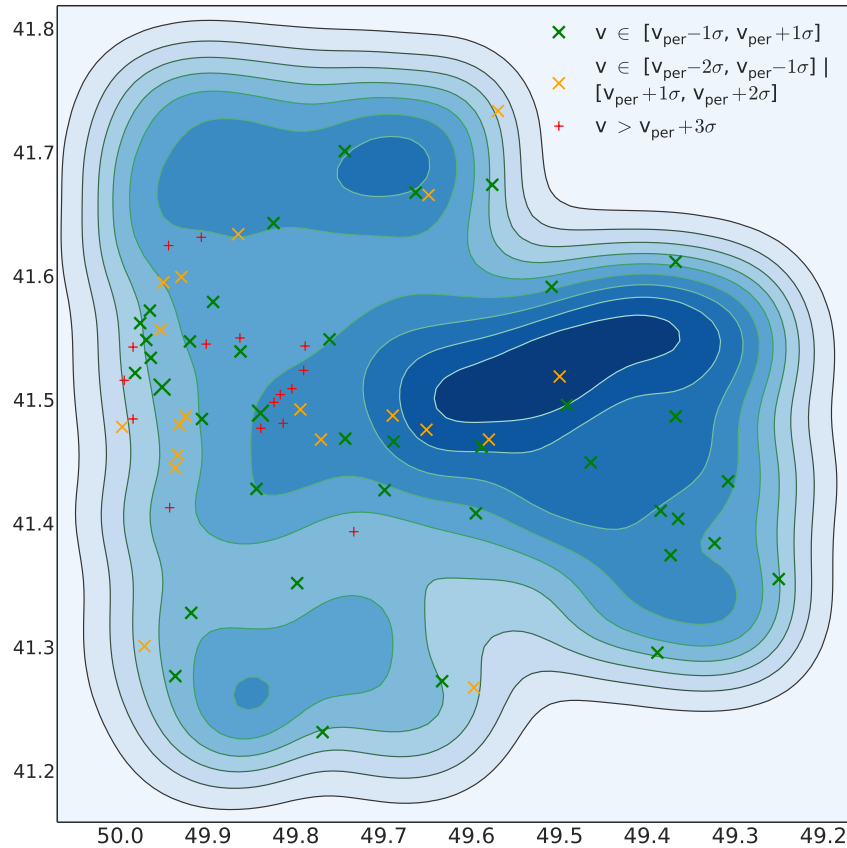
FIGURE 5.14: Spatial distribution of LMG candidates in the Perseus cluster core and positions of brighter galaxies with redshift measurements. This plot is the same as shown in Fig. 5.12 (right-hand panel) showing the 2D-density distribution of the Perseus LMG candidates. In this figure we additionally indicated the positions of brighter galaxies with available redshift measurements in the direction of the Perseus cluster. We divided the galaxies with redshift information into galaxies that have velocities within $\pm 1\,\sigma$ of the Perseus cluster mean velocity $v_{\mathrm{perseus}} \sim 5370\,\mathrm{km\,s^{-1}}$ (Struble and Rood 1999), where $\sigma = 1300\,\mathrm{km\,s^{-1}}$ denotes the cluster's velocity dispersion (Kent and Sargent 1983). We furthermore indicated galaxies with velocities between 1-2 σ of v_{perseus}, and galaxies with velocities larger than $v_{\mathrm{perseus}} + 3\,\sigma$. The two largest crosses mark the positions of the two brightest cluster galaxies NGC 1275 and NGC 1272. We note that the spectroscopic coverage of bright galaxies is likely neither complete nor continuous across our field of view.

we compared the 2D-density distribution of our sample to the positions of galaxies with available redshift information in the direction of the Perseus cluster.[10] We divided the galaxies into three different velocity bins with velocities within $\pm 1\,\sigma$, ± 1-2 σ and $> 3\,\sigma$ within the Perseus cluster mean velocity of $v_{\mathrm{perseus}} \sim 5370\,\mathrm{km\,s^{-1}}$ (Struble and Rood 1999).[11] Spectroscopically confirmed cluster members are distributed all around the overdensity, but very few spectra are available inside it. There is one galaxy at $v \sim 3250\,\mathrm{km\,s^{-1}}$ which is within ± 1-2 σ of the Perseus cluster mean velocity. We note, however, that this could be a projection effect. We also emphasize that the spectroscopic coverage is likely neither complete nor continuous across our observed region of Perseus.

---

10 C. Wittmann thanks Ralf Kotulla for sharing his catalogue compilation of velocity measurements in the direction of the Perseus cluster.

11 We note that 11 sources from our sample are galaxies in the background of Perseus, with $v > v_{\mathrm{perseus}} + 3\,\sigma$. These are commonly characterised by small sizes with $r_{50} < 500\,\mathrm{pc}$ and bright surface brightnesses with $\langle \mu_V \rangle_{50} < 22.6\,\mathrm{mag\,arcsec^{-2}}$.

In addition, the number density profiles of our sample with $M_V \leqslant -13$ mag reveal a peak at cluster-centric distances 500-600 kpc. This peak is again only seen in the profiles of the more compact LMG candidates. Figs 5.12 (left-hand panel) and 5.14 show that a subgroup of luminous galaxies with velocities within $\pm 1\,\sigma$ of the Perseus cluster mean velocity is located in this region. Thus, the peak in the number density profile might be caused by a population of LMGs which are associated with the subgroup in this region.

With our new catalogue of LMGs we are able to identify local structures within the Perseus cluster core, like the ones seen in Figs 5.12, 5.13 and 5.14. We are thereby highlighting regions where spectroscopic coverage would be most needed and most interesting.

5.8 SUMMARY

We established a catalogue of faint galaxies in the direction of the Perseus galaxy cluster, based on deep *V*-band imaging data of the cluster core region obtained with the PFIP at the *WHT*. We performed an automated source detection with SExtractor and included all brighter sources with $M_{V,\texttt{petro}} \leqslant -12$ mag (obtained by SExtractor) in our working sample. We subsequently measured the photometry and structure parameters of our working sample with GALFIT.

To reduce the contamination through background galaxies, we defined a sample of Perseus cluster LMG candidates according to a criterion based on the well defined relation between luminosity and Sérsic index. Our sample of over 2000 LMG candidates spans a parameter range of $-9.55 \geqslant M_V \geqslant -19.23$ mag, $47 \leqslant r_{50} \leqslant 5164$ pc and $17.35 \leqslant \langle\mu_V\rangle_{50} \leqslant 26.48$ mag arcsec^{-2}. For $M_V \leqslant -13$ mag our 50 per cent completeness limit is at $\langle\mu_V\rangle_{50} = 26$ mag arcsec^{-2}. In the magnitude–size diagram, the Perseus LMG candidates follow a similar trend as the LMG population in Virgo. Our sample additionally includes sources in the parameter range of cEs, and sources that fill the formerly well defined gap between the M_V–r_{50} sequences formed by compact stellar systems and dwarf ellipticals.

The projected spatial distribution reveals that the Perseus LMG candidates are not centrally concentrated around the brightest cluster galaxy NGC 1275. Instead we detected an overdensity to the west of the cluster centre, which is also indicated by a rising projected radial number density profile of brighter surface brightness LMG candidates with $\langle\mu_V\rangle_{50} \lesssim 22.5$ mag arcsec^{-2} and $M_V \leqslant -13$ mag. The same population also shows a peak in the number density profile between cluster-centric distances 500-600 kpc. If the majority of the LMG candidates were true cluster members, this could represent a true substructure of the Perseus cluster, possibly associated to a recently infalling group of galaxies. To confirm this it would be essential to gather further spectroscopy. The fainter surface brightness LMG candidates show a fairly constant projected number density profile, with a drop at cluster-centric distances smaller than 100 kpc. This is consistent with the result found for the faint low surface brightness galaxy candidates in Chapter 4, possibly indicating a depletion of diffuse LMGs towards the cluster centre due to the strong tidal field generated by NGC 1275 and the overall cluster potential.

SUMMARY AND DISCUSSION

The relevance of tidal disruption processes for low-mass galaxies was recognized in our Milky Way in the early 1970's. For example, the Small Magellanic Cloud is thought to suffer from tidal disruption by the Large Magellanic Cloud and the Milky Way, which gives rise to the prominent Magellanic Stream (e.g. Wannier and Wrixon 1972; Mathewson et al. 1974; Connors et al. 2006). The Sagittarius dwarf galaxy also shows clear signatures of ongoing tidal dissolution, indicated by its elongated shape as well as associated trailing and leading tidal streams (e.g. Ibata et al. 1994; Mateo et al. 1998; Martínez-Delgado et al. 2004). Only recently, faint low surface brightness (LSB) galaxies with similar stellar densities but larger sizes compared to those of the Milky Way satellites were reported to exist in large numbers in the centres of massive galaxy clusters (e.g. van Dokkum et al. 2015a; Mihos et al. 2015; Koda et al. 2015). This immediately triggered the question how these fragile systems are able to survive the tidal forces in the densest known environments. Tidal processes are also discussed as possible origins for much more compact low-mass stellar systems, which were discovered about 20 years ago in the core of the Fornax galaxy cluster by Hilker et al. (1999) and Drinkwater et al. (2000b). Due to their similar appearance and properties to galaxy nuclei, Hilker et al. (1999) proposed that the newly discovered objects could be the remnant nuclei of disrupted low-mass galaxies. In this thesis we investigated both a population of ultra-compact as well as a population of ultra-diffuse low-mass stellar systems in the cores of the nearby Fornax and Perseus galaxy clusters for signs of environmental influence in the form of tidal disruption.

In the Fornax cluster we analysed a sample of 355 spectroscopically confirmed compact stellar systems in the magnitude range of ultra-compact dwarf galaxies (UCDs) with $M_{Ve} = -10$ to -14 mag. We aimed to find indications for the origin of this population, whether these could be the remnant nuclei of tidally stripped low-mass galaxies, or genuine star clusters. In deep optical wide-field imaging data we searched for tidal streams or debris around the compact objects that could indicate the possible disruption of the former host galaxy. Our data did not reveal long tidal streams around any of the investigated objects. However, we found that a significant fraction of our sample shows a distorted, asymmetric or elongated outer structure. We showed, based on an estimate of the tidal radius, that the distortions could have been caused by tidal forces. We argued, however, that disruption signs do not necessarily reveal the nature of the deformed object, which may either point to the tidal disruption of a nucleated low-mass galaxy, or to the deformation of a massive star cluster. We performed a quantitative parameter characterisation of our sample, introducing parameters that describe the outer asymmetry and ellipticity as well as the core concentration. This allowed us to divide the sample into subsamples with different parameter values and to study the spatial and phase-space distribution. We found that a subsample with high asymmetry (or high ellipticity) and low core concentration parameters is predominantly distributed at larger cluster-centric distances, compared to other compact objects in the same magnitude range. Since the spatial distribution is more similar to the extended spatial distribution seen for low-mass cluster galaxies than to the concentrated distribu-

tion of globular clusters (GCs), we took this as an indication that at least some objects of this subsample might originate from disrupted low-mass galaxies. This is further supported by the phase-space distribution and comparatively high velocities relative to the Fornax cluster mean velocity, and could signify a more recent accretion compared to the overall population of compact stellar systems in Fornax.

In the Perseus cluster we investigated whether galaxies of very low stellar density, and thus low surface brightness, are able to exist in the dense core region. We identified a population of 89 LSB galaxy candidates in the parameter range $\langle \mu_V \rangle_{50} = 24.8\text{–}27.1 \, \text{mag arcsec}^{-2}$, $M_V = -11.8$ to $-15.5 \, \text{mag}$ and $r_{50} = 0.7\text{–}4.1 \, \text{kpc}$. The majority of our sample does not show direct signs of ongoing tidal disruption. We argued that disruption may be prevented by a high dark matter content characterising this population. Based on an estimate of the tidal radius and the observed distribution of half-light radii, we found that a typical galaxy from our sample would require a mass-to-light ratio on the order of $M/L = 100$ to be stable against disruption. This estimate is consistent with mass-to-light ratios derived from dynamical measurements of a few faint LSB galaxies in the literature. Nevertheless, our study revealed possible indirect signs of environmental influence on this population. We found that large LSB galaxy candidates with $r_{50} > 3 \, \text{kpc}$, which are known to exist in other environments, seem to be very rare in the Perseus cluster core, with only one LSB candidate in this parameter range. Compared to the core region of the Coma cluster, however, we found a similar number of LSB galaxy candidates in the parameter range $M_V < -14 \, \text{mag}$ and $r_{50} > 2 \, \text{kpc}$, with the same dearth of large objects. We concluded that larger systems possibly cannot exist in the dense core regions of massive galaxy clusters due to the strong tidal field. In addition, we observed a nearly constant projected radial number density profile for our sample when the cluster-centric distances are larger than $100 \, \text{kpc}$, which might indicate a depletion of LSB galaxy candidates towards the cluster centre. In Perseus we identified three LSB galaxy candidates which appear to be associated with tidal streams, and two regular dwarf galaxies of brighter surface brightness with tidal tails and/or a disturbed morphology. We interpreted this as signs for their ongoing tidal disruption. Recent disruption of low-mass galaxies also seems to take place in the core of the Fornax galaxy cluster, where we identified one LSB galaxy candidate with a very elongated shape and a truncated surface brightness profile, as well as a dwarf galaxy with prominent tidal tails. In Fornax our data revealed one long tidal stream and several other low surface brightness structures, which may represent the ultimate fate of disrupted low-mass stellar systems.

In summary we found a comparatively low number of disruption events for the abundant population of low-mass galaxies in the cores of the Perseus and Fornax galaxy clusters. Even the most diffuse systems with the lowest stellar densities seem to be able to survive in these environments. This supports the hypothesis that gravitational interactions driving galaxy evolution in dense cluster cores might be of minor relevance today. However, there are indications for tidal stripping events during the lifetimes of massive galaxy clusters, indicated by the presence of diffuse intracluster light and numerous tidal streams (cf. Chapter 3; Mihos et al. 2017). Indeed, studies based on cosmological simulations with semi-analytical models showed that today's low-mass cluster population experienced strong mass loss due to tidal stripping at high redshifts (Lisker et al. 2013; Pfeffer et al. 2014). On the other hand, results of other cosmological simulations reported only mild tidal stripping, mainly affecting the dark matter halo with little or no influence on the stellar component (Smith et al. 2015; Mistani et al. 2016). Possibly the major

gravitational structural transformation of low-mass galaxies already took place in galaxy groups, before being accreted onto the cluster (De Lucia et al. 2012).

To probe the importance of gravitational interactions on the past evolution of the low-mass population, deep and high-resolution high-redshift observations of galaxy clusters would be required. Would these reveal numerous low-mass galaxies undergoing strong structural perturbations, suggesting that they were once more massive and of different structure? Or would they bring to light another dominant past formation channel, like the formation of tidal dwarf galaxies during gas-rich galaxy mergers (e.g. Schweizer 1978; Okazaki and Taniguchi 2000; Bournaud and Duc 2006; Dabringhausen and Kroupa 2013; Duc et al. 2014)? Instead, if a population of structurally similar low-mass galaxies was already in place in high-redshift clusters, this would be a strong indication that the majority of the diffuse low-mass population in nearby galaxy clusters possibly formed as genuine low-mass systems. This is in line with the findings of Janz et al. (2017), who observed that quenched low-mass galaxies in isolation – although a very rare species – share similar structural and kinematical properties as compared to quenched low-mass galaxies in clusters. Since the isolated quenched galaxies cannot have undergone environmental transformations, this implies that the cluster analogues need not necessarily be a product of strong structural transformation.

The low number of disruption signs observed for low-mass galaxies likewise implies a low present-day formation rate of compact stellar systems by tidal stripping of nucleated dwarf galaxies. Although a few examples of nucleated dwarf ellipticals with tidal tails are seen in nearby galaxy clusters (e.g. Chapters 3 and 4), it is unclear whether the present-day tidal effects will be strong enough to strip them further down to their nuclei, given that very specific orbits are required for their total disruption (see Goerdt et al. 2008, their fig. 7). Observations showing compact stellar systems embedded in tidal streams that would indicate the last stage of disruption of their respective host galaxy have so far not been detected for systems in the magnitude range of UCDs or GCs. However, such signatures were revealed around several compact elliptical galaxies (cEs) by Huxor et al. (2011) and Chilingarian and Zolotukhin (2015). Since cEs are more luminous and more massive than UCDs and GCs, their progenitor galaxies should also have been more massive, and therefore even harder to disrupt compared to the possible progenitors of UCDs and GCs. Thus, if the formation channel via tidal disruption plays a role for the production of cEs, this channel should contribute as well to the formation of at least some of the fainter compact objects. Indeed, Pfeffer et al. (2016) showed, using a semi-analytical model based on the Millenium II cosmological simulation, that the number of stripped low-mass galaxies predicted by the simulation agrees well with the number of observed compact stellar systems in the mass range of cEs or massive UCDs. However, at intermediate to low masses there are many more compact stellar systems observed than stripped nuclei predicted, suggesting that the majority could have formed as genuine star clusters. Nevertheless, in the case of star cluster origins, it remains to be established whether compact stellar systems in the mass range 10^6-$10^8 \, M_\odot$ could have formed in sufficient numbers, and also have survived until today, during regular star formation in high-redshift galaxies (Kruijssen 2015) or during gas-rich galaxy mergers (Renaud et al. 2015), which are thought to give rise to today's GC populations. One key aspect would be to constrain the conditions in high redshift galaxies that regulate the high-mass end of the GC mass function.

To enable systematic studies and comparisons of the low-mass galaxy populations of different nearby galaxy clusters, we established a catalogue of faint galaxies in the direction of the Perseus cluster. We defined a sample of low-mass galaxy candidates based on the well defined relation between Sérsic index and luminosity. Our sample of over 2000 diffuse and compact sources spans a parameter range of $M_V = -9.55$ to -19.23 mag, $r_{50} = 47\text{-}5164$ pc and $\langle\mu_V\rangle_{50} = 17.35\text{-}26.48$ mag arcsec^{-2}, with a 50 per cent completeness limit of $\langle\mu_V\rangle_{50} = 26$ mag arcsec^{-2} at $M_V \leqslant -13$ mag. The Perseus low-mass candidates follow a similar trend in the magnitude size diagram as the low-mass galaxy population in the Virgo cluster. Our sample also includes compact sources in the parameter range of cEs. Interestingly, some sources fall in the formerly well defined gap between the magnitude-size sequences formed by the compact and diffuse stellar systems. This might indicate that both sequences will eventually merge to one sequence of low-mass stellar systems, as already observed in the fainter luminosity regime of GCs and dwarf spheroidal galaxies (e.g. Norris et al. 2014). The projected spatial distribution of our sample reveals that the low-mass galaxy candidates are not centrally concentrated around the brightest cluster galaxy NGC 1275. Instead we detected an overdensity to the west of the cluster centre. This is also reflected in the projected radial number density profile of the brighter surface brightness low-mass galaxy candidates, which increases towards larger cluster-centric distances. This may either be explained by contamination through an accumulation of galaxies in the background of Perseus, or represent a true substructure, possibly associated to a recently infalling group of galaxies. For the fainter surface brightness low-mass galaxy candidates in Perseus we found a similar constant projected radial number density profile as seen for the previously identified LSB galaxy candidates of the cluster.

In future work we aim to extend our study of Perseus cluster low-mass stellar systems to a wider cluster region, on the basis of multi-band imaging data acquired with the One Degree Imager (ODI) at the *WIYN telescope*.[1] We will probe the spatial distribution of low-mass galaxies and their possible association to subgroups within the cluster. We aim to compare the properties of low-mass galaxies still bound to subgroups to those that reside in the cluster centre. This will shed light on whether the low-mass population is shaped by environmental processes already in galaxy groups before being accreted onto the cluster. In addition, we will investigate whether large LSB galaxies of dwarf galaxy luminosity are present in the cluster outskirts, which we found to be absent in the Perseus cluster core region (see Chapter 4). We will also study the low-mass galaxy population in the Cancer cluster core, which is a much less evolved, still assembling galaxy cluster at a similar redshift, for which we have also acquired multi-band imaging data with *WIYN*/ODI.[1] This will allow a direct comparison of low-mass populations in cluster environments of different environmental density. Furthermore, we will analyse compact stellar systems in Perseus, on the basis of two-band *Hubble Space Telescope* imaging data.[2] We will search the cluster for new UCD and cE candidates and compare their properties to the known populations in the Fornax and Virgo galaxy cluster. We will also study the GC systems around some of the LSB galaxy candidates identified in Chapter 4 and compare the specific frequency of GCs as

---

well as their metallicty distribution to the GC systems of regular dwarf galaxies. Their GC systems will thus serve as a tracer to identify whether LSB systems originated from a possibly different formation and evolutionary path.

A

APPENDIX: PECULIAR COMPACT STELLAR SYSTEMS

Appendix A contains additional material to Chapter 2.

A.1 PARAMETER RELATIONS AND MAGNITUDE DISTRIBUTIONS OF THE SUB-SAMPLES

In Fig. A.1 we display the relations between the parameters core concentration, residual asymmetry, and ellipticity, which we derived in Section 2.3 for our working sample. Fig. A.2 shows the magnitude distributions of the subsamples defined in Section 2.4.2.
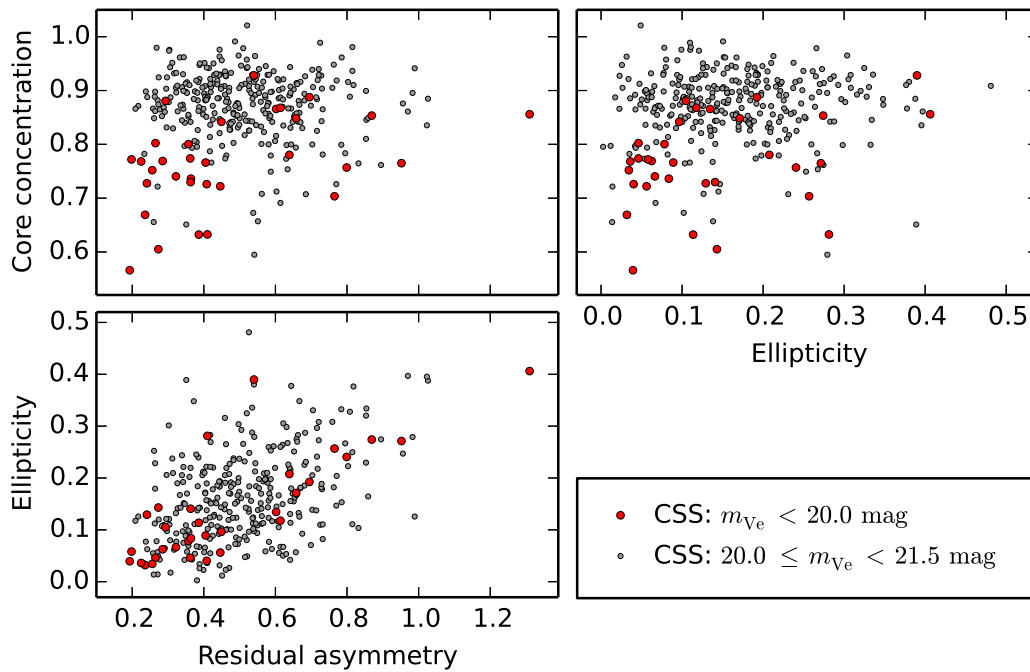
FIGURE A.1: Parameter relations for compact stellar systems from our working sample.
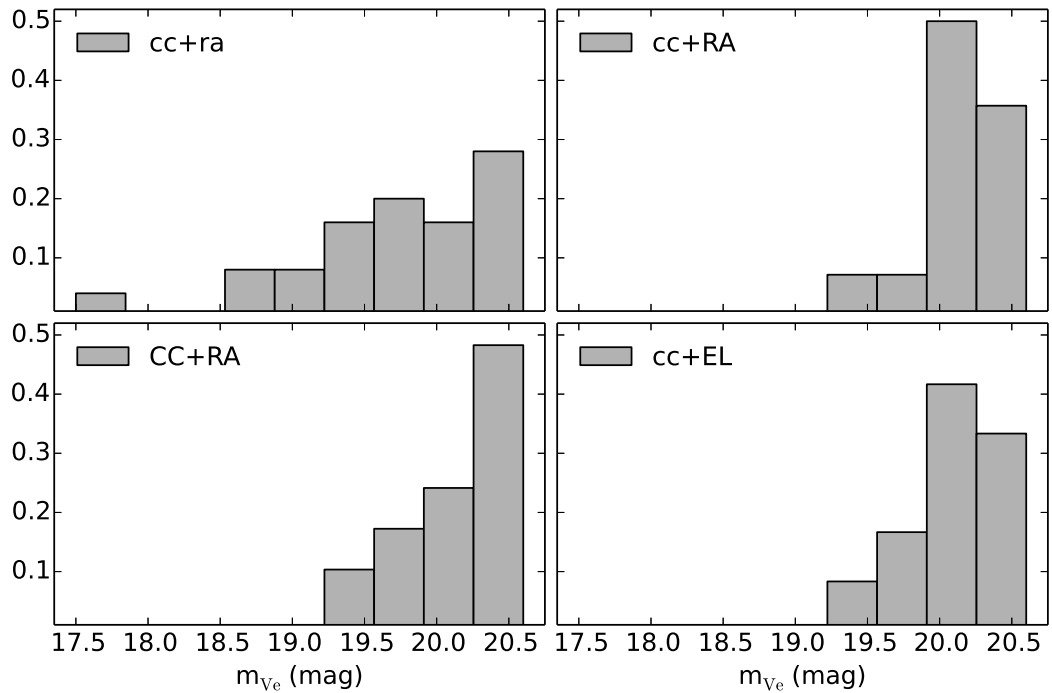
FIGURE A.2:   Magnitude distributions of the subsamples defined in Section 2.4.2.

A.2   ALTERNATIVE SUBSAMPLE DEFINITION

In Table A.1 we defined alternative subsamples, where we set the cut for the core concentration to a higher value in order to increase the number of objects in the subsamples with low core concentration. We show the spatial distributions of the alternative subsamples in Fig. A.3, and summarise the KS test results in Table A.2, in analogy to Section 2.4.2.

Fig. A.4 shows the distribution of the alternative subsamples in phase-space. We include the velocity dispersions of the alternative subsamples in Table A.3.

TABLE A.1:   Parameter ranges for the alternative subsamples cc+ra, cc+RA, CC+RA and cc+EL. We applied slightly different parameter cuts for the bright ($m_{Ve} < 20.0$ mag) and faint ($20.0 \leqslant m_{Ve} < 20.6$ mag) objects of each subsample, respectively (see Section 2.3.4). Compared to the definition in Table 2.5, the cut for the core concentration is set to a higher value. The residual asymmetry and ellipticity cuts remain unchanged. For each alternative subsample we give the fraction of objects in the respective magnitude range and the overlap fractions with the artificial objects.

ALTERNATIVE SUBSAMPLE	ALTERNATIVE PARAMETER CUTS	OBJECTS (per cent)	ART. OBJECTS (per cent)
cc+ra (bright)	cc < 0.80 and ra < 0.5	53.1	50.3
cc+ra (faint)	cc < 0.87 and ra < 0.55	26.3	24.0
cc+RA (bright)	cc < 0.80 and ra > 0.5	12.5	0.3
cc+RA (faint)	cc < 0.87 and ra > 0.55	31.6	1.4
CC+RA (bright)	cc > 0.80 and ra > 0.5	21.9	5.5
CC+RA (faint)	cc > 0.87 and ra > 0.55	24.6	2.2
cc+EL (bright)	cc < 0.80 and el > 0.2	15.6	1.5
cc+EL (faint)	cc < 0.87 and el > 0.22	22.8	4.6
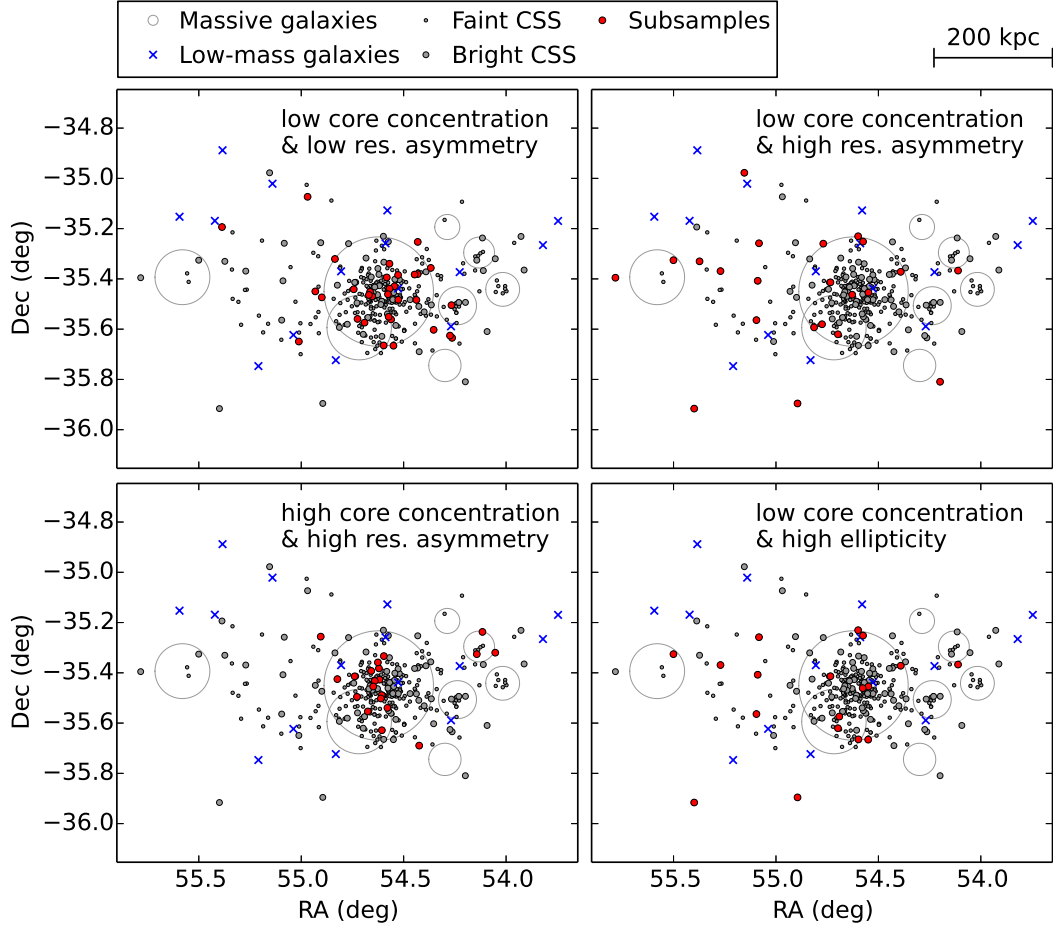
FIGURE A.3: Spatial distribution of compact stellar systems in the Fornax cluster. Same as Fig. 2.5, but illustrating the alternative subsamples. For comparison we also show the distribution of the cluster galaxies. Faint CSS: compact objects with $20.6 \leqslant m_{Ve} < 21.5\,\mathrm{mag}$. Bright CSS: compact objects with $m_{Ve} < 20.6\,\mathrm{mag}$. Alternative subsamples: cc+ra, cc+RA, CC+RA, cc+EL, as defined in Table A.1. Low-mass galaxies: galaxies with $-19 < M_r < -16\,\mathrm{mag}$ from the Fornax cluster catalogue (FCC, Ferguson 1989; based on the magnitude conversions of Weinmann et al. 2011). Massive galaxies: galaxies with $M_r \leqslant -19\,\mathrm{mag}$ from the FCC. Each massive galaxy is represented by a circle with three times its isophotal diameter at $\mu_B = 25\,\mathrm{mag\,arcsec}^{-2}$, $3\,d_{25}$ (we used the extinction-corrected values for d_{25}, obtained from HyperLEDA). The two brightest galaxies are NGC 1399 in the centre and NGC 1404 to the south-east from it.

TABLE A.2: Alternative subsamples: KS test probabilities (percentage) for the null hypothesis that two subsamples have the same cluster-centric distance distribution. In the last row the distributions of the individual subsamples are compared to the respective other compact objects with different parameters in the same magnitude range with $m_{Ve} < 20.6\,\mathrm{mag}$.

ALTERNATIVE SUBSAMPLE	cc+ra	cc+RA	CC+RA	cc+EL
cc+ra	100.0	0.3	19.2	5.1
cc+RA		100.0	0.0	97.4
CC+RA			100.0	0.4
cc+EL				100.0
respective other CSS	12.2	0.1	0.8	4.0
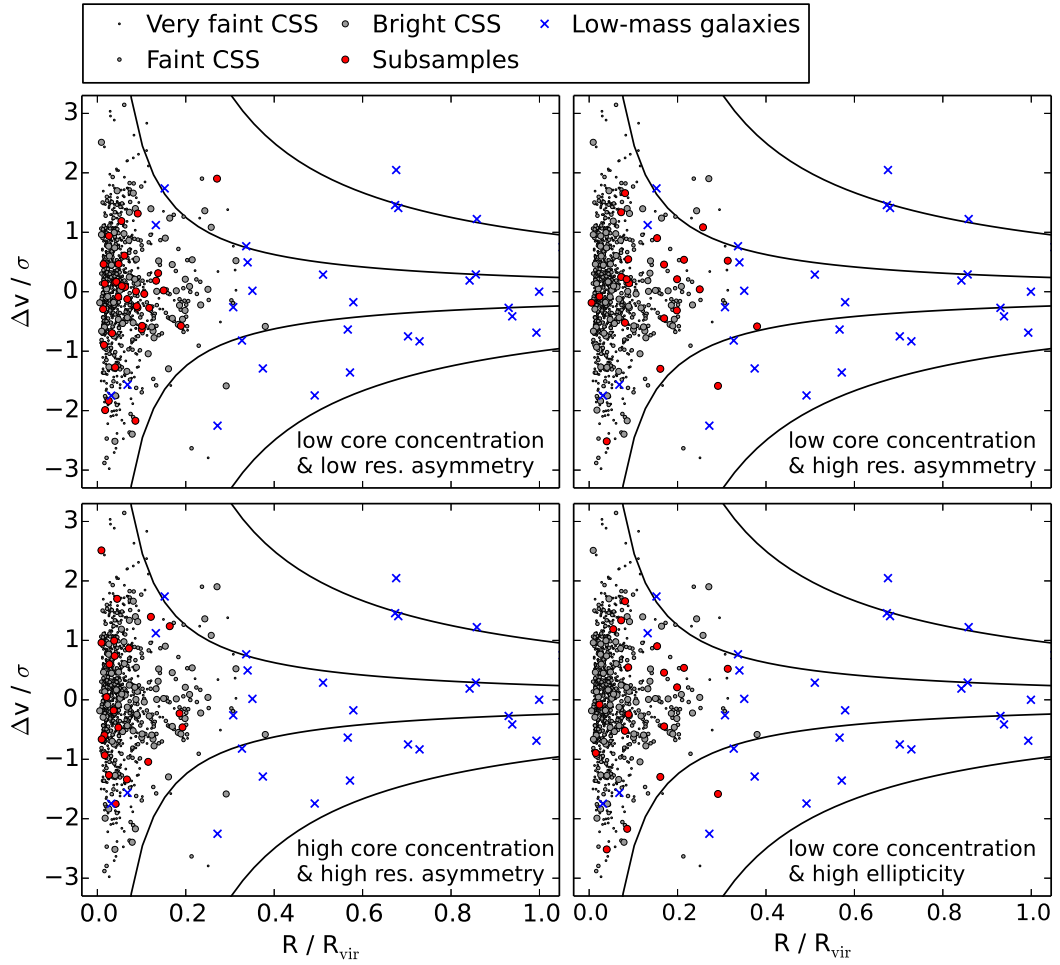
FIGURE A.4:   Phase-space distribution of compact stellar systems and low-mass galaxies in the Fornax cluster. Same as Fig. 2.7, but illustrating the alternative subsamples. Very faint CSS: compact objects with $m_{Ve} \geqslant 21.5$ mag (not part of our working sample). Faint CSS: compact objects with $20.6 \leqslant m_{Ve} < 21.5$ mag. Bright CSS: compact objects with $m_{Ve} < 20.6$ mag. Subsamples: cc+ra, cc+RA, CC+RA, cc+EL, as defined in Table 2.5. Low-mass galaxies: galaxies with $-19 < M_r < -16$ mag from the FCC (Ferguson 1989; based on the magnitude conversions of Weinmann et al. 2011). Δv is the relative velocity of an object with respect to the cluster mean velocity (1460 km s^{-1}). We denote σ as the cluster velocity dispersion (324 km s^{-1}), R as the cluster-centric distance, and R_{vir} as its virial radius ($2.5°$, see Section 2.4.3). The mean velocity and dispersion were calculated from all compact stellar systems and FCC galaxies within a cluster-centric distance of $1.0°$. The solid lines correspond to caustic lines of constant $(\Delta v / \sigma) \times (R/R_{vir})$ at ± 0.1 and ± 0.4, respectively.

TABLE A.3: Velocity dispersion for the alternative subsamples. The velocity dispersion of each subsample is calculated as standard deviation within a cluster-centric distance of $R \leqslant 1.0°$ (σ_{tot}), $R \leqslant 0.4°$ (σ_{in}) or $0.4 < R \leqslant 1.0°$ (σ_{out}), based on the velocities given in Table 2.1. N_{obj} corresponds to the number of objects from the respective subsample in the inner ($N_{obj,in}$) or outer ($N_{obj,out}$) cluster region. The velocity dispersion is given in $km\,s^{-1}$. $1.0°$ corresponds to 0.346 and $0.4°$ to 0.138 Mpc at the distance of Fornax.

ALTERNATIVE SUBSAMPLE	σ_{tot}	σ_{in}	$N_{obj,in}$	σ_{out}	$N_{obj,out}$
cc+ra	284	265	30	401	2
cc+RA	303	340	11	252	11
CC+RA	359	374	18	244	3
cc+EL	375	427	11	269	7

A.3   COMPLETE CATALOGUES

In Table A.4 we provide the complete sample of spectroscopically confirmed compact Fornax cluster members that were compiled from the literature. Table A.5 includes the measured parameter values for our working sample of confirmed Fornax cluster members with $m_{Ve} < 21.5$ mag.

TABLE A.4:   Complete catalogue of compact stellar systems compiled from the literature. For each object we list our ID, the position based on our astrometry, as well as the SIMBAD identifier. The object IDs are sorted by increasing right ascension. The given velocity corresponds to the velocity with the smallest error from all compiled velocities. The respective literature source is listed in the last column, where 1 = Schuberth et al. (2010), 2 = Dirsch et al. (2004), 3 = Bergond et al. (2007), 4 = Firth et al. (2007), 5 = Gregg et al. (2009), 6 = Mieske et al. (2004), 7 = Mieske et al. (2002), 8 = Firth et al. (2008), 9 = Kissler-Patig et al. (1999), 10 = Drinkwater et al. (2000a), 11 = Kissler-Patig et al. (1998).

ID	R.A. (J2000)	DEC. (J2000)	SIMBAD ID	v (km s^{-1})	LIT.
1	03 35 38.87	−35 21 53.3	[BAL2007] gc144.6	1388 ± 32	3
2	03 35 42.52	−35 13 51.8	[BAL2007] gc290.6	1901 ± 16	3
3	03 35 50.49	−35 15 24.2	[BAL2007] gc302.6	1166 ± 6	3
4	03 35 59.56	−35 26 56.7	[BAL2007] gc21.70	1272 ± 12	3
5	03 36 01.09	−35 25 43.0	[BAL2007] gc69.70	1389 ± 8	3
6	03 36 01.10	−35 26 22.3	[BAL2007] gc39.70	1324 ± 19	3
7	03 36 03.87	−35 27 26.6	[BAL2007] gc7.700	1411 ± 11	3
8	03 36 06.19	−35 27 32.9	[BAL2007] gc4.700	1252 ± 9	3
9	03 36 09.11	−35 25 43.7	[BAL2007] gc70.70	1403 ± 8	3
10	03 36 10.83	−35 24 22.4	[BAL2007] gc114.7	1362 ± 6	3
11	03 36 12.12	−35 27 07.8	[BAL2007] gc12.70	1419 ± 6	3
12	03 36 12.68	−35 19 11.4	[BAL2007] gc235.7	1310 ± 21	3
13	03 36 22.25	−35 36 34.1	[FDE2007] J033622.23-353634.4	1282 ± 10	4
14	03 36 23.56	−35 21 52.1	[BAL2007] gc173.7	1413 ± 10	3
15	03 36 26.69	−35 22 01.4	[FDE2007] J033626.67-352201.5	1315 ± 8	4
16	03 36 27.07	−35 17 33.2	[BAL2007] gc272.7	1573 ± 10	3
17	03 36 27.69	−35 14 13.9	[BAL2007] uc329.7	1386 ± 4	3
18	03 36 30.12	−35 17 53.9	[BAL2007] gc260.7	1879 ± 7	3
19	03 36 31.25	−35 26 58.2	[BAL2007] gc18.70	1320 ± 7	3
20	03 36 32.78	−35 18 30.1	[BAL2007] gc248.7	1611 ± 6	3
21	03 36 34.33	−35 19 32.4	[BAL2007] gc230.7	1861 ± 5	3
22	03 36 36.12	−35 18 38.4	[BAL2007] gc247.7	1447 ± 8	3
23	03 36 36.31	−35 21 58.5	[BAL2007] gc170.7	1472 ± 10	3
24	03 36 47.59	−35 29 36.8	[FDE2007] J033647.58-352937.1	1628 ± 7	4
25	03 36 47.72	−35 48 33.7	[FDE2007] J033647.69-354834.0	1358 ± 11	4
26	03 36 48.83	−35 22 46.3	[BAL2007] gc153.8	1223 ± 7	3
27	03 36 50.35	−35 20 16.7	[BAL2007] gc220.8	1606 ± 6	3
28	03 36 51.65	−35 30 38.8	[BAL2007] gc41.40	1462 ± 7	4
29	03 36 51.67	−35 05 35.0	[FDE2007] J033651.67-350535.1	1869 ± 20	4
30	03 36 53.20	−35 30 14.6	[BAL2007] gc57.40	1342 ± 16	3
31	03 36 54.58	−35 39 26.6	[FDE2007] J033654.57-353926.9	1469 ± 10	4
32	03 36 55.14	−35 30 36.0	[BAL2007] gc1387sw	1340 ± 10	3
33	03 36 55.26	−35 28 57.2	[FDE2007] J033655.24-352857.6	1273 ± 14	4
34	03 36 55.35	−35 29 37.8	[BAL2007] gc89.40	1209 ± 9	3
35	03 36 55.74	−35 29 21.7	[BAL2007] gc107.4	1260 ± 6	3
36	03 36 57.26	−35 29 56.9	[BAL2007] gc76.40	1246 ± 7	3
37	03 36 58.03	−35 34 32.1	[BAL2007] gc362.5	950 ± 7	3
38	03 36 58.23	−35 32 01.2	[FDE2007] J033658.21-353201.6	1327 ± 11	4
39	03 36 58.34	−35 32 07.0	[BAL2007] gc388.5	1314 ± 10	3
40	03 36 58.52	−35 29 45.5	[BAL2007] uc82.40	1379 ± 19	3
41	03 36 58.71	−35 30 36.3	[BAL2007] gc1387se	1273 ± 7	3

TABLE A.4 – *continued*

ID	R.A. (J2000)	DEC. (J2000)	SIMBAD ID	v (km s^{-1})	LIT.
42	03 36 59.59	−35 29 39.3	[BAL2007] gc90.40	1304 ± 7	3
43	03 37 00.05	−35 30 36.2	[BAL2007] gc44.40	1268 ± 13	3
44	03 37 00.35	−35 31 14.0	[BAL2007] gc19.40	1265 ± 7	3
45	03 37 00.66	−35 31 17.4	[FDE2007] J033700.64-353117.6	1337 ± 10	4
46	03 37 03.24	−35 38 04.4	[BAL2007] uc257.5	1561 ± 3	4
47	03 37 04.01	−35 30 16.5	[BAL2007] gc56.40	1372 ± 9	3
48	03 37 05.71	−35 37 32.1	[BAL2007] gc271.5	1520 ± 7	3
49	03 37 06.88	−35 30 48.6	[FDE2007] J033706.84-353048.8	1258 ± 12	4
50	03 37 06.93	−35 19 47.9	[SRH2010] 1 111	1720 ± 62	1
51	03 37 07.43	−35 24 14.5	[SRH2010] 1 33	1222 ± 93	1
52	03 37 09.50	−35 33 45.3	[FDE2007] J033709.48-353345.5	1555 ± 11	4
53	03 37 10.29	−35 24 56.4	[SRH2010] 1 18	2058 ± 61	1
54	03 37 11.18	−35 21 00.8	[SRH2010] 1 90	1302 ± 47	1
55	03 37 12.06	−35 09 54.9	[FDE2007] J033712.05-350955.1	1345 ± 13	4
56	03 37 12.66	−35 19 27.4	[SRH2010] 1 118	2145 ± 54	1
57	03 37 13.14	−35 30 41.3	[BAL2007] gc43.40	1465 ± 11	3
58	03 37 13.77	−35 24 48.3	[SRH2010] 1 21	1261 ± 49	1
59	03 37 15.52	−35 19 39.4	[SRH2010] 1 114	2229 ± 52	1
60	03 37 16.07	−35 23 21.0	[SRH2010] 2 49	1520 ± 65	1
61	03 37 16.49	−35 24 06.2	[SRH2010] 1 36	912 ± 35	1
62	03 37 17.69	−35 20 34.3	[SRH2010] 1 98	1463 ± 71	1
63	03 37 20.21	−35 23 05.4	[SRH2010] 2 54	1320 ± 80	1
64	03 37 20.29	−35 19 40.6	[SRH2010] 2 115	1384 ± 82	1
65	03 37 21.13	−35 32 57.2	[BAL2007] gc398.5	1713 ± 11	3
66	03 37 21.21	−35 19 05.1	[SRH2010] 2 126	1502 ± 56	1
67	03 37 21.32	−35 27 53.4	[BAL2007] gc155.4	1218 ± 12	3
68	03 37 21.35	−35 24 50.8	[SRH2010] 2 20	2209 ± 44	1
69	03 37 22.61	−35 19 22.5	[SRH2010] 2 121	1485 ± 35	1
70	03 37 23.49	−35 24 59.2	[SRH2010] 2 17	1048 ± 54	1
71	03 37 24.27	−35 22 57.4	[SRH2010] 2 57	1589 ± 42	1
72	03 37 24.85	−35 36 09.6	[FDE2007] J033724.83-353610.0	1448 ± 4	4
73	03 37 26.26	−35 41 05.7	[BAL2007] gc177.6	985 ± 8	3
74	03 37 26.32	−35 23 30.4	[SRH2010] 2 46	1516 ± 47	1
75	03 37 27.57	−35 30 12.5	[SRH2010] 3 94	1913 ± 5	3
76	03 37 27.82	−35 21 14.8	[SRH2010] 2 87	1343 ± 43	1
77	03 37 27.93	−35 33 41.1	[SRH2010] 3 29	1136 ± 54	1
78	03 37 28.00	−35 32 32.1	[SRH2010] 3 53	1437 ± 42	1
79	03 37 28.22	−35 21 22.7	[SRH2010] 2 84	1373 ± 19	8
80	03 37 29.04	−35 32 39.8	[SRH2010] 3 50	1119 ± 72	1
81	03 37 30.60	−35 19 28.8	[SRH2010] 2 119	1539 ± 15	1
82	03 37 31.04	−35 28 51.6	[SRH2010] 3 117	1144 ± 24	1
83	03 37 32.05	−35 33 24.1	[SRH2010] 3 34	1972 ± 48	1
84	03 37 32.25	−35 20 58.2	[SRH2010] 2 92	1198 ± 43	1
85	03 37 32.93	−35 16 51.8	[FDE2007] J033732.93-351652.0	1234 ± 16	4
86	03 37 33.04	−35 29 41.0	[SRH2010] 3 103	1396 ± 22	1
87	03 37 33.48	−35 28 12.4	[SRH2010] 3 129	1692 ± 15	4
88	03 37 33.79	−35 31 15.0	[SRH2010] 3 75	1638 ± 49	1
89	03 37 33.88	−35 22 18.8	FCOS 2-2161	1997 ± 15	8
90	03 37 33.90	−35 32 47.1	[SRH2010] 3 47	1748 ± 8	3
91	03 37 34.29	−35 25 10.1	[SRH2010] 2 14	1418 ± 36	1
92	03 37 34.57	−35 21 09.3	[SRH2010] 2 89	995 ± 76	1
93	03 37 34.69	−35 28 59.8	[SRH2010] 3 114	1304 ± 28	1
94	03 37 35.25	−35 25 29.5	[SRH2010] 2 7	1726 ± 33	1
95	03 37 35.26	−35 34 12.6	[SRH2010] 3 20	1261 ± 14	4
96	03 37 35.90	−35 17 36.4	[SRH2010] GS04-M03 199	1086 ± 59	1
97	03 37 35.94	−35 31 02.4	[SRH2010] 3 79	1761 ± 30	1
98	03 37 35.98	−35 31 52.4	[SRH2010] 3 64	684 ± 26	1

TABLE A.4 – *continued*

ID	R.A. (J2000)	DEC. (J2000)	SIMBAD ID	v (km s^{-1})	LIT.
99	03 37 36.70	−35 28 32.5	[SRH2010] 4 127	1988 ± 65	1
100	03 37 37.17	−35 31 51.8	[SRH2010] 4 64	989 ± 75	1
101	03 37 37.22	−35 28 38.1	[SRH2010] 3 122	1734 ± 43	1
102	03 37 38.10	−35 32 20.0	[SRH2010] 4 57	1550 ± 52	1
103	03 37 38.25	−35 20 20.5	[SRH2010] GS04-M03 97	2050 ± 16	1
104	03 37 38.31	−35 30 55.0	[SRH2010] 3 81	1695 ± 54	1
105	03 37 38.39	−35 18 50.5	[SRH2010] GS04-M03 170	936 ± 49	1
106	03 37 38.51	−35 34 01.4	[SRH2010] 3 24	2313 ± 51	1
107	03 37 39.71	−35 22 25.9	[SRH2010] GS04-M03 7	1361 ± 24	1
108	03 37 39.77	−35 21 11.9	[SRH2010] GS04-M03 56	1180 ± 35	1
109	03 37 40.01	−35 25 35.4	[SRH2010] GS04-M05 201	1321 ± 24	1
110	03 37 40.13	−35 32 21.2	[SRH2010] 3 57	794 ± 60	1
111	03 37 40.53	−35 34 23.1	[SRH2010] 3 17	1487 ± 45	1
112	03 37 41.05	−35 30 22.7	[SRH2010] 3 91	1501 ± 56	1
113	03 37 41.48	−35 34 52.4	[SRH2010] 3 7	1375 ± 40	1
114	03 37 41.51	−35 32 15.4	[SRH2010] 3 59	1348 ± 146	1
115	03 37 41.80	−35 41 22.9	[FDE2007] J033741.77-354123.2	1122 ± 5	4
116	03 37 41.94	−35 31 54.1	[SRH2010] 4 63	1677 ± 70	1
117	03 37 41.95	−35 26 11.0	[SRH2010] GS04-M05 129	1587 ± 52	1
118	03 37 42.25	−35 30 33.8	[SRH2010] 3 88	1319 ± 9	3
119	03 37 42.29	−35 25 46.3	[SRH2010] GS04-M05 134	1336 ± 27	1
120	03 37 42.37	−35 21 39.6	[SRH2010] GS04-M04 23	1679 ± 51	1
121	03 37 42.39	−35 25 24.1	[SRH2010] GS04-M05 144	1564 ± 59	1
122	03 37 43.03	−35 22 11.9	[GDE2009] UCD 15	1146 ± 86	5
123	03 37 43.50	−35 15 10.0	[FDE2007] J033743.49-351510.2	1255 ± 6	4
124	03 37 43.56	−35 30 40.1	[SRH2010] 3 86	1362 ± 47	1
125	03 37 43.57	−35 22 51.5	[BAL2007] gc302.3	1420 ± 7	4
126	03 37 44.05	−35 29 05.7	[SRH2010] 4 117	1002 ± 59	1
127	03 37 44.18	−35 26 13.8	[SRH2010] GS04-M05 114	1565 ± 44	1
128	03 37 44.20	−35 26 57.3	[KGM99] aat 4	2478 ± 150	9
129	03 37 44.72	−35 19 18.5	[SRH2010] GS04-M03 106	1192 ± 14	4
130	03 37 45.08	−35 29 01.4	[SRH2010] 4 118	1657 ± 9	3
131	03 37 45.39	−35 30 10.7	[SRH2010] 4 96	1909 ± 62	1
132	03 37 45.53	−35 26 41.6	[SRH2010] GS04-M05 96	1488 ± 21	1
133	03 37 45.67	−35 19 38.2	[SRH2010] GS04-M03 92	1425 ± 31	1
134	03 37 46.00	−35 28 39.9	[SRH2010] 4 125	1277 ± 28	1
135	03 37 46.45	−35 28 05.1	FCOS 2-095	1495 ± 45	7
136	03 37 46.72	−35 34 42.3	[SRH2010] 4 10	1386 ± 13	3
137	03 37 46.77	−35 30 02.3	[SRH2010] 4 99	1133 ± 39	1
138	03 37 46.80	−35 39 23.5	[BAL2007] gc225.6	1337 ± 9	4
139	03 37 47.03	−35 27 48.1	[BAL2007] gc133.3	1835 ± 20	3
140	03 37 47.18	−35 22 57.4	[SRH2010] GS04-M06 202	1486 ± 17	1
141	03 37 47.65	−35 32 47.9	[SRH2010] 4 47	1362 ± 34	1
142	03 37 47.74	−35 31 46.9	[SRH2010] 4 65	1083 ± 44	1
143	03 37 47.83	−35 31 34.9	[SRH2010] 4 69	1364 ± 46	1
144	03 37 48.12	−35 22 11.8	[SRH2010] GS04-M05 185	1297 ± 46	1
145	03 37 49.16	−35 28 51.7	[SRH2010] 4 121	1708 ± 35	1
146	03 37 49.84	−35 28 22.4	[SRH2010] 4 129	1379 ± 36	1
147	03 37 51.03	−35 34 35.5	[SRH2010] 4 12	938 ± 35	1
148	03 37 51.18	−35 23 01.5	[SRH2010] GS04-M06 127	1338 ± 51	1
149	03 37 51.34	−35 27 14.0	[SRH2010] GS04-M06 36	1581 ± 35	1
150	03 37 51.45	−35 25 58.2	[SRH2010] GS04-M05 68	1644 ± 24	1
151	03 37 51.81	−35 31 35.9	[SRH2010] 91 45	1466 ± 36	1
152	03 37 52.48	−35 28 57.6	[SRH2010] 92 99	1468 ± 18	1
153	03 37 52.67	−35 24 35.0	[SRH2010] GS04-M05 87	1515 ± 43	1
154	03 37 52.67	−35 30 52.0	[SRH2010] 91 57	1048 ± 19	1
155	03 37 53.00	−35 29 37.3	[SRH2010] 91 81	1091 ± 33	2

TABLE A.4 – *continued*

ID	R.A. (J2000)	DEC. (J2000)	SIMBAD ID	v (km s^{-1})	LIT.
156	03 37 53.05	−35 29 25.6	[SRH2010] 92 97	1753 ± 105	1
157	03 37 53.11	−35 27 20.6	[SRH2010] GS04-M06 15	848 ± 52	1
158	03 37 53.44	−35 26 16.1	[SRH2010] GS04-M05 40	1235 ± 19	1
159	03 37 53.57	−35 39 08.7	[SRH2010] 5 51	1529 ± 107	1
160	03 37 53.86	−35 35 17.9	[SRH2010] 5 119	1621 ± 55	1
161	03 37 53.88	−35 35 03.7	[SRH2010] 5 124	1392 ± 72	1
162	03 37 54.41	−35 26 33.3	[SRH2010] GS04-M05 22	1624 ± 42	1
163	03 37 54.47	−35 30 47.1	[SRH2010] 4 85	1209 ± 56	1
164	03 37 54.90	−35 29 53.4	[SRH2010] 91 75	1322 ± 47	1
165	03 37 55.14	−35 32 14.4	[SRH2010] 91 36	1222 ± 80	1
166	03 37 55.21	−35 30 14.2	[SRH2010] 91 69	1259 ± 29	1
167	03 37 55.31	−35 38 04.0	[SRH2010] 5 69	1124 ± 55	1
168	03 37 55.51	−35 29 33.9	[DRG2004] 92:88	1315 ± 49	2
169	03 37 55.55	−35 29 21.0	[SRH2010] 91 86	2120 ± 71	1
170	03 37 55.99	−35 32 53.9	[SRH2010] 91 24	971 ± 14	1
171	03 37 56.40	−35 39 15.0	[SRH2010] 5 49	1530 ± 18	4
172	03 37 56.86	−35 31 50.7	[SRH2010] 91 41	1472 ± 29	2
173	03 37 56.99	−35 41 01.8	[SRH2010] 5 15	1396 ± 64	1
174	03 37 57.16	−35 24 46.9	[SRH2010] GS04-M06 42	1302 ± 34	1
175	03 37 57.32	−35 26 21.0	[SRH2010] 82 4	2129 ± 37	1
176	03 37 57.74	−35 25 04.9	[SRH2010] 82 5	1076 ± 20	1
177	03 37 57.80	−35 31 13.7	[SRH2010] 91 51	1344 ± 27	2
178	03 37 57.91	−35 23 58.4	[SRH2010] GS04-M05 59	1268 ± 34	1
179	03 37 58.01	−35 26 47.0	[SRH2010] 82 6	607 ± 75	1
180	03 37 58.09	−35 32 00.1	[SRH2010] 91 39	1541 ± 60	1
181	03 37 58.37	−35 29 34.5	[SRH2010] 91 82	1694 ± 75	1
182	03 37 58.56	−35 25 58.5	[SRH2010] 82 8	1200 ± 38	1
183	03 37 58.69	−35 29 40.6	[SRH2010] 92 78	1952 ± 38	1
184	03 37 58.75	−35 29 32.2	[SRH2010] 91 83	1631 ± 21	1
185	03 37 58.76	−35 22 12.4	[KGM99] aat 13	1922 ± 150	9
186	03 37 58.97	−35 36 19.8	[SRH2010] 5 100	1316 ± 20	1
187	03 37 59.03	−35 32 56.1	[SRH2010] 91 23	1917 ± 61	2
188	03 37 59.38	−35 33 53.0	[SRH2010] 91 8	1977 ± 40	2
189	03 37 59.38	−35 30 25.1	[DRG2004] 92:76	1827 ± 57	2
190	03 37 59.45	−35 36 09.3	[SRH2010] 5 103	1564 ± 12	3
191	03 37 59.57	−35 36 25.3	[SRH2010] 5 99	1949 ± 9	3
192	03 38 00.18	−35 30 08.2	[SRH2010] 92 74	843 ± 10	2
193	03 38 00.50	−35 26 48.8	[SRH2010] 82 13	2025 ± 55	1
194	03 38 00.92	−35 26 24.4	[SRH2010] 82 14	1113 ± 24	1
195	03 38 00.95	−35 24 34.3	[SRH2010] GS04-M05 12	1527 ± 12	1
196	03 38 01.05	−35 30 25.0	[SRH2010] 91 66	1889 ± 36	2
197	03 38 01.09	−35 36 04.3	[SRH2010] 5 105	1624 ± 58	1
198	03 38 01.21	−35 28 01.4	[SRH2010] 91 111	2395 ± 34	2
199	03 38 01.73	−35 37 38.3	[SRH2010] 5 76	1329 ± 65	1
200	03 38 01.87	−35 37 01.6	[SRH2010] 5 87	877 ± 49	1
201	03 38 02.14	−35 25 57.0	[SRH2010] 81 17	1119 ± 54	1
202	03 38 02.20	−35 38 59.2	[SRH2010] 5 54	1358 ± 45	1
203	03 38 02.25	−35 34 23.2	[DRG2004] 91:1	1008 ± 74	2
204	03 38 02.34	−35 26 10.1	[SRH2010] 81 13	1868 ± 35	1
205	03 38 02.41	−35 30 36.1	[SRH2010] 91 63	789 ± 37	2
206	03 38 02.48	−35 41 18.6	[SRH2010] 5 9	933 ± 52	1
207	03 38 02.53	−35 25 03.5	[SRH2010] 81 32	1368 ± 44	1
208	03 38 02.82	−35 29 25.8	[SRH2010] 91 85	1517 ± 38	2
209	03 38 02.85	−35 24 57.7	[SRH2010] 81 34	1230 ± 34	2
210	03 38 03.01	−35 26 28.7	[SRH2010] 81 8	1783 ± 29	1
211	03 38 03.14	−35 28 25.9	[SRH2010] 91 102	1345 ± 19	1
212	03 38 03.18	−35 22 07.7	[SRH2010] 81 78	1386 ± 46	1

TABLE A.4 – *continued*

ID	R.A. (J2000)	DEC. (J2000)	SIMBAD ID	ν (km s^{-1})	LIT.
213	03 38 03.19	−35 26 44.2	[DRG2004] 81:3	1797 ± 82	2
214	03 38 03.23	−35 28 59.5	[DRG2004] 92:65	1268 ± 47	2
215	03 38 03.60	−35 26 05.5	[SRH2010] 81 14	1369 ± 32	1
216	03 38 03.92	−35 29 19.1	[SRH2010] 91 87	1410 ± 50	1
217	03 38 04.24	−35 31 39.6	[SRH2010] 91 44	1973 ± 53	1
218	03 38 04.25	−35 37 56.5	[SRH2010] 5 71	850 ± 45	1
219	03 38 04.30	−35 29 00.9	[SRH2010] 91 92	1435 ± 31	1
220	03 38 04.32	−35 27 46.8	[SRH2010] 91 115	1563 ± 29	1
221	03 38 04.44	−35 28 11.4	[SRH2010] 91 109	1648 ± 13	1
222	03 38 04.54	−35 30 58.8	[SRH2010] 91 55	1291 ± 28	1
223	03 38 04.66	−35 30 08.1	[SRH2010] 91 71	1544 ± 20	1
224	03 38 04.69	−35 23 25.2	[SRH2010] 81 57	1376 ± 43	1
225	03 38 04.79	−35 22 55.6	[SRH2010] 81 64	1433 ± 46	1
226	03 38 04.88	−35 19 21.6	[SRH2010] GS04-M01 135	743 ± 37	1
227	03 38 04.90	−35 31 09.9	[SRH2010] 91 52	1599 ± 25	1
228	03 38 05.05	−35 24 09.3	[GDE2009] UCD 19	1219 ± 7	8
229	03 38 05.18	−35 25 19.6	[SRH2010] 81 27	1686 ± 36	1
230	03 38 05.32	−35 29 32.2	[SRH2010] 92 58	1033 ± 37	2
231	03 38 05.61	−35 26 45.7	[SRH2010] 82 29	1511 ± 34	1
232	03 38 05.75	−35 26 48.3	[SRH2010] 81 2	1380 ± 27	1
233	03 38 05.93	−35 35 20.3	[SRH2010] 5 118	1514 ± 44	1
234	03 38 06.20	−35 33 21.6	[SRH2010] 91 15	1692 ± 85	1
235	03 38 06.29	−35 22 48.3	[SRH2010] 81 66	1736 ± 47	1
236	03 38 06.30	−35 28 58.6	[SRH2010] 91 93	1234 ± 5	3
237	03 38 06.50	−35 23 03.7	[GDE2009] UCD 21	1510 ± 64	5
238	03 38 06.50	−35 31 01.5	[SRH2010] 90 52	1098 ± 23	2
239	03 38 06.53	−35 28 16.0	[DRG2004] 91:106	2626 ± 42	2
240	03 38 06.67	−35 29 32.2	[SRH2010] 92 55	1643 ± 42	1
241	03 38 06.70	−35 26 46.3	[SRH2010] 82 31	1991 ± 38	1
242	03 38 07.02	−35 22 22.1	[SRH2010] 81 74	1388 ± 41	1
243	03 38 07.03	−35 26 39.4	[SRH2010] 81 5	858 ± 47	2
244	03 38 07.05	−35 29 31.2	[SRH2010] 92 54	1907 ± 37	2
245	03 38 07.06	−35 24 28.6	[SRH2010] 81 41	1270 ± 21	1
246	03 38 07.30	−35 25 48.4	[SRH2010] 81 20	1613 ± 17	1
247	03 38 07.48	−35 33 38.9	[SRH2010] 91 11	1106 ± 43	2
248	03 38 07.63	−35 20 49.7	[SRH2010] 81 98	1534 ± 48	2
249	03 38 07.67	−35 18 01.0	[SRH2010] GS04-M02 157	2172 ± 37	1
250	03 38 07.72	−35 21 59.2	[SRH2010] 81 81	1576 ± 25	1
251	03 38 07.74	−35 37 52.0	[SRH2010] 5 72	1576 ± 59	1
252	03 38 07.84	−35 19 37.2	[SRH2010] GS03-M03 166	1547 ± 24	1
253	03 38 07.86	−35 24 23.5	[SRH2010] 81 43	1634 ± 42	1
254	03 38 08.18	−35 27 52.0	[SRH2010] 91 113	1805 ± 21	2
255	03 38 08.47	−35 24 36.2	[SRH2010] 82 35	1686 ± 98	1
256	03 38 08.53	−35 23 55.4	[SRH2010] 81 49	1363 ± 42	2
257	03 38 08.54	−35 23 52.3	[SRH2010] 81 50	1658 ± 33	1
258	03 38 08.78	−35 29 13.5	[SRH2010] 90 82	1156 ± 37	1
259	03 38 08.81	−35 29 39.2	[SRH2010] 90 74	946 ± 20	2
260	03 38 08.82	−35 32 26.0	[BAL2007] gc466.7	1801 ± 10	3
261	03 38 08.92	−35 27 53.5	[SRH2010] 90 105	1743 ± 25	1
262	03 38 09.00	−35 18 45.5	[SRH2010] GS04-M01 164	1381 ± 33	1
263	03 38 09.00	−35 38 15.5	[SRH2010] 5 65	1303 ± 58	1
264	03 38 09.03	−35 23 11.6	[SRH2010] 81 60	1393 ± 37	1
265	03 38 09.15	−35 29 05.9	[SRH2010] 90 84	1292 ± 20	2
266	03 38 09.16	−35 38 13.9	[SRH2010] 5 66	1199 ± 24	1
267	03 38 09.24	−35 35 06.9	[SRH2010] 12 122	1776 ± 6	4
268	03 38 09.40	−35 31 00.1	[SRH2010] 89 52	1577 ± 26	2
269	03 38 09.43	−35 24 50.6	[SRH2010] 81 36	1524 ± 34	1

TABLE A.4 – *continued*

ID	R.A. (J2000)	DEC. (J2000)	SIMBAD ID	v (km s^{-1})	LIT.
270	03 38 09.59	−35 31 42.2	[SRH2010] 90 42	1053 ± 56	1
271	03 38 09.71	−35 24 37.3	[SRH2010] 81 39	1539 ± 22	1
272	03 38 09.75	−35 24 09.1	[SRH2010] 81 46	1837 ± 31	2
273	03 38 10.03	−35 25 33.2	[SRH2010] 81 24	1397 ± 53	2
274	03 38 10.03	−35 20 14.8	[SRH2010] 81 109	1627 ± 41	1
275	03 38 10.17	−35 26 32.0	[SRH2010] 81 7	1028 ± 37	1
276	03 38 10.21	−35 31 58.4	[SRH2010] 90 38	1718 ± 26	2
277	03 38 10.27	−35 24 26.0	[SRH2010] 81 42	1744 ± 50	1
278	03 38 10.34	−35 24 05.8	[SRH2010] 81 47	1605 ± 15	1
279	03 38 10.48	−35 28 54.4	[SRH2010] 90 87	1684 ± 44	1
280	03 38 10.50	−35 29 22.9	[SRH2010] 90 79	1385 ± 26	1
281	03 38 10.50	−35 24 36.5	[SRH2010] 82 41	1340 ± 67	1
282	03 38 10.73	−35 25 46.0	[GDE2009] UCD 24	1764 ± 55	5
283	03 38 10.91	−35 25 17.7	[SRH2010] 82 42	1771 ± 77	1
284	03 38 11.00	−35 28 46.9	[SRH2010] 90 89	1370 ± 66	1
285	03 38 11.00	−35 23 38.2	[SRH2010] 81 54	1342 ± 22	1
286	03 38 11.10	−35 24 53.8	[SRH2010] 81 35	1837 ± 25	1
287	03 38 11.21	−35 29 32.0	[SRH2010] 90 76	1051 ± 15	2
288	03 38 11.45	−35 29 30.0	[SRH2010] 90 77	1358 ± 19	2
289	03 38 11.67	−35 39 26.4	[SRH2010] 5 45	1625 ± 57	1
290	03 38 11.70	−35 27 16.2	[BAL2007] gc317.2	1434 ± 8	3
291	03 38 11.72	−35 26 45.0	[SRH2010] 82 44	741 ± 38	1
292	03 38 11.97	−35 39 57.1	[SRH2010] 12 34	1381 ± 6	4
293	03 38 12.01	−35 32 00.8	[SRH2010] 89 38	1336 ± 19	2
294	03 38 12.07	−35 25 36.9	[SRH2010] 81 23	1514 ± 18	1
295	03 38 12.09	−35 19 16.4	[SRH2010] GS03-M03 123	1645 ± 40	1
296	03 38 12.20	−35 26 27.3	[SRH2010] 82 45	1552 ± 32	1
297	03 38 12.25	−35 20 03.8	[SRH2010] GS03-M04 120	1060 ± 36	1
298	03 38 12.29	−35 22 11.3	[SRH2010] 81 77	1337 ± 32	1
299	03 38 12.45	−35 32 25.2	[SRH2010] 89 32	1532 ± 37	2
300	03 38 12.54	−35 21 26.9	[SRH2010] 81 88	1450 ± 41	1
301	03 38 12.57	−35 24 31.4	[SRH2010] 81 40	1610 ± 25	1
302	03 38 12.70	−35 28 57.0	[SRH2010] 89 84	1708 ± 13	2
303	03 38 12.78	−35 28 04.6	[SRH2010] 90 101	1559 ± 18	2
304	03 38 12.86	−35 32 47.2	[SRH2010] 89 26	1615 ± 30	2
305	03 38 13.08	−35 33 52.7	[SRH2010] 90 9	1566 ± 10	3
306	03 38 13.10	−35 31 07.0	[KGM99] aat 21	2085 ± 150	9
307	03 38 13.18	−35 28 56.9	[SRH2010] 92 37	1542 ± 21	1
308	03 38 13.30	−35 21 52.7	[SRH2010] 81 82	1131 ± 21	1
309	03 38 13.31	−35 31 42.3	[SRH2010] 89 42	1605 ± 37	2
310	03 38 13.38	−35 20 20.8	[SRH2010] 81 107	1233 ± 20	1
311	03 38 13.41	−35 37 38.0	[BAL2007] gc280.7	981 ± 13	3
312	03 38 13.55	−35 28 56.0	[BAL2007] gc156.2	1606 ± 14	3
313	03 38 13.66	−35 23 34.7	[SRH2010] 81 55	1662 ± 54	1
314	03 38 13.89	−35 34 08.5	[SRH2010] 90 4	954 ± 33	2
315	03 38 13.90	−35 25 52.3	[SRH2010] 81 19	1956 ± 34	1
316	03 38 13.92	−35 29 43.4	FCOS 2-089	1235 ± 45	7
317	03 38 14.15	−35 34 06.5	[SRH2010] GS04-M07 237	936 ± 43	1
318	03 38 14.18	−35 33 45.3	[SRH2010] 90 11	1257 ± 37	2
319	03 38 14.19	−35 26 43.6	[BAL2007] gc365.2	1143 ± 19	3
320	03 38 14.21	−35 30 24.5	[SRH2010] 92 34	1382 ± 43	2
321	03 38 14.69	−35 38 22.1	[SRH2010] 12 63	1367 ± 118	1
322	03 38 14.74	−35 22 18.5	[SRH2010] 81 75	995 ± 47	2
323	03 38 14.77	−35 33 24.7	[SRH2010] 90 15	1347 ± 11	3
324	03 38 14.77	−35 32 59.3	[DRG2004] 90:21	1464 ± 59	2
325	03 38 14.81	−35 33 39.6	[SRH2010] 90 12	1611 ± 23	1
326	03 38 14.90	−35 26 21.6	[SRH2010] 82 50	922 ± 47	1

TABLE A.4 – *continued*

ID	R.A. (J2000)	DEC. (J2000)	SIMBAD ID	ν (km s^{-1})	LIT.
327	03 38 15.10	−35 27 57.4	[SRH2010] 89 103	1711 ± 32	2
328	03 38 15.25	−35 18 31.1	[SRH2010] GS03-M03 97	1281 ± 35	1
329	03 38 15.28	−35 25 30.2	[SRH2010] 82 51	1736 ± 31	11
330	03 38 15.39	−35 29 46.4	[SRH2010] 90 72	1311 ± 35	2
331	03 38 15.49	−35 26 43.9	[SRH2010] 82 52	1155 ± 33	1
332	03 38 15.56	−35 32 03.5	[SRH2010] 89 37	1524 ± 23	2
333	03 38 15.61	−35 30 46.0	[SRH2010] 89 56	1719 ± 28	1
334	03 38 15.61	−35 21 35.9	[DRG2004] 80:94	1811 ± 79	2
335	03 38 15.61	−35 28 05.7	[DRG2004] 92:29	1103 ± 38	2
336	03 38 15.62	−35 31 12.2	[SRH2010] 89 49	1410 ± 30	2
337	03 38 15.68	−35 28 24.0	[SRH2010] 89 94	1573 ± 61	2
338	03 38 15.69	−35 26 00.4	[SRH2010] 80 17	1066 ± 15	1
339	03 38 16.03	−35 29 36.2	[SRH2010] 92 28	1604 ± 37	1
340	03 38 16.14	−35 25 40.3	[SRH2010] 82 54	1678 ± 31	1
341	03 38 16.24	−35 25 31.2	[DRG2004] 82:54	1726 ± 37	2
342	03 38 16.25	−35 27 48.7	[SRH2010] 90 107	1170 ± 39	2
343	03 38 16.39	−35 35 43.9	[SRH2010] 12 111	1570 ± 62	1
344	03 38 16.47	−35 30 25.0	[SRH2010] 90 62	2100 ± 30	2
345	03 38 16.48	−35 27 53.4	[SRH2010] 89 104	1088 ± 85	1
346	03 38 16.50	−35 26 19.5	[GDE2009] UCD 27	815 ± 30	11
347	03 38 16.51	−35 31 07.5	[SRH2010] 89 50	1487 ± 29	2
348	03 38 16.66	−35 20 22.8	[SRH2010] 80 115	1432 ± 20	2
349	03 38 16.66	−35 28 30.3	[SRH2010] 89 92	1484 ± 25	2
350	03 38 16.67	−35 29 35.0	[SRH2010] 89 74	1669 ± 9	3
351	03 38 16.73	−35 33 45.2	[DRG2004] 89:11	1585 ± 58	2
352	03 38 16.75	−35 27 56.3	[SRH2010] 90 104	1784 ± 30	2
353	03 38 16.79	−35 28 13.4	[DRG2004] 89:97	1571 ± 61	2
354	03 38 16.83	−35 25 12.8	[DRG2004] 80:31	1390 ± 45	2
355	03 38 16.84	−35 34 44.6	[SRH2010] GS04-M08 184	1630 ± 65	1
356	03 38 16.91	−35 30 20.2	[SRH2010] 89 63	2041 ± 40	2
357	03 38 16.92	−35 25 52.8	[SRH2010] 82 56	1935 ± 65	1
358	03 38 16.94	−35 38 12.5	[SRH2010] 12 66	1483 ± 67	1
359	03 38 17.07	−35 28 04.5	[SRH2010] 92 25	1146 ± 46	1
360	03 38 17.08	−35 26 30.9	[SRH2010] 82 57	1235 ± 12	3
361	03 38 17.13	−35 34 15.7	[SRH2010] 90 2	817 ± 27	2
362	03 38 17.27	−35 30 31.8	[SRH2010] 8 959	1936 ± 43	2
363	03 38 17.55	−35 21 48.6	[SRH2010] 80 90	1917 ± 26	2
364	03 38 17.60	−35 33 02.5	[SRH2010] 89 22	1514 ± 26	2
365	03 38 17.64	−35 29 35.3	[SRH2010] 90 75	1349 ± 21	2
366	03 38 17.65	−35 28 37.6	[SRH2010] 89 90	1306 ± 29	1
367	03 38 17.67	−35 28 26.5	[SRH2010] 89 93	1280 ± 37	1
368	03 38 17.71	−35 22 51.2	[SRH2010] 80 71	1499 ± 24	1
369	03 38 17.77	−35 29 14.4	[SRH2010] 92 23	1592 ± 61	1
370	03 38 17.80	−35 35 40.5	[SRH2010] 12 112	1466 ± 25	1
371	03 38 17.81	−35 27 50.4	[DRG2004] 89:105	859 ± 51	2
372	03 38 17.88	−35 30 05.1	[SRH2010] 89 67	1804 ± 46	2
373	03 38 17.89	−35 35 31.6	[SRH2010] 12 115	1818 ± 41	1
374	03 38 17.95	−35 36 08.9	[SRH2010] GS04-M07 111	1659 ± 55	1
375	03 38 17.98	−35 15 06.0	[FDE2007] J033817.97-351506.4	1291 ± 11	4
376	03 38 18.10	−35 30 53.5	[SRH2010] 90 54	1593 ± 31	2
377	03 38 18.20	−35 28 34.8	[SRH2010] 90 93	1446 ± 43	1
378	03 38 18.25	−35 24 54.5	[SRH2010] 80 35	1530 ± 17	2
379	03 38 18.25	−35 25 16.4	[SRH2010] 82 59	1282 ± 41	1
380	03 38 18.39	−35 25 52.5	[KBS98] 13	1247 ± 30	9
381	03 38 18.41	−35 27 39.7	[SRH2010] 89 107	1170 ± 39	2
382	03 38 18.42	−35 31 33.8	[SRH2010] 89 44	1590 ± 31	2
383	03 38 18.52	−35 22 03.5	[SRH2010] 80 86	1228 ± 17	1

TABLE A.4 – *continued*

ID	R.A. (J2000)	DEC. (J2000)	SIMBAD ID	v $(km\,s^{-1})$	LIT.
384	03 38 18.56	−35 28 08.6	[SRH2010] 89 99	527 ± 20	1
385	03 38 18.64	−35 36 05.8	[SRH2010] 12 105	1482 ± 37	1
386	03 38 18.77	−35 27 44.3	[SRH2010] 90 108	1376 ± 55	1
387	03 38 18.94	−35 25 59.2	[SRH2010] 82 61	1363 ± 39	1
388	03 38 18.97	−35 32 27.7	[SRH2010] 90 28	1108 ± 46	2
389	03 38 19.03	−35 29 51.0	[DRG2004] 90:71	2824 ± 29	2
390	03 38 19.03	−35 32 22.3	[SRH2010] 89 33	1782 ± 13	1
391	03 38 19.07	−35 26 37.3	[SRH2010] 80 6	1527 ± 14	1
392	03 38 19.13	−35 21 27.0	[SRH2010] 80 96	1760 ± 30	2
393	03 38 19.36	−35 26 10.9	[SRH2010] 82 62	1074 ± 25	1
394	03 38 19.49	−35 25 52.4	[SRH2010] 80 19	1245 ± 12	1
395	03 38 19.55	−35 31 47.6	[SRH2010] 89 41	942 ± 53	2
396	03 38 19.62	−35 33 27.4	[DRG2004] 89:16	965 ± 54	2
397	03 38 19.65	−35 29 17.5	[SRH2010] 90 81	1409 ± 49	2
398	03 38 19.70	−35 19 10.1	[SRH2010] GS03-M03 79	2014 ± 45	1
399	03 38 19.80	−35 23 39.2	[SRH2010] 80 56	865 ± 22	1
400	03 38 19.81	−35 27 44.8	[SRH2010] 92 15	1659 ± 55	1
401	03 38 19.88	−35 21 23.9	[SRH2010] 80 97	1062 ± 48	2
402	03 38 19.90	−35 40 58.4	[SRH2010] 12 14	1946 ± 52	1
403	03 38 20.00	−35 26 43.6	[SRH2010] 80 4	1452 ± 17	1
404	03 38 20.01	−35 30 01.6	[SRH2010] 89 68	1625 ± 54	2
405	03 38 20.25	−35 20 19.0	[SRH2010] 80 116	1339 ± 26	1
406	03 38 20.36	−35 25 07.4	[SRH2010] 82 65	1738 ± 44	1
407	03 38 20.45	−35 29 28.0	[SRH2010] 89 76	1256 ± 19	2
408	03 38 20.61	−35 26 10.9	[SRH2010] 80 13	1799 ± 23	2
409	03 38 20.84	−35 34 26.6	[SRH2010] GS04-M07 194	1524 ± 31	1
410	03 38 20.84	−35 28 28.5	[SRH2010] 92 11	1639 ± 38	1
411	03 38 20.87	−35 21 55.7	[SRH2010] 80 88	653 ± 59	2
412	03 38 20.93	−35 25 28.0	[SRH2010] 82 67	1563 ± 91	1
413	03 38 21.01	−35 30 12.8	[SRH2010] 89 65	1584 ± 26	2
414	03 38 21.23	−35 29 18.5	[SRH2010] 89 78	1343 ± 47	2
415	03 38 21.23	−35 29 23.6	[SRH2010] 92 10	1340 ± 40	1
416	03 38 21.34	−35 24 35.9	[SRH2010] 80 40	881 ± 18	2
417	03 38 21.39	−35 31 21.5	[DRG2004] 89:47	1416 ± 63	2
418	03 38 21.45	−35 24 20.6	[SRH2010] 80 46	1344 ± 32	1
419	03 38 21.46	−35 25 46.4	[SRH2010] 82 69	1265 ± 51	1
420	03 38 21.48	−35 26 05.1	[SRH2010] 80 15	1542 ± 26	2
421	03 38 21.54	−35 20 08.3	[SRH2010] 80 119	1416 ± 51	2
422	03 38 21.55	−35 23 18.5	[SRH2010] 80 62	1570 ± 40	1
423	03 38 21.56	−35 26 15.7	[SRH2010] 80 12	1458 ± 17	1
424	03 38 21.73	−35 25 15.0	[SRH2010] 80 30	1519 ± 20	1
425	03 38 21.76	−35 18 15.2	[SRH2010] GS03-M03 51	1308 ± 73	1
426	03 38 21.79	−35 33 50.6	[SRH2010] 89 10	1416 ± 31	1
427	03 38 21.82	−35 29 23.3	[SRH2010] 89 77	1648 ± 31	2
428	03 38 21.97	−35 25 29.2	[SRH2010] 82 71	1801 ± 29	1
429	03 38 21.99	−35 28 52.2	[SRH2010] 89 86	973 ± 37	2
430	03 38 22.03	−35 22 31.6	[SRH2010] 80 77	1257 ± 40	2
431	03 38 22.04	−35 29 36.6	[SRH2010] 92 8	1256 ± 28	2
432	03 38 22.16	−35 23 42.2	[SRH2010] 80 55	1031 ± 30	1
433	03 38 22.20	−35 21 04.3	[SRH2010] 80 103	1894 ± 70	1
434	03 38 22.24	−35 33 23.8	[SRH2010] 89 17	1569 ± 30	2
435	03 38 22.26	−35 29 31.3	[SRH2010] 89 75	1557 ± 68	1
436	03 38 22.43	−35 26 32.9	[SRH2010] 80 7	1197 ± 22	2
437	03 38 22.58	−35 25 46.4	[SRH2010] 82 73	1629 ± 81	1
438	03 38 22.58	−35 30 49.0	[SRH2010] 89 55	1723 ± 42	2
439	03 38 22.65	−35 26 49.1	[SRH2010] 80 2	974 ± 33	1
440	03 38 22.73	−35 28 48.6	[SRH2010] 89 87	1435 ± 49	2

TABLE A.4 – *continued*

ID	R.A. (J2000)	DEC. (J2000)	SIMBAD ID	v (km s^{-1})	LIT.
441	03 38 22.85	−35 16 55.6	[SRH2010] GS03-M04 38	1646 ± 24	1
442	03 38 22.86	−35 24 23.4	[SRH2010] 80 45	1541 ± 28	1
443	03 38 22.97	−35 25 03.7	[SRH2010] 80 33	1414 ± 15	1
444	03 38 23.06	−35 25 49.5	[SRH2010] 82 74	1693 ± 51	1
445	03 38 23.10	−35 30 54.1	[SRH2010] 89 54	1379 ± 33	2
446	03 38 23.20	−35 25 29.5	[SRH2010] 80 26	1651 ± 17	1
447	03 38 23.23	−35 24 29.8	[SRH2010] 80 42	1258 ± 31	1
448	03 38 23.24	−35 20 00.6	[SRH2010] GS03-M03 35	1309 ± 16	1
449	03 38 23.28	−35 26 33.0	[BAL2007] gc387.2	1505 ± 9	3
450	03 38 23.32	−35 30 22.1	[SRH2010] 89 62	1255 ± 30	1
451	03 38 23.37	−35 25 22.2	[SRH2010] 82 75	1531 ± 45	1
452	03 38 23.42	−35 39 53.3	[BAL2007] uc218.7	757 ± 21	3
453	03 38 23.43	−35 21 20.3	[SRH2010] 80 98	1517 ± 35	2
454	03 38 23.45	−35 30 48.4	[SRH2010] 92 4	906 ± 38	1
455	03 38 23.46	−35 21 18.3	[SRH2010] 80 99	1798 ± 49	1
456	03 38 23.54	−35 23 15.9	[SRH2010] 80 63	1917 ± 18	2
457	03 38 23.56	−35 23 32.6	[SRH2010] 80 58	1314 ± 18	1
458	03 38 23.60	−35 29 52.1	[DRG2004] 89:70	1468 ± 73	2
459	03 38 23.62	−35 25 33.3	[SRH2010] 82 76	1402 ± 53	1
460	03 38 23.74	−35 13 49.4	[FDE2007] J033823.73-351349.8	1637 ± 14	8
461	03 38 23.83	−35 28 48.7	[SRH2010] 92 3	1735 ± 27	2
462	03 38 23.89	−35 22 12.2	[SRH2010] 80 83	1614 ± 24	2
463	03 38 23.89	−35 35 55.5	[SRH2010] GS04-M07 76	1753 ± 59	1
464	03 38 23.93	−35 25 07.8	[SRH2010] 82 77	1633 ± 32	1
465	03 38 23.97	−35 29 37.5	[SRH2010] 89 73	1497 ± 35	2
466	03 38 24.07	−35 28 56.7	[SRH2010] 92 2	1415 ± 36	2
467	03 38 24.26	−35 25 32.3	[SRH2010] 82 78	1297 ± 50	1
468	03 38 24.65	−35 26 22.5	[SRH2010] 80 10	1181 ± 27	1
469	03 38 24.75	−35 25 25.7	[SRH2010] 82 80	1480 ± 51	1
470	03 38 25.04	−35 29 25.2	[GDE2009] UCD 34	1158 ± 64	5
471	03 38 25.28	−35 23 25.3	[SRH2010] 80 60	1407 ± 22	1
472	03 38 25.51	−35 22 44.7	[DRG2004] 80:73	2443 ± 71	2
473	03 38 25.54	−35 37 42.6	[SRH2010] 9 110	1740 ± 32	1
474	03 38 25.55	−35 16 05.6	[SRH2010] GS03-M04 15	1452 ± 20	1
475	03 38 25.66	−35 19 05.8	[SRH2010] GS03-M03 14	1421 ± 28	1
476	03 38 25.66	−35 29 19.9	FCOS 2-2107	1267 ± 101	6
477	03 38 25.75	−35 24 56.5	[SRH2010] 82 82	1462 ± 35	1
478	03 38 26.01	−35 24 37.1	[SRH2010] 82 83	1552 ± 35	1
479	03 38 26.24	−35 25 25.9	[SRH2010] 80 27	1231 ± 16	1
480	03 38 26.25	−35 22 24.7	[SRH2010] 80 79	1120 ± 28	1
481	03 38 26.42	−35 24 25.2	[SRH2010] 80 44	1808 ± 19	2
482	03 38 26.43	−35 34 25.1	[SRH2010] GS04-M08 120	1548 ± 45	1
483	03 38 26.43	−35 25 21.7	[SRH2010] 80 28	1753 ± 18	2
484	03 38 26.45	−35 38 38.2	[SRH2010] 9 94	1429 ± 63	1
485	03 38 26.51	−35 33 43.7	[SRH2010] GS04-M07 198	1334 ± 27	1
486	03 38 26.58	−35 35 18.5	[SRH2010] GS04-M07 80	997 ± 56	1
487	03 38 26.62	−35 41 42.9	[SRH2010] 9 43	1739 ± 15	3
488	03 38 26.64	−35 25 33.9	[SRH2010] 80 24	1434 ± 19	1
489	03 38 26.71	−35 30 07.4	[GDE2009] UCD 36	1475 ± 72	5
490	03 38 26.95	−35 20 31.8	[SRH2010] 80 112	1498 ± 37	1
491	03 38 27.18	−35 24 34.1	[SRH2010] 82 86	1891 ± 34	1
492	03 38 27.37	−35 25 37.4	[SRH2010] 80 23	1421 ± 24	2
493	03 38 27.79	−35 32 36.3	[SRH2010] GS04-M08 179	1509 ± 25	1
494	03 38 28.28	−35 39 10.8	[SRH2010] 9 84	777 ± 29	1
495	03 38 28.34	−35 34 12.5	[SRH2010] GS04-M07 116	1779 ± 29	1
496	03 38 28.35	−35 25 38.3	FCOS 0-2030	1771 ± 56	6
497	03 38 28.45	−35 28 21.1	[BAL2007] gc212.2	1804 ± 19	3

TABLE A.4 – *continued*

ID	R.A. (J2000)	DEC. (J2000)	SIMBAD ID	v (km s^{-1})	LIT.
498	03 38 28.47	−35 25 12.2	[SRH2010] 78 119	1102 ± 56	1
499	03 38 28.87	−35 25 00.4	[SRH2010] 78 117	1462 ± 27	1
500	03 38 28.97	−35 22 56.1	[GDE2009] UCD 38	1654 ± 69	6
501	03 38 29.53	−35 25 08.2	[SRH2010] 78 115	1362 ± 24	1
502	03 38 29.61	−35 37 09.1	[SRH2010] 9 120	2025 ± 39	1
503	03 38 29.69	−35 31 08.2	[SRH2010] 86 50	1453 ± 24	1
504	03 38 30.03	−35 33 27.3	[SRH2010] GS04-M07 135	1491 ± 23	1
505	03 38 30.17	−35 28 47.9	[BAL2007] gc172.2a	1946 ± 8	3
506	03 38 30.18	−35 25 07.8	[SRH2010] 78 113	1019 ± 31	1
507	03 38 30.20	−35 21 31.1	FCOS 0-2032	1402 ± 73	6
508	03 38 30.40	−35 34 20.7	[SRH2010] GS04-M07 93	1263 ± 10	3
509	03 38 30.68	−35 27 46.3	FCOS 0-2033	1400 ± 113	6
510	03 38 30.74	−35 24 40.5	[SRH2010] 77 40	1302 ± 20	1
511	03 38 30.78	−35 39 56.6	[SRH2010] 9 71	1676 ± 9	3
512	03 38 30.97	−35 31 56.8	[SRH2010] 86 35	1880 ± 29	1
513	03 38 30.98	−35 24 38.7	[SRH2010] 78 110	1642 ± 43	1
514	03 38 31.35	−35 24 16.9	[SRH2010] 78 109	1720 ± 64	2
515	03 38 31.38	−35 20 11.3	[SRH2010] 13 16	1711 ± 49	1
516	03 38 31.43	−35 30 05.9	[SRH2010] 86 69	1670 ± 30	1
517	03 38 31.59	−35 29 43.4	[SRH2010] 86 75	1231 ± 29	1
518	03 38 31.61	−35 24 53.4	[SRH2010] 77 35	1515 ± 26	1
519	03 38 31.64	−35 24 33.1	[SRH2010] 78 108	1156 ± 31	2
520	03 38 31.75	−35 30 58.9	[SRH2010] 86 53	1627 ± 32	2
521	03 38 31.75	−35 29 28.7	[SRH2010] 86 80	1184 ± 82	1
522	03 38 31.89	−35 30 32.7	[SRH2010] 86 60	1289 ± 34	1
523	03 38 31.99	−35 14 52.4	[SRH2010] 13 109	1528 ± 37	1
524	03 38 32.08	−35 28 12.8	FCOS 0-2072	1559 ± 102	6
525	03 38 32.09	−35 33 24.1	[SRH2010] 86 13	1580 ± 23	2
526	03 38 32.13	−35 24 54.7	[SRH2010] 78 106	1263 ± 25	1
527	03 38 32.43	−35 37 47.2	[SRH2010] 9 109	1685 ± 29	1
528	03 38 32.49	−35 17 12.8	[SRH2010] 13 71	1296 ± 34	1
529	03 38 32.60	−35 29 58.4	[SRH2010] 86 71	1318 ± 23	2
530	03 38 32.61	−35 25 29.5	[SRH2010] 77 25	1686 ± 37	2
531	03 38 32.85	−35 16 18.6	[SRH2010] 13 86	1633 ± 48	1
532	03 38 32.88	−35 30 22.6	[SRH2010] 86 63	1813 ± 52	2
533	03 38 32.97	−35 29 01.3	[SRH2010] 86 89	1819 ± 42	2
534	03 38 33.26	−35 25 18.9	[SRH2010] 78 102	1040 ± 43	2
535	03 38 33.29	−35 40 46.0	[SRH2010] 9 57	1744 ± 52	1
536	03 38 33.38	−35 32 28.9	[SRH2010] 86 26	1862 ± 15	1
537	03 38 33.39	−35 19 47.2	[SRH2010] 13 24	1403 ± 53	1
538	03 38 33.48	−35 22 12.1	[SRH2010] 77 86	808 ± 46	2
539	03 38 33.58	−35 31 50.7	[SRH2010] 86 37	1736 ± 31	1
540	03 38 33.58	−35 23 23.9	[SRH2010] 77 63	1176 ± 40	1
541	03 38 33.63	−35 25 08.8	[SRH2010] 77 30	1401 ± 58	1
542	03 38 33.82	−35 25 57.1	FCOS 1-2095	1245 ± 220	6
543	03 38 33.87	−35 25 21.6	[SRH2010] 78 100	1321 ± 23	1
544	03 38 33.92	−35 21 54.5	[SRH2010] 77 92	1235 ± 23	1
545	03 38 34.01	−35 28 44.7	[SRH2010] 86 94	1938 ± 33	2
546	03 38 34.03	−35 31 55.1	[SRH2010] 86 36	1182 ± 54	1
547	03 38 34.06	−35 36 08.4	[SRH2010] GS04-M07 21	1521 ± 34	1
548	03 38 34.11	−35 33 53.9	[SRH2010] 86 6	1519 ± 30	1
549	03 38 34.27	−35 30 48.3	[SRH2010] 86 56	1946 ± 34	1
550	03 38 34.28	−35 24 35.4	[DRG2004] 77:42	1288 ± 58	2
551	03 38 34.33	−35 33 58.6	[SRH2010] 86 4	1502 ± 17	2
552	03 38 34.47	−35 34 31.1	[SRH2010] GS04-M07 69	1307 ± 31	1
553	03 38 34.58	−35 25 36.5	[SRH2010] 77 23	1228 ± 28	1
554	03 38 34.75	−35 29 12.0	[SRH2010] 86 85	1561 ± 22	2

TABLE A.4 – *continued*

ID	R.A. (J2000)	DEC. (J2000)	SIMBAD ID	v (km s^{-1})	LIT.
555	03 38 34.76	−35 25 40.9	[SRH2010] 78 98	1497 ± 49	1
556	03 38 34.93	−35 25 46.9	[SRH2010] 77 20	1282 ± 42	2
557	03 38 35.15	−35 39 05.6	[SRH2010] 9 86	1539 ± 35	1
558	03 38 35.23	−35 23 18.5	[SRH2010] 77 65	1061 ± 39	1
559	03 38 35.25	−35 25 39.1	[SRH2010] 78 96	1614 ± 27	1
560	03 38 35.36	−35 30 35.8	[SRH2010] 86 59	1516 ± 17	1
561	03 38 35.49	−35 25 29.4	[SRH2010] 78 95	1276 ± 23	1
562	03 38 35.66	−35 20 05.7	[SRH2010] 77 127	1546 ± 27	2
563	03 38 35.66	−35 31 02.0	[SRH2010] 86 52	1395 ± 18	2
564	03 38 35.67	−35 27 15.7	FCOS 0-2074	2274 ± 112	6
565	03 38 35.79	−35 25 34.0	[SRH2010] 77 24	1319 ± 28	1
566	03 38 35.81	−35 24 48.2	[SRH2010] 77 37	1304 ± 33	1
567	03 38 35.91	−35 22 49.3	[SRH2010] 77 75	1535 ± 28	2
568	03 38 35.95	−35 32 36.4	[SRH2010] 86 24	1471 ± 17	2
569	03 38 36.08	−35 32 16.8	[SRH2010] 86 29	1371 ± 16	2
570	03 38 36.13	−35 32 11.8	[KGM99] aat 36	1038 ± 150	9
571	03 38 36.76	−35 31 36.7	[SRH2010] 86 42	1566 ± 30	2
572	03 38 36.77	−35 29 54.2	[SRH2010] 86 72	1563 ± 42	1
573	03 38 36.82	−35 24 19.1	[SRH2010] 77 47	1411 ± 38	1
574	03 38 36.85	−35 28 09.3	[GDE2009] UCD 40	1365 ± 56	5
575	03 38 37.00	−35 37 16.9	[SRH2010] 10 119	2024 ± 47	1
576	03 38 37.07	−35 20 51.9	[SRH2010] 77 112	1563 ± 35	1
577	03 38 37.22	−35 28 12.9	[BAL2007] gc221.2	1578 ± 15	3
578	03 38 37.60	−35 32 25.3	[SRH2010] 86 27	1393 ± 56	2
579	03 38 37.67	−35 39 45.7	[SRH2010] 10 72	1795 ± 70	1
580	03 38 37.71	−35 26 01.5	[SRH2010] 78 88	1385 ± 49	2
581	03 38 37.73	−35 28 17.8	[DRG2004] 86:101	1264 ± 38	2
582	03 38 37.78	−35 21 12.7	[SRH2010] 77 106	856 ± 51	2
583	03 38 37.82	−35 22 33.6	[SRH2010] 77 80	1258 ± 21	2
584	03 38 37.98	−35 23 32.9	[BAL2007] gc613.2	1050 ± 15	3
585	03 38 38.00	−35 28 00.8	[SRH2010] 86 107	1382 ± 18	1
586	03 38 38.09	−35 26 14.9	[SRH2010] 77 12	2008 ± 49	1
587	03 38 38.10	−35 33 26.9	[SRH2010] 86 12	1861 ± 24	2
588	03 38 38.14	−35 26 46.6	[SRH2010] 77 2	1800 ± 13	3
589	03 38 38.16	−35 43 42.0	[SRH2010] 10 8	2378 ± 105	1
590	03 38 38.24	−35 15 22.1	[SRH2010] 13 102	1769 ± 82	1
591	03 38 38.24	−35 23 31.4	[SRH2010] 77 61	1925 ± 23	1
592	03 38 38.25	−35 30 38.8	[SRH2010] 86 58	1122 ± 18	1
593	03 38 38.25	−35 24 43.2	[SRH2010] 77 39	1797 ± 33	1
594	03 38 38.29	−35 21 26.4	[SRH2010] 77 102	1552 ± 31	1
595	03 38 38.29	−35 38 00.4	[SRH2010] 10 106	1406 ± 46	1
596	03 38 38.43	−35 26 02.5	[SRH2010] 77 16	1391 ± 43	1
597	03 38 38.44	−35 31 05.5	[SRH2010] 86 51	1565 ± 23	1
598	03 38 38.46	−35 26 13.6	[SRH2010] 78 85	1528 ± 54	1
599	03 38 38.46	−35 23 50.5	[SRH2010] 77 55	1478 ± 37	1
600	03 38 38.50	−35 29 26.0	[SRH2010] 86 81	1300 ± 16	1
601	03 38 38.55	−35 27 51.9	[SRH2010] 86 110	1524 ± 17	1
602	03 38 38.61	−35 33 35.2	[SRH2010] 86 10	1606 ± 22	1
603	03 38 38.63	−35 24 58.8	[SRH2010] 76 38	1012 ± 36	1
604	03 38 38.64	−35 24 26.9	[SRH2010] 77 45	1566 ± 39	1
605	03 38 38.75	−35 25 42.7	[SRH2010] 77 21	1647 ± 18	1
606	03 38 38.78	−35 20 39.6	[SRH2010] 77 115	1471 ± 57	2
607	03 38 38.78	−35 25 54.9	[SRH2010] 78 84	1019 ± 18	1
608	03 38 38.80	−35 25 04.2	[SRH2010] 77 31	1247 ± 30	1
609	03 38 38.87	−35 26 38.4	[SRH2010] 77 4	1303 ± 43	2
610	03 38 38.92	−35 31 32.4	[SRH2010] 86 43	1833 ± 25	2
611	03 38 38.93	−35 28 56.1	[SRH2010] 86 91	1337 ± 38	2

TABLE A.4 – *continued*

ID	R.A. (J2000)	DEC. (J2000)	SIMBAD ID	v (km s^{-1})	LIT.
612	03 38 38.98	−35 32 56.0	[SRH2010] 86 19	1387 ± 31	1
613	03 38 39.03	−35 27 37.6	[SRH2010] 86 113	1239 ± 21	1
614	03 38 39.08	−35 24 32.8	[SRH2010] 77 43	1391 ± 33	2
615	03 38 39.12	−35 33 40.9	[SRH2010] 86 9	1472 ± 20	1
616	03 38 39.21	−35 28 13.9	[SRH2010] 86 102	2249 ± 38	2
617	03 38 39.23	−35 32 01.1	[SRH2010] 86 33	1623 ± 20	1
618	03 38 39.34	−35 27 06.0	[GDE2009] UCD 42	1610 ± 40	7
619	03 38 39.36	−35 28 47.9	[KGM99] aat 39	1639 ± 150	9
620	03 38 39.42	−35 25 41.7	[SRH2010] 78 82	1387 ± 23	2
621	03 38 39.56	−35 29 16.0	[SRH2010] 86 84	1088 ± 22	2
622	03 38 39.72	−35 31 23.0	[SRH2010] 86 46	1423 ± 31	2
623	03 38 40.05	−35 29 20.4	[SRH2010] 86 83	1781 ± 20	1
624	03 38 40.22	−35 31 44.8	[SRH2010] 86 39	1455 ± 14	1
625	03 38 40.24	−35 21 09.0	[SRH2010] 76 108	1293 ± 38	1
626	03 38 40.26	−35 29 07.6	[SRH2010] 86 87	930 ± 18	1
627	03 38 40.27	−35 21 33.1	[SRH2010] 76 101	1893 ± 26	1
628	03 38 40.28	−35 31 17.4	[SRH2010] 86 48	1328 ± 12	2
629	03 38 40.33	−35 21 39.7	[SRH2010] 76 98	1571 ± 22	1
630	03 38 40.41	−35 28 47.4	[SRH2010] 86 93	1353 ± 13	1
631	03 38 40.42	−35 22 53.2	[SRH2010] 76 76	1954 ± 27	1
632	03 38 40.48	−35 26 47.1	[SRH2010] 76 2	1760 ± 53	1
633	03 38 40.56	−35 29 24.1	[SRH2010] 86 82	1009 ± 22	1
634	03 38 40.56	−35 20 06.0	[DRG2004] 76:123	1280 ± 57	2
635	03 38 40.56	−35 29 09.6	[SRH2010] 86 86	660 ± 16	2
636	03 38 40.59	−35 27 34.3	[SRH2010] 86 114	1517 ± 54	1
637	03 38 40.70	−35 27 49.9	[KGM99] aat 42	1504 ± 150	9
638	03 38 40.72	−35 26 08.0	[SRH2010] 77 14	1222 ± 66	2
639	03 38 40.73	−35 26 20.7	[SRH2010] 76 10	1826 ± 38	1
640	03 38 40.79	−35 29 34.2	[SRH2010] 86 78	1210 ± 24	2
641	03 38 40.83	−35 24 32.7	[SRH2010] 76 46	1349 ± 32	2
642	03 38 40.87	−35 31 39.2	[SRH2010] 86 41	1811 ± 37	2
643	03 38 41.02	−35 22 42.0	[SRH2010] 76 80	1665 ± 17	1
644	03 38 41.24	−35 25 23.4	[DRG2004] 76:30	1680 ± 66	2
645	03 38 41.35	−35 28 46.4	FCOS 1-2080	1647 ± 124	6
646	03 38 41.38	−35 28 53.3	[SRH2010] 86 92	961 ± 26	1
647	03 38 41.43	−35 27 41.0	[SRH2010] 86 112	891 ± 22	2
648	03 38 41.53	−35 34 02.4	[SRH2010] 7 46	1941 ± 69	1
649	03 38 41.60	−35 31 37.1	[SRH2010] 7 86	1464 ± 43	1
650	03 38 41.61	−35 26 42.2	[SRH2010] 77 3	1783 ± 28	2
651	03 38 41.81	−35 24 43.0	[SRH2010] 76 43	1536 ± 24	2
652	03 38 41.82	−35 23 04.8	[SRH2010] 76 73	1483 ± 30	1
653	03 38 41.84	−35 26 00.6	[SRH2010] 76 18	1874 ± 18	1
654	03 38 41.92	−35 29 48.5	[BAL2007] gc91.20	1484 ± 9	3
655	03 38 41.95	−35 33 13.0	[FDE2007] J033841.94-353313.0	2010 ± 5	4
656	03 38 41.97	−35 37 11.4	[SRH2010] 10 121	1760 ± 51	1
657	03 38 41.98	−35 28 03.6	[SRH2010] 86 106	878 ± 48	1
658	03 38 42.03	−35 37 37.4	[SRH2010] 10 113	1341 ± 99	1
659	03 38 42.07	−35 26 18.7	[SRH2010] 76 11	1405 ± 22	1
660	03 38 42.20	−35 25 55.0	[SRH2010] 77 18	1762 ± 36	1
661	03 38 42.28	−35 33 34.9	[SRH2010] 7 55	2016 ± 47	1
662	03 38 42.30	−35 26 11.9	[SRH2010] 78 71	1327 ± 35	2
663	03 38 42.34	−35 38 24.6	[SRH2010] 10 98	1378 ± 75	1
664	03 38 42.39	−35 26 33.9	[SRH2010] 76 6	1404 ± 42	1
665	03 38 42.39	−35 21 16.8	[SRH2010] 76 106	1895 ± 32	1
666	03 38 42.55	−35 26 12.7	[SRH2010] 76 13	1120 ± 30	1
667	03 38 42.56	−35 41 40.8	[SRH2010] 10 43	2033 ± 27	1
668	03 38 43.06	−35 23 21.4	[SRH2010] 76 67	1565 ± 29	2

TABLE A.4 – *continued*

ID	R.A. (J2000)	DEC. (J2000)	SIMBAD ID	v (km s^{-1})	LIT.
669	03 38 43.06	−35 16 47.8	[SRH2010] 13 78	1395 ± 90	1
670	03 38 43.14	−35 29 39.6	[SRH2010] 86 76	1369 ± 28	1
671	03 38 43.27	−35 24 14.4	[SRH2010] 76 51	496 ± 43	2
672	03 38 43.33	−35 33 44.5	[SRH2010] 7 52	1657 ± 57	1
673	03 38 43.41	−35 21 58.9	[SRH2010] 76 93	1424 ± 23	1
674	03 38 43.41	−35 25 40.2	[SRH2010] 76 24	1977 ± 43	2
675	03 38 43.44	−35 28 06.4	[SRH2010] 86 105	555 ± 25	2
676	03 38 43.52	−35 26 03.8	[SRH2010] 78 66	1381 ± 40	2
677	03 38 43.53	−35 33 08.0	[BAL2007] gc465.7	1743 ± 13	3
678	03 38 43.57	−35 24 04.1	[SRH2010] 76 54	1557 ± 29	1
679	03 38 43.59	−35 30 22.9	[SRH2010] 7 109	1880 ± 43	1
680	03 38 43.68	−35 31 40.9	[SRH2010] 7 85	1677 ± 48	1
681	03 38 43.96	−35 30 19.7	[SRH2010] 7 110	1655 ± 41	1
682	03 38 44.00	−35 25 04.3	[SRH2010] 76 36	1467 ± 27	1
683	03 38 44.09	−35 19 01.7	FCOS 0-2041	1287 ± 66	6
684	03 38 44.09	−35 39 32.5	[SRH2010] 10 77	1672 ± 68	1
685	03 38 44.21	−35 24 53.7	[SRH2010] 76 40	1194 ± 37	2
686	03 38 44.26	−35 30 28.4	[SRH2010] 7 107	1957 ± 42	1
687	03 38 44.27	−35 35 40.3	[SRH2010] 7 14	2084 ± 50	1
688	03 38 44.36	−35 22 59.9	[SRH2010] 76 74	1317 ± 82	1
689	03 38 44.41	−35 30 06.5	[SRH2010] 7 114	1249 ± 35	1
690	03 38 44.56	−35 23 30.0	[SRH2010] 76 65	1454 ± 96	1
691	03 38 44.76	−35 31 52.2	[SRH2010] 7 83	1748 ± 20	1
692	03 38 44.79	−35 25 22.4	[DRG2004] 78:61	843 ± 68	2
693	03 38 44.89	−35 37 30.8	[SRH2010] 10 115	2017 ± 15	1
694	03 38 44.95	−35 30 13.1	[SRH2010] 86 67	781 ± 18	1
695	03 38 45.19	−35 34 42.4	[SRH2010] 7 32	1642 ± 19	1
696	03 38 45.64	−35 23 42.2	[SRH2010] 76 61	1146 ± 44	2
697	03 38 45.82	−35 34 26.8	[FDE2007] J033845.80-353426.6	1845 ± 87	5
698	03 38 45.88	−35 25 28.2	[SRH2010] 76 28	1665 ± 38	1
699	03 38 45.91	−35 43 36.0	[SRH2010] 10 10	1518 ± 50	1
700	03 38 45.91	−35 24 41.6	[DRG2004] 78:58	1158 ± 64	2
701	03 38 46.17	−35 34 31.4	[SRH2010] 7 36	1740 ± 38	1
702	03 38 46.40	−35 25 54.0	[SRH2010] 76 20	1282 ± 31	2
703	03 38 46.42	−35 37 23.1	[SRH2010] 10 117	2052 ± 10	3
704	03 38 46.48	−35 40 23.9	[SRH2010] 10 61	1402 ± 52	1
705	03 38 46.50	−35 30 48.2	[SRH2010] 7 101	1854 ± 50	1
706	03 38 46.51	−35 32 40.3	[SRH2010] 7 68	688 ± 37	1
707	03 38 46.92	−35 23 48.5	[SRH2010] 76 59	1680 ± 30	1
708	03 38 47.02	−35 20 50.6	[SRH2010] 76 112	1074 ± 62	1
709	03 38 47.33	−35 24 50.3	[SRH2010] 76 41	1050 ± 23	1
710	03 38 47.34	−35 34 55.5	[SRH2010] 7 27	1983 ± 38	1
711	03 38 47.41	−35 37 13.5	[FDE2007] J033847.41-353713.6	1893 ± 68	5
712	03 38 47.42	−35 23 09.5	[SRH2010] 76 70	785 ± 72	1
713	03 38 47.44	−35 37 49.9	[SRH2010] 10 109	2005 ± 39	1
714	03 38 47.51	−35 26 06.1	[SRH2010] 76 16	1602 ± 40	1
715	03 38 47.56	−35 38 38.0	[SRH2010] 10 94	1847 ± 52	1
716	03 38 47.59	−35 32 03.5	[SRH2010] 7 80	1562 ± 21	1
717	03 38 47.90	−35 34 27.0	[SRH2010] 7 37	1941 ± 17	1
718	03 38 47.90	−35 24 47.6	[SRH2010] 76 42	2417 ± 55	2
719	03 38 48.23	−35 24 54.2	[DRG2004] 75:35	1154 ± 38	2
720	03 38 48.48	−35 25 05.1	[SRH2010] 78 48	1975 ± 33	1
721	03 38 48.86	−35 27 43.9	FCOS 1-2089	1821 ± 150	9
722	03 38 48.92	−35 22 49.9	[SRH2010] 75 71	1688 ± 42	1
723	03 38 48.94	−35 21 22.4	[SRH2010] 76 104	1704 ± 28	1
724	03 38 48.99	−35 33 57.1	[SRH2010] 7 48	1240 ± 38	1
725	03 38 49.02	−35 35 33.1	[BAL2007] gc1404w	1730 ± 36	3

TABLE A.4 – *continued*

ID	R.A. (J2000)	DEC. (J2000)	SIMBAD ID	v (km s^{-1})	LIT.
726	03 38 49.05	−35 39 05.0	[SRH2010] 10 85	1441 ± 25	1
727	03 38 49.16	−35 21 42.2	[SRH2010] 75 92	889 ± 18	2
728	03 38 49.34	−35 22 59.0	[SRH2010] 75 68	1335 ± 55	2
729	03 38 49.36	−35 38 30.5	[SRH2010] 10 96	2189 ± 38	1
730	03 38 49.37	−35 34 02.1	[SRH2010] 84 6	1894 ± 52	2
731	03 38 49.51	−35 29 39.0	[SRH2010] 7 123	1949 ± 12	3
732	03 38 49.74	−35 24 57.8	[SRH2010] 75 34	1408 ± 40	1
733	03 38 49.83	−35 34 49.5	[SRH2010] 7 29	1782 ± 39	1
734	03 38 49.85	−35 23 35.8	[SRH2010] 76 63	972 ± 16	3
735	03 38 50.40	−35 22 07.8	[SRH2010] 75 85	1557 ± 20	1
736	03 38 50.59	−35 26 32.5	[DRG2004] 75:8	1137 ± 65	2
737	03 38 50.60	−35 24 29.2	[SRH2010] 75 43	1662 ± 26	2
738	03 38 50.69	−35 24 27.0	[SRH2010] 75 44	1371 ± 34	2
739	03 38 50.74	−35 24 48.2	[SRH2010] 75 37	1293 ± 47	2
740	03 38 51.08	−35 24 20.8	[SRH2010] 75 46	1268 ± 26	1
741	03 38 51.32	−35 33 54.8	[SRH2010] 84 8	1525 ± 31	1
742	03 38 51.61	−35 36 10.6	[BAL2007] gc1404s	2174 ± 16	3
743	03 38 51.66	−35 27 34.9	[SRH2010] 84 110	1154 ± 30	2
744	03 38 51.73	−35 29 39.5	[DRG2004] 84:73	2039 ± 72	2
745	03 38 51.92	−35 24 30.9	[DRG2004] 78:35	1046 ± 137	2
746	03 38 52.05	−35 35 15.0	[BAL2007] gc1404n	1816 ± 16	3
747	03 38 52.32	−35 31 29.6	[SRH2010] 7 88	813 ± 43	1
748	03 38 52.37	−35 32 23.6	[SRH2010] 84 31	1406 ± 36	1
749	03 38 52.69	−35 26 40.7	[DRG2004] 76:4	1175 ± 44	2
750	03 38 52.79	−35 32 26.9	[SRH2010] 7 72	1093 ± 42	1
751	03 38 52.93	−35 26 35.6	[SRH2010] 75 7	1234 ± 78	1
752	03 38 53.08	−35 25 27.4	[DRG2004] 75:25	1804 ± 57	2
753	03 38 53.15	−35 31 01.4	[SRH2010] 84 53	1772 ± 32	1
754	03 38 53.25	−35 36 51.8	[BAL2007] gc269.8	2000 ± 13	3
755	03 38 54.03	−35 31 57.8	[SRH2010] 84 39	1487 ± 15	2
756	03 38 54.05	−35 33 33.4	[FDE2007] J033854.05-353333.6	1491 ± 2	4
757	03 38 54.21	−35 24 36.3	[DRG2004] 78 : 28	811 ± 48	2
758	03 38 54.26	−35 21 37.9	[SRH2010] 75 93	1221 ± 59	1
759	03 38 54.38	−35 24 43.3	[SRH2010] 75 39	1335 ± 58	1
760	03 38 54.41	−35 31 14.0	[SRH2010] 84 49	1000 ± 27	1
761	03 38 54.58	−35 35 30.3	[BAL2007] gc1404e	1911 ± 44	3
762	03 38 54.69	−35 29 44.2	[SRH2010] 84 72	1699 ± 19	2
763	03 38 54.71	−35 30 16.2	[SRH2010] 84 64	1034 ± 32	1
764	03 38 54.78	−35 29 15.8	[DRG2004] 84:80	1936 ± 54	2
765	03 38 54.89	−35 33 46.5	[SRH2010] 84 10	1542 ± 58	1
766	03 38 54.98	−35 32 15.7	[SRH2010] 84 33	1325 ± 47	1
767	03 38 55.03	−35 29 35.7	[SRH2010] 84 74	1574 ± 25	2
768	03 38 55.04	−35 32 53.1	[SRH2010] 7 65	1936 ± 60	1
769	03 38 55.10	−35 22 42.1	[SRH2010] 75 73	1365 ± 56	1
770	03 38 55.22	−35 21 57.2	[SRH2010] 75 88	1175 ± 31	1
771	03 38 55.40	−35 30 21.8	[DRG2004] 84:63	1076 ± 37	2
772	03 38 55.55	−35 26 52.4	[SRH2010] 75 1	1328 ± 39	1
773	03 38 55.60	−35 30 51.7	[SRH2010] 84 55	2121 ± 55	1
774	03 38 55.86	−35 24 59.8	[SRH2010] 75 33	1616 ± 38	2
775	03 38 56.18	−35 24 48.9	FCOS 1-063	645 ± 45	7
776	03 38 56.39	−35 23 36.9	[SRH2010] 75 56	647 ± 58	1
777	03 38 56.55	−35 28 28.6	[SRH2010] 84 94	1382 ± 22	1
778	03 38 56.88	−35 27 42.9	[SRH2010] 84 107	584 ± 42	1
779	03 38 57.04	−35 32 08.0	[SRH2010] 84 35	1344 ± 18	1
780	03 38 57.39	−35 24 50.3	[SRH2010] 75 36	893 ± 17	2
781	03 38 57.44	−35 31 42.5	[DRG2004] 84:42	1570 ± 46	2
782	03 38 57.51	−35 28 19.2	[SRH2010] 84 96	1283 ± 45	2

TABLE A.4 – *continued*

ID	R.A. (J2000)	DEC. (J2000)	SIMBAD ID	ν (km s^{-1})	LIT.
783	03 38 57.80	−35 21 12.3	[SRH2010] 75 99	1671 ± 39	1
784	03 38 58.08	−35 26 28.0	[SRH2010] 78 13	1379 ± 33	1
785	03 38 58.28	−35 30 13.2	[SRH2010] 84 65	1212 ± 30	1
786	03 38 58.31	−35 32 28.7	[SRH2010] 84 30	1741 ± 31	2
787	03 38 58.48	−35 26 28.2	[DRG2004] 78:12	1048 ± 18	2
788	03 38 58.85	−35 25 05.9	[SRH2010] 78 11	1635 ± 39	1
789	03 38 59.06	−35 20 32.8	[SRH2010] 75 111	1603 ± 70	1
790	03 38 59.09	−35 29 54.1	[SRH2010] 84 69	1948 ± 36	2
791	03 38 59.31	−35 33 43.5	[SRH2010] 84 11	2016 ± 15	3
792	03 38 59.40	−35 21 29.8	[SRH2010] 75 95	760 ± 44	2
793	03 39 00.41	−35 26 09.9	[SRH2010] 75 14	1813 ± 40	2
794	03 39 00.69	−35 30 32.4	[SRH2010] 84 60	1311 ± 23	2
795	03 39 00.83	−35 20 49.8	[SRH2010] 75 106	1519 ± 45	1
796	03 39 01.44	−35 23 58.1	[DRG2004] 75:51	1715 ± 93	2
797	03 39 01.49	−35 25 30.7	[SRH2010] 75 24	1093 ± 43	1
798	03 39 01.50	−35 26 30.3	[SRH2010] 75 9	1934 ± 39	1
799	03 39 03.86	−35 24 28.6	[BAL2007] gc280.1	1880 ± 16	3
800	03 39 04.57	−35 15 35.2	[FDE2007] J033904.55-351535.2	1506 ± 4	4
801	03 39 05.01	−35 26 53.7	[BAL2007] gc175.1	1057 ± 10	3
802	03 39 05.62	−35 28 59.5	[BAL2007] gc89.10	1037 ± 12	3
803	03 39 06.04	−35 34 49.6	[BAL2007] gc324.8	1540 ± 10	3
804	03 39 06.47	−35 31 27.7	[SRH2010] GS03-M02 217	659 ± 42	1
805	03 39 07.78	−35 31 56.7	[SRH2010] GS03-M01 169	1313 ± 37	1
806	03 39 08.30	−35 30 41.0	[SRH2010] GS03-M01 208	1488 ± 34	1
807	03 39 09.16	−35 27 29.8	[KGM99] aat 68	1166 ± 150	9
808	03 39 09.18	−35 34 58.0	[BAL2007] gc378.8	1751 ± 10	3
809	03 39 09.83	−35 30 16.6	[SRH2010] GS03-M02 198	1580 ± 84	1
810	03 39 10.06	−35 24 04.3	[KGM99] aat 69	1938 ± 150	9
811	03 39 10.49	−35 31 27.5	[SRH2010] GS03-M01 216	1393 ± 20	1
812	03 39 11.28	−35 31 03.0	[SRH2010] GS03-M01 152	1421 ± 19	1
813	03 39 11.84	−35 31 06.8	[SRH2010] GS03-M02 155	1351 ± 31	1
814	03 39 14.23	−35 29 47.0	[SRH2010] GS03-M01 200	1351 ± 21	1
815	03 39 14.23	−35 21 03.6	[SRH2010] 8 68	1387 ± 61	1
816	03 39 14.40	−35 21 25.0	[SRH2010] 8 60	1672 ± 32	1
817	03 39 15.09	−35 32 34.6	[SRH2010] GS03-M01 92	1741 ± 15	1
818	03 39 15.34	−35 35 34.5	[FDE2007] J033915.34-353534.7	1528 ± 13	4
819	03 39 15.84	−35 34 56.1	[BAL2007] gc376.8	1506 ± 12	3
820	03 39 15.92	−35 33 40.2	[SRH2010] GS03-M01 55	1018 ± 59	1
821	03 39 16.10	−35 29 45.1	[SRH2010] GS03-M02 144	1665 ± 44	1
822	03 39 16.31	−35 30 00.1	[KGM99] aat 71	1843 ± 150	9
823	03 39 17.68	−35 25 30.1	[BAL2007] gc241.1	1026 ± 5	4
824	03 39 19.07	−35 34 06.8	[SRH2010] GS03-M01 32	1526 ± 10	3
825	03 39 20.51	−35 19 14.3	[SRH2010] 8 104	1462 ± 5	4
826	03 39 21.39	−35 33 32.6	[SRH2010] GS03-M01 37	1464 ± 84	1
827	03 39 21.53	−35 23 31.8	[SRH2010] 8 28	1744 ± 96	1
828	03 39 22.03	−35 28 45.1	[BAL2007] gc101.1	693 ± 7	3
829	03 39 22.26	−35 29 35.8	[SRH2010] GS03-M01 131	1158 ± 79	1
830	03 39 22.64	−35 34 10.9	[SRH2010] GS03-M02 19	1217 ± 29	1
831	03 39 22.94	−35 32 33.1	[SRH2010] GS03-M01 63	1203 ± 62	1
832	03 39 23.17	−35 18 31.0	[SRH2010] 8 116	1051 ± 60	1
833	03 39 23.92	−35 29 10.1	[SRH2010] GS03-M01 204	1252 ± 46	1
834	03 39 24.55	−35 20 34.2	[SRH2010] 8 78	1260 ± 69	1
835	03 39 24.67	−35 05 17.7	[FDE2007] J033924.66-350517.6	1315 ± 10	4
836	03 39 26.85	−35 33 48.9	[SRH2010] GS03-M02 15	1280 ± 54	1
837	03 39 32.20	−35 33 33.7	[SRH2010] GS03-M01 7	1497 ± 51	1
838	03 39 34.74	−35 53 44.2	[GDE2009] UCD 52	1528 ± 74	5
839	03 39 35.92	−35 28 24.4	[BAL2007] uc dB	1886 ± 3	4

TABLE A.4 – *continued*

ID	R.A. (J2000)	DEC. (J2000)	SIMBAD ID	v (km s^{-1})	LIT.
840	03 39 36.04	−35 15 13.1	[FDE2007] J033936.05-351513.3	1520 ± 12	4
841	03 39 37.16	−35 15 21.7	[FDE2007] J033937.16-351521.9	1912 ± 6	4
842	03 39 39.43	−35 36 58.4	[BAL2007] gc152.5	1729 ± 7	3
843	03 39 39.75	−35 25 51.6	[BAL2007] gc417.5	1141 ± 15	3
844	03 39 39.85	−35 31 53.5	[BAL2007] gc317.5	1689 ± 11	3
845	03 39 40.14	−35 18 35.4	[FDE2007] J033940.13-351835.7	1402 ± 9	4
846	03 39 40.29	−35 28 53.6	[BAL2007] gc516.5	1414 ± 14	3
847	03 39 43.11	−35 33 10.3	[BAL2007] gc269.5	1274 ± 12	3
848	03 39 43.52	−35 26 59.1	[BAL2007] uc464.5	1274 ± 7	3
849	03 39 44.27	−35 29 15.7	[BAL2007] gc391.5	1520 ± 10	3
850	03 39 45.83	−35 17 46.1	[FDE2007] J033945.82-351746.3	1356 ± 8	4
851	03 39 49.16	−35 34 46.0	[BAL2007] gc212.5	1770 ± 8	3
852	03 39 52.54	−35 04 24.0	[FDE2007] J033952.54-350424.2	1274 ± 4	4
853	03 39 53.64	−35 01 32.9	[FDE2007] J033953.63-350133.0	1409 ± 11	4
854	03 39 57.55	−35 24 32.8	[BAL2007] gc6.400	1564 ± 9	3
855	03 39 59.95	−35 26 31.6	[BAL2007] gc441.5	1775 ± 9	3
856	03 40 00.72	−35 41 58.5	[FDE2007] J034000.71-354158.6	1452 ± 10	4
857	03 40 00.99	−35 34 35.5	[BAL2007] gc223.5	1387 ± 7	3
858	03 40 02.53	−35 36 48.6	[BAL2007] gc159.5	1741 ± 6	3
859	03 40 02.81	−35 38 57.1	[BAL2007] gc70.50	1467 ± 5	3
860	03 40 06.76	−35 29 27.2	[BAL2007] gc382.5	1274 ± 5	3
861	03 40 08.11	−35 24 17.8	[BAL2007] gc13.40	1532 ± 8	3
862	03 40 09.73	−35 36 11.0	[BAL2007] gc173.5	1898 ± 9	3
863	03 40 11.40	−35 19 29.2	[BAL2007] gc172.4	1365 ± 9	3
864	03 40 11.60	−35 27 09.4	[BAL2007] gc467.5	1424 ± 9	3
865	03 40 12.55	−35 21 11.6	[BAL2007] gc115.4	1233 ± 8	3
866	03 40 12.98	−35 27 03.4	[BAL2007] gc459.5	1366 ± 9	3
867	03 40 19.89	−35 15 29.7	[FDE2007] J034019.89-351530.0	1608 ± 6	4
868	03 40 21.41	−35 24 27.4	[BAL2007] gc6.300	1752 ± 5	3
869	03 40 22.91	−35 33 50.5	[BAL2007] gc199.6	1040 ± 5	3
870	03 40 23.32	−35 38 31.9	[BAL2007] gc71.60	1301 ± 8	3
871	03 40 24.71	−35 35 13.5	[BAL2007] gc164.6	949 ± 10	3
872	03 40 24.93	−35 06 37.3	[FDE2007] J034024.92-350637.5	1489 ± 11	4
873	03 40 32.51	−35 36 22.8	[BAL2007] gc131.6	1465 ± 5	3
874	03 40 37.06	−34 58 40.0	[GDE2009] UCD 59	1811 ± 159	5
875	03 40 38.83	−35 34 42.9	[BAL2007] gc175.6	1693 ± 7	3
876	03 40 40.88	−35 12 30.5	[BAL2007] gc398.3	1250 ± 11	3
877	03 40 44.62	−35 36 46.6	[BAL2007] gc120.6	1241 ± 9	3
878	03 40 45.97	−35 14 51.7	[BAL2007] gc311.3	1632 ± 17	3
879	03 40 49.59	−35 32 46.6	[BAL2007] gc236.6	1479 ± 5	3
880	03 41 03.83	−35 26 34.1	[BAL2007] gc395.7	1459 ± 8	3
881	03 41 05.00	−35 17 45.4	[BAL2007] gc187.2	1575 ± 12	3
882	03 41 05.01	−35 22 08.4	[BAL2007] gc69.20	1634 ± 8	3
883	03 41 05.91	−35 26 38.0	[BAL2007] gc381.7	607 ± 9	3
884	03 41 10.46	−35 34 57.3	[BAL2007] gc163.7	1448 ± 7	3
885	03 41 11.31	−35 09 20.0	[BAL2007] gc388.2	555 ± 12	3
886	03 41 13.61	−35 29 28.8	[BAL2007] gc332.7	1527 ± 13	3
887	03 41 13.71	−35 18 17.5	[BAL2007] gc172.2b	1861 ± 9	3
888	03 41 20.35	−35 28 46.2	[BAL2007] gc428.7	1514 ± 6	3
889	03 41 20.53	−35 12 53.6	[BAL2007] gc350.2	1415 ± 9	3
890	03 41 21.18	−35 21 46.1	[BAL2007] gc77.20	2076 ± 20	3
891	03 41 29.52	−35 19 48.6	[BAL2007] gc129.2	1473 ± 6	3
892	03 41 32.84	−35 11 37.2	[BAL2007] uc411.2	2076 ± 11	3
893	03 41 35.83	−35 54 57.9	[GDE2009] UCD 60	1629 ± 57	5
894	03 41 48.41	−35 17 40.2	[BAL2007] gc201.1	1295 ± 10	3
895	03 41 49.46	−35 30 12.5	[BAL2007] gc304.8	1570 ± 12	3
896	03 41 51.51	−35 11 24.7	[BAL2007] gc375.1	1907 ± 27	3

TABLE A.4 – *continued*

ID	R.A. (J2000)	DEC. (J2000)	SIMBAD ID	ν (km s^{-1})	LIT.
897	03 42 00.13	−35 19 32.4	[BAL2007] gc152.1	947 ± 15	3
898	03 42 11.92	−35 24 42.9	[BAL2007] gc2.100	1413 ± 9	3
899	03 42 13.71	−35 22 41.0	[BAL2007] gc73.10	1398 ± 12	3
900	03 42 14.51	−35 23 00.1	[BAL2007] gc67.10	1708 ± 12	3
901	03 42 16.26	−35 24 06.1	[BAL2007] gc32.10	1399 ± 12	3
902	03 42 17.04	−35 22 08.3	[BAL2007] gc85.10	1578 ± 11	3
903	03 42 18.71	−35 22 40.2	[BAL2007] gc74.10	1468 ± 13	3
904	03 43 08.11	−35 23 43.2	[FDK2008] J034308.16-352343.4	1271 ± 24	8

TABLE A.5: Complete parameter catalogue for our working sample of spectroscopically confirmed Fornax cluster members with $m_{Ve} < 21.5$ mag. ID: our object ID from Table 2.1. m_{Ve}: V-equivalent magnitude and corresponding uncertainty. Note that the magnitude uncertainties are purely based on S/N and do not include the calibration uncertainties mentioned in Section 2.2.1. Flag: 1 = magnitude and uncertainty obtained from SEXTRACTOR; 2 = magnitude and uncertainty obtained from PSF-fitting. cc: core concentration (uncorrected values, not used in the analysis). cc$_{corr}$: PSF-corrected core concentration (see Section 2.3.4). An estimate for the uncertainty in core concentration, which is given for each region, can be inferred from column 8 of Table 2.2. ra: residual asymmetry and corresponding uncertainty. el: ellipticity and corresponding uncertainty. For 17 objects it was not possible to determine the ellipticity or residual asymmetry due to too little flux remaining in the residual image. S1: subsample as defined in Table 2.5; cc + ra = 1, cc + RA = 2, CC + RA = 3, cc + EL = 4; S1 = 0 indicates that the object is not part of any subsample. S2: alternative subsample as defined in Table A.1. Reg.: PSF-region (see Table 2.2).

ID	m_{Ve} (mag)	FLAG	cc	cc$_{corr}$	ra	el	S1	S2	REG.
1	20.394 ± 0.003	1	0.946	0.946	0.504 ± 0.094	0.161 ± 0.067	0	0	12
2	20.576 ± 0.004	1	0.929	0.929	0.429 ± 0.114	0.129 ± 0.097	0	0	12
3	21.379 ± 0.008	1	0.908	0.908	0.403 ± 0.125	0.066 ± 0.078	0	0	12
4	20.737 ± 0.003	1	0.942	0.942	0.520 ± 0.101	0.325 ± 0.084	0	0	6
5	20.645 ± 0.004	1	0.905	0.905	0.759 ± 0.044	0.308 ± 0.028	0	0	6
6	21.385 ± 0.008	1	0.851	0.851	—	—	0	0	6
7	21.184 ± 0.006	1	0.942	0.942	0.414 ± 0.072	0.156 ± 0.047	0	0	6
9	21.417 ± 0.006	1	0.976	0.976	0.304 ± 0.130	0.110 ± 0.078	0	0	6
10	21.059 ± 0.004	1	0.925	0.925	0.297 ± 0.100	0.098 ± 0.073	0	0	6
11	21.149 ± 0.005	1	0.915	0.915	0.353 ± 0.100	0.170 ± 0.065	0	0	6
12	20.289 ± 0.003	1	0.981	0.981	0.815 ± 0.072	0.111 ± 0.058	30	30	6
13	19.768 ± 0.002	1	0.800	0.800	0.357 ± 0.025	0.078 ± 0.026	0	0	8
15	19.357 ± 0.002	1	0.765	0.765	0.952 ± 0.007	0.271 ± 0.004	24	24	6
16	20.799 ± 0.006	1	1.021	1.021	0.521 ± 0.130	0.049 ± 0.078	0	0	6
17	19.282 ± 0.002	1	0.856	0.856	1.310 ± 0.017	0.406 ± 0.012	30	30	6
18	20.719 ± 0.006	1	1.037	1.037	—	—	0	0	6
19	20.968 ± 0.004	1	0.913	0.913	0.349 ± 0.110	0.088 ± 0.085	0	0	6
20	20.605 ± 0.004	1	1.004	1.004	—	—	0	0	6
21	20.116 ± 0.003	1	0.940	0.940	0.721 ± 0.060	0.273 ± 0.037	30	30	6
22	21.249 ± 0.006	2	1.018	1.018	—	—	0	0	6
23	21.428 ± 0.007	1	0.943	0.943	0.306 ± 0.127	0.080 ± 0.084	0	0	6
24	20.174 ± 0.002	1	0.897	0.897	0.419 ± 0.056	0.269 ± 0.054	0	0	6
25	20.151 ± 0.003	1	0.658	0.691	0.614 ± 0.045	0.067 ± 0.038	20	20	10
26	20.957 ± 0.004	1	0.961	0.961	0.333 ± 0.116	0.167 ± 0.076	0	0	6
27	20.659 ± 0.004	1	0.921	0.921	0.388 ± 0.083	0.034 ± 0.069	0	0	6
28	19.863 ± 0.004	1	0.884	0.884	—	—	0	0	6
29	20.927 ± 0.005	1	0.801	0.866	0.399 ± 0.151	0.023 ± 0.112	0	0	9
31	20.882 ± 0.005	1	0.767	0.767	0.408 ± 0.072	0.138 ± 0.059	0	0	4
32	20.734 ± 0.005	1	0.934	0.934	—	—	0	0	4
34	20.078 ± 0.003	1	0.950	0.950	0.427 ± 0.078	0.126 ± 0.064	0	0	4

TABLE A.5 – *continued*

ID	m_{Ve} (mag)	FLAG	cc	cc_{corr}	ra	el	S1	S2	REG.
35	20.841 ± 0.003	1	0.956	0.956	—	—	0	0	4
36	19.775 ± 0.002	1	0.815	0.815	—	—	0	0	4
37	21.121 ± 0.008	1	0.657	0.657	0.551 ± 0.077	0.138 ± 0.054	0	0	4
38	21.417 ± 0.009	1	0.943	0.943	0.522 ± 0.103	0.166 ± 0.061	0	0	4
39	20.887 ± 0.005	1	0.965	0.965	0.497 ± 0.104	0.304 ± 0.072	0	0	4
40	20.875 ± 0.034	2	0.782	0.782	0.234 ± 0.012	0.035 ± 0.008	0	0	4
41	20.986 ± 0.021	2	0.957	0.957	—	—	0	0	4
43	20.593 ± 0.003	1	1.007	1.007	—	—	0	0	4
44	21.031 ± 0.004	1	0.983	0.983	—	—	0	0	4
46	18.994 ± 0.001	1	0.669	0.669	0.236 ± 0.008	0.032 ± 0.007	10	10	4
47	20.330 ± 0.003	1	0.869	0.869	0.387 ± 0.032	0.067 ± 0.023	0	10	4
48	20.462 ± 0.004	1	0.804	0.804	0.380 ± 0.055	0.068 ± 0.042	10	10	4
52	21.305 ± 0.007	1	0.962	0.962	0.344 ± 0.139	0.151 ± 0.074	0	0	4
55	21.294 ± 0.007	1	0.801	0.866	0.343 ± 0.137	0.075 ± 0.091	0	0	9
57	21.180 ± 0.005	1	0.980	0.980	0.268 ± 0.139	0.078 ± 0.083	0	0	4
60	21.196 ± 0.006	1	0.818	0.871	0.497 ± 0.085	0.200 ± 0.049	0	0	7
61	21.473 ± 0.006	1	0.834	0.882	0.271 ± 0.130	0.057 ± 0.091	0	0	7
63	21.376 ± 0.010	1	0.781	0.846	0.425 ± 0.101	0.178 ± 0.056	0	0	7
65	20.890 ± 0.004	1	0.926	0.926	0.683 ± 0.081	0.287 ± 0.053	0	0	4
67	20.822 ± 0.004	1	0.932	0.932	0.317 ± 0.097	0.062 ± 0.071	0	0	4
72	19.628 ± 0.002	1	0.726	0.726	0.408 ± 0.023	0.040 ± 0.022	10	10	4
73	21.383 ± 0.009	1	0.885	0.885	0.465 ± 0.192	0.101 ± 0.132	0	0	4
75	19.759 ± 0.001	1	0.881	0.881	0.293 ± 0.035	0.105 ± 0.032	0	0	4
78	21.047 ± 0.005	1	0.797	0.797	0.346 ± 0.053	0.042 ± 0.042	0	0	4
79	20.354 ± 0.003	1	0.712	0.795	0.381 ± 0.051	0.003 ± 0.047	10	10	7
81	21.065 ± 0.006	1	0.952	0.952	0.312 ± 0.178	0.238 ± 0.109	0	0	7
82	21.372 ± 0.006	1	0.974	0.974	0.303 ± 0.126	0.121 ± 0.084	0	0	4
85	21.393 ± 0.008	1	0.860	0.899	0.375 ± 0.160	0.054 ± 0.108	0	0	7
86	21.104 ± 0.006	1	0.906	0.906	0.339 ± 0.118	0.205 ± 0.086	0	0	4
89	20.307 ± 0.003	1	0.816	0.870	0.620 ± 0.062	0.264 ± 0.044	30	24	7
90	20.984 ± 0.005	1	0.898	0.898	0.350 ± 0.103	0.109 ± 0.076	0	0	4
98	20.582 ± 0.003	1	0.916	0.916	0.385 ± 0.084	0.240 ± 0.068	0	0	4
103	20.726 ± 0.005	1	0.780	0.846	0.444 ± 0.097	0.184 ± 0.065	0	0	7
105	21.474 ± 0.011	1	0.812	0.868	0.499 ± 0.135	0.173 ± 0.075	0	0	7
107	21.497 ± 0.007	1	0.822	0.874	0.273 ± 0.150	0.048 ± 0.103	0	0	7
110	21.444 ± 0.008	1	0.800	0.800	0.581 ± 0.066	0.260 ± 0.040	0	0	4
115	20.370 ± 0.003	1	0.916	0.916	0.566 ± 0.110	0.193 ± 0.075	30	30	4
118	20.363 ± 0.003	1	0.933	0.933	0.476 ± 0.051	0.192 ± 0.036	0	0	4
119	20.887 ± 0.004	1	0.865	0.865	0.277 ± 0.065	0.042 ± 0.054	0	0	4
122	20.605 ± 0.004	1	0.621	0.722	0.271 ± 0.028	0.014 ± 0.022	0	0	7
123	20.069 ± 0.003	1	0.803	0.861	0.327 ± 0.051	0.142 ± 0.037	0	10	7
125	19.510 ± 0.001	1	0.678	0.769	0.285 ± 0.017	0.062 ± 0.015	10	10	7
128	21.375 ± 0.006	1	0.896	0.896	0.353 ± 0.107	0.058 ± 0.072	0	0	4
129	21.035 ± 0.007	1	0.880	0.910	0.360 ± 0.118	0.095 ± 0.072	0	0	7
130	20.048 ± 0.002	1	0.840	0.840	0.347 ± 0.027	0.150 ± 0.021	0	10	4
135	20.725 ± 0.003	1	0.908	0.908	0.458 ± 0.077	0.140 ± 0.060	0	0	4
136	20.631 ± 0.004	1	0.831	0.831	0.495 ± 0.087	0.073 ± 0.069	0	0	4
138	21.047 ± 0.006	1	0.856	0.856	0.398 ± 0.106	0.212 ± 0.066	0	0	4
139	20.980 ± 0.004	1	0.905	0.905	0.322 ± 0.086	0.132 ± 0.061	0	0	4
140	20.484 ± 0.003	1	0.753	0.826	0.383 ± 0.055	0.140 ± 0.044	10	10	7
152	20.414 ± 0.002	1	0.894	0.894	0.401 ± 0.077	0.057 ± 0.068	0	0	5
154	21.155 ± 0.004	1	0.874	0.874	0.341 ± 0.095	0.097 ± 0.066	0	0	5
158	20.972 ± 0.004	1	0.852	0.852	0.357 ± 0.083	0.099 ± 0.059	0	0	5
172	20.848 ± 0.004	1	0.766	0.766	0.421 ± 0.041	0.110 ± 0.032	0	0	5
174	21.312 ± 0.005	1	0.845	0.845	0.339 ± 0.083	0.244 ± 0.055	0	0	5
184	21.081 ± 0.004	1	0.866	0.866	0.258 ± 0.079	0.055 ± 0.069	0	0	5
185	21.010 ± 0.004	1	0.887	0.887	0.307 ± 0.108	0.017 ± 0.089	0	0	5
186	20.734 ± 0.004	1	0.853	0.853	0.490 ± 0.087	0.085 ± 0.067	0	0	5

TABLE A.5 – *continued*

ID	m$_{Ve}$ (mag)	FLAG	cc	cc$_{corr}$	ra	el	S1	S2	REG.
190	20.927 ± 0.005	1	0.847	0.847	0.444 ± 0.098	0.183 ± 0.068	0	0	5
191	21.128 ± 0.006	1	0.806	0.806	0.374 ± 0.088	0.111 ± 0.062	0	0	5
192	20.700 ± 0.003	1	0.803	0.803	0.483 ± 0.041	0.188 ± 0.030	0	0	5
194	21.266 ± 0.005	1	0.871	0.871	0.217 ± 0.095	0.126 ± 0.067	0	0	5
195	21.009 ± 0.004	1	0.901	0.901	0.527 ± 0.068	0.248 ± 0.043	0	0	5
202	21.366 ± 0.006	1	0.869	0.869	0.288 ± 0.137	0.109 ± 0.092	0	0	5
209	21.423 ± 0.005	1	0.862	0.862	0.264 ± 0.134	0.228 ± 0.096	0	0	5
210	21.171 ± 0.005	1	0.848	0.848	0.261 ± 0.099	0.252 ± 0.070	0	0	5
211	21.205 ± 0.005	1	0.852	0.852	0.283 ± 0.085	0.107 ± 0.058	0	0	5
220	21.436 ± 0.006	1	0.896	0.896	0.323 ± 0.103	0.093 ± 0.066	0	0	5
221	20.987 ± 0.004	1	0.930	0.930	0.342 ± 0.087	0.192 ± 0.054	0	0	5
223	20.743 ± 0.003	1	0.898	0.898	0.264 ± 0.087	0.179 ± 0.081	0	0	5
228	18.576 ± 0.001	1	0.802	0.802	0.265 ± 0.009	0.046 ± 0.009	0	0	5
233	21.272 ± 0.006	1	0.872	0.872	0.425 ± 0.122	0.089 ± 0.093	0	0	5
235	21.498 ± 0.006	1	0.866	0.866	0.209 ± 0.095	0.117 ± 0.072	0	0	5
236	18.835 ± 0.001	1	0.728	0.728	0.241 ± 0.009	0.129 ± 0.008	10	10	5
237	19.708 ± 0.001	1	0.774	0.774	0.362 ± 0.023	0.046 ± 0.025	0	10	5
245	21.094 ± 0.004	1	0.831	0.831	0.296 ± 0.087	0.206 ± 0.065	0	0	5
246	21.360 ± 0.005	1	0.898	0.898	0.238 ± 0.117	0.077 ± 0.088	0	0	5
250	21.375 ± 0.006	1	0.889	0.889	0.263 ± 0.105	0.112 ± 0.072	0	0	5
254	20.736 ± 0.003	1	0.958	0.958	0.520 ± 0.093	0.080 ± 0.069	0	0	5
259	20.847 ± 0.003	1	0.889	0.889	0.404 ± 0.096	0.172 ± 0.083	0	0	5
260	20.803 ± 0.004	1	0.964	0.964	0.543 ± 0.090	0.213 ± 0.063	0	0	5
263	21.267 ± 0.005	1	0.816	0.816	0.602 ± 0.096	0.136 ± 0.089	0	0	5
265	21.296 ± 0.005	1	0.903	0.903	0.295 ± 0.113	0.121 ± 0.077	0	0	5
266	21.010 ± 0.004	1	0.887	0.887	0.572 ± 0.095	0.059 ± 0.096	0	0	5
267	20.471 ± 0.003	1	0.895	0.895	0.532 ± 0.092	0.156 ± 0.068	0	0	5
271	21.022 ± 0.005	1	0.858	0.858	0.430 ± 0.069	0.153 ± 0.038	0	0	5
276	21.458 ± 0.008	1	0.948	0.948	0.388 ± 0.166	0.026 ± 0.114	0	0	5
278	19.318 ± 0.001	1	0.842	0.842	0.449 ± 0.023	0.096 ± 0.022	0	0	5
282	19.463 ± 0.001	1	0.772	0.772	0.198 ± 0.016	0.058 ± 0.015	0	10	5
287	21.057 ± 0.004	1	0.933	0.933	0.323 ± 0.131	0.077 ± 0.118	0	0	5
288	21.317 ± 0.005	1	0.924	0.924	0.274 ± 0.109	0.120 ± 0.089	0	0	5
289	21.327 ± 0.006	1	0.814	0.814	0.417 ± 0.093	0.083 ± 0.075	0	0	5
290	20.470 ± 0.003	1	0.846	0.846	0.854 ± 0.049	0.334 ± 0.035	30	24	5
292	20.109 ± 0.002	1	0.859	0.859	0.483 ± 0.050	0.238 ± 0.038	0	14	5
293	21.057 ± 0.005	1	0.913	0.913	0.426 ± 0.115	0.220 ± 0.080	0	0	5
302	20.430 ± 0.003	1	0.909	0.909	0.326 ± 0.073	0.190 ± 0.061	0	0	5
303	21.233 ± 0.006	1	0.860	0.860	0.291 ± 0.083	0.064 ± 0.057	0	0	5
305	21.392 ± 0.008	1	0.877	0.877	0.493 ± 0.107	0.154 ± 0.062	0	0	5
306	20.688 ± 0.004	1	0.849	0.849	0.859 ± 0.070	0.164 ± 0.051	0	0	5
308	21.427 ± 0.006	1	0.888	0.888	0.242 ± 0.106	0.063 ± 0.074	0	0	5
311	21.171 ± 0.006	1	0.936	0.936	0.459 ± 0.132	0.205 ± 0.079	0	0	5
312	20.902 ± 0.004	1	0.888	0.888	0.411 ± 0.093	0.102 ± 0.074	0	0	5
315	21.292 ± 0.006	1	0.855	0.855	0.357 ± 0.069	0.069 ± 0.047	0	0	5
316	20.602 ± 0.003	1	0.926	0.926	0.462 ± 0.075	0.265 ± 0.054	0	0	5
319	20.614 ± 0.003	1	0.896	0.896	0.382 ± 0.083	0.138 ± 0.066	0	0	5
323	20.874 ± 0.004	1	0.882	0.882	0.383 ± 0.096	0.184 ± 0.072	0	0	5
325	20.484 ± 0.003	1	0.655	0.655	0.260 ± 0.030	0.014 ± 0.029	10	10	5
327	21.473 ± 0.007	1	0.857	0.857	0.483 ± 0.079	0.234 ± 0.048	0	0	5
332	21.038 ± 0.006	1	0.882	0.882	0.404 ± 0.088	0.170 ± 0.063	0	0	5
346	20.081 ± 0.002	1	0.794	0.794	0.367 ± 0.033	0.043 ± 0.031	10	10	5
347	21.192 ± 0.006	1	0.899	0.899	0.343 ± 0.115	0.221 ± 0.075	0	0	5
348	19.658 ± 0.002	1	0.768	0.768	0.225 ± 0.012	0.036 ± 0.010	10	10	5
350	21.109 ± 0.006	1	0.943	0.943	0.408 ± 0.099	0.189 ± 0.060	0	0	5
360	20.683 ± 0.003	1	0.919	0.919	0.438 ± 0.098	0.162 ± 0.073	0	0	5
364	20.133 ± 0.003	1	0.821	0.821	0.444 ± 0.058	0.124 ± 0.053	10	10	5
366	20.742 ± 0.004	1	0.906	0.906	0.420 ± 0.093	0.151 ± 0.064	0	0	5

TABLE A.5 – *continued*

ID	m_{Ve} (mag)	FLAG	cc	cc_{corr}	ra	el	S1	S2	REG.
367	21.158 ± 0.006	1	0.909	0.909	0.526 ± 0.077	0.481 ± 0.044	0	0	5
375	20.593 ± 0.005	1	0.842	0.842	0.663 ± 0.098	0.283 ± 0.066	30	24	1
378	20.981 ± 0.004	1	0.873	0.873	0.335 ± 0.111	0.143 ± 0.087	0	0	5
380	21.224 ± 0.005	1	0.886	0.886	0.409 ± 0.083	0.036 ± 0.050	0	0	5
381	20.467 ± 0.003	1	0.851	0.851	0.407 ± 0.069	0.222 ± 0.058	0	14	5
384	21.306 ± 0.006	1	0.830	0.830	0.314 ± 0.085	0.210 ± 0.061	0	0	5
390	20.389 ± 0.004	1	0.906	0.906	0.705 ± 0.075	0.331 ± 0.053	30	30	5
391	20.627 ± 0.003	1	0.886	0.886	0.442 ± 0.068	0.092 ± 0.051	0	0	5
392	21.181 ± 0.006	1	0.842	0.842	0.363 ± 0.068	0.220 ± 0.049	0	0	5
394	20.650 ± 0.004	1	0.906	0.906	0.396 ± 0.079	0.205 ± 0.056	0	0	5
399	20.249 ± 0.002	1	0.797	0.797	0.451 ± 0.037	0.012 ± 0.034	10	10	5
403	20.935 ± 0.005	1	0.874	0.874	0.491 ± 0.101	0.123 ± 0.076	0	0	5
407	20.891 ± 0.006	1	0.867	0.867	0.644 ± 0.058	0.378 ± 0.032	0	0	5
408	21.340 ± 0.007	1	0.863	0.863	0.459 ± 0.139	0.149 ± 0.097	0	0	5
409	20.695 ± 0.006	1	0.919	0.919	0.771 ± 0.106	0.204 ± 0.065	0	0	5
413	21.209 ± 0.007	1	0.849	0.849	0.500 ± 0.112	0.104 ± 0.071	0	0	5
416	21.132 ± 0.006	1	0.905	0.905	0.471 ± 0.126	0.027 ± 0.089	0	0	5
424	21.434 ± 0.007	1	0.911	0.911	0.438 ± 0.098	0.186 ± 0.065	0	0	5
427	20.795 ± 0.005	1	0.979	0.979	0.510 ± 0.132	0.266 ± 0.079	0	0	5
436	20.950 ± 0.010	1	0.920	0.920	0.526 ± 0.110	0.096 ± 0.068	0	0	5
438	20.795 ± 0.005	1	0.867	0.867	0.469 ± 0.090	0.066 ± 0.066	0	0	5
441	20.650 ± 0.005	1	0.842	0.842	0.648 ± 0.085	0.170 ± 0.070	0	0	1
448	19.853 ± 0.002	1	0.928	0.928	0.540 ± 0.039	0.390 ± 0.032	30	30	5
449	20.787 ± 0.006	1	0.945	0.945	0.573 ± 0.112	0.199 ± 0.070	0	0	5
452	19.728 ± 0.002	1	0.633	0.633	0.410 ± 0.012	0.281 ± 0.009	14	14	5
457	21.279 ± 0.006	1	0.912	0.912	0.418 ± 0.089	0.221 ± 0.053	0	0	5
460	19.540 ± 0.002	1	0.780	0.780	0.639 ± 0.025	0.208 ± 0.023	30	24	1
470	20.255 ± 0.003	1	0.948	0.948	0.763 ± 0.087	0.182 ± 0.067	30	30	5
473	19.818 ± 0.002	1	0.848	0.848	0.658 ± 0.039	0.171 ± 0.032	30	30	5
474	21.022 ± 0.006	1	0.851	0.851	0.652 ± 0.094	0.251 ± 0.058	0	0	1
476	20.162 ± 0.003	1	0.961	0.961	0.785 ± 0.112	0.153 ± 0.082	30	30	5
479	20.963 ± 0.005	1	0.951	0.951	0.402 ± 0.120	0.210 ± 0.086	0	0	5
481	20.956 ± 0.005	1	0.916	0.916	0.540 ± 0.103	0.380 ± 0.064	0	0	5
483	20.964 ± 0.005	1	0.919	0.919	0.379 ± 0.103	0.245 ± 0.069	0	0	5
487	20.673 ± 0.004	1	0.836	0.836	0.418 ± 0.066	0.055 ± 0.056	0	0	5
488	21.193 ± 0.007	1	0.950	0.950	0.389 ± 0.098	0.143 ± 0.064	0	0	5
489	20.456 ± 0.004	1	0.944	0.944	0.641 ± 0.074	0.131 ± 0.054	30	30	5
492	20.900 ± 0.008	1	0.904	0.904	0.730 ± 0.072	0.178 ± 0.039	0	0	5
493	21.353 ± 0.009	1	0.879	0.879	0.559 ± 0.082	0.151 ± 0.047	0	0	5
494	21.458 ± 0.009	1	0.876	0.876	0.496 ± 0.101	0.192 ± 0.055	0	0	5
495	21.476 ± 0.012	1	0.916	0.916	0.803 ± 0.098	0.223 ± 0.051	0	0	5
496	19.784 ± 0.002	1	0.866	0.866	0.602 ± 0.040	0.134 ± 0.032	30	30	5
497	20.965 ± 0.006	1	0.980	0.980	$-$	$-$	0	0	5
500	19.591 ± 0.002	1	0.888	0.888	0.695 ± 0.035	0.192 ± 0.030	30	30	5
501	20.931 ± 0.005	1	0.963	0.963	0.444 ± 0.115	0.032 ± 0.098	0	0	5
505	20.904 ± 0.006	1	0.874	0.874	0.537 ± 0.106	0.112 ± 0.073	0	0	2
506	21.355 ± 0.010	1	0.882	0.882	0.405 ± 0.124	0.119 ± 0.081	0	0	2
507	20.511 ± 0.003	1	0.894	0.894	0.681 ± 0.060	0.185 ± 0.048	30	30	2
508	20.679 ± 0.006	1	0.907	0.907	0.550 ± 0.131	0.109 ± 0.089	0	0	2
509	20.200 ± 0.003	1	0.849	0.849	0.583 ± 0.073	0.170 ± 0.059	30	20	2
510	20.866 ± 0.005	1	0.902	0.902	0.651 ± 0.134	0.155 ± 0.092	0	0	2
511	20.651 ± 0.005	1	0.836	0.836	0.546 ± 0.084	0.184 ± 0.065	0	0	2
522	21.464 ± 0.011	1	0.898	0.898	0.590 ± 0.120	0.063 ± 0.062	0	0	2
523	21.365 ± 0.009	1	0.827	0.827	0.474 ± 0.101	0.170 ± 0.070	0	0	1
524	20.609 ± 0.005	1	0.907	0.907	0.642 ± 0.090	0.216 ± 0.063	0	0	2
526	21.406 ± 0.009	1	0.930	0.930	0.445 ± 0.115	0.194 ± 0.062	0	0	2
527	21.270 ± 0.008	1	0.901	0.901	0.610 ± 0.126	0.056 ± 0.074	0	0	2
528	20.900 ± 0.006	1	0.855	0.855	0.654 ± 0.095	0.162 ± 0.063	0	0	1

TABLE A.5 – *continued*

ID	m_{Ve} (mag)	FLAG	cc	cc_{corr}	ra	el	S1	S2	REG.
533	21.298 ± 0.008	1	0.892	0.892	0.544 ± 0.111	0.228 ± 0.065	0	0	2
535	21.049 ± 0.010	1	0.837	0.837	–	–	0	0	2
536	21.369 ± 0.008	1	0.929	0.929	0.443 ± 0.130	0.193 ± 0.076	0	0	2
537	21.334 ± 0.009	1	0.832	0.832	0.472 ± 0.092	0.134 ± 0.061	0	0	2
542	20.065 ± 0.003	1	0.928	0.928	0.728 ± 0.069	0.182 ± 0.061	30	30	2
543	21.192 ± 0.012	1	0.895	0.895	0.554 ± 0.088	0.198 ± 0.046	0	0	2
547	21.274 ± 0.008	1	0.842	0.842	0.476 ± 0.102	0.100 ± 0.073	0	0	2
548	21.284 ± 0.008	1	0.877	0.877	0.581 ± 0.110	0.156 ± 0.074	0	0	2
551	21.189 ± 0.009	1	0.885	0.885	1.026 ± 0.064	0.388 ± 0.031	0	0	2
557	21.277 ± 0.007	1	0.830	0.830	0.675 ± 0.083	0.093 ± 0.056	0	0	2
559	21.383 ± 0.009	1	0.857	0.857	0.581 ± 0.090	0.123 ± 0.058	0	0	2
561	21.182 ± 0.007	1	0.936	0.936	0.815 ± 0.102	0.250 ± 0.058	0	0	2
563	20.866 ± 0.005	1	0.939	0.939	0.703 ± 0.137	0.139 ± 0.090	0	0	2
564	20.219 ± 0.007	1	0.904	0.904	0.620 ± 0.090	0.150 ± 0.051	30	30	2
565	21.446 ± 0.008	1	0.940	0.940	0.554 ± 0.139	0.181 ± 0.082	0	0	2
570	21.204 ± 0.008	1	0.651	0.651	0.351 ± 0.034	0.389 ± 0.031	0	0	2
574	19.916 ± 0.003	1	0.736	0.736	0.364 ± 0.020	0.084 ± 0.019	10	10	2
577	20.985 ± 0.007	1	0.929	0.929	0.578 ± 0.125	0.191 ± 0.075	0	0	2
584	20.523 ± 0.003	1	0.914	0.914	0.659 ± 0.074	0.275 ± 0.061	30	30	2
588	20.709 ± 0.005	1	0.896	0.896	0.983 ± 0.094	0.279 ± 0.063	0	0	2
592	21.172 ± 0.008	1	0.921	0.921	0.545 ± 0.143	0.112 ± 0.086	0	0	2
595	21.388 ± 0.008	1	0.876	0.876	0.579 ± 0.175	0.143 ± 0.122	0	0	2
597	21.325 ± 0.008	1	0.929	0.929	0.549 ± 0.158	0.094 ± 0.107	0	0	2
600	21.384 ± 0.008	1	0.913	0.913	0.515 ± 0.138	0.047 ± 0.087	0	0	2
601	21.087 ± 0.008	1	0.916	0.916	0.670 ± 0.145	0.180 ± 0.093	0	0	2
604	21.441 ± 0.008	1	0.881	0.881	0.665 ± 0.121	0.132 ± 0.076	0	0	2
605	21.383 ± 0.008	1	0.905	0.905	0.562 ± 0.122	0.112 ± 0.074	0	0	2
607	20.877 ± 0.005	1	0.912	0.912	0.661 ± 0.077	0.270 ± 0.045	0	0	2
612	21.348 ± 0.008	1	0.787	0.787	0.417 ± 0.101	0.124 ± 0.082	0	0	2
613	21.228 ± 0.008	1	0.876	0.876	0.956 ± 0.073	0.247 ± 0.042	0	0	2
615	21.468 ± 0.011	1	0.925	0.925	0.540 ± 0.137	0.098 ± 0.079	0	0	2
618	20.292 ± 0.004	1	0.826	0.826	0.526 ± 0.048	0.135 ± 0.042	10	10	2
619	20.905 ± 0.005	1	0.929	0.929	0.582 ± 0.139	0.077 ± 0.091	0	0	2
620	21.435 ± 0.008	1	0.932	0.932	0.435 ± 0.166	0.151 ± 0.119	0	0	2
621	20.872 ± 0.006	1	0.801	0.801	0.360 ± 0.053	0.202 ± 0.041	0	0	2
623	21.399 ± 0.010	1	0.884	0.884	0.716 ± 0.107	0.297 ± 0.052	0	0	2
627	21.120 ± 0.006	1	0.863	0.863	0.566 ± 0.094	0.113 ± 0.063	0	0	2
630	21.102 ± 0.007	1	0.927	0.927	0.461 ± 0.131	0.023 ± 0.090	0	0	2
635	20.611 ± 0.005	1	0.844	0.844	0.525 ± 0.083	0.141 ± 0.071	0	0	2
637	19.381 ± 0.005	1	0.605	0.605	0.273 ± 0.014	0.143 ± 0.011	10	10	2
643	20.851 ± 0.005	1	0.839	0.839	0.471 ± 0.079	0.208 ± 0.057	0	0	2
645	20.809 ± 0.006	1	0.859	0.859	0.667 ± 0.096	0.125 ± 0.065	0	0	2
647	20.972 ± 0.007	1	0.892	0.892	0.641 ± 0.127	0.042 ± 0.102	0	0	2
652	21.148 ± 0.007	1	0.891	0.891	0.639 ± 0.124	0.220 ± 0.097	0	0	2
653	20.916 ± 0.006	1	0.907	0.907	0.449 ± 0.125	0.103 ± 0.093	0	0	2
654	21.154 ± 0.007	1	0.886	0.886	0.609 ± 0.112	0.105 ± 0.071	0	0	2
655	19.473 ± 0.002	1	0.853	0.853	0.869 ± 0.049	0.274 ± 0.039	30	30	2
667	20.818 ± 0.007	1	0.842	0.842	0.535 ± 0.073	0.288 ± 0.046	0	0	2
674	21.468 ± 0.009	1	0.991	0.991	0.487 ± 0.072	0.151 ± 0.058	0	0	2
675	20.995 ± 0.006	1	0.853	0.853	0.586 ± 0.092	0.181 ± 0.070	0	0	2
677	20.799 ± 0.006	1	0.887	0.887	0.614 ± 0.113	0.260 ± 0.063	0	0	2
678	21.323 ± 0.007	1	0.921	0.921	0.622 ± 0.108	0.305 ± 0.059	0	0	2
683	20.571 ± 0.004	1	0.910	0.910	0.505 ± 0.093	0.293 ± 0.076	0	0	2
689	21.450 ± 0.008	1	0.892	0.892	0.459 ± 0.153	0.316 ± 0.105	0	0	2
693	21.295 ± 0.007	1	0.919	0.919	0.609 ± 0.130	0.167 ± 0.081	0	0	2
695	21.489 ± 0.009	1	0.922	0.922	0.418 ± 0.152	0.283 ± 0.089	0	0	2
697	20.404 ± 0.007	1	0.595	0.595	0.541 ± 0.022	0.279 ± 0.015	14	14	2
703	21.132 ± 0.006	1	0.905	0.905	0.499 ± 0.130	0.237 ± 0.077	0	0	2

TABLE A.5 – *continued*

ID	m_{Ve} (mag)	FLAG	cc	cc_{corr}	ra	el	S1	S2	REG.
707	20.807 ± 0.004	1	0.882	0.882	0.681 ± 0.077	0.225 ± 0.058	0	0	2
709	21.356 ± 0.008	1	0.899	0.899	0.853 ± 0.079	0.320 ± 0.038	0	0	2
711	20.008 ± 0.003	1	0.799	0.799	0.784 ± 0.030	0.333 ± 0.020	24	24	2
716	21.415 ± 0.009	1	0.883	0.883	0.407 ± 0.144	0.157 ± 0.090	0	0	2
717	21.193 ± 0.007	1	0.921	0.921	0.606 ± 0.173	0.117 ± 0.112	0	0	2
721	20.662 ± 0.005	1	0.841	0.841	0.670 ± 0.084	0.181 ± 0.062	0	0	2
723	21.378 ± 0.007	1	0.878	0.878	0.469 ± 0.145	0.119 ± 0.097	0	0	2
725	21.108 ± 0.006	1	0.989	0.989	0.725 ± 0.218	0.110 ± 0.184	0	0	2
726	21.428 ± 0.008	1	0.842	0.842	0.481 ± 0.106	0.123 ± 0.068	0	0	2
727	20.636 ± 0.004	1	0.844	0.844	0.517 ± 0.062	0.143 ± 0.051	0	0	2
731	21.088 ± 0.006	1	0.936	0.936	0.595 ± 0.140	0.261 ± 0.090	0	0	2
733	21.500 ± 0.010	1	0.929	0.929	0.538 ± 0.251	0.124 ± 0.166	0	0	2
734	20.689 ± 0.004	1	0.929	0.929	0.721 ± 0.112	0.308 ± 0.088	0	0	2
735	21.083 ± 0.005	1	0.861	0.861	0.970 ± 0.062	0.397 ± 0.039	0	0	2
743	21.430 ± 0.010	1	0.930	0.930	0.535 ± 0.096	0.336 ± 0.054	0	0	2
746	21.283 ± 0.020	2	0.941	0.941	0.989 ± 0.307	0.126 ± 0.112	0	0	2
754	21.184 ± 0.006	1	0.801	0.801	0.561 ± 0.073	0.141 ± 0.049	0	0	2
755	20.884 ± 0.005	1	0.898	0.898	0.470 ± 0.111	0.171 ± 0.074	0	0	2
756	17.518 ± 0.001	1	0.566	0.566	0.193 ± 0.001	0.039 ± 0.001	10	10	2
762	20.407 ± 0.004	1	0.887	0.887	0.714 ± 0.071	0.137 ± 0.049	30	30	2
763	21.289 ± 0.008	1	0.836	0.836	0.499 ± 0.097	0.081 ± 0.067	0	0	2
775	20.051 ± 0.002	1	0.783	0.783	0.795 ± 0.028	0.267 ± 0.024	24	24	2
777	20.916 ± 0.005	1	0.910	0.910	0.818 ± 0.078	0.377 ± 0.044	0	0	2
779	21.364 ± 0.008	1	0.885	0.885	0.536 ± 0.144	0.122 ± 0.090	0	0	2
780	20.473 ± 0.003	1	0.919	0.919	0.718 ± 0.087	0.218 ± 0.060	30	30	2
787	19.875 ± 0.003	1	0.766	0.766	0.405 ± 0.018	0.089 ± 0.014	10	10	2
794	21.162 ± 0.009	1	0.843	0.843	0.729 ± 0.088	0.189 ± 0.051	0	0	2
798	21.369 ± 0.011	1	0.826	0.826	0.527 ± 0.120	0.184 ± 0.080	0	0	2
799	21.199 ± 0.015	2	0.903	0.903	0.448 ± 0.084	0.143 ± 0.054	0	0	2
800	20.314 ± 0.003	1	0.858	0.858	0.659 ± 0.064	0.167 ± 0.048	30	20	1
801	20.687 ± 0.005	1	0.872	0.872	0.699 ± 0.075	0.071 ± 0.053	0	0	2
802	21.400 ± 0.008	1	0.854	0.854	0.494 ± 0.123	0.166 ± 0.090	0	0	2
803	20.388 ± 0.006	1	0.857	0.857	0.572 ± 0.076	0.196 ± 0.053	30	20	2
805	21.456 ± 0.010	1	0.886	0.886	0.438 ± 0.142	0.107 ± 0.096	0	0	2
807	20.622 ± 0.004	1	0.831	0.831	0.642 ± 0.068	0.114 ± 0.051	0	0	2
808	20.886 ± 0.005	1	0.879	0.879	0.462 ± 0.107	0.100 ± 0.096	0	0	2
814	21.462 ± 0.010	1	0.956	0.956	0.450 ± 0.127	0.094 ± 0.077	0	0	2
815	21.485 ± 0.007	1	0.883	0.883	0.621 ± 0.079	0.050 ± 0.049	0	0	2
816	21.278 ± 0.004	1	0.879	0.879	0.302 ± 0.611	0.301 ± 0.263	0	0	2
817	21.482 ± 0.007	1	0.891	0.891	0.571 ± 0.102	0.197 ± 0.060	0	0	2
818	20.438 ± 0.004	1	0.779	0.779	0.587 ± 0.027	0.198 ± 0.020	20	20	2
819	20.969 ± 0.005	1	0.896	0.896	0.642 ± 0.082	0.156 ± 0.057	0	0	2
823	19.857 ± 0.002	1	0.868	0.868	0.614 ± 0.039	0.118 ± 0.037	30	30	2
824	20.804 ± 0.004	1	0.842	0.842	0.591 ± 0.067	0.117 ± 0.046	0	0	2
825	19.360 ± 0.002	1	0.740	0.740	0.322 ± 0.010	0.066 ± 0.011	10	10	2
828	20.674 ± 0.004	1	0.976	0.976	0.444 ± 0.150	0.099 ± 0.105	0	0	2
835	21.171 ± 0.006	1	0.856	0.856	0.514 ± 0.081	0.087 ± 0.055	0	0	1
838	19.859 ± 0.004	1	0.755	0.703	0.765 ± 0.030	0.257 ± 0.023	24	24	13
839	18.776 ± 0.001	1	0.752	0.752	0.256 ± 0.006	0.034 ± 0.005	10	10	2
840	21.368 ± 0.008	1	0.873	0.873	0.667 ± 0.107	0.348 ± 0.062	0	0	1
841	20.147 ± 0.003	1	0.888	0.888	0.808 ± 0.065	0.328 ± 0.043	30	30	1
842	20.851 ± 0.006	1	0.779	0.779	0.463 ± 0.048	0.219 ± 0.038	0	0	2
843	21.314 ± 0.006	1	0.871	0.871	0.488 ± 0.102	0.073 ± 0.079	0	0	2
844	21.472 ± 0.007	1	0.897	0.897	0.586 ± 0.109	0.161 ± 0.081	0	0	2
845	20.742 ± 0.004	1	0.867	0.867	0.636 ± 0.073	0.226 ± 0.053	0	0	2
847	21.340 ± 0.006	1	0.834	0.834	−	−	0	0	2
848	19.714 ± 0.003	1	0.722	0.722	0.446 ± 0.016	0.056 ± 0.014	10	10	2
850	21.065 ± 0.006	1	0.862	0.862	0.385 ± 0.084	0.142 ± 0.065	0	0	2

TABLE A.5 – *continued*

ID	m_{Ve} (mag)	FLAG	cc	cc_{corr}	ra	el	S1	S2	REG.
851	20.827 ± 0.004	1	0.806	0.806	0.599 ± 0.057	0.220 ± 0.047	0	0	2
852	19.140 ± 0.002	1	0.730	0.730	0.363 ± 0.007	0.141 ± 0.005	10	10	1
853	20.758 ± 0.005	1	0.823	0.823	0.568 ± 0.060	0.209 ± 0.043	0	0	1
856	21.028 ± 0.005	1	0.827	0.827	0.472 ± 0.080	0.227 ± 0.062	0	0	2
857	21.147 ± 0.004	1	0.884	0.884	0.372 ± 0.058	0.348 ± 0.056	0	0	2
858	21.002 ± 0.004	1	0.814	0.814	—	—	0	0	2
859	20.522 ± 0.004	1	0.774	0.774	0.460 ± 0.042	0.191 ± 0.036	10	10	2
860	20.809 ± 0.005	1	0.871	0.871	0.577 ± 0.085	0.210 ± 0.070	0	0	2
865	21.326 ± 0.006	1	0.839	0.839	0.476 ± 0.080	0.183 ± 0.057	0	0	2
867	20.236 ± 0.003	1	0.749	0.749	0.587 ± 0.034	0.253 ± 0.030	24	24	1
868	19.984 ± 0.003	1	0.757	0.757	0.799 ± 0.017	0.241 ± 0.011	24	24	2
869	20.288 ± 0.003	1	0.707	0.707	0.685 ± 0.024	0.231 ± 0.020	24	24	2
870	21.153 ± 0.006	1	0.799	0.799	0.631 ± 0.070	0.298 ± 0.045	0	0	2
872	19.838 ± 0.002	1	0.703	0.703	—	—	0	0	1
873	20.126 ± 0.003	1	0.789	0.828	—	—	0	0	11
874	20.363 ± 0.003	1	0.865	0.865	0.732 ± 0.069	0.111 ± 0.055	30	20	1
875	21.083 ± 0.007	1	0.653	0.712	0.603 ± 0.089	0.145 ± 0.056	0	0	11
877	20.953 ± 0.007	1	0.700	0.754	0.634 ± 0.103	0.267 ± 0.065	0	0	11
878	21.233 ± 0.007	1	0.673	0.673	0.538 ± 0.046	0.102 ± 0.036	0	0	1
879	21.001 ± 0.008	1	0.648	0.708	0.562 ± 0.099	0.127 ± 0.065	0	0	11
880	21.322 ± 0.013	1	0.794	0.794	0.657 ± 0.115	0.057 ± 0.073	0	0	3
882	20.591 ± 0.007	1	0.825	0.825	0.716 ± 0.137	0.241 ± 0.077	24	24	3
883	21.379 ± 0.017	1	0.781	0.781	0.732 ± 0.121	0.082 ± 0.062	0	0	3
884	21.403 ± 0.010	1	0.817	0.817	0.514 ± 0.146	0.232 ± 0.084	0	0	3
886	21.375 ± 0.012	1	0.833	0.833	0.560 ± 0.145	0.170 ± 0.080	0	0	3
888	20.612 ± 0.007	1	0.773	0.773	0.630 ± 0.080	0.053 ± 0.051	0	0	3
889	20.976 ± 0.009	1	0.800	0.800	0.644 ± 0.105	0.180 ± 0.057	0	0	3
890	21.128 ± 0.010	1	0.800	0.800	0.703 ± 0.127	0.205 ± 0.073	0	0	3
891	20.346 ± 0.006	1	0.726	0.726	0.770 ± 0.087	0.147 ± 0.050	20	20	3
892	19.348 ± 0.005	1	0.632	0.632	0.386 ± 0.025	0.114 ± 0.018	10	10	3
893	20.090 ± 0.005	1	0.810	0.810	0.853 ± 0.089	0.230 ± 0.046	24	24	14
897	20.264 ± 0.006	1	0.762	0.762	0.895 ± 0.064	0.275 ± 0.034	24	24	3
898	21.350 ± 0.014	1	0.835	0.835	0.622 ± 0.137	0.067 ± 0.078	0	0	3
899	21.404 ± 0.016	1	0.835	0.835	1.023 ± 0.100	0.395 ± 0.040	0	0	3
904	20.179 ± 0.009	1	0.765	0.765	0.832 ± 0.105	0.104 ± 0.056	20	20	15

BIBLIOGRAPHY

Abell, G. O. (1958). *The Distribution of Rich Clusters of Galaxies.* ApJS, 3, 211

Abell, G. O., Corwin Jr., H. G., and Olowin, R. P. (1989). *A catalog of rich clusters of galaxies.* ApJS, 70, 1

Adami, C., Scheidegger, R., Ulmer, M., Durret, F., Mazure, A., West, M. J., Conselice, C. J., Gregg, M., Kasun, S., Pelló, R., and Picat, J. P. (2006). *A deep wide survey of faint low surface brightness galaxies in the direction of the Coma cluster of galaxies.* A&A, 459, 679

Ahn, C. P., Alexandroff, R., Allende Prieto, C., Anderson, S. F., Anderton, T., Andrews, B. H., Aubourg, É., Bailey, S., Balbinot, E., Barnes, R., and al., et (2012). *The Ninth Data Release of the Sloan Digital Sky Survey: First Spectroscopic Data from the SDSS-III Baryon Oscillation Spectroscopic Survey.* ApJS, 203, 21

Ahn, C. P., Seth, A. C., den Brok, M., Strader, J., Baumgardt, H., van den Bosch, R., Chilingarian, I., Frank, M., Hilker, M., McDermid, R., Mieske, S., Romanowsky, A. J., Spitler, L., Brodie, J., Neumayer, N., and Walsh, J. L. (2017). *Detection of Supermassive Black Holes in Two Virgo Ultracompact Dwarf Galaxies.* ApJ, 839, 72

Alpher, R. A. (1948). *A Neutron-Capture Theory of the Formation and Relative Abundance of the Elements.* Physical Review, 74, 1577

Alpher, R. A. and Herman, R. C. (1949). *Remarks on the Evolution of the Expanding Universe.* Physical Review, 75, 1089

Alpher, R. A., Bethe, H., and Gamow, G. (1948). *The Origin of Chemical Elements.* Physical Review, 73, 803

Andreon, S. (1994). *Morphological segregation of galaxies in clusters. 1: The non-uniform distribution of types in the inner region of Perseus.* A&A, 284, 801

Andreon, S. (2010). *The stellar mass fraction and baryon content of galaxy clusters and groups.* MNRAS, 407, 263

Ashman, K. M. and Zepf, S. E. (1992). *The formation of globular clusters in merging and interacting galaxies.* ApJ, 384, 50

Bamford, S. P., Nichol, R. C., Baldry, I. K., Land, K., Lintott, C. J., Schawinski, K., Slosar, A., Szalay, A. S., Thomas, D., Torki, M., Andreescu, D., Edmondson, E. M., Miller, C. J., Murray, P., Raddick, M. J., and Vandenberg, J. (2009). *Galaxy Zoo: the dependence of morphology and colour on environment.* MNRAS, 393, 1324

Beasley, M. A. and Trujillo, I. (2016). *Globular Clusters Indicate That Ultra-diffuse Galaxies Are Dwarfs.* ApJ, 830, 23

Beasley, M. A., Romanowsky, A. J., Pota, V., Navarro, I. M., Martinez Delgado, D., Neyer, F., and Deich, A. L. (2016). *An Overmassive Dark Halo around an Ultradiffuse Galaxy in the Virgo Cluster.* ApJ, 819, L20

Begeman, K. G., Broeils, A. H., and Sanders, R. H. (1991). *Extended rotation curves of spiral galaxies - Dark haloes and modified dynamics.* MNRAS, 249, 523

Bekki, K. (2009). *Ram-pressure stripping of halo gas in disc galaxies: implications for galactic star formation in different environments.* MNRAS, 399, 2221

Bekki, K., Couch, W. J., Drinkwater, M. J., and Gregg, M. D. (2001a). *A New Formation Model for M32: A Threshed Early-Type Spiral Galaxy?* ApJ, 557, L39

Bekki, K., Couch, W. J., and Drinkwater, M. J. (2001b). *Galaxy Threshing and the Formation of Ultracompact Dwarf Galaxies.* ApJ, 552, L105

Bekki, K., Forbes, D. A., Beasley, M. A., and Couch, W. J. (2003a). *Dynamical evolution of globular cluster systems in clusters of galaxies - I. The case of NGC 1404 in the Fornax cluster*. MNRAS, 344, 1334

Bekki, K., Couch, W. J., Drinkwater, M. J., and Shioya, Y. (2003b). *Galaxy threshing and the origin of ultra-compact dwarf galaxies in the Fornax cluster*. MNRAS, 344, 399

Bell, E. F. and de Jong, R. S. (2000). *The stellar populations of spiral galaxies*. MNRAS, 312, 497

Belokurov, V., Evans, N. W., Irwin, M. J., Lynden-Bell, D., Yanny, B., Vidrih, S., Gilmore, G., Seabroke, G., Zucker, D. B., Wilkinson, M. I., Hewett, P. C., Bramich, D. M., Fellhauer, M., Newberg, H. J., Wyse, R. F. G., Beers, T. C., Bell, E. F., Barentine, J. C., Brinkmann, J., Cole, N., Pan, K., and York, D. G. (2007). *An Orphan in the "Field of Streams"*. ApJ, 658, 337

Bender, R., Burstein, D., and Faber, S. M. (1992). *Dynamically hot galaxies. I - Structural properties*. ApJ, 399, 462

Bennett, C. L., Halpern, M., Hinshaw, G., Jarosik, N., Kogut, A., Limon, M., Meyer, S. S., Page, L., Spergel, D. N., Tucker, G. S., Wollack, E., Wright, E. L., Barnes, C., Greason, M. R., Hill, R. S., Komatsu, E., Nolta, M. R., Odegard, N., Peiris, H. V., Verde, L., and Weiland, J. L. (2003). *First-Year Wilkinson Microwave Anisotropy Probe (WMAP) Observations: Preliminary Maps and Basic Results*. ApJS, 148, 1

Bennett, C. L., Larson, D., Weiland, J. L., Jarosik, N., Hinshaw, G., Odegard, N., Smith, K. M., Hill, R. S., Gold, B., Halpern, M., Komatsu, E., Nolta, M. R., Page, L., Spergel, D. N., Wollack, E., Dunkley, J., Kogut, A., Limon, M., Meyer, S. S., Tucker, G. S., and Wright, E. L. (2013). *Nine-year Wilkinson Microwave Anisotropy Probe (WMAP) Observations: Final Maps and Results*. ApJS, 208, 20

Bergond, G., Athanassoula, E., Leon, S., Balkowski, C., Cayatte, V., Chemin, L., Guzmán, R., Meylan, G., and Prugniel, P. (2007). *Globular clusters and dwarf galaxies in Fornax. I. Kinematics in the cluster core from multi-object spectroscopy*. A&A, 464, L21

Beringer, J. et al. (2012). *Review of Particle Physics*. Phys. Rev. D, 86 (1), 010001

Bertin, E. (2006). *Automatic Astrometric and Photometric Calibration with SCAMP. Astronomical Data Analysis Software and Systems XV*. Ed. by C. Gabriel, C. Arviset, D. Ponz, and S. Enrique. Vol. 351. Astronomical Society of the Pacific Conference Series, 112

Bertin, E. and Arnouts, S. (1996). *SExtractor: Software for source extraction*. A&AS, 117, 393

Bertin, E., Mellier, Y., Radovich, M., Missonnier, G., Didelon, P., and Morin, B. (2002). *The TERAPIX Pipeline. Astronomical Data Analysis Software and Systems XI*. Ed. by D. A. Bohlender, D. Durand, and T. H. Handley. Vol. 281. Astronomical Society of the Pacific Conference Series, 228

Bialas, D., Lisker, T., Olczak, C., Spurzem, R., and Kotulla, R. (2015). *On the occurrence of galaxy harassment*. A&A, 576, A103

Binggeli, B., Sandage, A., and Tammann, G. A. (1985). *Studies of the Virgo Cluster. II - A catalog of 2096 galaxies in the Virgo Cluster area*. AJ, 90, 1681

Binggeli, B., Tammann, G. A., and Sandage, A. (1987). *Studies of the Virgo cluster. VI - Morphological and kinematical structure of the Virgo cluster*. AJ, 94, 251

Blakeslee, J. P., Jordán, A., Mei, S., Côté, P., Ferrarese, L., Infante, L., Peng, E. W., Tonry, J. L., and West, M. J. (2009). *The ACS Fornax Cluster Survey. V. Measurement and Recalibration of Surface Brightness Fluctuations and a Precise Value of the Fornax-Virgo Relative Distance*. ApJ, 694, 556

Blumenthal, G. R., Faber, S. M., Primack, J. R., and Rees, M. J. (1984). *Formation of galaxies and large-scale structure with cold dark matter*. Nature, 311, 517

Boissier, S., Boselli, A., Ferrarese, L., Côté, P., Roehlly, Y., Gwyn, S. D. J., Cuillandre, J.-C., Roediger, J., Koda, J., Muños Mateos, J. C., Gil de Paz, A., and Madore, B. F. (2016). *The properties of the Malin 1 galaxy giant disk. A panchromatic view from the NGVS and GUViCS surveys*. A&A, 593, A126

Bond, J. R., Efstathiou, G., and Silk, J. (1980). *Massive neutrinos and the large-scale structure of the universe*. Physical Review Letters, 45, 1980

Boselli, A. and Gavazzi, G. (2006). *Environmental Effects on Late-Type Galaxies in Nearby Clusters*. PASP, 118, 517

Boselli, A. and Gavazzi, G. (2014). *On the origin of the faint-end of the red sequence in high-density environments*. A&ARv, 22, 74

Boselli, A., Cortese, L., Boquien, M., Boissier, S., Catinella, B., Gavazzi, G., Lagos, C., and Saintonge, A. (2014). *Cold gas properties of the Herschel Reference Survey. III. Molecular gas stripping in cluster galaxies*. A&A, 564, A67

Bothun, G. D., Impey, C. D., and Malin, D. F. (1991). *Extremely low surface brightness galaxies in the Fornax Cluster - Properties, stability, and luminosity fluctuations*. ApJ, 376, 404

Bournaud, F. and Duc, P.-A. (2006). *From tidal dwarf galaxies to satellite galaxies*. A&A, 456, 481

Bournaud, F., Elmegreen, B. G., and Elmegreen, D. M. (2007). *Rapid Formation of Exponential Disks and Bulges at High Redshift from the Dynamical Evolution of Clump-Cluster and Chain Galaxies*. ApJ, 670, 237

Bournaud, F., Duc, P.-A., and Emsellem, E. (2008). *High-resolution simulations of galaxy mergers: resolving globular cluster formation*. MNRAS, 389, L8

Boylan-Kolchin, M., Springel, V., White, S. D. M., Jenkins, A., and Lemson, G. (2009). *Resolving cosmic structure formation with the Millennium-II Simulation*. MNRAS, 398, 1150

Brodie, J. P. and Strader, J. (2006). *Extragalactic Globular Clusters and Galaxy Formation*. ARA&A, 44, 193

Brüns, R. C. and Kroupa, P. (2011). *A New Formation Scenario for the Milky Way Cluster NGC 2419*. ApJ, 729, 69

Brüns, R. C. and Kroupa, P. (2012). *A catalog of extended clusters and ultra-compact dwarf galaxies. An analysis of their parameters in early- and late-type galaxies*. A&A, 547, A65

Bruzual, G. and Charlot, S. (2003). *Stellar population synthesis at the resolution of 2003*. MNRAS, 344, 1000

Burstein, D., Bender, R., Faber, S., and Nolthenius, R. (1997). *Global Relationships Among the Physical Properties of Stellar Systems*. AJ, 114, 1365

Butcher, H. and Oemler Jr., A. (1978). *The evolution of galaxies in clusters. I - ISIT photometry of C1 0024+1654 and 3C 295*. ApJ, 219, 18

Cappellari, M. (2016). *Structure and Kinematics of Early-Type Galaxies from Integral Field Spectroscopy*. ARA&A, 54, 597

Cappellari, M., Emsellem, E., Krajnović, D., McDermid, R. M., Serra, P., Alatalo, K., Blitz, L., Bois, M., Bournaud, F., Bureau, M., Davies, R. L., Davis, T. A., de Zeeuw, P. T., Khochfar, S., Kuntschner, H., Lablanche, P.-Y., Morganti, R., Naab, T., Oosterloo, T., Sarzi, M., Scott, N., Weijmans, A.-M., and Young, L. M. (2011). *The ATLAS^{3D} project - VII. A new look at the morphology of nearby galaxies: the kinematic morphology-density relation*. MNRAS, 416, 1680

Cappellari, M., Scott, N., Alatalo, K., Blitz, L., Bois, M., Bournaud, F., Bureau, M., Crocker, A. F., Davies, R. L., Davis, T. A., de Zeeuw, P. T., Duc, P.-A., Emsellem, E., Khochfar, S., Krajnović, D., Kuntschner, H., McDermid, R. M., Morganti, R., Naab, T., Oosterloo, T., Sarzi, M., Serra, P., Weijmans, A.-M., and Young, L. M. (2013). *The ATLAS^{3D} project - XV. Benchmark for early-type galaxies scaling relations from 260 dynamical models: mass-to-light ratio, dark matter, Fundamental Plane and Mass Plane*. MNRAS, 432, 1709

Caso, J. P., Bassino, L. P., Richtler, T., Smith Castelli, A. V., and Faifer, F. R. (2013). *Ultracompact dwarfs around NGC 3258 in the Antlia cluster*. MNRAS, 430, 1088

Chilingarian, I. V. (2009). *Evolution of dwarf early-type galaxies - I. Spatially resolved stellar populations and internal kinematics of Virgo cluster dE/dS0 galaxies*. MNRAS, 394, 1229

Chilingarian, I. and Zolotukhin, I. (2015). *Isolated compact elliptical galaxies: Stellar systems that ran away*. Science, 348, 418

Colless, M., Dalton, G., Maddox, S., Sutherland, W., Norberg, P., Cole, S., Bland-Hawthorn, J., Bridges, T., Cannon, R., Collins, C., Couch, W., Cross, N., Deeley, K., De Propris, R., Driver, S. P., Efstathiou, G., Ellis, R. S., Frenk, C. S., Glazebrook, K., Jackson, C., Lahav, O., Lewis, I., Lumsden, S., Madgwick, D., Peacock, J. A., Peterson, B. A., Price, I., Seaborne, M., and Taylor, K. (2001). *The 2dF Galaxy Redshift Survey: spectra and redshifts*. MNRAS, 328, 1039

Connors, T. W., Kawata, D., and Gibson, B. K. (2006). *N-body simulations of the Magellanic stream*. MNRAS, 371, 108

Conselice, C. J., Bershady, M. A., and Jangren, A. (2000). *The Asymmetry of Galaxies: Physical Morphology for Nearby and High-Redshift Galaxies*. ApJ, 529, 886

Conselice, C. J., Gallagher III, J. S., and Wyse, R. F. G. (2001). *Galaxy Populations and Evolution in Clusters. I. Dynamics and the Origin of Low-Mass Galaxies in the Virgo Cluster*. ApJ, 559, 791

Conselice, C. J., Gallagher III, J. S., and Wyse, R. F. G. (2002). *Galaxy Populations and Evolution in Clusters. II. Defining Cluster Populations*. AJ, 123, 2246

Conselice, C. J., Gallagher III, J. S., and Wyse, R. F. G. (2003). *Galaxy Populations and Evolution in Clusters. III. The Origin of Low-Mass Galaxies in Clusters: Constraints from Stellar Populations*. AJ, 125, 66

Cortese, L. and Hughes, T. M. (2009). *Evolutionary paths to and from the red sequence: star formation and HI properties of transition galaxies at z ∼ 0*. MNRAS, 400, 1225

Côté, P., Marzke, R. O., and West, M. J. (1998). *The Formation of Giant Elliptical Galaxies and Their Globular Cluster Systems*. ApJ, 501, 554

Côté, P., Piatek, S., Ferrarese, L., Jordán, A., Merritt, D., Peng, E. W., Haşegan, M., Blakeslee, J. P., Mei, S., West, M. J., Milosavljević, M., and Tonry, J. L. (2006). *The ACS Virgo Cluster Survey. VIII. The Nuclei of Early-Type Galaxies*. ApJS, 165, 57

Côté, S., Carignan, C., and Freeman, K. C. (2000). *The Various Kinematics of Dwarf Irregular Galaxies in Nearby Groups and Their Dark Matter Distributions*. AJ, 120, 3027

Couch, W. J., Ellis, R. S., Sharples, R. M., and Smail, I. (1994). *Morphological studies of the galaxy populations in distant 'Butcher-Oemler' clusters with HST. 1: AC 114 at z = 0.31 and Abell 370 at z = 0.37*. ApJ, 430, 121

Courteau, S. and Dutton, A. A. (2015). *On the Global Mass Distribution in Disk Galaxies*. ApJ, 801, L20

Cox, T. J., Dutta, S. N., Di Matteo, T., Hernquist, L., Hopkins, P. F., Robertson, B., and Springel, V. (2006). *The Kinematic Structure of Merger Remnants*. ApJ, 650, 791

D'Abrusco, R., Cantiello, M., Paolillo, M., Pota, V., Napolitano, N. R., Limatola, L., Spavone, M., Grado, A., Iodice, E., Capaccioli, M., Peletier, R., Longo, G., Hilker, M., Mieske, S., Grebel, E. K., Lisker, T., Wittmann, C., van de Ven, G., Schipani, P., and Fabbiano, G. (2016). *The Extended Spatial Distribution of Globular Clusters in the Core of the Fornax Cluster*. ApJ, 819, L31

Dabringhausen, J. and Kroupa, P. (2013). *Dwarf elliptical galaxies as ancient tidal dwarf galaxies*. MNRAS, 429, 1858

Dalcanton, J. J., Spergel, D. N., Gunn, J. E., Schmidt, M., and Schneider, D. P. (1997). *The Number Density of Low-Surface Brightness Galaxies with* $23 < \mu_0 < 25$ *V Mag/arcsec^2*. AJ, 114, 635

De Lucia, G., Weinmann, S., Poggianti, B. M., Aragón-Salamanca, A., and Zaritsky, D. (2012). *The environmental history of group and cluster galaxies in a Λ cold dark matter universe*. MNRAS, 423, 1277

De Propris, R., Phillipps, S., Drinkwater, M. J., Gregg, M. D., Jones, J. B., Evstigneeva, E., and Bekki, K. (2005). *A Comparison of Surface Brightness Profiles for Ultracompact Dwarfs and Dwarf Elliptical Nuclei: Implications for the "Threshing" Scenario*. ApJ, 623, L105

De Rijcke, S., Dejonghe, H., Zeilinger, W. W., and Hau, G. K. T. (2003). *Embedded disks in Fornax dwarf elliptical galaxies*. A&A, 400, 119

De Rijcke, S., Penny, S. J., Conselice, C. J., Valcke, S., and Held, E. V. (2009). *Hubble Space Telescope survey of the Perseus cluster - II. Photometric scaling relations in different environments*. MNRAS, 393, 798

Dekel, A., Sari, R., and Ceverino, D. (2009). *Formation of Massive Galaxies at High Redshift: Cold Streams, Clumpy Disks, and Compact Spheroids*. ApJ, 703, 785

Delgado-Serrano, R., Hammer, F., Yang, Y. B., Puech, M., Flores, H., and Rodrigues, M. (2010). *How was the Hubble sequence 6 Gyr ago?* A&A, 509, A78

Di Cintio, A., Brook, C. B., Dutton, A. A., Macciò, A. V., Obreja, A., and Dekel, A. (2017). *NIHAO - XI. Formation of ultra-diffuse galaxies by outflows*. MNRAS, 466, L1

Dicke, R. H. and Peebles, P. J. E. (1979). *The big bang cosmology - enigmas and nostrums. General Relativity: An Einstein centenary survey*. Ed. by S. W. Hawking and W. Israel, 504

Dine, M. and Kusenko, A. (2003). *Origin of the matter-antimatter asymmetry*. Reviews of Modern Physics, 76, 1

Dirsch, B., Richtler, T., Geisler, D., Gebhardt, K., Hilker, M., Alonso, M. V., Forte, J. C., Grebel, E. K., Infante, L., Larsen, S., Minniti, D., and Rejkuba, M. (2004). *The Globular Cluster System of NGC 1399. III. VLT Spectroscopy and Database*. AJ, 127, 2114

Doroshkevich, A. G., Khlopov, M. I., Sunyaev, R. A., Szalay, A. S., and Zeldovich, I. B. (1981). *Cosmological impact of the neutrino rest mass*. Annals of the New York Academy of Sciences, 375, 32

Dressler, A. (1980). *Galaxy morphology in rich clusters - Implications for the formation and evolution of galaxies*. ApJ, 236, 351

Dressler, A. and Shectman, S. A. (1988). *Evidence for substructure in rich clusters of galaxies from radial-velocity measurements*. AJ, 95, 985

Dressler, A., Oemler Jr., A., Couch, W. J., Smail, I., Ellis, R. S., Barger, A., Butcher, H., Poggianti, B. M., and Sharples, R. M. (1997). *Evolution since z = 0.5 of the Morphology-Density Relation for Clusters of Galaxies*. ApJ, 490, 577

Drinkwater, M. J., Jones, J. B., Gregg, M. D., and Phillipps, S. (2000a). *Compact Stellar Systems in the Fornax Cluster: Super-massive Star Clusters or Extremely Compact Dwarf Galaxies?* Publ. Astron. Soc. Australia, 17, 227

Drinkwater, M. J., Phillipps, S., Jones, J. B., Gregg, M. D., Deady, J. H., Davies, J. I., Parker, Q. A., Sadler, E. M., and Smith, R. M. (2000b). *The Fornax spectroscopic survey. I. Survey strategy and preliminary results on the redshift distribution of a complete sample of stars and galaxies*. A&A, 355, 900

Drinkwater, M. J., Gregg, M. D., and Colless, M. (2001). *Substructure and Dynamics of the Fornax Cluster*. ApJ, 548, L139

Drinkwater, M. J., Gregg, M. D., Hilker, M., Bekki, K., Couch, W. J., Ferguson, H. C., Jones, J. B., and Phillipps, S. (2003). *A class of compact dwarf galaxies from disruptive processes in galaxy clusters*. Nature, 423, 519

Duc, P.-A. (2012). *Birth, Life and Survival of Tidal Dwarf Galaxies*. Astrophysics and Space Science Proceedings, 28, 305

Duc, P.-A., Paudel, S., McDermid, R. M., Cuillandre, J.-C., Serra, P., Bournaud, F., Cappellari, M., and Emsellem, E. (2014). *Identification of old tidal dwarfs near early-type galaxies from deep imaging and H I observations*. MNRAS, 440, 1458

Dunn, J. M. (2010). *The evolution of dwarf galaxies: a comparison of UBVR photometry*. MNRAS, 408, 392

Einstein, A. (1916). *Die Grundlage der allgemeinen Relativitätstheorie*. Annalen der Physik, 354, 769

Eke, V. R., Baugh, C. M., Cole, S., Frenk, C. S., Norberg, P., Peacock, J. A., Baldry, I. K., Bland-Hawthorn, J., Bridges, T., Cannon, R., Colless, M., Collins, C., Couch, W., Dalton, G., de Propris, R., Driver, S. P., Efstathiou, G., Ellis, R. S., Glazebrook, K., Jackson, C., Lahav, O., Lewis, I., Lumsden, S., Maddox, S., Madgwick, D., Peterson, B. A., Sutherland, W., and Taylor, K. (2004). *Galaxy groups in the 2dFGRS: the group-finding algorithm and the 2PIGG catalogue*. MNRAS, 348, 866

Elmegreen, B. G. and Elmegreen, D. M. (2005). *Stellar Populations in 10 Clump-Cluster Galaxies of the Hubble Ultra Deep Field*. ApJ, 627, 632

Emsellem, E., Cappellari, M., Krajnović, D., Alatalo, K., Blitz, L., Bois, M., Bournaud, F., Bureau, M., Davies, R. L., Davis, T. A., de Zeeuw, P. T., Khochfar, S., Kuntschner, H., Lablanche, P.-Y., McDermid, R. M., Morganti, R., Naab, T., Oosterloo, T., Sarzi, M., Scott, N., Serra, P., van de Ven, G., Weijmans, A.-M., and Young, L. M. (2011). *The ATLAS^{3D} project - III. A census of the stellar angular momentum within the effective radius of early-type galaxies: unveiling the distribution of fast and slow rotators*. MNRAS, 414, 888

Erben, T., Schirmer, M., Dietrich, J. P., Cordes, O., Haberzettl, L., Hetterscheidt, M., Hildebrandt, H., Schmithuesen, O., Schneider, P., Simon, P., Deul, E., Hook, R. N., Kaiser, N., Radovich, M., Benoist, C., Nonino, M., Olsen, L. F., Prandoni, I., Wichmann, R., Zaggia, S., Bomans, D., Dettmar, R. J., and Miralles, J. M. (2005). *GaBoDS: The Garching-Bonn Deep Survey. IV. Methods for the image reduction of multi-chip cameras demonstrated on data from the ESO Wide-Field Imager*. Astronomische Nachrichten, 326, 432

Evstigneeva, E. A., Gregg, M. D., Drinkwater, M. J., and Hilker, M. (2007). *Internal Properties of Ultracompact Dwarf Galaxies in the Virgo Cluster*. AJ, 133, 1722

Evstigneeva, E. A., Drinkwater, M. J., Peng, C. Y., Hilker, M., De Propris, R., Jones, J. B., Phillipps, S., Gregg, M. D., and Karick, A. M. (2008). *Structural Properties of Ultra-Compact Dwarf Galaxies in the Fornax and Virgo Clusters*. AJ, 136, 461

Faber, S. M. (1973). *Tidal Origin of Elliptical Galaxies of High Surface Brightness*. ApJ, 179, 423

Fellhauer, M. and Kroupa, P. (2002). *The formation of ultracompact dwarf galaxies*. MNRAS, 330, 642

Fellhauer, M. and Kroupa, P. (2005). *Star Cluster Survival in Star Cluster Complexes under Extreme Residual Gas Expulsion*. ApJ, 630, 879

Ferguson, H. C. (1989). *Population studies in groups and clusters of galaxies. II - A catalog of galaxies in the central 3.5 deg of the Fornax Cluster*. AJ, 98, 367

Ferguson, H. C. and Sandage, A. (1988). *Population studies in groups and clusters of galaxies. I - The luminosity function of galaxies in the Fornax Cluster*. AJ, 96, 1520

Ferrarese, L., Côté, P., Jordán, A., Peng, E. W., Blakeslee, J. P., Piatek, S., Mei, S., Merritt, D., Milosavljević, M., Tonry, J. L., and West, M. J. (2006). *The ACS Virgo Cluster Survey. VI. Isophotal Analysis and the Structure of Early-Type Galaxies*. ApJS, 164, 334

Ferrarese, L., Côté, P., Cuillandre, J.-C., Gwyn, S. D. J., Peng, E. W., MacArthur, L. A., Duc, P.-A., and Boselli, A. et al. (2012). *The Next Generation Virgo Cluster Survey (NGVS). I. Introduction to the Survey*. ApJS, 200, 4

Ferrarese, L., Côté, P., Sánchez-Janssen, R., Roediger, J., McConnachie, A. W., Durrell, P. R., MacArthur, L. A., Blakeslee, J. P., Duc, P.-A., Boissier, S., Boselli, A., Courteau, S., Cuillandre, J.-C., Emsellem, E., Gwyn, S. D. J., Guhathakurta, P., Jordán, A., Lançon, A., Liu, C., Mei, S., Mihos, J. C., Navarro, J. F., Peng, E. W., Puzia, T. H., Taylor, J. E., Toloba, E., and Zhang, H. (2016). *The Next Generation Virgo Cluster Survey (NGVS). XIII. The Luminosity and Mass Function of Galaxies in the Core of the Virgo Cluster and the Contribution from Disrupted Satellites*. ApJ, 824, 10

Firth, P., Drinkwater, M. J., Evstigneeva, E. A., Gregg, M. D., Karick, A. M., Jones, J. B., and Phillipps, S. (2007). *Compact stellar systems around NGC1399*. MNRAS, 382, 1342

Firth, P., Drinkwater, M. J., and Karick, A. M. (2008). *Compact stellar systems and cluster environments*. MNRAS, 389, 1539

Fixsen, D. J. (2009). *The Temperature of the Cosmic Microwave Background*. ApJ, 707, 916

Forbes, D. A., Pota, V., Usher, C., Strader, J., Romanowsky, A. J., Brodie, J. P., Arnold, J. A., and Spitler, L. R. (2013). *Filling the gap: a new class of old star cluster?* MNRAS, 435, L6

Forbes, D. A., Norris, M. A., Strader, J., Romanowsky, A. J., Pota, V., Kannappan, S. J., Brodie, J. P., and Huxor, A. (2014). *The AIMSS Project II: dynamical-to-stellar mass ratios across the star cluster-galaxy divide*. MNRAS, 444, 2993

Forman, W. and Jones, C. (1982). *X-ray-imaging observations of clusters of galaxies*. ARA&A, 20, 547

Francis, K. J., Drinkwater, M. J., Chilingarian, I. V., Bolt, A. M., and Firth, P. (2012). *The chemical composition of ultracompact dwarf galaxies in the Virgo and Fornax clusters*. MNRAS, 425, 325

Frank, M. J., Hilker, M., Mieske, S., Baumgardt, H., Grebel, E. K., and Infante, L. (2011). *Spatially resolved kinematics of an ultracompact dwarf galaxy*. MNRAS, 414, L70

Friedmann, A. (1922). *Über die Krümmung des Raumes*. Zeitschrift für Physik, 10, 377

Gallagher, S. C., Charlton, J. C., Hunsberger, S. D., Zaritsky, D., and Whitmore, B. C. (2001). *Hubble Space Telescope Images of Stephan's Quintet: Star Cluster Formation in a Compact Group Environment*. AJ, 122, 163

Gao, L. and Theuns, T. (2007). *Lighting the Universe with Filaments*. Science, 317, 1527

Gavazzi, G., Contursi, A., Carrasco, L., Boselli, A., Kennicutt, R., Scodeggio, M., and Jaffe, W. (1995). *The radio and optical structure of three peculiar galaxies in A 1367*. A&A, 304, 325

Gavazzi, G., Donati, A., Cucciati, O., Sabatini, S., Boselli, A., Davies, J., and Zibetti, S. (2005). *The structure of elliptical galaxies in the Virgo cluster. Results from the INT Wide Field Survey*. A&A, 430, 411

Gavazzi, G., Fumagalli, M., Fossati, M., Galardo, V., Grossetti, F., Boselli, A., Giovanelli, R., and Haynes, M. P. (2013a). *Hα3: an Hα imaging survey of HI selected galaxies from ALFALFA. II. Star formation properties of galaxies in the Virgo cluster and surroundings*. A&A, 553, A89

Gavazzi, G., Savorgnan, G., Fossati, M., Dotti, M., Fumagalli, M., Boselli, A., Gutiérrez, L., Hernández Toledo, H., Giovanelli, R., and Haynes, M. P. (2013b). *Hα3: an Hα imaging survey of HI selected galaxies from ALFALFA. III. Nurture builds up the Hubble sequence in the Great Wall*. A&A, 553, A90

Geha, M., Guhathakurta, P., and van der Marel, R. P. (2002). *Internal Dynamics, Structure, and Formation of Dwarf Elliptical Galaxies. I. A Keck/Hubble Space Telescope Study of Six Virgo Cluster Dwarf Galaxies*. AJ, 124, 3073

Geha, M., Blanton, M. R., Yan, R., and Tinker, J. L. (2012). *A Stellar Mass Threshold for Quenching of Field Galaxies*. ApJ, 757, 85

Geller, M. J. and Beers, T. C. (1982). *Substructure within clusters of galaxies*. PASP, 94, 421

Gillessen, S., Eisenhauer, F., Trippe, S., Alexander, T., Genzel, R., Martins, F., and Ott, T. (2009). *Monitoring Stellar Orbits Around the Massive Black Hole in the Galactic Center*. ApJ, 692, 1075

Gnedin, O. Y. (2003a). *Dynamical Evolution of Galaxies in Clusters*. ApJ, 589, 752

Gnedin, O. Y. (2003b). *Tidal Effects in Clusters of Galaxies*. ApJ, 582, 141

Goerdt, T., Moore, B., Kazantzidis, S., Kaufmann, T., Macciò, A. V., and Stadel, J. (2008). *The formation of ultra-compact dwarf galaxies and nucleated dwarf galaxies*. MNRAS, 385, 2136

Graham, A. W. and Driver, S. P. (2005). *A Concise Reference to (Projected) Sérsic $R^{1/n}$ Quantities, Including Concentration, Profile Slopes, Petrosian Indices, and Kron Magnitudes*. Publ. Astron. Soc. Australia, 22, 118

Graham, A. W. and Guzmán, R. (2003). *HST Photometry of Dwarf Elliptical Galaxies in Coma, and an Explanation for the Alleged Structural Dichotomy between Dwarf and Bright Elliptical Galaxies*. AJ, 125, 2936

Graham, A. W. and Guzmán, R. (2004). *On the unification of dwarf and giant elliptical galaxies. Penetrating Bars Through Masks of Cosmic Dust*. Ed. by D. L. Block, I. Puerari, K. C. Freeman, R. Groess, and E. K. Block. Vol. 319. Astrophysics and Space Science Library, 723

Graham, A. W., Driver, S. P., Petrosian, V., Conselice, C. J., Bershady, M. A., Crawford, S. M., and Goto, T. (2005). *Total Galaxy Magnitudes and Effective Radii from Petrosian Magnitudes and Radii*. AJ, 130, 1535

Grebel, E. K., Gallagher III, J. S., and Harbeck, D. (2003). *The Progenitors of Dwarf Spheroidal Galaxies*. AJ, 125, 1926

Gregg, M. D., Drinkwater, M. J., Evstigneeva, E., Jurek, R., Karick, A. M., Phillipps, S., Bridges, T., Jones, J. B., Bekki, K., and Couch, W. J. (2009). *A Large Population of Ultra-Compact Dwarfs and Bright Intracluster Globulars in the Fornax Cluster*. AJ, 137, 498

Grillmair, C. J., Freeman, K. C., Bicknell, G. V., Carter, D., Couch, W. J., Sommer-Larsen, J., and Taylor, K. (1994). *The velocity dispersion of globular clusters in NGC 1399*. ApJ, 422, L9

Gunn, J. E. and Gott III, J. R. (1972). *On the infall of matter into clusters of galaxies and some effects on their evolution*. ApJ, 176, 1

Guo, Q., White, S., Boylan-Kolchin, M., De Lucia, G., Kauffmann, G., Lemson, G., Li, C., Springel, V., and Weinmann, S. (2011). *From dwarf spheroidals to cD galaxies: simulating the galaxy population in a ΛCDM cosmology*. MNRAS, 413, 101

Guth, A. H. (1981). *Inflationary universe: A possible solution to the horizon and flatness problems*. Phys. Rev. D, 23, 347

Haşegan, M., Jordán, A., Côté, P., Djorgovski, S. G., McLaughlin, D. E., Blakeslee, J. P., Mei, S., West, M. J., Peng, E. W., Ferrarese, L., Milosavljević, M., Tonry, J. L., and Merritt, D. (2005). *The ACS Virgo Cluster Survey. VII. Resolving the Connection between Globular Clusters and Ultracompact Dwarf Galaxies*. ApJ, 627, 203

Haines, C. P., Pereira, M. J., Sanderson, A. J. R., Smith, G. P., Egami, E., Babul, A., Edge, A. C., Finoguenov, A., Moran, S. M., and Okabe, N. (2012). *LoCuSS: A Dynamical Analysis of X-Ray Active Galactic Nuclei in Local Clusters*. ApJ, 754, 97

Heymans, C., Grocutt, E., Heavens, A., Kilbinger, M., Kitching, T. D., Simpson, F., Benjamin, J., Erben, T., Hildebrandt, H., Hoekstra, H., Mellier, Y., Miller, L., Van Waerbeke, L., Brown, M. L., Coupon, J., Fu, L., Harnois-Déraps, J., Hudson, M. J., Kuijken, K., Rowe, B., Schrabback, T., Semboloni, E., Vafaei, S., and Velander, M. (2013). *CFHTLenS tomographic weak lensing cosmological parameter constraints: Mitigating the impact of intrinsic galaxy alignments*. MNRAS, 432, 2433

Hilker, M. (2011). *A Census of Ultra-Compact Dwarf Galaxies in Nearby Galaxy Clusters*. EAS Publications Series, 48, 219

Hilker, M. (2017). *Stellar population properties of the most massive globular clusters and ultra-compact dwarf galaxies of the Fornax cluster. Formation, Evolution, and Survival of Massive Star Clusters*. Ed. by C. Charbonnel and A. Nota. Vol. 316. IAU Symposium, 99

Hilker, M., Infante, L., Vieira, G., Kissler-Patig, M., and Richtler, T. (1999). *The central region of the Fornax cluster. II. Spectroscopy and radial velocities of member and background galaxies*. A&AS, 134, 75

Hilker, M., Mieske, S., and Infante, L. (2003). *Faint dwarf spheroidals in the Fornax Cluster. A flat luminosity function*. A&A, 397, L9

Hilker, Michael (2009). *UCDs – A Mixed Bag of Objects. Globular Clusters - Guides to Galaxies: Proceedings of the Joint ESO-FONDAP Workshop on Globular Clusters held in Concepción, Chile, 6–10 March 2006*. Ed. by Tom Richtler and Søren Larsen. Berlin, Heidelberg: Springer Berlin Heidelberg, 51. ISBN: 978-3-540-76961-3

Hubble, E. P. (1926). *Extragalactic nebulae*. ApJ, 64, 321

Hubble, E. P. (1936). *Realm of the Nebulae*

Hubble, E. (1929). *A Relation between Distance and Radial Velocity among Extra-Galactic Nebulae*. Proceedings of the National Academy of Science, 15, 168

Hubble, E. and Humason, M. L. (1931). *The Velocity-Distance Relation among Extra-Galactic Nebulae*. ApJ, 74, 43

Hudson, D. S., Mittal, R., Reiprich, T. H., Nulsen, P. E. J., Andernach, H., and Sarazin, C. L. (2010). *What is a cool-core cluster? a detailed analysis of the cores of the X-ray flux-limited HIFLUGCS cluster sample*. A&A, 513, A37

Hunter, D. A. and Elmegreen, B. G. (2006). *Broadband Imaging of a Large Sample of Irregular Galaxies*. ApJS, 162, 49

Huxor, A. P., Tanvir, N. R., Irwin, M. J., Ibata, R., Collett, J. L., Ferguson, A. M. N., Bridges, T., and Lewis, G. F. (2005). *A new population of extended, luminous star clusters in the halo of M31*. MNRAS, 360, 1007

Huxor, A. P., Phillipps, S., Price, J., and Harniman, R. (2011). *Tidal streams in newly discovered M32 analogues: evidence for the stripping scenario*. MNRAS, 414, 3557

Huxor, A. P., Phillipps, S., and Price, J. (2013). *Discovery of an isolated compact elliptical galaxy in the field*. MNRAS, 430, 1956

Ibata, R. A., Gilmore, G., and Irwin, M. J. (1994). *A dwarf satellite galaxy in Sagittarius*. Nature, 370, 194

Impey, C. D., Sprayberry, D., Irwin, M. J., and Bothun, G. D. (1996). *Low Surface Brightness Galaxies in the Local Universe. I. The Catalog*. ApJS, 105, 209

Impey, C., Bothun, G., and Malin, D. (1988). *Virgo dwarfs - New light on faint galaxies*. ApJ, 330, 634

Iodice, E., Capaccioli, M., Grado, A., Limatola, L., Spavone, M., Napolitano, N. R., Paolillo, M., Peletier, R. F., Cantiello, M., Lisker, T., Wittmann, C., Venhola, A., Hilker, M., D'Abrusco, R., Pota, V., and Schipani, P. (2016). *The Fornax Deep Survey with VST. I. The Extended and Diffuse Stellar Halo of NGC 1399 out to 192 kpc*. ApJ, 820, 42

Janz, J., Forbes, D. A., Norris, M. A., Strader, J., Penny, S. J., Fagioli, M., and Romanowsky, A. J. (2015). *How elevated is the dynamical-to-stellar mass ratio of the ultracompact dwarf S999?* MNRAS, 449, 1716

Janz, J., Norris, M. A., Forbes, D. A., Huxor, A., Romanowsky, A. J., Frank, M. J., Escudero, C. G., Faifer, F. R., Forte, J. C., Kannappan, S. J., Maraston, C., Brodie, J. P., Strader, J., and Thompson, B. R. (2016). *The AIMSS Project - III. The stellar populations of compact stellar systems*. MNRAS, 456, 617

Janz, J., Penny, S. J., Graham, A. W., Forbes, D. A., and Davies, R. L. (2017). *Implications for the origin of early-type dwarf galaxies - the discovery of rotation in isolated, low-mass early-type galaxies*. MNRAS, 468, 2850

Jerjen, H. and Binggeli, B. (1997). *Are "Dwarf" Ellipticals Genuine Ellipticals? The Nature of Elliptical Galaxies; 2nd Stromlo Symposium*. Ed. by M. Arnaboldi, G. S. Da Costa, and P. Saha. Vol. 116. Astronomical Society of the Pacific Conference Series, 239

Jester, S., Schneider, D. P., Richards, G. T., Green, R. F., Schmidt, M., Hall, P. B., Strauss, M. A., Vanden Berk, D. E., Stoughton, C., Gunn, J. E., Brinkmann, J., Kent, S. M., Smith, J. A., Tucker, D. L., and Yanny, B. (2005). *The Sloan Digital Sky Survey View of the Palomar-Green Bright Quasar Survey*. AJ, 130, 873

Jordán, A., Blakeslee, J. P., Côté, P., Ferrarese, L., Infante, L., Mei, S., Merritt, D., Peng, E. W., Tonry, J. L., and West, M. J. (2007). *The ACS Fornax Cluster Survey. I. Introduction to the Survey and Data Reduction Procedures*. ApJS, 169, 213

Joye, W. A. and Mandel, E. (2003). *New Features of SAOImage DS9. Astronomical Data Analysis Software and Systems XII*. Ed. by H. E. Payne, R. I. Jedrzejewski, and R. N. Hook. Vol. 295. Astronomical Society of the Pacific Conference Series, 489

Kadowaki, J., Zaritsky, D., and Donnerstein, R. L. (2017). *Spectroscopy of Ultra-diffuse Galaxies in the Coma Cluster*. ApJ, 838, L21

Kambas, A., Davies, J. I., Smith, R. M., Bianchi, S., and Haynes, J. A. (2000). *The Low Surface Brightness Extent of the Fornax Cluster*. AJ, 120, 1316

Kenney, J. D. P., van Gorkom, J. H., and Vollmer, B. (2004). *VLA H I Observations of Gas Stripping in the Virgo Cluster Spiral NGC 4522*. AJ, 127, 3361

Kent, S. M. and Sargent, W. L. W. (1983). *The dynamics of rich clusters of galaxies. II - The Perseus cluster*. AJ, 88, 697

Khochfar, S. and Burkert, A. (2005). *On the origin of isophotal shapes in elliptical galaxies*. MNRAS, 359, 1379

Khochfar, S., Emsellem, E., Serra, P., Bois, M., Alatalo, K., Bacon, R., Blitz, L., Bournaud, F., Bureau, M., Cappellari, M., Davies, R. L., Davis, T. A., de Zeeuw, P. T., Duc, P.-A., Krajnović, D., Kuntschner, H., Lablanche, P.-Y., McDermid, R. M., Morganti, R., Naab, T., Oosterloo, T., Sarzi, M., Scott, N., Weijmans, A.-M., and Young, L. M. (2011). *The ATLAS^{3D} project - VIII. Modelling the formation and evolution of fast and slow rotator early-type galaxies within ΛCDM*. MNRAS, 417, 845

Kim, H.-S., Yoon, S.-J., Sohn, S. T., Kim, S. C., Kim, E., Chung, C., Lee, S.-Y., and Lee, Y.-W. (2013). *Wide-field Multiband Photometry of Globular Cluster Systems in the Fornax Galaxy Cluster*. ApJ, 763, 40

King, I. (1962). *The structure of star clusters. I. An empirical density law*. AJ, 67, 471

Kissler-Patig, M., Brodie, J. P., Schroder, L. L., Forbes, D. A., Grillmair, C. J., and Huchra, J. P. (1998). *Keck spectroscopy of globular clusters around NGC 1399*. AJ, 115, 105

Kissler-Patig, M., Grillmair, C. J., Meylan, G., Brodie, J. P., Minniti, D., and Goudfrooij, P. (1999). *Toward an Understanding of the Globular Cluster Overabundance around the Central Giant Elliptical Galaxy NGC 1399*. AJ, 117, 1206

Kniazev, A. Y., Grebel, E. K., Pustilnik, S. A., Pramskij, A. G., Kniazeva, T. F., Prada, F., and Harbeck, D. (2004). *Low Surface Brightness Galaxies in the Sloan Digital Sky Survey. I. Search Method and Test Sample*. AJ, 127, 704

Koch, A., Burkert, A., Rich, R. M., Collins, M. L. M., Black, C. S., Hilker, M., and Benson, A. J. (2012). *Threshing in Action: The Tidal Disruption of a Dwarf Galaxy by the Hydra I Cluster*. ApJ, 755, L13

Koda, J., Yagi, M., Yamanoi, H., and Komiyama, Y. (2015). *Approximately a Thousand Ultra-diffuse Galaxies in the Coma Cluster*. ApJ, 807, L2

Koester, B. P., McKay, T. A., Annis, J., Wechsler, R. H., Evrard, A., Bleem, L., Becker, M., Johnston, D., Sheldon, E., Nichol, R., Miller, C., Scranton, R., Bahcall, N., Barentine, J., Brewington, H., Brinkmann, J., Harvanek, M., Kleinman, S., Krzesinski, J., Long, D., Nitta, A., Schneider, D. P., Sneddin, S., Voges, W., and York, D. (2007). *A MaxBCG Catalog of 13,823 Galaxy Clusters from the Sloan Digital Sky Survey*. ApJ, 660, 239

Kormendy, J. and Bender, R. (1996). *A Proposed Revision of the Hubble Sequence for Elliptical Galaxies*. ApJ, 464, L119

Kormendy, J. and Bender, R. (2012). *A Revised Parallel-sequence Morphological Classification of Galaxies: Structure and Formation of S0 and Spheroidal Galaxies*. ApJS, 198, 2

Kormendy, J., Bender, R., Magorrian, J., Tremaine, S., Gebhardt, K., Richstone, D., Dressler, A., Faber, S. M., Grillmair, C., and Lauer, T. R. (1997). *Spectroscopic Evidence for a Supermassive Black Hole in NCG 4486B*. ApJ, 482, L139

Kormendy, J., Fisher, D. B., Cornell, M. E., and Bender, R. (2009). *Structure and Formation of Elliptical and Spheroidal Galaxies*. ApJS, 182, 216

Kruijssen, J. M. D. (2014). *Globular cluster formation in the context of galaxy formation and evolution*. Classical and Quantum Gravity, 31.24, 244006

Kruijssen, J. M. D. (2015). *Globular clusters as the relics of regular star formation in 'normal' high-redshift galaxies*. MNRAS, 454, 1658

Lacey, C. and Cole, S. (1993). *Merger rates in hierarchical models of galaxy formation*. MNRAS, 262, 627

Larsen, S. S. and Brodie, J. P. (2000). *Hubble Space Telescope Observations of Star Clusters in NGC 1023: Evidence for Three Cluster Populations?* AJ, 120, 2938

Larsen, S. S. and Brodie, J. P. (2002). *Keck Spectroscopy of Young and Old Star Clusters in NGC 1023*. AJ, 123, 1488

Lemaître, G. (1927). *Un Univers homogène de masse constante et de rayon croissant rendant compte de la vitesse radiale des nébuleuses extra-galactiques*. Annales de la Société Scientifique de Bruxelles, 47, 49

Lieder, S., Lisker, T., Hilker, M., Misgeld, I., and Durrell, P. (2012). *A deep view on the Virgo cluster core*. A&A, 538, A69

Lisker, T., Grebel, E. K., and Binggeli, B. (2006a). *Virgo Cluster Early-Type Dwarf Galaxies with the Sloan Digital Sky Survey. I. On the Possible Disk Nature of Bright Early-Type Dwarfs*. AJ, 132, 497

Lisker, T., Glatt, K., Westera, P., and Grebel, E. K. (2006b). *Virgo Cluster Early-Type Dwarf Galaxies with the Sloan Digital Sky Survey. II. Early-Type Dwarfs with Central Star Formation*. AJ, 132, 2432

Lisker, T., Grebel, E. K., Binggeli, B., and Glatt, K. (2007). *Virgo Cluster Early-Type Dwarf Galaxies with the Sloan Digital Sky Survey. III. Subpopulations: Distributions, Shapes, Origins*. ApJ, 660, 1186

Lisker, T., Weinmann, S. M., Janz, J., and Meyer, H. T. (2013). *Dwarf galaxy populations in present-day galaxy clusters - II. The history of early-type and late-type dwarfs*. MNRAS, 432, 1162

Lisker, T., Wittmann, C., Pasquali, A., Hilker, M., and Grebel, E. K. (submitted to A&A)

Liu, C., Peng, E. W., Côté, P., Ferrarese, L., Jordán, A., Mihos, J. C., Zhang, H.-X., Muñoz, R. P., Puzia, T. H., Lançon, A., Gwyn, S., Cuillandre, J.-C., Blakeslee, J. P., Boselli, A., Durrell, P. R., Duc, P.-A., Guhathakurta, P., MacArthur, L. A., Mei, S., Sánchez-Janssen, R., and Xu, H. (2015). *The Next Generation Virgo Cluster Survey. X. Properties of Ultra-compact Dwarfs in the M87, M49, and M60 Regions*. ApJ, 812, 34

Łokas, E. L. and Mamon, G. A. (2003). *Dark matter distribution in the Coma cluster from galaxy kinematics: breaking the mass-anisotropy degeneracy*. MNRAS, 343, 401

Lyth, D. H. D. H. and Riotto, A. A. (1999). *Particle physics models of inflation and the cosmological density perturbation*. Phys. Rep., 314, 1

Makarov, D., Prugniel, P., Terekhova, N., Courtois, H., and Vauglin, I. (2014). *HyperLEDA. III. The catalogue of extragalactic distances*. A&A, 570, A13

Mann, A. W. and Ebeling, H. (2012). *X-ray-optical classification of cluster mergers and the evolution of the cluster merger fraction*. MNRAS, 420, 2120

Marinova, I., Jogee, S., Weinzirl, T., Erwin, P., Trentham, N., Ferguson, H. C., Hammer, D., den Brok, M., Graham, A. W., Carter, D., Balcells, M., Goudfrooij, P., Guzmán, R., Hoyos, C., Mobasher, B., Mouhcine, M., Peletier, R. F., Peng, E. W., and Verdoes Kleijn, G. (2012). *The HST/ACS Coma Cluster Survey. VIII. Barred Disk Galaxies in the Core of the Coma Cluster*. ApJ, 746, 136

Martínez-Delgado, D., Gómez-Flechoso, M. Á., Aparicio, A., and Carrera, R. (2004). *Tracing Out the Northern Tidal Stream of the Sagittarius Dwarf Spheroidal Galaxy.* ApJ, 601, 242

Martínez-Delgado, D., Gabany, R. J., Crawford, K., Zibetti, S., Majewski, S. R., Rix, H.-W., Fliri, J., Carballo-Bello, J. A., Bardalez-Gagliuffi, D. C., Peñarrubia, J., Chonis, T. S., Madore, B., Trujillo, I., Schirmer, M., and McDavid, D. A. (2010). *Stellar Tidal Streams in Spiral Galaxies of the Local Volume: A Pilot Survey with Modest Aperture Telescopes.* AJ, 140, 962

Mastropietro, C., Moore, B., Mayer, L., Debattista, V. P., Piffaretti, R., and Stadel, J. (2005). *Morphological evolution of discs in clusters.* MNRAS, 364, 607

Mateo, M. L. (1998). *Dwarf Galaxies of the Local Group.* ARA&A, 36, 435

Mateo, M., Olszewski, E. W., and Morrison, H. L. (1998). *Tracing the Outer Structure of the Sagittarius Dwarf Galaxy: Detections at Angular Distances between 10° and 34°.* ApJ, 508, L55

Mathews, W. G., Faltenbacher, A., and Brighenti, F. (2006). *Heating Cooling Flows with Weak Shock Waves.* ApJ, 638, 659

Mathewson, D. S., Cleary, M. N., and Murray, J. D. (1974). *The Magellanic stream.* ApJ, 190, 291

Mayer, L., Governato, F., Colpi, M., Moore, B., Quinn, T., Wadsley, J., Stadel, J., and Lake, G. (2001). *The Metamorphosis of Tidally Stirred Dwarf Galaxies.* ApJ, 559, 754

Mayer, L., Mastropietro, C., Wadsley, J., Stadel, J., and Moore, B. (2006). *Simultaneous ram pressure and tidal stripping; how dwarf spheroidals lost their gas.* MNRAS, 369, 1021

McConnachie, A. W. (2012). *The Observed Properties of Dwarf Galaxies in and around the Local Group.* AJ, 144, 4

McConnachie, A. W., Irwin, M. J., Lewis, G. F., Ibata, R. A., Chapman, S. C., Ferguson, A. M. N., and Tanvir, N. R. (2004). *The tidal trail of NGC 205?* MNRAS, 351, L94

McGaugh, S. S. (2011). *Novel Test of Modified Newtonian Dynamics with Gas Rich Galaxies.* Physical Review Letters, 106.12, 121303

McGaugh, S. S. and de Blok, W. J. G. (1997). *Gas Mass Fractions and the Evolution of Spiral Galaxies.* ApJ, 481, 689

McGaugh, S. S. and de Blok, W. J. G. (1998). *Testing the Hypothesis of Modified Dynamics with Low Surface Brightness Galaxies and Other Evidence.* ApJ, 499, 66

McLaughlin, D. E. (1999). *Evidence in Virgo for the Universal Dark Matter Halo.* ApJ, 512, L9

Meisner, A. M. and Finkbeiner, D. P. (2014). *A Full-sky, High-resolution Atlas of Galactic 12 μm Dust Emission with WISE.* ApJ, 781, 5

Merritt, A., van Dokkum, P., Danieli, S., Abraham, R., Zhang, J., Karachentsev, I. D., and Makarova, L. N. (2016). *The Dragonfly Nearby Galaxies Survey. II. Ultra-Diffuse Galaxies near the Elliptical Galaxy NGC 5485.* ApJ, 833, 168

Metz, M. and Kroupa, P. (2007). *Dwarf spheroidal satellites: are they of tidal origin?* MNRAS, 376, 387

Michielsen, D., Boselli, A., Conselice, C. J., Toloba, E., Whiley, I. M., Aragón-Salamanca, A., Balcells, M., Cardiel, N., Cenarro, A. J., Gorgas, J., Peletier, R. F., and Vazdekis, A. (2008). *The relation between stellar populations, structure and environment for dwarf elliptical galaxies from the MAGPOP-ITP.* MNRAS, 385, 1374

Mieske, S., Hilker, M., and Infante, L. (2002). *Ultra compact objects in the Fornax cluster of galaxies: Globular clusters or dwarf galaxies?* A&A, 383, 823

Mieske, S., Hilker, M., and Infante, L. (2004). *Fornax compact object survey FCOS: On the nature of Ultra Compact Dwarf galaxies*. A&A, 418, 445

Mieske, S., Hilker, M., Infante, L., and Mendes de Oliveira, C. (2007). *The early-type dwarf galaxy population of the Fornax cluster*. A&A, 463, 503

Mieske, S., Dabringhausen, J., Kroupa, P., Hilker, M., and Baumgardt, H. (2008a). *High M/L ratios of UCDs: A variation of the IMF?* Astronomische Nachrichten, 329, 964

Mieske, S., Hilker, M., Jordán, A., Infante, L., Kissler-Patig, M., Rejkuba, M., Richtler, T., Côté, P., Baumgardt, H., West, M. J., Ferrarese, L., and Peng, E. W. (2008b). *The nature of UCDs: Internal dynamics from an expanded sample and homogeneous database*. A&A, 487, 921

Mieske, S., Hilker, M., and Misgeld, I. (2012). *The specific frequencies of ultra-compact dwarf galaxies*. A&A, 537, A3

Mieske, S., Frank, M. J., Baumgardt, H., Lützgendorf, N., Neumayer, N., and Hilker, M. (2013). *On central black holes in ultra-compact dwarf galaxies*. A&A, 558, A14

Mihos, J. C., Harding, P., Feldmeier, J., and Morrison, H. (2005). *Diffuse Light in the Virgo Cluster*. ApJ, 631, L41

Mihos, J. C., Durrell, P. R., Ferrarese, L., Feldmeier, J. J., Côté, P., Peng, E. W., Harding, P., Liu, C., Gwyn, S., and Cuillandre, J.-C. (2015). *Galaxies at the Extremes: Ultra-diffuse Galaxies in the Virgo Cluster*. ApJ, 809, L21

Mihos, J. C., Harding, P., Feldmeier, J. J., Rudick, C., Janowiecki, S., Morrison, H., Slater, C., and Watkins, A. (2017). *The Burrell Schmidt Deep Virgo Survey: Tidal Debris, Galaxy Halos, and Diffuse Intracluster Light in the Virgo Cluster*. ApJ, 834, 16

Milgrom, M. (1983a). *A modification of the Newtonian dynamics - Implications for galaxies*. ApJ, 270, 371

Milgrom, M. (1983b). *A modification of the Newtonian dynamics as a possible alternative to the hidden mass hypothesis*. ApJ, 270, 365

Milgrom, M. (2015). *Ultra-diffuse cluster galaxies as key to the MOND cluster conundrum*. MNRAS, 454, 3810

Misgeld, I. and Hilker, M. (2011). *Families of dynamically hot stellar systems over 10 orders of magnitude in mass*. MNRAS, 414, 3699

Misgeld, I., Mieske, S., and Hilker, M. (2008). *The early-type dwarf galaxy population of the Hydra I cluster*. A&A, 486, 697

Misgeld, I., Hilker, M., and Mieske, S. (2009). *The early-type dwarf galaxy population of the Centaurus cluster*. A&A, 496, 683

Misner, C. W., Thorne, K. S., and Wheeler, J. A. (1973). *Gravitation*

Mistani, P. A., Sales, L. V., Pillepich, A., Sanchez-Janssen, R., Vogelsberger, M., Nelson, D., Rodriguez-Gomez, V., Torrey, P., and Hernquist, L. (2016). *On the assembly of dwarf galaxies in clusters and their efficient formation of globular clusters*. MNRAS, 455, 2323

Miville-Deschênes, M.-A., Duc, P.-A., Marleau, F., Cuillandre, J.-C., Didelon, P., Gwyn, S., and Karabal, E. (2016). *Probing interstellar turbulence in cirrus with deep optical imaging: no sign of energy dissipation at 0.01 pc scale*. A&A, 593, A4

Mo, H., van den Bosch, F. C., and White, S. (2010). *Galaxy Formation and Evolution*

Moore, B., Katz, N., Lake, G., Dressler, A., and Oemler, A. (1996). *Galaxy harassment and the evolution of clusters of galaxies*. Nature, 379, 613

Moore, B., Lake, G., and Katz, N. (1998). *Morphological Transformation from Galaxy Harassment*. ApJ, 495, 139

Moore, B., Lake, G., Quinn, T., and Stadel, J. (1999). *On the survival and destruction of spiral galaxies in clusters*. MNRAS, 304, 465

Moster, B. P., Naab, T., and White, S. D. M. (2013). *Galactic star formation and accretion histories from matching galaxies to dark matter haloes*. MNRAS, 428, 3121

Muñoz, R. P., Eigenthaler, P., Puzia, T. H., Taylor, M. A., Ordenes-Briceño, Y., Alamo-Martínez, K., Ribbeck, K. X., Ángel, S., Capaccioli, M., Côté, P., Ferrarese, L., Galaz, G., Hempel, M., Hilker, M., Jordán, A., Lançon, A., Mieske, S., Paolillo, M., Richtler, T., Sánchez-Janssen, R., and Zhang, H. (2015). *Unveiling a Rich System of Faint Dwarf Galaxies in the Next Generation Fornax Survey*. ApJ, 813, L15

Mulchaey, J. S. (2000). *X-ray Properties of Groups of Galaxies*. ARA&A, 38, 289

Murakami, H., Komiyama, M., Matsushita, K., Nagino, R., Sato, T., Sato, K., Kawaharada, M., Nakazawa, K., Ohashi, T., and Takei, Y. (2011). *Suzaku and XMM-Newton Observations of the Fornax Cluster: Temperature and Metallicity Distribution*. PASJ, 63, S963

Noble, A. G., Webb, T. M. A., Muzzin, A., Wilson, G., Yee, H. K. C., and van der Burg, R. F. J. (2013). *A Kinematic Approach to Assessing Environmental Effects: Star-forming Galaxies in a z ∼ 0.9 SpARCS Cluster Using Spitzer 24 μm Observations*. ApJ, 768, 118

Norris, M. A., Kannappan, S. J., Forbes, D. A., Romanowsky, A. J., Brodie, J. P., Faifer, F. R., Huxor, A., Maraston, C., Moffett, A. J., Penny, S. J., Pota, V., Smith-Castelli, A., Strader, J., Bradley, D., Eckert, K. D., Fohring, D., McBride, J., Stark, D. V., and Vaduvescu, O. (2014). *The AIMSS Project - I. Bridging the star cluster-galaxy divide*. MNRAS, 443, 1151

Norris, M. A., Escudero, C. G., Faifer, F. R., Kannappan, S. J., Forte, J. C., and van den Bosch, R. C. E. (2015). *An extended star formation history in an ultra-compact dwarf*. MNRAS, 451, 3615

Oemler Jr., A. (1974). *The Systematic Properties of Clusters of Galaxies. Photometry of 15 Clusters*. ApJ, 194, 1

Okazaki, T. and Taniguchi, Y. (2000). *Dwarf Galaxy Formation Induced by Galaxy Interactions*. ApJ, 543, 149

Papastergis, E., Adams, E. A. K., and Romanowsky, A. J. (2017). *The HI content of isolated ultra-diffuse galaxies: A sign of multiple formation mechanisms?* A&A, 601, L10

Paudel, S., Lisker, T., and Janz, J. (2010). *Nuclei of Early-type Dwarf Galaxies: Are They Progenitors of Ultracompact Dwarf Galaxies?* ApJ, 724, L64

Paudel, S., Lisker, T., and Kuntschner, H. (2011). *Nuclei of early-type dwarf galaxies: insights from stellar populations*. MNRAS, 413, 1764

Paudel, S., Lisker, T., Hansson, K. S. A., and Huxor, A. P. (2014). *An isolated, compact early-type galaxy with a diffuse stellar component: merger origin?* MNRAS, 443, 446

Peacock, J. A. and Smith, R. E. (2000). *Halo occupation numbers and galaxy bias*. MNRAS, 318, 1144

Peebles, P. J. E. (1982). *Large-scale background temperature and mass fluctuations due to scale-invariant primeval perturbations*. ApJ, 263, L1

Peebles, P. J. E. and Yu, J. T. (1970). *Primeval Adiabatic Perturbation in an Expanding Universe*. ApJ, 162, 815

Peletier, R. F., Valentijn, E. A., and Jameson, R. F. (1990). *Near-infrared photometry of bright elliptical galaxies*. A&A, 233, 62

Peng, C. Y., Ho, L. C., Impey, C. D., and Rix, H.-W. (2002). *Detailed Structural Decomposition of Galaxy Images*. AJ, 124, 266

Peng, C. Y., Ho, L. C., Impey, C. D., and Rix, H.-W. (2010). *Detailed Decomposition of Galaxy Images. II. Beyond Axisymmetric Models.* AJ, 139, 2097

Peng, E. W. and Lim, S. (2016). *A Rich Globular Cluster System in Dragonfly 17: Are Ultra-diffuse Galaxies Pure Stellar Halos?* ApJ, 822, L31

Penny, S. J., Conselice, C. J., de Rijcke, S., and Held, E. V. (2009). *Hubble Space Telescope survey of the Perseus Cluster - I. The structure and dark matter content of cluster dwarf spheroidals.* MNRAS, 393, 1054

Penny, S. J., Forbes, D. A., and Conselice, C. J. (2012). *Hubble Space Telescope survey of the Perseus cluster - IV. Compact stellar systems in the Perseus cluster core and ultracompact dwarf formation in star-forming filaments.* MNRAS, 422, 885

Penny, S. J., Forbes, D. A., Strader, J., Usher, C., Brodie, J. P., and Romanowsky, A. J. (2014). *Ultracompact dwarfs in the Perseus Cluster: UCD formation via tidal stripping.* MNRAS, 439, 3808

Penzias, A. A. and Wilson, R. W. (1965). *A Measurement of Excess Antenna Temperature at 4080 Mc/s.* ApJ, 142, 419

Percival, W. J., Reid, B. A., Eisenstein, D. J., Bahcall, N. A., Budavari, T., Frieman, J. A., Fukugita, M., Gunn, J. E., Ivezić, Ž., Knapp, G. R., Kron, R. G., Loveday, J., Lupton, R. H., McKay, T. A., Meiksin, A., Nichol, R. C., Pope, A. C., Schlegel, D. J., Schneider, D. P., Spergel, D. N., Stoughton, C., Strauss, M. A., Szalay, A. S., Tegmark, M., Vogeley, M. S., Weinberg, D. H., York, D. G., and Zehavi, I. (2010). *Baryon acoustic oscillations in the Sloan Digital Sky Survey Data Release 7 galaxy sample.* MNRAS, 401, 2148

Perlmutter, S., Aldering, G., Goldhaber, G., Knop, R. A., Nugent, P., Castro, P. G., Deustua, S., Fabbro, S., Goobar, A., Groom, D. E., Hook, I. M., Kim, A. G., Kim, M. Y., Lee, J. C., Nunes, N. J., Pain, R., Pennypacker, C. R., Quimby, R., Lidman, C., Ellis, R. S., Irwin, M., McMahon, R. G., Ruiz-Lapuente, P., Walton, N., Schaefer, B., Boyle, B. J., Filippenko, A. V., Matheson, T., Fruchter, A. S., Panagia, N., Newberg, H. J. M., Couch, W. J., and Project, T. S. C. (1999). *Measurements of Ω and Λ from 42 High-Redshift Supernovae.* ApJ, 517, 565

Petrosian, V. (1976). *Surface brightness and evolution of galaxies.* ApJ, 209, L1

Pfeffer, J. and Baumgardt, H. (2013). *Ultra-compact dwarf galaxy formation by tidal stripping of nucleated dwarf galaxies.* MNRAS, 433, 1997

Pfeffer, J., Griffen, B. F., Baumgardt, H., and Hilker, M. (2014). *Contribution of stripped nuclear clusters to globular cluster and ultracompact dwarf galaxy populations.* MNRAS, 444, 3670

Pfeffer, J., Hilker, M., Baumgardt, H., and Griffen, B. F. (2016). *Constraining ultra-compact dwarf galaxy formation with galaxy clusters in the local universe.* MNRAS, 458, 2492

Phillipps, S., Drinkwater, M. J., Gregg, M. D., and Jones, J. B. (2001). *Ultracompact Dwarf Galaxies in the Fornax Cluster.* ApJ, 560, 201

Piffaretti, R., Arnaud, M., Pratt, G. W., Pointecouteau, E., and Melin, J.-B. (2011). *The MCXC: A meta-catalogue of X-ray detected clusters of galaxies.* A&A, 534, A109

Planck Collaboration, Ade, P. A. R., Aghanim, N., Alves, M. I. R., Armitage-Caplan, C., Arnaud, M., Ashdown, M., Atrio-Barandela, F., Aumont, J., Aussel, H., and al., et (2014). *Planck 2013 results. I. Overview of products and scientific results.* A&A, 571, A1

Planck Collaboration, Ade, P. A. R., Aghanim, N., Arnaud, M., Ashdown, M., Aumont, J., Baccigalupi, C., Banday, A. J., Barreiro, R. B., Bartlett, J. G., and al., et (2016). *Planck 2015 results. XIII. Cosmological parameters.* A&A, 594, A13

Poggianti, B. M., De Lucia, G., Varela, J., Aragon-Salamanca, A., Finn, R., Desai, V., von der Linden, A., and White, S. D. M. (2010). *The evolution of the density of galaxy clusters and groups: denser environments at higher redshifts*. MNRAS, 405, 995

Postman, M., Franx, M., Cross, N. J. G., Holden, B., Ford, H. C., Illingworth, G. D., Goto, T., Demarco, R., Rosati, P., Blakeslee, J. P., Tran, K.-V., Benítez, N., Clampin, M., Hartig, G. F., Homeier, N., Ardila, D. R., Bartko, F., Bouwens, R. J., Bradley, L. D., Broadhurst, T. J., Brown, R. A., Burrows, C. J., Cheng, E. S., Feldman, P. D., Golimowski, D. A., Gronwall, C., Infante, L., Kimble, R. A., Krist, J. E., Lesser, M. P., Martel, A. R., Mei, S., Menanteau, F., Meurer, G. R., Miley, G. K., Motta, V., Sirianni, M., Sparks, W. B., Tran, H. D., Tsvetanov, Z. I., White, R. L., and Zheng, W. (2005). *The Morphology-Density Relation in z ∼ 1 Clusters*. ApJ, 623, 721

Press, W. H. and Schechter, P. (1974). *Formation of Galaxies and Clusters of Galaxies by Self-Similar Gravitational Condensation*. ApJ, 187, 425

Rakos, K. and Schombert, J. (2004). *The Ages of Dwarf Elliptical Galaxies*. AJ, 127, 1502

Recchi, S., Theis, C., Kroupa, P., and Hensler, G. (2007). *The early evolution of tidal dwarf galaxies*. A&A, 470, L5

Renaud, F., Bournaud, F., and Duc, P.-A. (2015). *A parsec-resolution simulation of the Antennae galaxies: formation of star clusters during the merger*. MNRAS, 446, 2038

Rest, A., Scolnic, D., Foley, R. J., Huber, M. E., Chornock, R., Narayan, G., Tonry, J. L., Berger, E., Soderberg, A. M., Stubbs, C. W., Riess, A., Kirshner, R. P., Smartt, S. J., Schlafly, E., Rodney, S., Botticella, M. T., Brout, D., Challis, P., Czekala, I., Drout, M., Hudson, M. J., Kotak, R., Leibler, C., Lunnan, R., Marion, G. H., McCrum, M., Milisavljevic, D., Pastorello, A., Sanders, N. E., Smith, K., Stafford, E., Thilker, D., Valenti, S., Wood-Vasey, W. M., Zheng, Z., Burgett, W. S., Chambers, K. C., Denneau, L., Draper, P. W., Flewelling, H., Hodapp, K. W., Kaiser, N., Kudritzki, R.-P., Magnier, E. A., Metcalfe, N., Price, P. A., Sweeney, W., Wainscoat, R., and Waters, C. (2014). *Cosmological constraints from measurements of type Ia supernovae discovered during the first 1.5 yr of the Pan-STARRS1 Survey*. ApJ, 795, 44

Richtler, T., Dirsch, B., Larsen, S., Hilker, M., and Infante, L. (2005). *The globular cluster system of NGC 1399. IV. Some noteworthy objects*. A&A, 439, 533

Richtler, T., Schuberth, Y., Hilker, M., Dirsch, B., Bassino, L., and Romanowsky, A. J. (2008). *The dark matter halo of NGC 1399 - CDM or MOND?* A&A, 478, L23

Riess, A. G., Filippenko, A. V., Challis, P., Clocchiatti, A., Diercks, A., Garnavich, P. M., Gilliland, R. L., Hogan, C. J., Jha, S., Kirshner, R. P., Leibundgut, B., Phillips, M. M., Reiss, D., Schmidt, B. P., Schommer, R. A., Smith, R. C., Spyromilio, J., Stubbs, C., Suntzeff, N. B., and Tonry, J. (1998). *Observational Evidence from Supernovae for an Accelerating Universe and a Cosmological Constant*. AJ, 116, 1009

Riess, A. G., Macri, L. M., Hoffmann, S. L., Scolnic, D., Casertano, S., Filippenko, A. V., Tucker, B. E., Reid, M. J., Jones, D. O., Silverman, J. M., Chornock, R., Challis, P., Yuan, W., Brown, P. J., and Foley, R. J. (2016). *A 2.4% Determination of the Local Value of the Hubble Constant*. ApJ, 826, 56

Rindler, W. (1956). *Visual horizons in world models*. MNRAS, 116, 662

Robertson, H. P. (1929). *On the Foundations of Relativistic Cosmology*. Proceedings of the National Academy of Science, 15, 822

Román, J. and Trujillo, I. (2017). *Ultra-diffuse galaxies outside clusters: clues to their formation and evolution*. MNRAS, 468, 4039

Ryś, A., Falcón-Barroso, J., and van de Ven, G. (2013). *Virgo cluster and field dwarf ellipticals in 3D - I. On the variety of stellar kinematic and line-strength properties.* MNRAS, 428, 2980

Ryś, A., van de Ven, G., and Falcón-Barroso, J. (2014). *Virgo Cluster and field dwarf ellipticals in 3D - II. Internal dynamics points to tidal harassment?* MNRAS, 439, 284

Ryś, A., Koleva, M., Falcón-Barroso, J., Vazdekis, A., Lisker, T., Peletier, R., and van de Ven, G. (2015). *Virgo cluster and field dwarf ellipticals in 3D - III. Spatially and temporally resolved stellar populations.* MNRAS, 452, 1888

Sandage, A. and Binggeli, B. (1984). *Studies of the Virgo cluster. III - A classification system and an illustrated atlas of Virgo cluster dwarf galaxies.* AJ, 89, 919

Sawala, T., Frenk, C. S., Fattahi, A., Navarro, J. F., Theuns, T., Bower, R. G., Crain, R. A., Furlong, M., Jenkins, A., Schaller, M., and Schaye, J. (2016). *The chosen few: the low-mass haloes that host faint galaxies.* MNRAS, 456, 85

Schindler, S., Binggeli, B., and Böhringer, H. (1999). *Morphology of the Virgo cluster: Gas versus galaxies.* A&A, 343, 420

Schirmer, M. (2013). *THELI: Convenient Reduction of Optical, Near-infrared, and Mid-infrared Imaging Data.* ApJS, 209, 21

Schlafly, E. F. and Finkbeiner, D. P. (2011). *Measuring Reddening with Sloan Digital Sky Survey Stellar Spectra and Recalibrating SFD.* ApJ, 737, 103

Schombert, J., Maciel, T., and McGaugh, S. (2011). *Stellar Populations and the Star Formation Histories of LSB Galaxies – Part I: Optical and Hα Imaging.* Advances in Astronomy 2011, 143698

Schuberth, Y., Richtler, T., Bassino, L., and Hilker, M. (2008). *Intra-cluster globular clusters around NGC 1399 in Fornax?* A&A, 477, L9

Schuberth, Y., Richtler, T., Hilker, M., Dirsch, B., Bassino, L. P., Romanowsky, A. J., and Infante, L. (2010). *The globular cluster system of NGC 1399. V. Dynamics of the cluster system out to 80 kpc.* A&A, 513, A52

Schweizer, F. (1978). *Galaxies with long tails. Structure and Properties of Nearby Galaxies.* Ed. by E. M. Berkhuijsen and R. Wielebinski. Vol. 77. IAU Symposium, 279

Seth, A. C., van den Bosch, R., Mieske, S., Baumgardt, H., Brok, M. D., Strader, J., Neumayer, N., Chilingarian, I., Hilker, M., McDermid, R., Spitler, L., Brodie, J., Frank, M. J., and Walsh, J. L. (2014). *A supermassive black hole in an ultra-compact dwarf galaxy.* Nature, 513, 398

Simionescu, A., Allen, S. W., Mantz, A., Werner, N., Takei, Y., Morris, R. G., Fabian, A. C., Sanders, J. S., Nulsen, P. E. J., George, M. R., and Taylor, G. B. (2011). *Baryons at the Edge of the X-ray-Brightest Galaxy Cluster.* Science, 331, 1576

Skibba, R. A., Bamford, S. P., Nichol, R. C., Lintott, C. J., Andreescu, D., Edmondson, E. M., Murray, P., Raddick, M. J., Schawinski, K., Slosar, A., Szalay, A. S., Thomas, D., and Vandenberg, J. (2009). *Galaxy Zoo: disentangling the environmental dependence of morphology and colour.* MNRAS, 399, 966

Skrutskie, M. F., Cutri, R. M., Stiening, R., Weinberg, M. D., Schneider, S., Carpenter, J. M., Beichman, C., Capps, R., Chester, T., Elias, J., Huchra, J., Liebert, J., Lonsdale, C., Monet, D. G., Price, S., Seitzer, P., Jarrett, T., Kirkpatrick, J. D., Gizis, J. E., Howard, E., Evans, T., Fowler, J., Fullmer, L., Hurt, R., Light, R., Kopan, E. L., Marsh, K. A., McCallon, H. L., Tam, R., Van Dyk, S., and Wheelock, S. (2006). *The Two Micron All Sky Survey (2MASS).* AJ, 131, 1163

Slipher, V. M. (1917). *Nebulae.* Proceedings of the American Philosophical Society, 56, 403

Smith, B. J., Giroux, M. L., Struck, C., and Hancock, M. (2010). *Spirals, Bridges, and Tails: A Galaxy Evolution Explorer Ultraviolet Atlas of Interacting Galaxies*. AJ, 139, 1212

Smith, R., Fellhauer, M., and Assmann, P. (2012). *Ram pressure drag - the effects of ram pressure on dark matter and stellar disc dynamics*. MNRAS, 420, 1990

Smith, R., Sánchez-Janssen, R., Beasley, M. A., Candlish, G. N., Gibson, B. K., Puzia, T. H., Janz, J., Knebe, A., Aguerri, J. A. L., Lisker, T., Hensler, G., Fellhauer, M., Ferrarese, L., and Yi, S. K. (2015). *The sensitivity of harassment to orbit: mass loss from early-type dwarfs in galaxy clusters*. MNRAS, 454, 2502

Smoot, G. F., Bennett, C. L., Kogut, A., Wright, E. L., Aymon, J., Boggess, N. W., Cheng, E. S., de Amici, G., Gulkis, S., Hauser, M. G., Hinshaw, G., Jackson, P. D., Janssen, M., Kaita, E., Kelsall, T., Keegstra, P., Lineweaver, C., Loewenstein, K., Lubin, P., Mather, J., Meyer, S. S., Moseley, S. H., Murdock, T., Rokke, L., Silverberg, R. F., Tenorio, L., Weiss, R., and Wilkinson, D. T. (1992). *Structure in the COBE differential microwave radiometer first-year maps*. ApJ, 396, L1

Sprayberry, D., Impey, C. D., Bothun, G. D., and Irwin, M. J. (1995). *Properties of the class of giant low surface brightness spiral galaxies*. AJ, 109, 558

Springel, V., White, S. D. M., Jenkins, A., Frenk, C. S., Yoshida, N., Gao, L., Navarro, J., Thacker, R., Croton, D., Helly, J., Peacock, J. A., Cole, S., Thomas, P., Couchman, H., Evrard, A., Colberg, J., and Pearce, F. (2005). *Simulations of the formation, evolution and clustering of galaxies and quasars*. Nature, 435, 629

Strader, J., Seth, A. C., Forbes, D. A., Fabbiano, G., Romanowsky, A. J., Brodie, J. P., Conroy, C., Caldwell, N., Pota, V., Usher, C., and Arnold, J. A. (2013). *The Densest Galaxy*. ApJ, 775, L6

Strömberg, G. (1925). *Analysis of radial velocities of globular clusters and non-galactic nebulae*. ApJ, 61, 353

Struble, M. F. and Rood, H. J. (1999). *A Compilation of Redshifts and Velocity Dispersions for ACO Clusters*. ApJS, 125, 35

Suzuki, N., Rubin, D., Lidman, C., Aldering, G., Amanullah, R., Barbary, K., Barrientos, L. F., Botyanszki, J., Brodwin, M., Connolly, N., Dawson, K. S., Dey, A., Doi, M., Donahue, M., Deustua, S., Eisenhardt, P., Ellingson, E., Faccioli, L., Fadeyev, V., Fakhouri, H. K., Fruchter, A. S., Gilbank, D. G., Gladders, M. D., Goldhaber, G., Gonzalez, A. H., Goobar, A., Gude, A., Hattori, T., Hoekstra, H., Hsiao, E., Huang, X., Ihara, Y., Jee, M. J., Johnston, D., Kashikawa, N., Koester, B., Konishi, K., Kowalski, M., Linder, E. V., Lubin, L., Melbourne, J., Meyers, J., Morokuma, T., Munshi, F., Mullis, C., Oda, T., Panagia, N., Perlmutter, S., Postman, M., Pritchard, T., Rhodes, J., Ripoche, P., Rosati, P., Schlegel, D. J., Spadafora, A., Stanford, S. A., Stanishev, V., Stern, D., Strovink, M., Takanashi, N., Tokita, K., Wagner, M., Wang, L., Yasuda, N., Yee, H. K. C., and Supernova Cosmology Project, T. (2012). *The Hubble Space Telescope Cluster Supernova Survey. V. Improving the Dark-energy Constraints above $z > 1$ and Building an Early-type-hosted Supernova Sample*. ApJ, 746, 85

Swinbank, A. M., Smail, I., Sobral, D., Theuns, T., Best, P. N., and Geach, J. E. (2012). *The Properties of the Star-forming Interstellar Medium at $z = 0.8$-2.2 from HiZELS: Star Formation and Clump Scaling Laws in Gas-rich, Turbulent Disks*. ApJ, 760, 130

Sybilska, A., Lisker, T., Kuntschner, H., Vazdekis, A., van de Ven, G., Peletier, R., Falcón-Barroso, J., Vijayaraghavan, R., and Janz, J. (2017). *The hELENa project - I. Stellar populations of early-type galaxies linked with local environment and galaxy mass*. MNRAS, 470, 815

Tody, D. (1993). *IRAF in the Nineties. Astronomical Data Analysis Software and Systems II*. Ed. by R. J. Hanisch, R. J. V. Brissenden, and J. Barnes. Vol. 52. Astronomical Society of the Pacific Conference Series, 173

Toloba, E., Boselli, A., Gorgas, J., Peletier, R. F., Cenarro, A. J., Gadotti, D. A., Gil de Paz, A., Pedraz, S., and Yildiz, U. (2009). *Kinematic Properties as Probes of the Evolution of Dwarf Galaxies in the Virgo Cluster*. ApJ, 707, L17

Toloba, E., Boselli, A., Cenarro, A. J., Peletier, R. F., Gorgas, J., Gil de Paz, A., and Muñoz-Mateos, J. C. (2011). *Formation and evolution of dwarf early-type galaxies in the Virgo cluster. I. Internal kinematics*. A&A, 526, A114

Toloba, E., Guhathakurta, P., van de Ven, G., Boissier, S., Boselli, A., den Brok, M., Falcón-Barroso, J., Hensler, G., Janz, J., Laurikainen, E., Lisker, T., Paudel, S., Peletier, R. F., Ryś, A., and Salo, H. (2014a). *Stellar Kinematics and Structural Properties of Virgo Cluster Dwarf Early-type Galaxies from the SMAKCED Project. I. Kinematically Decoupled Cores and Implications for Infallen Groups in Clusters*. ApJ, 783, 120

Toloba, E., Guhathakurta, P., Peletier, R. F., Boselli, A., Lisker, T., Falcón-Barroso, J., Simon, J. D., van de Ven, G., Paudel, S., Emsellem, E., Janz, J., den Brok, M., Gorgas, J., Hensler, G., Laurikainen, E., Niemi, S.-M., Ryś, A., and Salo, H. (2014b). *Stellar Kinematics and Structural Properties of Virgo Cluster Dwarf Early-type Galaxies from the SMAKCED Project. II. The Survey and a Systematic Analysis of Kinematic Anomalies and Asymmetries*. ApJS, 215, 17

Tonnesen, S., Bryan, G. L., and van Gorkom, J. H. (2007). *Environmentally Driven Evolution of Simulated Cluster Galaxies*. ApJ, 671, 1434

Trentham, N. and Tully, R. B. (2002). *The faint end of the galaxy luminosity function*. MNRAS, 335, 712

Tully, R. B., Courtois, H., Hoffman, Y., and Pomarède, D. (2014). *The Laniakea super-cluster of galaxies*. Nature, 513, 71

Urban, O., Werner, N., Simionescu, A., Allen, S. W., and Böhringer, H. (2011). *X-ray spectroscopy of the Virgo Cluster out to the virial radius*. MNRAS, 414, 2101

Urich, L., Lisker, T., Janz, J., van de Ven, G., Leaman, R., Boselli, A., Paudel, S., Sybilska, A., Peletier, R. F., den Brok, M., Hensler, G., Toloba, E., Falcón-Barroso, J., and Niemi, S.-M. (2017). *Young, metal-enriched cores in early-type dwarf galaxies in the Virgo cluster based on colour gradients*. A&A, 606, A135

Venhola, A., Peletier, R., Laurikainen, E., Salo, H., Lisker, T., Iodice, E., Capaccioli, M., Verdoes Kleijn, G., Valentijn, E., Mieske, S., Hilker, M., Wittman, C., Van de Venn, G., Grado, A., Spavone, M., Cantiello, M., Napolitano, N., Paolillo, M., and Falcón-Barroso, J. (2017). *The Fornax Deep Survey (FDS) with the VST: III. Low Surface Brightness (LSB) dwarfs and Ultra Diffuse Galaxies (UDGs) in the center of the Fornax cluster*. ArXiv e-prints

Vijayaraghavan, R., Gallagher, J. S., and Ricker, P. M. (2015). *The dynamical origin of early-type dwarfs in galaxy clusters: a theoretical investigation*. MNRAS, 447, 3623

Villalobos, Á., De Lucia, G., Borgani, S., and Murante, G. (2012). *Simulating the evolution of disc galaxies in a group environment - I. The influence of the global tidal field*. MNRAS, 424, 2401

Vogelsberger, M., Genel, S., Springel, V., Torrey, P., Sijacki, D., Xu, D., Snyder, G., Nelson, D., and Hernquist, L. (2014). *Introducing the Illustris Project: simulating the coevolution of dark and visible matter in the Universe*. MNRAS, 444, 1518

Voggel, K., Hilker, M., and Richtler, T. (2016). *Globular cluster clustering and tidal features around ultra-compact dwarf galaxies in the halo of NGC 1399*. A&A, 586, A102

Walker, A. G. (1935). *On Riemannian spaces with spherical symmetry about a line, and the conditions for isotropy in general relativity*. The Quarterly Journal of Mathematics, 6, 81

Wannier, P. and Wrixon, G. T. (1972). *An Unusual High-Velocity Hydrogen Feature*. ApJ, 173, L119

Weilbacher, P. M., Duc, P.-A., Fritze v. Alvensleben, U., Martin, P., and Fricke, K. J. (2000). *Tidal dwarf candidates in a sample of interacting galaxies*. A&A, 358, 819

Weinberg, S. (1972). *Gravitation and Cosmology: Principles and Applications of the General Theory of Relativity*, 688

Weinmann, S. M., Lisker, T., Guo, Q., Meyer, H. T., and Janz, J. (2011). *Dwarf galaxy populations in present-day galaxy clusters - I. Abundances and red fractions*. MNRAS, 416, 1197

Wenger, M., Ochsenbein, F., Egret, D., Dubois, P., Bonnarel, F., Borde, S., Genova, F., Jasniewicz, G., Laloë, S., Lesteven, S., and Monier, R. (2000). *The SIMBAD astronomical database. The CDS reference database for astronomical objects*. A&AS, 143, 9

White, S. D. M. and Rees, M. J. (1978). *Core condensation in heavy halos - A two-stage theory for galaxy formation and clustering*. MNRAS, 183, 341

Whitmore, B. C. and Schweizer, F. (1995). *Hubble space telescope observations of young star clusters in NGC-4038/4039, 'the antennae' galaxies*. AJ, 109, 960

Whitmore, B. C., Zhang, Q., Leitherer, C., Fall, S. M., Schweizer, F., and Miller, B. W. (1999). *The Luminosity Function of Young Star Clusters in "the Antennae" Galaxies (NGC 4038-4039)*. AJ, 118, 1551

Willman, B., Governato, F., Wadsley, J., and Quinn, T. (2004). *The origin and properties of intracluster stars in a rich cluster*. MNRAS, 355, 159

Wirth, A. and Gallagher III, J. S. (1984). *The families of elliptical-like galaxies*. ApJ, 282, 85

Wittmann, C. (2014). *The dwarf galaxy population of the Perseus cluster core*. M.Sc. thesis. Zentrum für Astronomie der Universität Heidelberg

Wittmann, C., Lisker, T., Pasquali, A., Hilker, M., and Grebel, E. K. (2016). *Peculiar compact stellar systems in the Fornax cluster*. MNRAS, 459, 4450

Wittmann, C., Lisker, T., Ambachew Tilahun, L., Grebel, E. K., Conselice, C. J., Penny, S., Janz, J., Gallagher, J. S., Kotulla, R., and McCormac, J. (2017). *A population of faint low surface brightness galaxies in the Perseus cluster core*. MNRAS, 470, 1512

Wright, E. L., Eisenhardt, P. R. M., Mainzer, A. K., Ressler, M. E., Cutri, R. M., Jarrett, T., Kirkpatrick, J. D., Padgett, D., McMillan, R. S., Skrutskie, M., Stanford, S. A., Cohen, M., Walker, R. G., Mather, J. C., Leisawitz, D., Gautier III, T. N., McLean, I., Benford, D., Lonsdale, C. J., Blain, A., Mendez, B., Irace, W. R., Duval, V., Liu, F., Royer, D., Heinrichsen, I., Howard, J., Shannon, M., Kendall, M., Walsh, A. L., Larsen, M., Cardon, J. G., Schick, S., Schwalm, M., Abid, M., Fabinsky, B., Naes, L., and Tsai, C.-W. (2010). *The Wide-field Infrared Survey Explorer (WISE): Mission Description and Initial On-orbit Performance*. AJ, 140, 1868

Yagi, M., Koda, J., Komiyama, Y., and Yamanoi, H. (2016). *Catalog of Ultra-diffuse Galaxies in the Coma Clusters from Subaru Imaging Data*. ApJS, 225, 11

Yozin, C. and Bekki, K. (2015). *The quenching and survival of ultra diffuse galaxies in the Coma cluster*. MNRAS, 452, 937

Zhang, H.-X., Peng, E. W., Côté, P., Liu, C., Ferrarese, L., Cuillandre, J.-C., Caldwell, N., Gwyn, S. D. J., Jordán, A., Lançon, A., Li, B., Muñoz, R. P., Puzia, T. H.,

Bekki, K., Blakeslee, J. P., Boselli, A., Drinkwater, M. J., Duc, P.-A., Durrell, P., Emsellem, E., Firth, P., and Sánchez-Janssen, R. (2015). *The Next Generation Virgo Cluster Survey. VI. The Kinematics of Ultra-compact Dwarfs and Globular Clusters in M87*. ApJ, 802, 30

Zhao, Y., Gao, Y., and Gu, Q. (2013). *A Study on the Chemical Properties of Blue Compact Dwarf Galaxies*. ApJ, 764, 44

de Blok, W. J. G. and McGaugh, S. S. (1998). *Testing Modified Newtonian Dynamics with Low Surface Brightness Galaxies: Rotation Curve FITS*. ApJ, 508, 132

de Blok, W. J. G., McGaugh, S. S., and van der Hulst, J. M. (1996). *HI observations of low surface brightness galaxies: probing low-density galaxies*. MNRAS, 283, 18

de Vaucouleurs, G. (1959). *Classification and Morphology of External Galaxies.* Handbuch der Physik, 53, 275

van Dokkum, P. G., Abraham, R., Merritt, A., Zhang, J., Geha, M., and Conroy, C. (2015a). *Forty-seven Milky Way-sized, Extremely Diffuse Galaxies in the Coma Cluster*. ApJ, 798, L45

van Dokkum, P. G., Romanowsky, A. J., Abraham, R., Brodie, J. P., Conroy, C., Geha, M., Merritt, A., Villaume, A., and Zhang, J. (2015b). *Spectroscopic Confirmation of the Existence of Large, Diffuse Galaxies in the Coma Cluster*. ApJ, 804, L26

van Dokkum, P., Abraham, R., Brodie, J., Conroy, C., Danieli, S., Merritt, A., Mowla, L., Romanowsky, A., and Zhang, J. (2016). *A High Stellar Velocity Dispersion and ∼100 Globular Clusters for the Ultra-diffuse Galaxy Dragonfly 44*. ApJ, 828, L6

van den Bergh, S. (1959). *A catalogue of dwarf galaxies*. Publications of the David Dunlap Observatory, 2, 147

van den Bergh, S. (1976). *A new classification system for galaxies*. ApJ, 206, 883

van der Burg, R. F. J., Muzzin, A., and Hoekstra, H. (2016). *The abundance and spatial distribution of ultra-diffuse galaxies in nearby galaxy clusters*. A&A, 590, A20

van der Marel, R. P., de Zeeuw, P. T., Rix, H.-W., and Quinlan, G. D. (1997). *A massive black hole at the centre of the quiescent galaxy M32*. Nature, 385, 610

ACKNOWLEDGMENTS

Thanks also to Daniel Haydon for kindly proofreading the summary and discussion chapter.

My warmest thanks go to my parents, Doris and Arnd Wittmann, for their continuous encouragement and support, and for being the best parents I could think of!

Thanks also to my boyfriend, Günther Ehrlich, for his love, endless patience, and interest in science.

***

This thesis was typeset using the typographical look-and-feel `classicthesis` developed by André Miede. The style was inspired by Robert Bringhurst's seminal book on typography "*The Elements of Typographic Style*". `classicthesis` is available for both LATEX and LYXat https://bitbucket.org/amiede/classicthesis/

Wenn man alles auf physikalische Gesetzmäßigkeiten zurückführen würde, wäre das eine Abbildung mit inadäquaten Mitteln, so als ob man eine Beethoven-Symphonie als Luftdruckkurve darstellte.

— Albert Einstein